Thermomechanical Modeling of Amorphous Polymers Through the Glass Transition Region

Vom Fachbereich Bau- und Umweltingenieurwissenschaften
der Technischen Universität Darmstadt

zur Erlangung des akademischen Grades eines
Doktor-Ingenieurs (Dr.-Ing.)

genehmigte

Dissertation

von

M.Sc. Thomas Blome
aus Groß-Zimmern

Erstreferent:	Prof. Dr.-Ing. habil. F. Gruttmann
Korreferent:	Prof. Dr.-Ing. habil. R. Müller
Tag der Einreichung:	22.06.2022
Tag der mündlichen Prüfung:	14.09.2022

Darmstadt 2022
D 17

Blome, Thomas

Thermomechanical Modeling of Amorphous Polymers Through the Glass Transition Region

Dissertationsort:
Darmstadt, Technische Universität Darmstadt

Tag der Einreichung:	22.06.2022
Tag der mündlichen Prüfung:	14.09.2022

Veröffentlichung:
Jahr der Veröffentlichung der Dissertation auf TUprints: 2022
URI: https://tuprints.ulb.tu-darmstadt.de/id/eprint/22487

Contents

List of Symbols

Symbols related to continuum mechanics

$\alpha_\infty, \alpha_\mathrm{g}$	linear coefficients of thermal expansion
α_l	Prony parameters for thermal stress relaxation
β_l	Prony parameters for entropy relaxation
δ	Kronecker delta
η_l^G	shear viscosity
η_l^K	bulk viscosity
θ	absolute temperature
θ_0	reference temperature
θ_g	glass transition temperature
ρ_0	referential mass density
τ_l^K, τ_l^G	bulk and shear relaxation times
χ_l, ζ_l	internal variables
ψ	specific Helmholtz energy
$\Psi_\alpha, \Psi_\beta, \Psi_G, \Psi_K$	prefactors of transient Helmholtz energy
ψ_i	rubbery material parameters
Ω	reference configuration
a	thermoviscoelastic shift function
A	referential area
B	continuum body
$\mathcal{B}_l, \mathcal{C}_l$	rate of internal variables
$c, c_\infty, c_\mathrm{g}$	heat capacities
C_1, C_2	Williams-Landel-Ferry constants
$\tilde{C}_i$	glassy material parameters
$\mathcal{D}_\mathrm{int}$	internal dissipation
g	specific Gibbs energy
G_∞, G_g	equilibrium and glassy shear modulus
G_l	Prony parameters for shear relaxation
$\mathcal{H}_\mathrm{e}$	structural thermoelastic heating
$\mathcal{H}_\mathrm{in}$	structural thermoviscoelastic heating
K_∞, K_g	equilibrium and glassy bulk modulus
K_l	Prony parameters for bulk relaxation
m	number of Maxwell elements
M	referential mass
$\mathcal{P}$	referential mechanical power
$\mathcal{Q}$	referential thermal power
R	heat source
S	specific entropy
$\mathcal{S}$	entropy

t	point in time
$\mathcal{U}$	total internal energy
U	specific internal energy
U_{p}	specific potential internal energy
v	current volume
V	referential volume
$\boldsymbol{I}$	second order unit tensor
$\mathbb{1}$	fourth order unit tensor
$\boldsymbol{\varepsilon}$	strain tensor
$\boldsymbol{\lambda}$	spatial thermal conductivity tensor
$\boldsymbol{\sigma}$	generalized stresses
$\boldsymbol{\mathcal{A}}_l$	rate of internal variables
$\boldsymbol{B}$	referential body forces
$\boldsymbol{C}$	Right Cauchy-Green tensor
$\boldsymbol{E}$	Green-Lagrange strain
$\boldsymbol{\mathcal{E}}_l$	internal variables
$\boldsymbol{F}$	deformation gradient
$\boldsymbol{H}$	material Hencky strain
$\boldsymbol{\mathcal{J}}$	linear momentum
$\boldsymbol{\mathcal{L}}_{\mathcal{O}}$	angular momentum
$\boldsymbol{M}$	thermal stresses
$\boldsymbol{N}$	referential unit normal
$\boldsymbol{P}$	First Piola-Kirchhoff stresses
$\boldsymbol{q}$	spatial heat flux
$\boldsymbol{Q}$	referential heat flux
$\boldsymbol{S}$	Second Piola-Kirchhoff stresses
$\boldsymbol{T}$	referential traction vector
$\boldsymbol{u}$	displacement vector
$\boldsymbol{x}$	current position
$\boldsymbol{X}, \boldsymbol{Y}$	reference position
$\boldsymbol{\mathcal{Z}}_l$	internal variables

Symbols related to algorithms

Δt_n	nth time increment
ϵ_r, ϵ_a	relative and absolute error tolerances
θ_I	element temperature degrees of freedom
a_{ij}, b_i, c_i	Runge-Kutta coefficients
d_{IK}	element nodal capacitance
f_I	nodal heat generation
g	residuals of balance equations
$\mathcal{H}_l, \mathcal{R}_l$	residuals of evolution equations
N_I	Lagrangian shape function
s	number of stages
t_n	nth time step
$\mathcal{V}$	space of test functions
$\boldsymbol{\Lambda}$	matrix of Lagrange multipliers

$\mathbf{1}$	identity matrix
$\boldsymbol{B}_I$	B-matrix
$\mathbf{B}$	boundary residual
$\mathbf{D}, \boldsymbol{d}_e, \boldsymbol{d}_{IK}$	damping matrices
$\boldsymbol{e}$	element vector of internal variables
$\hat{e}$	local stepsize error
$\mathbf{E}$	global vector of internal variables
$\mathbf{F}, \mathbf{R}$	global residuals
$\boldsymbol{f}_e, \boldsymbol{f}_I$	element nodal values
$\boldsymbol{g}$	g-vector
$\mathbf{G}, \boldsymbol{G}$	residuals of balance equations
$\mathbf{K}, \boldsymbol{k}_e, \boldsymbol{k}_{IK}$	stiffness matrices
$\mathbf{L}, \boldsymbol{L}, \mathcal{R}_l$	residuals of evolution equations
$\mathbf{M}$	filter matrix for boundary conditions
$\mathbf{P}, \mathcal{P}_l$	rate of internal variables
$\boldsymbol{u}_I$	element translational degrees of freedom
$\mathbf{V}, \mathbf{U}$	global degrees of freedom

Operators

$\otimes$	dyadic product
$\cdot$	scalar product
$\times$	vector product
δ	variation
Δ	increment operator
det	determinant operator
dev	deviator operator
Div	material divergence operator
grad	spatial gradient operator
Grad	material gradient operator
tr	trace operator
$\mathbf{A}$	assembly operator

Abstract

In this thesis, we propose a novel thermodynamically consistent constitutive framework to model amorphous polymers through the glass transition region based on the internal variables approach. The model assumes the thermorheological simplicity hypothesis and covers different relaxation mechanisms related to bulk, shear, thermal stress and entropy relaxation, which are implemented by means of Prony parameters. Although the model is restricted to sufficiently slow processes, it is capable to span a wide range of temperatures of about $\pm 75\,^{\circ}\mathrm{C}$ around a defined reference temperature and predicts finite deformations up to engineering strain levels of $15\,\%$. A key ingredient is the thermoviscoelastic shift function, which is defined in terms of the polymer's potential internal energy. This allows to capture a variety of material properties intrinsic to amorphous polymers, such as physical aging and pseudo-yielding in tension and compression. In addition, we provide detailed information on the entire algorithmic solution procedure. The spatial discretization is accomplished using the finite element method, while diagonally implicit Runge-Kutta methods serve as the temporal integrator. Finally, we validate the constitutive model on four different polymeric systems, which comprise one thermoplastic (polyvinyl butyral) and three thermosets. The validation includes dilatometric and calorimetric experiments, tension and compression tests at various temperatures as well as three-point and four-point bending tests of laminated glasses with a polyvinyl butyral interlayer.

Zusammenfassung

In dieser Arbeit wird ein neuartiges Materialmodell zur Simulation von thermorheologisch einfachen, amorphen Polymerstrukturen entwickelt, welches auf dem Konzept der internen Variablen beruht. Die thermodynamisch konsistenten Materialgleichungen umfassen unterschiedliche Relaxationsmechanismen, welche sowohl das zeitabhängige Verhalten der Volumen- und Gestaltänderung, als auch die Relaxation der thermischen Spannungen und der Entropie abbildet. Das diskrete Relaxationsspektrum wird mit Hilfe von Prony-Parametern umgesetzt. Das Materialmodell umspannt einen weiten Temperaturbereich von ungefähr $\pm 75\,°C$ um eine definierte Referenztemperatur und ermöglicht die Wiedergabe von nichtlinearen Deformationen bis zu $15\,\%$ Ingenieursdehnung, wobei von hinreichend langsamen Deformationsvorgängen ausgegangen wird. Ein besonderes Merkmal stellt der thermoviskoelastische Shiftfaktor dar, welcher über die potentielle innere Energie des Polymers definiert ist. Dies ermöglicht die numerische Vorhersage unterschiedlicher konstitutiver Phänomene, wie beispielsweise physikalische Alterung und fließähnliches Verhalten von amorphen Polymeren unter Zug- als auch Druckbeanspruchung. Darüber hinaus wird eine umfangreiche Darstellung der algorithmischen Umsetzung bereitgestellt. Dies umfasst zum einen die Ortsdiskretisierung mit Hilfe der Methode der finiten Elemente, als auch die Zeitdiskretisierung unter Verwendung von diagonal-impliziten Runge-Kutta Verfahren. Das Modell wird schließlich anhand einer Reihe von experimentellen Versuchen an einem Thermoplast (Polyvinylbutyral) und drei Duroplasten validiert. Hierzu zählen dilatometrische und kalorimetrische Simulationen, die numerische Berechnung von Zug- und Druckversuchen bei unterschiedlichen Temperaturen sowie Drei- und Vierpunktbiegeversuche von Verbundsicherheitsgläsern mit einer Zwischenschicht aus Polyvinylbutyral.

Danksagung

Diese Arbeit ist das Ergebnis von vier spannenden und herausfordernden Jahren als wissenschaftlicher Mitarbeiter am Fachgebiet Festkörpermechanik der TU Darmstadt. Viele Menschen haben zu dem erfolgreichen Gelingen dieser Arbeit beigetragen, welchen ich an dieser Stelle meinen Dank aussprechen möchte.

Besonderer Dank gilt meinem Betreuer Prof. Dr.-Ing. Friedrich Gruttmann, der mir die Umsetzung eines interessanten und sehr vielseitigen Forschungsprojekts ermöglichte. Das dabei entgegengebrachte Vertrauen erlaubte mir größtmöglichen Freiraum in der Ausgestaltung meiner Arbeit. Für die fortwährende Unterstützung möchte ich mich recht herzlich bedanken. Desweiteren bedanke ich mich bei Prof. Dr.-Ing. Ralf Müller für die unkomplizierte Übernahme des Korreferats und dem damit einhergehenden Interesse an meiner Arbeit. Bedanken möchte ich mich ebenfalls bei Prof. Dr.-Ing. Werner Wagner für den ein oder anderen hilfreichen Tipp zur Implementierung während der wiederkehrenden Softwareupdates. Großer Dank gilt der finanziellen Unterstützung des Projektes durch die Deutsche Forschungsgemeinschaft (DFG) sowie der zeitweisen finanziellen Unterstützung von Prof. Dr.-Ing. Wilfried Becker, ohne welche ich diese Arbeit nicht hätte fertigstellen können.

Ansonsten verbleiben viele schöne Erinnerungen an die gemeinsame Zeit mit meinen ehemaligen Kollegen. Besonderer Dank gilt Dr.-Ing. Simon Klarmann für das stete Interesse an der Betreuung meiner Abschlussarbeiten während meiner Zeit als Student. Sein Blick und Verständnis für zahlreiche fachliche Themen fernab des Tellerrands haben mich stets beeindruckt. Meinem Büronachbarn Dr.-Ing. Jan Zoller gilt ein besonderes Dankeschön für die vielen fachlichen und außerfachlichen Diskussionen sowie die spontanen, wiederkehrenden Freizeitaktivitäten. Auch den vielen neuen Mitarbeitern, welche erst spät das Institutsleben bereichert haben, möchte ich an dieser Stelle meinen Dank aussprechen. Insbesondere die interessanten Gespräche mit meinem Bürokollegen Hari Kisan Thammineni werde ich immer positiv in Erinnerung behalten. Ebenso gilt mein Dank allen Mitarbeitern des Fachgebiets Strukturmechanik für das freundliche Arbeitsverhältnis, welches ich dort während meiner kurzen Zeit immer genossen habe. Weiterhin bedanke ich mich bei den Studierenden Steffen Bißwanger und Mariana Lara für ihren unterstützenden Beitrag zu dieser Arbeit.

Ein herzliches Dankeschön gilt der wertvollen Unterstützung durch unsere Sekretärin Frau Angelika Prießnigg, die für uns alle zu jeder Zeit ein offenes Ohr hatte und alle im Hintergrund anfallenden Aufgaben erledigte, so dass wir ungestört unserer Forschung nachgehen konnten.

Auf den uneingeschränkten Rückhalt meiner Familie konnte ich mich in jeder Lebenslage verlassen. Meinen Eltern und meiner Schwester gilt abschließend mein größter Dank.

Groß-Zimmern, September 2022 Thomas Blome

1. Introduction

1.1. Motivation and State of the Art

Amorphous polymers such as polyvinyl butyral form an essential part in structural components such as laminated safety glass often encountered in civil engineering applications and the automobile industry, see Figure 1.1. Because of their special chemical constitution, amorphous polymers exhibit some outstanding material characteristics. These include strong time-dependent stiffness parameters as well as a high sensitivity with respect to environmental changes in terms of moisture or thermal radiation. Sometimes, however, these effects are detrimental to the structural integrity of the laminate structure, causing delaminations between the interlayer material and the glass [1]. Since industrial applications naturally demand an on-going improvement to develop tailor-made material properties to account for evolving needs in specific application scenarios (for example sound insulation, UV protection, decorative glazing, safety and security applications, photovoltaic modules), polymeric interlayers of laminated safety glass need to be thoroughly tested prior to application, see Figure 1.1. However, in order to circumvent time-consuming, costly experimental settings, it is desirable to simulate the material behavior numerically by means of a computer. This necessitates the development of mathematically well-defined and physically motivated constitutive equations to model amorphous polymers subjected to different load situations.

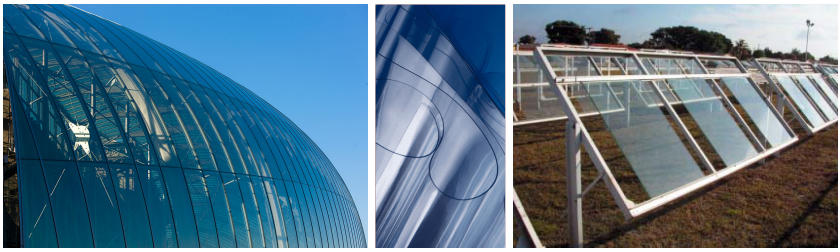

Figure 1.1.: Illustration of polymeric interlayer applications by the example of polyvinyl butyral. From left to right: Strasbourg Railway Station, France [2], Mowital® Thin Film interlayer sheets [3], testing facility of laminated glass at the DuPont Weathering Site, Hileah Florida [1]. Laminated safety glass contains a thin polymeric interlayer such as those depicted in the middle.

The literature dealing with the constitutive modeling of amorphous polymers provides several distinct approaches, each of them with their own merits and shortcomings. To give the reader an impression on the various modeling approaches, the following lists compile some of these models in terms of the thermodynamic state the polymer may take on. The lists are far from being comprehensive and we refer to the literature cited therein for further information. Unless stated otherwise, the different models have

in common that they allow for the three-dimensional, phenomenological modeling of amorphous polymers undergoing large strains using some form of internal variables.

The following references focus on the constitutive modeling below the glass transition. The results of the papers mainly feature uniaxial stress-strain relations for different strain rates and temperature states:

- [4] base their model on the Eulerian Hencky strain and use a multiplicative decomposition of the deformation gradient into elastic, viscoplastic and thermal parts. Mechanical material parameters depend linearly on temperature, while thermal parameters such as specific heat and thermal conductivity are taken as constant. The material model predicts strain softening and strain hardening and is validated on polycarbonate. The authors also perform three-point bending tests and corresponding FEM simulations.
- [5] develop a constitutive model to capture the strain rate-dependent behavior, thereby allowing for pressure dependency. The authors validate their model on an epoxy, polycarbonate and on poly(methyl methacrylate) using uniaxial tension and compression tests at room temperature and also perform Dynamic Mechanical Thermal Analyses. Thermal properties such as the specific heat capacity are neglected.
- [6] establish a thermodynamically consistent material model which accounts for strain softening and strain hardening behavior and validate it for compressive (including cyclic loading) and torsional loads on polycarbonate. The deformation gradient is split into elastic, viscoplastic and thermal contributions.
- [7] enhance their purely mechanical model published earlier [8] to a fully coupled, thermodynamically consistent model incorporating thermoviscoplastic effects. The model is based on the free volume theory and an additive split of the Lagrangian Hencky strain tensor into elastic and plastic parts. Bulk modulus, coefficient of thermal expansion and specific heat capacity are assumed to be constant. The authors perform tests on polycarbonate to validate their model. The paper also includes details on the numerical treatment of the constitutive equations.
- [9, 10] develop a coupled elasto-viscoplastic model using a multiplicative split of the deformation gradient into elastic and plastic components. The model assumes a constant coefficient of thermal expansion and a linearly temperature-dependent specific heat capacity. A backstress tensor allows to predict the Bauschinger effect. The authors validate their model in [10] on three representative polymers. The model is not only thermodynamically consistent and fully thermomechanically coupled, but also covers the glass transition region of amorphous polymers.

The references to follow provide constitutive frameworks which are capable of modeling amorphous polymers through the glass transition and, therefore, span a wide range of temperature states. As above, the results of the papers mainly feature uniaxial stress-strain relations for different strain rates and temperature states:

- [11] develop a mechanical constitutive model which is based on a fictive temperature theory. The model uses a shift function which depends on the absolute as well as a fictive temperature and, therefore, allows to incorporate physical aging effects. However, the model does not consider heat flux and related thermal variables such as the specific heat. The authors validate their model on poly(ethylene

terephthalate) by simulating uniaxial tensile tests in the small and large strain regime in a companion paper.

- [12] extend their material model developed in [9] to span the glass transition temperature. The model is capable of reproducing experimental stress-strain curves of three representative amorphous polymers. The authors use a bilinear temperature dependence for the coefficient of thermal expansion and do not consider physical aging effects. The model is thermodynamically consistent and fully coupled.
- [13] develop an elasto-viscoplastic model accounting for temperature changes and validate the model on a poly(methyl methacrylate) and a polycarbonate sample below and in the glass transition region. The authors use the tripartite split of the deformation gradient into elastic, viscoplastic and thermal parts. The model uses empirical equations to account for the temperature dependence of various material parameters such as the density, thermal conductivity, specific heat capacity and Poisson's ratio. No heat flux is considered and, therefore, the authors only consider homogeneous temperature fields.
- [14] use an effective temperature theory to model amorphous polymers, including temperature and strain rate dependency as well as physical aging. The fully coupled, thermodynamically consistent material model also predicts enthalpy relaxation effects. The authors apply a multiplicative split of the deformation gradient into elastic and viscous deformation. However, thermally induced deformation effects are neglected. The constitutive model is validated on a tBA-co-XLS polymer.

Finally, we provide a list of references which focus on the constitutive modeling of amorphous polymers in and above the glass transition:

- [15] formulate constitutive equations which center on the mechanical behavior of poly(ethylene terephthalate)-glycol and poly(ethylene terephthalate) including rate and temperature effects[1]. The authors use a split of the deformation gradient into elastic and plastic parts and account for the shear stiffness drop through the glass transition region by means of hyperbolic functions. The model predicts yield and strain hardening behavior at large strains. However, it neither includes heat flux nor captures physical aging effects.
- Other publications directly relating to the constitutive investigation into polyvinyl butyral (PVB) as an interlayer material commonly found in laminated safety glass applications generally apply engineering approaches [16–31]. These are predominantly characterized by Prony series approximations of the shear stress response paired with the application of a time-temperature shift using the famous WLF approach. Hence, these material models are restricted to *small* strains under *homogeneous* temperature states within the rubbery region. The authors of [32] combine the linear-viscoelastic approach with an hyperelastic mechanism to incorporate large strains in the rubbery region. Literature covering experimental investigations into PVB samples subjected to different strain rates in uniaxial tension include [27, 33–38].

A quite different approach to model amorphous polymers through the glass transition region is described in [39]. Here, the authors develop a thermodynamically consistent *thermoviscoelastic* constitutive model based on *rational thermodynamics* capable to predict yield-like behavior, physical aging, as well as volume, stress and entropy relaxation.

[1] The title of the paper reads "in and above the glass transition". However, within the document also the glassy state is included.

A key feature of the material model is the so-called *potential internal energy clock* [40]. In a companion paper [41], the authors do extensive validation of various mechanical and thermal material properties on four different polymer systems.

As outlined above, the literature is abundant with constitutive models for amorphous polymers, so why should we make the effort and develop another one? There are several reasons to do so. First, many of the proposed material models are restricted to certain temperature intervals with respect to the polymer's glass transition. However, in common civil engineering applications, many plastics such as commercial polyvinyl butyral are subject to variations in temperature *through* their glass transition region. Thus, a lot of existing constitutive models are inadequate for this purpose. Second, some of the proposed constitutive equations do not fulfill established physical principles such as the first and second law of thermodynamics. Usually, this is not always obvious and requires a closer look at the stress-strain relations, since these models are often declared as being "thermomechanical" in the sense that they contain some form of temperature-dependent material parameters. Third, even if they fulfill these principles, they are often lacking the ability to predict essential properties of amorphous polymers, for example physical aging. Fourth, the numerical solution of nonlinear, time-dependent constitutive equations requires the use of efficient time integration schemes. The proper choice of an integrator is *at least* as important as the constitutive framework itself. What is more, the mathematical structure of the constitutive equations generally imposes restrictions on the type of integrator. Hence, it is vital to consider these limitations *prior* to the material modeling process.

1.2. Objectives

This thesis pursues three different but related goals. The first goal is to develop thermodynamically consistent constitutive equations to model amorphous polymers through the glass transition region by means of *internal variables*. Naturally, this goes well beyond the usual mechanical modeling in terms of time- and temperature-dependent shear stiffness properties. In contrast, modeling amorphous polymers under *nonisothermal* conditions requires the full spectrum of relaxation mechanisms, including bulk relaxation, entropy relaxation as well as relaxation with respect to thermal expansion. The former is critical when we seek to capture aging effects in amorphous polymers within the glassy regime, while the latter is particularly important when variations in temperature induce thermal stresses. Besides the time dependency of material properties, the constitutive model should equally be capable to reproduce the experimentally observed temperature dependencies of material parameters. This necessitates a fully coupled thermomechanical setting by evaluating the first law of thermodynamics next to the balance of linear momentum. In addition, we demand that the constitutive model properly predicts other material characteristics intrinsic to amorphous polymers, such as yield-like behavior in both tension and compression. In doing so, we restrict ourselves to moderate strains (up to 15 % engineering strain) and sufficiently slow processes, but otherwise allow for finite deformations and large temperature changes (usually $\pm 75\,^{\circ}\mathrm{C}$ around a reference temperature).

The second goal concerns the algorithmic solution strategy. The constitutive framework based on the internal variables approach allows the application of mathemati-

cally well-defined one-step time integration schemes in the form of diagonally implicit Runge-Kutta methods and iteration-free Rosenbrock methods. The application of efficient time integration schemes to run transient simulations was the major incentive to develop a new thermoviscoelastic material formalism in terms of internal variables. Furthermore, embedded Runge-Kutta methods provide a simple means to implement an adaptive time-stepping mechanism, which is essential when solving highly transient initial boundary value problems. We therefore put special emphasis on the numerical treatment of the constitutive equations, but equally highlight the spatial discretization in terms of the finite element method.

The third and final goal of this thesis is to validate the proposed constitutive framework and to verify its numerical implementation on different polymeric systems under various load scenarios. This gives an impression to which extend the material formulation is able to predict the most salient features observed experimentally on amorphous polymers.

1.3. Outline of the Thesis

The content of this thesis is arranged into three distinct parts, see Figure 1.2.

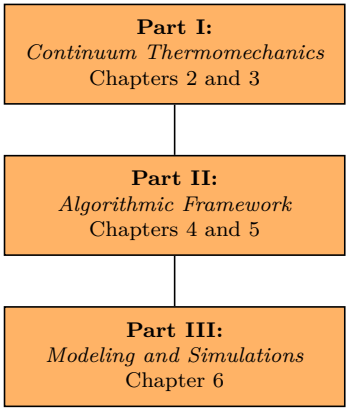

Figure 1.2.: Outline of the thesis.

Chapter 2 in the first part introduces the fundamentals associated with continuum thermomechanics. This includes not only the general concepts (kinematics, balance principles and dissipation postulate) and terminology, but also an overview and comparison of several thermodynamic theories found in the literature. This allows to classify the phenomenological constitutive modeling approach used in this thesis, which bases on the use of internal variables. Furthermore, a general constitutive framework is presented, which is essential to formulate objective constitutive equations in line with the fundamental laws of continuum thermodynamics.

Chapter 3 deals with the actual constitutive modeling process of amorphous polymers. First, important material characteristics are outlined. These should be taken

into account when modeling amorphous polymers through a wide range of temperatures. Besides some microscopic aspects, we discuss phenomenological principles such as time-temperature-pressure equivalences and physical aging. Special attention is on polyvinyl butyral, a polymer of high practical relevance in industrial applications. Following these constitutive basics of amorphous polymers, the simplest thermoviscoelastic material formulation based on the internal variables approach is presented. This serves as a stepping stone to the constitutive extension developed in this thesis to model amorphous polymers through the glass transition region. A key ingredient of this model is the so-called potential internal energy clock. Finally, the proposed constitutive framework is compared with related constitutive formulations in terms of rational thermodynamics.

Chapter 4 presents the algorithmic framework, thereby initiating the second part of this thesis. Here, the focus is on the global algorithms applied to solve transient problems in the context of finite thermoviscoelasticity of quasistatic processes. Specifically, we first apply the finite element method for the spatial discretization, followed by the temporal integration using diagonally implicit Runge-Kutta methods. In doing so, we discuss the complete linearization procedure and derive expressions for the effective global stiffness matrix and the corresponding residual vector. Runge-Kutta time integrators are often equipped with an embedded scheme for automatic step size control. We discuss these at the end of the chapter.

In **Chapter 5** we continue the algorithmic procedure with the focus on the local level. That is, the balance of linear momentum and energy are considered for a single finite element to provide a closer link to the actual implementation of finite element code into existing FEM software. In addition, we discuss the implementation of the nonlinear thermoviscoelastic constitutive model proposed in Chapter 3. Specifically, the general procedure to derive the consistent material tangent is provided in detail, along with specific algorithmic steps concerning the update of the internal variables at integration point level. Finally, we discuss some problems related to the integration of the evolution equations of the internal variables, provide some information on the storage requirements and briefly resume the step size adaptivity on integration point level.

Chapter 6 deals with the modeling and simulation of amorphous polymers and forms the third part of this thesis. More precisely, the proposed constitutive model is validated on four different polymeric systems, including polyvinyl butyral as a representative for amorphous thermoplastics and three further thermosetting polymers. The validation includes a wide range of different experimental settings such as dilatometry, calorimetry as well as uniaxial tension and compression tests at various temperatures. Finally, we simulate three-point and four-point bending tests of laminated glasses with a polyvinyl butyral interlayer.

Part I.

Continuum Thermomechanics

2. Fundamentals of Continuum Thermomechanics

This chapter serves as an introduction to some of the fundamental concepts of continuum thermomechanics. The order of individual sections follows the general structure found in most textbooks on the subject. We begin with the description of the kinematics of deformable bodies, followed by the fundamental balance relations and the dissipation postulate. A separate section briefly summarizes different thermodynamic theories in order to give a bigger picture on how to classify the approach followed in this thesis. As the entire numerical setting is based on the Lagrangian formalism, we will restrict ourselves solely to the material description. Finally, we give an overview of important principles of material modeling and derive a thermodynamic consistent constitutive framework based on the internal variables approach. This forms the basis for the phenomenological constitutive description of polymers in subsequent chapters.

2.1. Kinematics of Finite Deformations

In this section, we will introduce some basic notions concerning the geometric description of a continuum body in the three-dimensional space. This comprises a few technical details such as the definition of configurations to formally describe the geometry of the motion of a body. Afterwards we specify the deformation as a mapping between different configurations, thereby deriving an important kinematic quantity, the deformation gradient. Finally, we present a whole family of nonlinear strain tensors and provide two useful ways how to decompose them.

2.1.1. Motion of a Body

From a macroscopic perspective a *continuum body* B consists of matter which is continuously distributed throughout the space and is characterized by certain physical properties such as mass and temperature. The continuum itself consists of a fixed set of an infinite number of material points $P \in B$. The simultaneous position of the set of material points which constitute the body in the three-dimensional Euclidean vector space $\mathbb{E}^3$ is called a *configuration* χ of the body. That is, a configuration is defined as a one-to-one mapping

$$\chi : \begin{cases} B \to \chi(B) \subset \mathbb{E}^3, \\ P \mapsto \boldsymbol{x} = \chi(P), \end{cases} \tag{2.1}$$

representing a smooth mapping of the body onto a region of the three-dimensional Euclidean space. The vector $\boldsymbol{x}$ is called the *current* or *spatial position* of the material point P at time t. As time passes, the continuum will possibly move and occupy different regions in the three-dimensional space at distinct instants of time $t \in \mathbb{R}$. A sequence of

mappings which defines the configurations at arbitrary times t is called the *motion* of a body

$$t \mapsto \chi_t : \begin{cases} B \to \chi_t(B) \subset \mathbb{E}^3, \\ P \mapsto \boldsymbol{x} = \chi_t(P), \end{cases} \tag{2.2}$$

which takes place during the time interval $T = [t_0, t_\Omega] \subset \mathbb{R}$. The time-dependent configuration $\chi_t(\cdot) = \chi(\cdot, t)$ is called the *current configuration*. In order to clearly identify each material point $P \in B$, a *reference configuration* is defined. Specifically, the *fixed* configuration

$$R : \begin{cases} B \to R(B) \subset \mathbb{E}^3_R, \\ P \mapsto \boldsymbol{X} = R(P) \end{cases} \tag{2.3}$$

uniquely designates the material points by its inverse mapping $P = R^{-1}(\boldsymbol{X})$, where $\boldsymbol{X} \in R(B)$ is called the *reference* or *material position* of the material point $P \in B$.

Remark 1. *Note that the choice of the reference configuration is arbitrary. Further note that, while the reference configuration is not required to be occupied by the body at any time during the course of its motion, it is nevertheless possible to choose a special current configuration at a fixed time t_R as the reference configuration. It is usually chosen in such a way that it corresponds to a natural stress-free state of the continuum.*

To summarize some of the notions introduced above, Figure 2.1 depicts a continuum body B during its motion through the Euclidean space.

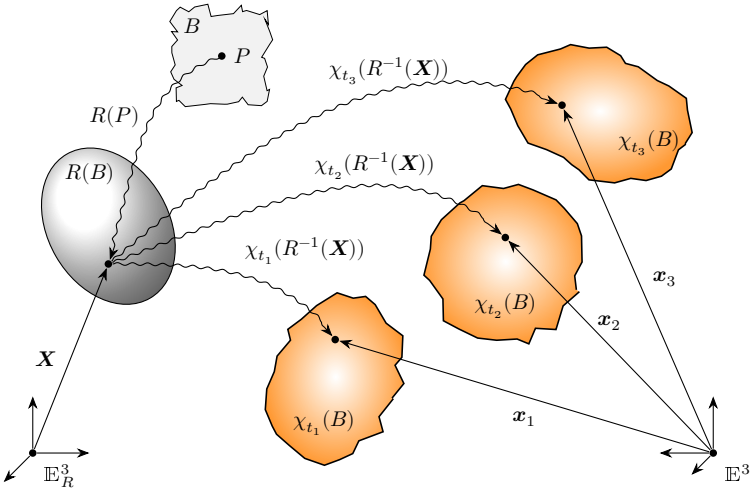

Figure 2.1.: The motion of a continuum body B by the example of three instants of time t through the Euclidean vector space $\mathbb{E}^3$. The current position $\boldsymbol{x}$ of material point $P = R^{-1}(\boldsymbol{X})$ at each instant is uniquely identified by its reference position $\boldsymbol{X}$.

2.1.2. Deformation of a Body

By combining equations (2.2) and (2.3) we can now describe the spatial position $\boldsymbol{x} \in \chi_t(B)$ of any material point $P \in B$ through its material position $\boldsymbol{X} \in R(B)$ at any instant of time $t \in \mathbb{R}$ by means of the vector function

$$\boldsymbol{x} = \chi_t(P) = \chi_t(R^{-1}(\boldsymbol{X})) = \boldsymbol{\varphi}_t(\boldsymbol{X}) = \boldsymbol{\varphi}(\boldsymbol{X}, t), \tag{2.4}$$

where the composition $\boldsymbol{\varphi}_t := \chi_t \circ R^{-1}$ is referred to as the *deformation* of the continuum. Assuming that the vector function (2.4) is continuously differentiable we can form its Taylor series expansion in the first argument as

$$\boldsymbol{\varphi}(\boldsymbol{Y}, t) = \boldsymbol{\varphi}(\boldsymbol{X}, t) + \frac{\partial \boldsymbol{\varphi}}{\partial \boldsymbol{X}}(\boldsymbol{X}, t)(\boldsymbol{Y} - \boldsymbol{X}) + \mathcal{O}(||\boldsymbol{Y} - \boldsymbol{X}||^2). \tag{2.5}$$

The derivative term in equation (2.5) is an important measure of deformation in classical continuum mechanics. It is called the *material deformation gradient* (the gradient with respect to the material position $\boldsymbol{X} \in R(B)$) and defined as

$$\boldsymbol{F}(\boldsymbol{X}, t) = \mathrm{Grad}\boldsymbol{\varphi}_t(\boldsymbol{X}) = \frac{\partial \boldsymbol{\varphi}}{\partial \boldsymbol{X}}(\boldsymbol{X}, t). \tag{2.6}$$

The deformation gradient is an unsymmetric second-order *two-point tensor*, that is it maps line elements (i.e. tangent vectors) between *distinct* configurations. Thus, it characterizes the behavior of the motion in the neighborhood of a material point. To demonstrate this we define the vectors $d\boldsymbol{X} := \boldsymbol{Y} - \boldsymbol{X}$ and $d\boldsymbol{x} := \boldsymbol{\varphi}(\boldsymbol{Y}, t) - \boldsymbol{\varphi}(\boldsymbol{X}, t)$ and choose the two position vectors in the reference configuration to be very close to each other such that $||\boldsymbol{Y} - \boldsymbol{X}|| \to 0$. Hence, in the limit case from the Taylor series (2.5) we derive the relation

$$d\boldsymbol{x} = \boldsymbol{F}(\boldsymbol{X}, t) d\boldsymbol{X}. \tag{2.7}$$

The *line map* (2.7) clearly defines a *linear transformation* which generates a material line element $d\boldsymbol{x} \in \chi_t(B)$ in the current configuration by applying the deformation gradient on a material line element $d\boldsymbol{X} \in R(B)$ in the reference configuration of the *same* material point $P \in B$ as shown in Figure 2.2. We now define the reference configuration of a continuum body B as the current configuration $R(B) := \chi_{t_0}(B)$ occupied by the continuum at some instant of time t_0 such that each material point $P \in B$ is identified by its reference position $\boldsymbol{X} = \chi_{t_0}(P) \in \chi_t(B)$ (see also Remark 1). This motivates the introduction of the *displacement vector*

$$\boldsymbol{u} = \boldsymbol{\varphi}_{t_0}(\boldsymbol{X}, t) - \boldsymbol{X} = \boldsymbol{x} - \boldsymbol{X}, \tag{2.8}$$

where $\boldsymbol{\varphi}_{t_0}(\boldsymbol{X}, t) = \chi_t(R^{-1}(\boldsymbol{X})) = \chi_t(\chi_{t_0}^{-1}(\boldsymbol{X}))$. Thus, the difference between the present and the past position vectors describes the displacement of the continuum. Note that our definition of the reference configuration as a special current configuration is a prerequisite for the physical significance of expression (2.8).

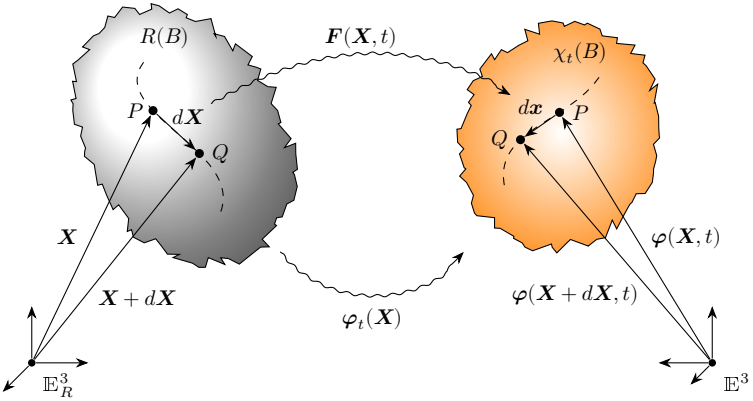

Figure 2.2.: Mapping of line elements at a material point P by applying the deformation gradient $\boldsymbol{F}$ on a tangent vector $d\boldsymbol{X}$ in the reference configuration $R(B)$ to generate the corresponding tangent vector $d\boldsymbol{x}$ in the current configuration $\chi_t(B)$ along the same (deformed) material line.

2.1.3. Introduction to Generalized Strains

In Section 2.1.2 we introduced some basic notions to describe general changes a continuum body experiences in the course of time, for example a change of its position in space via the displacements $\boldsymbol{u}$ or — in a more *local view* — the change of line elements at a material point by means of the deformation gradient $\boldsymbol{F}$. In this section, we will take a closer look at the later concept and provide further (local) deformation measures required for the specification of constitutive equations and the finite element implementation in upcoming sections. Specifically, following the ideas of [42, 43] we define the *family of generalized strain tensors*

$$\boldsymbol{\varepsilon}(\boldsymbol{C}) := \begin{cases} \frac{1}{k}\left(\boldsymbol{C}^{\frac{k}{2}} - \boldsymbol{I}\right) & \text{if } k \neq 0, \\ \frac{1}{2}\ln(\boldsymbol{C}) & \text{if } k = 0, \end{cases} \tag{2.9}$$

where $k \in \mathbb{R}$, $\boldsymbol{C} = \boldsymbol{F}^T\boldsymbol{F}$ is the *right Cauchy-Green tensor* and $\boldsymbol{I}$ is the second-order identity tensor. If, for example, $k = 2$ we identify the so-called *Green-Lagrange strain tensor*

$$\boldsymbol{E} = \frac{1}{2}\left(\boldsymbol{F}^T\boldsymbol{F} - \boldsymbol{I}\right). \tag{2.10}$$

This type of strain is likely to be the first to be introduced in any textbook on the description of nonlinear kinematics of continua. On the other hand, the special case $k = 0$ recovers the *(material) logarithmic strains*

$$\boldsymbol{H} = \frac{1}{2}\ln\left(\boldsymbol{F}^T\boldsymbol{F}\right), \tag{2.11}$$

which are also referred to as the *true strains* or *Hencky strains* [44–46]. These are not as common as the former. However, they will play a crucial role in the material

modeling of polymers at finite deformations since they are furnished with some useful properties (see Remark 2). Further strain types provided by definition (2.9) are, among others, the *Biot strain* ($k = 1$) and the (material) *Almansi strain* ($k = -2$). The motivation behind the introduction of strain tensors is to clearly separate deformations which include changes in shape and size from those which do not. The latter are called *rigid body motions*. These are characterized by pure translations or rotations (or a combination of both) and will not change the position of material points relative to each other. In contrast to the deformation gradient, strain tensors vanish in the case of rigid body motions. Note that the strain family (2.9) solely pertains to the reference configuration. A corresponding definition of a family of generalized strain tensors in the current configuration may be found in the literature, see [45, p. 4] for example. As for every second-order tensor, the strain tensor $\boldsymbol{\varepsilon}$ may be decomposed into a *spherical* and a *deviatoric part*

$$\boldsymbol{\varepsilon} = \frac{1}{3}(\mathrm{tr}\boldsymbol{\varepsilon})\boldsymbol{I} + \mathrm{dev}\boldsymbol{\varepsilon}. \tag{2.12}$$

The first part is related to the volumetric deformation, while the second part describes changes of the shape of the continuum body.

Remark 2. *To contrast some properties of the Green-Lagrange and the Hencky strain tensors we consider an incompressible isotropic material which is deformed under uniaxial tension such that its length in the deformed state equals twice its initial length. In this case the cartesian components of the deformation gradient F_{ij}, the Green-Lagrange strain E_{ij} and the Hencky strain H_{ij} read*

$$[F_{ij}] = \begin{bmatrix} 2 & 0 & 0 \\ 0 & -\frac{1}{\sqrt{2}} & 0 \\ 0 & 0 & -\frac{1}{\sqrt{2}} \end{bmatrix}, \quad [E_{ij}] = \begin{bmatrix} \frac{3}{4} & 0 & 0 \\ 0 & -\frac{1}{4} & 0 \\ 0 & 0 & -\frac{1}{4} \end{bmatrix}, \quad [H_{ij}] = \frac{1}{2}\begin{bmatrix} \ln 4 & 0 & 0 \\ 0 & \ln\frac{1}{2} & 0 \\ 0 & 0 & \ln\frac{1}{2} \end{bmatrix}. \tag{2.13}$$

Notice that the incompressibility condition requires that the third invariant of the deformation gradient equals $\det \boldsymbol{F} = 1$. *Now, as any second order tensor may be decomposed into its volumetric and deviatoric parts, the first invariant of the strain tensor serves as the volumetric strain, that is* $d(\mathrm{tr}\boldsymbol{\varepsilon}) = d\varepsilon_{vol} = \frac{dv}{v}$. *Under these considerations the Green-Lagrange strain yields a volume increase of approximately* $28.4\,\%$, *whereas for the Hencky strain the volumetric part vanishes, just as expected for an incompressible material.*

Another useful type of decomposition is related to the eigenvalues of the strain tensor. Specifically, if the second-order tensor at hand is symmetric and positiv definite, we may form its *spectral decomposition*. For example, the right Cauchy-Green $\boldsymbol{C}(\boldsymbol{X}, t)$ tensor introduced above meets these requirements and allows for the spectral representation

$$\boldsymbol{C} = \sum_{\alpha=1}^{3} \lambda_\alpha \boldsymbol{n}_\alpha \otimes \boldsymbol{n}_\alpha, \quad \text{with} \quad \boldsymbol{C}\boldsymbol{n}_\alpha = \lambda_\alpha \boldsymbol{n}_\alpha, \quad \alpha = 1, \dots, 3, \tag{2.14}$$

where $\{\lambda_\alpha\}_{\alpha=1,\dots,3}$ are the eigenvalues of $\boldsymbol{C}$ (i.e. squares of the principal stretches), $\{\boldsymbol{n}_\alpha\}_{\alpha=1,\dots,3}$ are the orthogonal eigenvectors and $\otimes$ is the dyadic product. This type of representation is critical as it provides a means to calculate the components of the

logarithmic strain tensor (2.11) using the so-called *matrix logarithm*[1]. Using this, the generalized strains (2.9) may alternatively be formulated with respect to the principal directions as [47]

$$\boldsymbol{\varepsilon}(\boldsymbol{C}) = \sum_{\alpha=1}^{3} \varepsilon_\alpha \boldsymbol{n}_\alpha \otimes \boldsymbol{n}_\alpha, \quad \text{where} \quad \varepsilon_\alpha(\lambda_\alpha) := \begin{cases} \frac{1}{k}\left(\lambda_\alpha^{\frac{k}{2}} - 1\right) & \text{if } k \neq 0, \\ \frac{1}{2}\ln\lambda_\alpha & \text{if } k = 0. \end{cases} \tag{2.15}$$

After this brief introduction to the kinematics of continua we will next turn our focus to the general balance principles of continuum thermomechanics.

2.2. Balance Principles of Continuum Thermomechanics

In this section, we introduce five important equations necessary to adequately describe the physical behavior of a continuum body in a classical thermomechanical context, namely the balance of mass, linear momentum and angular momentum as well as the balance of energy and entropy. The balance of energy is also known as the first law of thermodynamics. These equations have to be fulfilled at any instant of time irrespective of the underlaying material behavior. They eventually form the basis for the mathematical formulation of initial boundary value problems. We will provide both global and local forms. However, we refrain from giving detailed transformation rules. For an in-depth discussion the interested reader is referred to the literature (e.g. [48, 49]).

2.2.1. Balance of Mass

Based on our experience we know that each object is affected by its surroundings because of its mass. For example, if the object is located within a gravitational field its mass makes it subject to forces (*gravitational mass*). In addition, due to its mass the object will offer resistance to any variation of its velocity (*inertial mass*). The *mass* M of a continuum body B is a scalar quantity which is represented by the volume integral over the *referential mass density* ρ_0, that is $M = \int_\Omega \rho_0(\boldsymbol{X}, t)\, dV$ with $\Omega \equiv R(B)$. Now, the *balance of mass* in its global form states that the mass is temporally constant for any given continuum body B,

$$\frac{d}{dt} M(\boldsymbol{X}, t) = \frac{d}{dt} \int_\Omega \rho_0(\boldsymbol{X}, t)\, dV = 0 \quad \Rightarrow \quad M(\boldsymbol{X}, t) \equiv M(\boldsymbol{X}). \tag{2.16}$$

Hence, in absence of mass supply, production and transport, the mass of a continuum body (or any arbitrary subdomain of the body) is conserved. By means of the so-called *localization principle* [49, p. 77] the global form of the balance of mass may be transformed to its corresponding local form,

$$\frac{d}{dt} \int_\Omega \rho_0(\boldsymbol{X}, t)\, dV = 0 \quad \Rightarrow \quad \dot{\rho}_0(\boldsymbol{X}, t) = 0 \quad \Rightarrow \quad \rho_0(\boldsymbol{X}, t) \equiv \rho_0(\boldsymbol{X}). \tag{2.17}$$

Accordingly, the referential mass density $\rho_0(\boldsymbol{X})$ remains constant with respect to time t if it is assumed to be a continuous function of $\boldsymbol{X} \in R(B)$. The local form of the balance of mass is also called the *continuity equation*.

[1] If $\boldsymbol{A}$, $\boldsymbol{B}$ are matrices of same dimensions and $\boldsymbol{A} = e^{\boldsymbol{B}}$, then $\boldsymbol{B}$ is called the matrix logarithm of $\boldsymbol{A}$.

2.2.2. Balance of Linear Mometum

We know that an object can have a strong impact when hitting a surface restraining its motion. Intuitively, we know that the degree of the impact depends on the object's mass as well as its velocity. In classical continuum mechanics this kind of observation is described by a mechanical quantity called the linear momentum. The *linear momentum* $\boldsymbol{\mathcal{J}}$ of a continuum body B is a vector quantity which is represented in terms of the velocity field $\dot{\boldsymbol{\varphi}}_t$ as $\boldsymbol{\mathcal{J}} = \int_\Omega \dot{\boldsymbol{\varphi}} \rho_0 \, dV$. If we introduce the *force resultant* $\boldsymbol{\mathcal{F}} = \int_\Omega \boldsymbol{B} \, dV + \int_{\partial\Omega} \boldsymbol{T} dA$ with body forces $\boldsymbol{B}(\boldsymbol{X}, t)$ and surface tractions $\boldsymbol{T}(\boldsymbol{X}, t)$ acting on the body (or any arbitrary subdomain through the *principle of intersection*, see Figure 2.3), the *balance of linear momentum* in its global form is given by the relation

$$\frac{d}{dt}\boldsymbol{\mathcal{J}}(t) = \boldsymbol{\mathcal{F}}(t) \quad \Leftrightarrow \quad \frac{d}{dt}\int_\Omega \dot{\boldsymbol{\varphi}}(\boldsymbol{X}, t)\rho_0(\boldsymbol{X}) \, dV = \int_\Omega \boldsymbol{B}(\boldsymbol{X}, t) \, dV + \int_{\partial\Omega} \boldsymbol{T}(\boldsymbol{X}, t) \, dA. \tag{2.18}$$

Thus, the material time derivative of the linear momentum is equal to the resultant force vector. From the global form of the balance of linear momentum we derive the local form using standard arguments to get

$$\rho_0(\boldsymbol{X})\ddot{\boldsymbol{\varphi}}(\boldsymbol{X}, t) = \mathrm{Div}\boldsymbol{P}(\boldsymbol{X}, t) + \boldsymbol{B}(\boldsymbol{X}, t), \tag{2.19}$$

where $\boldsymbol{P}(\boldsymbol{X}, t)$ designates the *first Piola-Kirchhoff stress tensor*. Note that the *two-point tensor* $\boldsymbol{P}(\boldsymbol{X}, t)$ has nine independent components due to its lack of symmetry (see Section 2.2.3). The balance of linear momentum in its local form is also referred to as *Cauchy's equation of motion*.

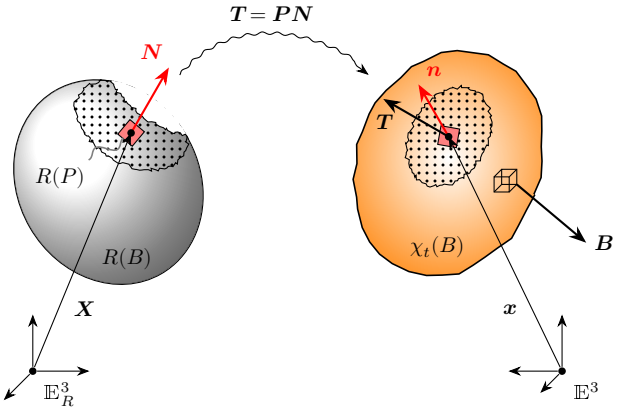

Figure 2.3.: Illustration of the principle of intersection (*free body principle*). While the reference configuration $R(B)$ of continuum body B is chosen as a stress-free state, the current configuration $\chi_t(B)$ is subject to external body forces $\boldsymbol{B}$. Additionally, Both configurations have (mentally) been cut free to reveal material point P. The (pseudo) traction vector $\boldsymbol{T}$ is generated by applying the first Piola-Kirchhoff stress tensor $\boldsymbol{P}$ to reference unit normal $\boldsymbol{N}$.

2.2.3. Balance of Angular Mometum

Similar to the balance of linear momentum with respect to translations it is reasonable to introduce analogue relations which apply to rotations. Any object spinning around an axis will continue its movement unless affected by some externally applied torque. The *angular momentum* $\boldsymbol{\mathcal{L}}_{\mathcal{O}}$ of a continuum body B with respect to the origin $\mathcal{O}$ of the coordinate system is a vector quantity which is represented by the volume integral $\boldsymbol{\mathcal{L}}_{\mathcal{O}} = \int_\Omega \boldsymbol{\varphi}_t \times \dot{\boldsymbol{\varphi}}_t \rho_0 \, dV$. Now, the *resultant torque* $\boldsymbol{\mathcal{T}}_{\mathcal{O}} = \int_\Omega \boldsymbol{\varphi}_t \times \boldsymbol{B} \, dV + \int_{\partial\Omega} \boldsymbol{\varphi}_t \times \boldsymbol{T} dA$ is related to the angular momentum through the *balance of angular momentum*, that is

$$\frac{d}{dt}\boldsymbol{\mathcal{L}}_{\mathcal{O}}(t) = \boldsymbol{\mathcal{T}}_{\mathcal{O}}(t) \quad \Leftrightarrow \quad \frac{d}{dt}\int_\Omega \boldsymbol{\varphi}_t \times \dot{\boldsymbol{\varphi}} \rho_0 \, dV = \int_\Omega \boldsymbol{\varphi}_t \times \boldsymbol{B} \, dV + \int_{\partial\Omega} \boldsymbol{\varphi}_t \times \boldsymbol{T} dA, \tag{2.20}$$

where we have left out the arguments for the sake of readability. Accordingly, the material time derivative of the angular momentum equals the resultant torque acting on the body. This equation governs rotational motions of continuum body B as well as any of its subdomains. As with the former balance principle it is possible to recast the balance of angular momentum into a corresponding local form

$$\boldsymbol{P}(\boldsymbol{X}, t)\boldsymbol{F}^T(\boldsymbol{X}, t) = \boldsymbol{F}(\boldsymbol{X}, t)\boldsymbol{P}^T(\boldsymbol{X}, t), \tag{2.21}$$

implying the aforementioned lack of symmetry of the first Piola-Kirchhoff stress tensor. The derivation of equation (2.21) involves the balance of linear momentum (2.19) as well as the property $\boldsymbol{T} = \boldsymbol{P}\boldsymbol{N}$ (see Figure 2.3).

2.2.4. Balance of Energy

While the first three balance principles presented so far are necessary to describe the purely mechanical behavior of a continuum body, they do not suffice to take account of thermal influences such as a variation in temperature or heat flux. In general, however, deformations of a body will induce both strains *and* a change in temperature, just as a change in temperature is usually accompanied by some form of deformation (thermal expansion of rail tracks caused by sunlight radiation, for example). Therefore, we have to enlarge the mechanical concepts and generalize it to a continuum thermomechanical theory involving additional thermodynamic quantities, namely the internal energy, heat, temperature and entropy. To this end, we introduce the *total internal energy* $\mathcal{U}$ of a continuum body B in terms of the *specific internal energy* $U(\boldsymbol{X}, t)$ per unit mass as $\mathcal{U} = \int_\Omega (U + \frac{1}{2}\dot{\boldsymbol{\varphi}}_t \cdot \dot{\boldsymbol{\varphi}}_t)\rho_0 \, dV$. The second part of the integrand represents the kinetic energy contribution (see also Remark 4). Next, the external mechanical power $\mathcal{P} = \int_\Omega \dot{\boldsymbol{\varphi}}_t \cdot \boldsymbol{B} \, dV + \int_{\partial\Omega} \dot{\boldsymbol{\varphi}}_t \cdot \boldsymbol{T} dA$ and the thermal power $\mathcal{Q} = \int_\Omega R \, dV - \int_{\partial\Omega} \boldsymbol{Q} \cdot \boldsymbol{N} \, dA$ are required. The thermal power comprises an internal heat source term $R(\boldsymbol{X}, t)$ per unit reference volume and a heat flux $\boldsymbol{Q}(\boldsymbol{X}, t)$ across the boundary of continuum body B (see Figure 2.4). The former is sometimes related to radiation, while the latter represents heat conduction. Now, the *balance of energy* in its global form postulates that

$$\frac{d}{dt}\mathcal{U}(t) = \mathcal{P}(t) + \mathcal{Q}(t) \;\Leftrightarrow\; \frac{d}{dt}\int_\Omega \left(U + \frac{1}{2}\dot{\boldsymbol{\varphi}}_t \cdot \dot{\boldsymbol{\varphi}}_t\right)\rho_0 \, dV = \int_\Omega \dot{\boldsymbol{\varphi}}_t \cdot \boldsymbol{B} + R \, dV + \int_{\partial\Omega} \dot{\boldsymbol{\varphi}}_t \cdot \boldsymbol{T} - \boldsymbol{Q} \cdot \boldsymbol{N} \, dA. \tag{2.22}$$

Thus, the total internal energy of a continuum body will change either through mechanical work done by external forces acting on the body or, equivalently, by a thermal

energy transfer into or out of the body. In other words, energy is a conserved quantity with different forms of energy being interconvertible. Reformulation of balance principle (2.22) into its corresponding local form yields[2]

$$\rho_0 \dot{U}(\boldsymbol{X},t) = \boldsymbol{P}(\boldsymbol{X},t) \cdot \dot{\boldsymbol{F}}(\boldsymbol{X},t) - \operatorname{Div} \boldsymbol{Q}(\boldsymbol{X},t) + R(\boldsymbol{X},t). \tag{2.23}$$

The balance of energy is also known as the *first law of thermodynamics*. Note that there exists more than one local form of the balance of energy (see also Remark 3). One of them is the so-called temperature form, which forms the basis for the numerical treatment within the context of finite element theories used in this thesis.

Remark 3. *Another potential known from physical chemistry is the so-called specific Helmholtz energy $\psi(\boldsymbol{X},t)$. It is calculated from the specific internal energy $U(\boldsymbol{X},t)$ by means of the Legendre transformation $\psi = U - S\theta$, where $S(\boldsymbol{X},t)$ is the specific entropy. Using this potential, the local form of the first law is recast into*

$$\rho_0 \dot{\psi} = \boldsymbol{P} \cdot \dot{\boldsymbol{F}} - \operatorname{Div} \boldsymbol{Q} + R - \rho_0 \dot{S}\theta - \rho_0 \dot{\theta} S, \tag{2.24}$$

where we have again dropped the arguments to alleviate the notation. The Helmholtz energy is the potential of choice when specifying constitutive equations for solids in the context of continuum thermomechanics.

Remark 4. *The specific internal energy $U(\boldsymbol{X},t)$ of a material point P is the sum of all the microscopic forms of energy attached to P, which amounts to the sum of the binding energy of individual atoms that constitute P as well as its thermal energy. The thermal energy at material point P, in turn, consists of the kinetic and potential energy of its atoms (not to be confused with its contribution $\frac{1}{2}\rho_0 \dot{\boldsymbol{\varphi}}_t \cdot \dot{\boldsymbol{\varphi}}_t$ to the kinetic energy of the continuum body during its motion through space). The specific internal energy $U(\boldsymbol{X},t)$ is an essential feature of the potential internal energy clock which we will introduce in Section 3.4.9.*

While the balance of energy describes the transformation between different forms of energy (in our case solely mechanical or thermal), it does not give any information on the direction in which thermodynamic processes will evolve (deformations, temperature changes or the direction of heat flow). Another quantity related to the irreversibility of a thermomechanical process is required, which we will explain in the upcoming section.

Remark 5. *In thermodynamic theories we often encounter related terms such as state variables and process variables which stem from classical thermomechanics (see also Section 2.4). The former comprises all thermodynamic quantities which uniquely characterize the current state of a thermodynamic system (in our context continuum body B). The absolute value of these quantities is independent of the path which led to the current state. Specifically, state variables include, among others, the internal energy $U(\boldsymbol{X},t)$, strain tensor $\boldsymbol{\varepsilon}(\boldsymbol{X},t)$ and temperature $\theta(\boldsymbol{X},t)$. Any equation that interrelates state variables is called a state function or constitutive equation (the specific internal energy $U(\boldsymbol{X},t)$ itself is a state function). In contrast, process variables are path-dependent and are significantly affected by external influences. External mechanical power $\mathcal{P}(t)$ and thermal power $\mathcal{Q}(t)$ belong to this category.*

[2] The scalar product between two second-order tensors $\boldsymbol{A}$ and $\boldsymbol{B}$ is defined as $\boldsymbol{A} \cdot \boldsymbol{B} := \operatorname{tr}\left(\boldsymbol{A}^T \boldsymbol{B}\right)$.

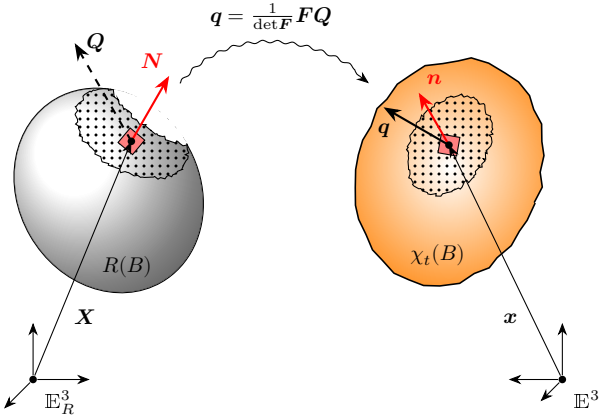

Figure 2.4.: Illustration of heat flux vectors by means of the principle of intersection. The spatial heat flux $\boldsymbol{q}$ in the current configuration $\chi_t(B)$ is also called *true heat flux*. The material heat flux $\boldsymbol{Q}$, on the other hand, is known as the *nominal heat flux*. It is a pseudo flux vector (indicated by dashed lines), which is located in the reference configuration $R(B)$ of continuum body B. The deformation gradient $\boldsymbol{F}$ acts as a mediator between configurations.

2.2.5. Balance of Entropy

In contrast to more familiar terms such as energy and temperature, entropy appears as a rather abstract concept, given the fact that it is more or less non-existent in common parlance and, therefore, quite unrelated do everyday life. However, we need to introduce entropy as a further thermodynamic variable to quantify the irreversiblity of natural processes. Later we will see that the entropy is the thermodynamic conjugate variable to temperature, just as stresses are thermodynamic conjugate to strains. First, we define the *entropy* $\mathcal{S}$ of continuum body B in terms of the *specific entropy* $S(\boldsymbol{X}, t)$ as the integral $\mathcal{S} = \int_\Omega S\rho_0 \, dV$. Next, we define the total entropy production Γ in terms of the *entropy production* $\gamma(\boldsymbol{X}, t)$ per unit reference volume as $\Gamma = \int_\Omega \gamma \, dV$ and the *resultant entropy supply* as $\mathcal{B} = \int_\Omega \tilde{R} \, dV - \int_{\partial\Omega} \tilde{\boldsymbol{Q}} \cdot \boldsymbol{N} \, dA$. The entropy supply $\mathcal{B}$ consists of a volume-distributed source term $\tilde{R}(\boldsymbol{X}, t)$ as well as a flux term $\tilde{\boldsymbol{Q}}(\boldsymbol{X}, t)$ across the boundary of continuum body B. Having defined these quantities, the *balance of entropy* in its global form reads

$$\frac{d}{dt}\mathcal{S}(t) = \mathcal{B}(t) + \Gamma(t) \quad \Leftrightarrow \quad \frac{d}{dt}\int_\Omega S\rho_0 \, dV = \int_\Omega \tilde{R} + \gamma \, dV - \int_{\partial\Omega} \tilde{\boldsymbol{Q}} \cdot \boldsymbol{N} \, dA. \tag{2.25}$$

Thus, the sum of entropy supply and entropy production is equal to the temporal change of entropy. With the help of the divergence theorem we arrive at the corresponding local form of the entropy balance,

$$\rho_0 \dot{S}(\boldsymbol{X}, t) = \tilde{R}(\boldsymbol{X}, t) - \mathrm{Div}\tilde{\boldsymbol{Q}}(\boldsymbol{X}, t) + \gamma(\boldsymbol{X}, t). \tag{2.26}$$

Notice that the specification of flux $\tilde{\boldsymbol{Q}}(\boldsymbol{X},t)$ and source $\tilde{R}(\boldsymbol{X},t)$ is still open. One special choice is motivated from equilibrium thermomechanics (see Section 2.4), where the expressions $\tilde{\boldsymbol{Q}} = \frac{\boldsymbol{Q}}{\theta}(\boldsymbol{X},t)$ and $\tilde{R} = \frac{R}{\theta}(\boldsymbol{X},t)$ including the *absolute temperature* $\theta(\boldsymbol{X},t) > 0$ are used. In the following we adopt this variant, which establishes our governing thermodynamic theory.

Remark 6. *Note that the formal introduction of entropy given above is in line with other thermodynamic quantities introduced so far. For example, the definition of entropy $\mathcal{S}$ is similar to the definition of total internal energy $\mathcal{U}(t)$ from Section 2.2.4, which is assumed to be an additive scalar quantity. Equally, the resultant entropy supply $\mathcal{B}(t)$ resembles the thermal power $\mathcal{Q}(t)$, composed of a volume-distributed and a surface-distributed part. The main difference lies in the production term $\Gamma(t)$, which plays a crucial role in describing the irreversibility of thermomechanial processes (see the Section 2.3).*

2.3. Principle of Irreversibility

The *principle of irreversibility* in its global form states that the entropy production $\Gamma(t)$ should always be non-negative,

$$\Gamma(t) \geq 0 \quad \Leftrightarrow \quad \int_\Omega \tilde{R} + \gamma \, dV = \frac{d}{dt} \int_\Omega S \rho_0 \, dV - \int_\Omega \tilde{R} \, dV + \int_{\partial\Omega} \tilde{\boldsymbol{Q}} \cdot \boldsymbol{N} \, dA \geq 0, \tag{2.27}$$

which governs every conceivable thermomechanical process of continuum body B for all times t. This inequality is also referred to as the *second law thermodynamics*. It places restrictions on the direction of energy transfer in continuum body B, in contrast to the balance of energy, which governs the transformation between different forms of energy. The so-called *Clausius-Duhem-Inequality* is a special variant which is characterized by the particular choice for the entropy supply already mentioned in the preceding section, that is

$$\frac{d}{dt} \int_\Omega S \rho_0 \, dV - \int_\Omega \frac{R}{\theta} \, dV + \int_{\partial\Omega} \frac{\boldsymbol{Q}}{\theta} \cdot \boldsymbol{N} \, dA \geq 0. \tag{2.28}$$

This inequality can be expressed by the equivalent local formulation

$$\gamma(\boldsymbol{X},t) = \rho_0 \dot{S}(\boldsymbol{X},t) + \operatorname{Div}\left(\frac{\boldsymbol{Q}}{\theta}(\boldsymbol{X},t)\right) - \frac{R}{\theta}(\boldsymbol{X},t) \geq 0. \tag{2.29}$$

If we assume that entropy production by conduction of heat must be non-negative, an even stronger form of inequality (2.29) in terms of the specific Helmholtz energy (see Remark 3) follows, that is

$$\mathcal{D}_{\text{int}}(\boldsymbol{X},t) = \boldsymbol{P}(\boldsymbol{X},t) \cdot \dot{\boldsymbol{F}}(\boldsymbol{X},t) - \rho_0 \dot{\psi}(\boldsymbol{X},t) - \rho_0 S(\boldsymbol{X},t) \dot{\theta}(\boldsymbol{X},t) \geq 0. \tag{2.30}$$

Expression (2.30) is called the *Clausius-Planck inequality*. The quantity $\mathcal{D}_{\text{int}}(\boldsymbol{X},t)$ designates the *internal dissipation* at material point $P \in R(B)$ of continuum body B. A material which fulfills above inequalities at every material point P for all instants of time t is said to be *thermodynamically consistent*.

Remark 7. *From a physical point of view, a scientist involved in the development of constitutive equations should always strive for a thermodynamically consistent material formulation. However, in practical applications such as those encountered in civil engineering, the principle of irreversibility is nevertheless most often ignored, which reflects the large gap between theory and practice.*

Remark 8. *The internal dissipation $\mathcal{D}_{\text{int}}$ is non-zero for any real material. The hypothetical case of zero dissipation, that is $\mathcal{D}_{\text{int}} = 0$, characterizes thermoelastic materials. The assumption of zero dissipation has proved quite useful as a first approximation for many practical applications (float glass, for example, may be regarded as thermoelastic).*

Table 2.1 summarizes a subset of the equations presented in the preceding sections supplemented by the unknown fields which yet remain to be determined. Obviously, the 7 equations listed do not suffice to solve for the 18 unknown quantities. This gap will be filled later with appropriate constitutive equations.

Summary of governing equations:

Balance of linear momentum (2.19):	$\rho_0 \ddot{\boldsymbol{\varphi}} = \text{Div}\boldsymbol{P} + \boldsymbol{B}$	(3 equations)
Balance of angular momentum (2.21):	$\boldsymbol{P}\boldsymbol{F}^T = \boldsymbol{F}\boldsymbol{P}^T$	(3 equations)
Balance of energy (2.30):	$\rho_0 \dot{\psi} = \boldsymbol{P} \cdot \dot{\boldsymbol{F}} - \mathcal{D}_{\text{int}} - \rho_0 S \dot{\theta}$	(1 equation)

Summary of unknown fields:

Deformation $\boldsymbol{\varphi}$	(3 unknowns)	*Temperature* θ	(1 unknown)
Helmholtz energy ψ	(1 unknown)	*Entropy* S	(1 unknown)
Stresses $\boldsymbol{P}$	(9 unknowns)	*Heat flux* $\boldsymbol{Q}$	(3 unknowns)

Table 2.1.: Comparison of relevant governing equations and unknown quantities within a thermomechanical theory. In total there are only 7 equations for 18 unknowns. The balance of mass does not appear, as the distribution of mass $\rho_0(\boldsymbol{X})$ is assumed to be known from the outset. The dissipation inequality is also not included, since it represents a constraint condition for the unknowns and will be incorporated at a later stage[3](see also Section 2.4).

2.4. Different Dialects of Thermodynamic Theories

When developing new constitutive equations in a thermomechanically coupled context it is not clear from the outset which theory to draw on. Rather, one has to decide upon one among several possible thermodynamic theories, each of them with their own merits and drawbacks. Put simply, a first approach is to distinguish between *statistical thermodynamics* and *phenomenological theories*. While the former revolves around the

[3]Indeed, the set of governing equations alongside the constitutive equations becomes overdetermined when the second law of thermodynamics comes into play. However, its validity will be guarantied later on by imposing certain restrictions on the constitutive equations, see Section 2.6.

smallest particles of matter (atoms and molecules) on a microscopic level, the latter deals with matter from a global or macroscopic perspective. Continuum thermomechanics belongs to the second kind, which in turn is further subdivided in theories of *reversible* and *irreversible processes*. What is more, there are numerous postulates to quantify the irreversibility of physical processes (i. e. second laws of thermodynamics), which are not necessarily equivalent. The aim of this section is to give a rough overview on the different possibilities out there in the thermomechanics jungle. Although the starting point of phenomenological theories of continuum thermomechanics is centered around the bulk material, it is important to bear in mind the following principle [50, p. 4]:

> *"First, a set of thermodynamic axioms should be as general as possible and second, it should in the course of its exploitation lead to as many 'reasonable' implications as possible. Furthermore, [...] a set of thermodynamic postulates or axioms should produce results which can be counterchecked by methods of statistical physics."*

In what follows, we give a short introduction to some established theories, starting with statistical methods. Figure 2.5 presents an overview and highlights some interrelations between the different approaches.

Statistical mechanics deals with systems composed of such a large number of particles (atoms and molecules) that their states (position, velocity, temperature etc.) can never be completely known and, therefore, need to be described by *statistical methods*. Important characteristics of a thermodynamic system are its number of particles, their kinetic energy and spatial distribution. Statistical mechanics serves as a bridge betweeen the unknown microscopic states and the observable macroscopic behavior of matter. In contrast to phenomenological theories, statistical thermodynamics gives more insight into the true nature of materials, since it is closer to the microscopic processes within a solid, liquid or gas. For example, the absolute temperature of an ideal gas is a measure for the *average kinetic energy* of its particles. Statistical mechanics evolved out of classical thermostatics. Its founders are James Clerk Maxwell, Josiah Willard Gibbs and Ludwig Boltzmann.

Equilibrium thermodynamics or *thermostatics*, which traces back to the 19th century, is the science of *reversible* processes. It is assumed that the transition between neighboring equilibrium states happens extremely slowly. The existence of *absolute temperature* and *entropy* follows from the balance of mass, the balance of energy and the assumption that heat cannot flow by itself from cold to hot. If one reads a treatise which contains some sort of infinite heat bath one is most likely dealing with thermostatics. Founders of equilibrium thermodynamics include, among others, Sadi Carnot, Émile Clapeyron and Rudolf Clausius.

Irreversible thermodynamics [51] (for short TIP) deals, as its name suggests, with *irreversible* processes. The second law of thermodynamics implies restrictions on the thermodynamic process a body can experience. The absolute temperature is assumed to be a primitive quantity. The theory is based on the balance of mass, linear momentum and balance of internal energy as well as Gibb's equation of equilibrium thermodynamics. Additionally, further equations describing the constitutive behavior are necessary (*phenomenological equations* in TIP parlance). The theory is concerned with states of matter in the vicinity of an equilibrium state ("*principle of local equilibrium*") and is, therefore, restricted to linear constitutive equations. TIP is further subdivided into

ordinary and *extended irreversible thermodynamics*. The foundations of irreversible thermodynamics were laid by Carl Eckart, Sybren Ruurds de Groot and Peter Mazur.
Rational thermodynamics evolved within the second half of the 20th century and deals with irreversible processes. It is based on all the balance principles introduced in Section 2.2. However, in contrast to irreversible thermodynamics, the second law is interpreted as a means to impose restrictions on the constitutive equations. The energy potential is cast in the form of a hereditary integral, where the present state is described by the present values of the deformation and the temperature as well as their past history (see [52] for linear thermoviscoelasticity and [53–55] for nonlinear theories in the context of thermorheologically simple materials, and also [56]). This functional framework for constitutive relations is well suited to highlight the general aspects of the theory of material behavior [49, p. 295]. However, the use of multiple integrals (double integrals, triple integrals etc.) often implies difficult mathematical manipulations. Leading figures of rational thermodynamics include Clifford Truesdell, Bernard Coleman and Walter Noll.
Thermodynamics with internal variables [57–59] is also applicable to describe irreversible processes and today encompasses a very broad range of applications (such as viscoelasticity, plasticity, damage and phase transitions). Its roots trace back to the 19th century. The underlying theoretical basis is similar to that of the rational thermodynamics approach (i. e. the balance equations and the Clausius-Duhem inequality). However, its major difference lies in the introduction of a sufficient number of internal state variables to describe the internal structure of the material. This implies the necessity to formulate additional evolution equations for the internal variables to complete the set of constitutive equations. In doing so, the energy potential depends not only on the present state of deformation and temperature, but also on the internal variables. This circumvents the complicated representation of the potential as a hereditary integral known from rational thermodynamics (see [56, 60, 61] for linear thermoviscoelasticity and some generalizations to thermorheologically simple materials). Important theoretical foundations were laid by Bernard Coleman and Morton Gurtin [62]. The internal variables approach forms the basis for the material formulation developed in this thesis.

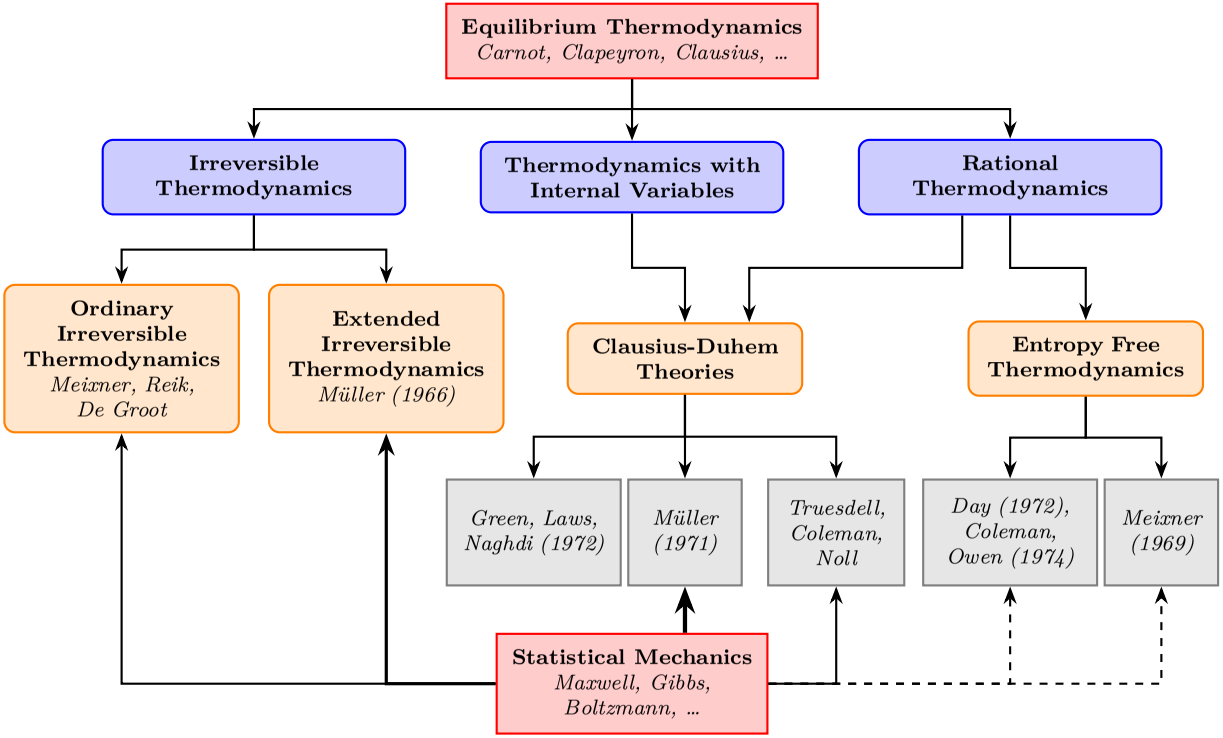

Figure 2.5.: Depiction of various thermodynamic theories, adapted from [50]. The theory of internal variables is located between irreversible and rational thermodynamics [57]. Variations in the influence of statistical mechanics on these theories are indicated by different arrows. For a historical overview on thermodynamics see [63].

2.5. Principles of Material Modeling

The task of developing constitutive equations for a material within a general thermomechanical context can be quite overwhelming. To guide the developer through the process of finding appropriate thermodynamically consistent equations which reflect the experimentally observed material response in accordance with the balance laws introduced above, certain principles of material modeling have been developed. A selection of these will be presented in the following (see [49],[54],[55]).

2.5.1. Principle of Equipresence

The *principle of equipresence* demands that any state variable appearing as an independent quantity in one constitutive equation should also appear in every other. For example, it makes no sense to assume from the outset that the stresses $\boldsymbol{P}(\boldsymbol{X},t)$ are only a function of the deformation $\boldsymbol{\varphi}(\boldsymbol{X},t)$ while the heat flux $\boldsymbol{Q}(\boldsymbol{X},t)$ is assumed to depend solely on the temperature $\theta(\boldsymbol{X},t)$.

2.5.2. Principle of Determinism

A very basic principle guiding the material modeling process is the so-called *principle of determinism*. It states that the values of the dependent constitutive variables specific Helmholtz energy $\psi(\boldsymbol{X},t)$, stresses $\boldsymbol{P}(\boldsymbol{X},t)$, specific entropy $S(\boldsymbol{X},t)$ and (spatial) heat flux $\boldsymbol{q}(\boldsymbol{X},t)$ at material point $\boldsymbol{X}\in R(B)$ of continuum body B at an arbitrary instant of time t are uniquely determined by the *entire past history of all points* $\boldsymbol{Y}\in R(B)$ of the body, that is by the deformation $\boldsymbol{\varphi}(\boldsymbol{Y},\tau)$ and the temperature $\theta(\boldsymbol{Y},\tau)$ for all past times $\tau\leq t$. This assumption also excludes the possibility that future values might influence the current material response. Thus, the constitutive equations assume the general functional forms

$$\begin{aligned}
\psi(\boldsymbol{X},t) &= \bar{\psi}(\boldsymbol{\varphi}(\boldsymbol{Y},\tau),\theta(\boldsymbol{Y},\tau),\boldsymbol{X},t),\\
\boldsymbol{P}(\boldsymbol{X},t) &= \bar{\boldsymbol{P}}(\boldsymbol{\varphi}(\boldsymbol{Y},\tau),\theta(\boldsymbol{Y},\tau),\boldsymbol{X},t),\\
S(\boldsymbol{X},t) &= \bar{S}(\boldsymbol{\varphi}(\boldsymbol{Y},\tau),\theta(\boldsymbol{Y},\tau),\boldsymbol{X},t),\\
\boldsymbol{q}(\boldsymbol{X},t) &= \bar{\boldsymbol{q}}(\boldsymbol{\varphi}(\boldsymbol{Y},\tau),\theta(\boldsymbol{Y},\tau),\boldsymbol{X},t),
\end{aligned} \tag{2.31}$$

where $\boldsymbol{Y}\in R(B)$ and $\tau\leq t$. Obviously, the functionals (2.31) are in line with the principle of equipresence mentioned above. Note that $(2.31)_4$ represents the true heat flux, rather than its referential counterpart. This is a natural choice, which reflects the actual thermal state at material point $\boldsymbol{X}$ of continuum body B. As already indicated in Section (2.4) we will base our material formalism on the *theory of internal variables* to describe memory effects in materials. The idea behind this concept is to turn constitutive functionals (2.31) into equations which only depend on the current deformation $\boldsymbol{\varphi}(\boldsymbol{Y},t)$ and temperature $\theta(\boldsymbol{Y},t)$ of all material points $\boldsymbol{Y}\in R(B)$, rather than on the entire history, as well as on a certain number of internal variables $\boldsymbol{\mathcal{E}}_k(\boldsymbol{Y},t)$, $k=1,\dots,m$. In addition, a set of m evolution equations for these variables will supplement the constitutive functions to fully take account of any past events. Thus, constitutive functionals

(2.31) are replaced by the following set of equations

$$\begin{aligned}
\psi(\boldsymbol{X},t) &= \tilde{\psi}(\boldsymbol{\varphi}(\boldsymbol{Y},t),\theta(\boldsymbol{Y},t),\boldsymbol{\mathcal{E}}(\boldsymbol{Y},t),\boldsymbol{X},t),\\
\boldsymbol{P}(\boldsymbol{X},t) &= \tilde{\boldsymbol{P}}(\boldsymbol{\varphi}(\boldsymbol{Y},t),\theta(\boldsymbol{Y},t),\boldsymbol{\mathcal{E}}(\boldsymbol{Y},t),\boldsymbol{X},t),\\
S(\boldsymbol{X},t) &= \tilde{S}(\boldsymbol{\varphi}(\boldsymbol{Y},t),\theta(\boldsymbol{Y},t),\boldsymbol{\mathcal{E}}(\boldsymbol{Y},t),\boldsymbol{X},t),\\
\boldsymbol{q}(\boldsymbol{X},t) &= \tilde{\boldsymbol{q}}(\boldsymbol{\varphi}(\boldsymbol{Y},t),\theta(\boldsymbol{Y},t),\boldsymbol{\mathcal{E}}(\boldsymbol{Y},t),\boldsymbol{X},t),\\
\dot{\boldsymbol{\mathcal{E}}}(\boldsymbol{X},t) &= \tilde{\boldsymbol{\mathcal{P}}}(\boldsymbol{\varphi}(\boldsymbol{Y},t),\theta(\boldsymbol{Y},t),\boldsymbol{\mathcal{E}}(\boldsymbol{Y},t),\boldsymbol{X},t),
\end{aligned} \tag{2.32}$$

where we consider the special case $m = 1$ of only one internal variable since a generalization to multiple variables is straightforward, see Section 3. We will postpone the physical interpretation of the quantities $\boldsymbol{\mathcal{E}}_k(\boldsymbol{X},t)$ until a later stage. For the time being it suffices to say that they represent a material state that depends on the process history and take on the form of second-order tensors. The material function $\tilde{\boldsymbol{\mathcal{P}}}$ thus models memory properties of the material.

Remark 9. *In general, continuum mechanics distinguishes between materials with fading memory and those with perfect memory. In the former case the material shows a stronger dependence on past events which took place in the recent past. This type of rate-dependent behavior is fully described by the theory of (thermo-)viscoelasticity, which implies different phenomena such as relaxation, creep, damping as well as rate-dependent hysteresis effects. The latter type of materials with perfect memory corresponds to the theory of plasticity, which is characterized by permanent deformation of solids, strain hardening and also rate-independent hysteresis effects [55, p. 4].*

While the principle of determinism constitutes a first restriction, it still does not suffice to formulate definite constitutive equations due to its extreme generality. Further principles of material modeling are required.

2.5.3. Principle of Local Action

The so-called *principle of local action* is very useful in that it places further restrictions on the material response functions. Specifically, it states that the material response at material point $\boldsymbol{X} \in R(B)$ of continuum body B only depends on the state of the fields (2.32) in the *vicinity of point* $\boldsymbol{X}$. Thus, it limits the dependence on every material point $\boldsymbol{Y} \in R(B)$ given by the principle of determinism to the neighborhood $\mathcal{N}(\boldsymbol{X})$ of point $\boldsymbol{X} \in R(B)$. In the following, this is formally achieved by introducing first-order Taylor series expansions for the deformation, the temperature and the internal variables

$$\begin{aligned}
\boldsymbol{\varphi}(\boldsymbol{Y},t) &\approx \boldsymbol{\varphi}(\boldsymbol{X},t) + \frac{\partial \boldsymbol{\varphi}}{\partial \boldsymbol{X}}(\boldsymbol{X},t)(\boldsymbol{Y}-\boldsymbol{X}),\\
\theta(\boldsymbol{Y},t) &\approx \theta(\boldsymbol{X},t) + \frac{\partial \theta}{\partial \boldsymbol{X}}(\boldsymbol{X},t)(\boldsymbol{Y}-\boldsymbol{X}),\\
\boldsymbol{\mathcal{E}}(\boldsymbol{Y},t) &\approx \boldsymbol{\mathcal{E}}(\boldsymbol{X},t) + \frac{\partial \boldsymbol{\mathcal{E}}}{\partial \boldsymbol{X}}(\boldsymbol{X},t)(\boldsymbol{Y}-\boldsymbol{X}),
\end{aligned} \tag{2.33}$$

where $\boldsymbol{Y} \in \mathcal{N}(\boldsymbol{X})$. We shall henceforth assume that the gradients of the internal variables are of minor influence and therefore can be neglected (see for example [64] for a gradient

based model). Thus, based on this assumption we may substitute approximations (2.33) into constitutive relations (2.32) to get

$$\begin{aligned}
\psi(\boldsymbol{X},t) &= \hat{\psi}(\boldsymbol{\varphi}(\boldsymbol{X},t),\boldsymbol{F}(\boldsymbol{X},t),\theta(\boldsymbol{X},t),\mathrm{Grad}\theta(\boldsymbol{X},t),\boldsymbol{\mathcal{E}}(\boldsymbol{X},t),\boldsymbol{X},t),\\
\boldsymbol{P}(\boldsymbol{X},t) &= \hat{\boldsymbol{P}}(\boldsymbol{\varphi}(\boldsymbol{X},t),\boldsymbol{F}(\boldsymbol{X},t),\theta(\boldsymbol{X},t),\mathrm{Grad}\theta(\boldsymbol{X},t),\boldsymbol{\mathcal{E}}(\boldsymbol{Y},t),\boldsymbol{X},t),\\
S(\boldsymbol{X},t) &= \hat{S}(\boldsymbol{\varphi}(\boldsymbol{X},t),\boldsymbol{F}(\boldsymbol{X},t),\theta(\boldsymbol{X},t),\mathrm{Grad}\theta(\boldsymbol{X},t),\boldsymbol{\mathcal{E}}(\boldsymbol{X},t),\boldsymbol{X},t),\\
\boldsymbol{q}(\boldsymbol{X},t) &= \hat{\boldsymbol{q}}(\boldsymbol{\varphi}(\boldsymbol{X},t),\boldsymbol{F}(\boldsymbol{X},t),\theta(\boldsymbol{X},t),\mathrm{Grad}\theta(\boldsymbol{X},t),\boldsymbol{\mathcal{E}}(\boldsymbol{X},t),\boldsymbol{X},t),\\
\dot{\boldsymbol{\mathcal{E}}}(\boldsymbol{X},t) &= \hat{\boldsymbol{\mathcal{P}}}(\boldsymbol{\varphi}(\boldsymbol{X},t),\boldsymbol{F}(\boldsymbol{X},t),\theta(\boldsymbol{X},t),\mathrm{Grad}\theta(\boldsymbol{X},t),\boldsymbol{\mathcal{E}}(\boldsymbol{X},t),\boldsymbol{X},t).
\end{aligned} \tag{2.34}$$

Thus, the dependence of the material response at material point $\boldsymbol{X} \in R(B)$ on every particle $\boldsymbol{Y} \in R(B)$ has been replaced by the gradients $\boldsymbol{F}(\boldsymbol{X},t)$ and $\mathrm{Grad}\theta(\boldsymbol{X},t)$. Note that this constitutes a very sharp application of the principle of local action, where the neighborhood $\mathcal{N}(\boldsymbol{X})$ becomes infinitesimal. Generally, it is by no means necessary to use first-order approximations. If we were to choose a series expansion up to the nth order we could describe a so-called *material of grade n*. Accordingly, response functions (2.34) constitute a material of grade one, which is also referred to as a *simple material* [54, p. 202].

2.5.4. Principle of Material Frame-Indifference

The constitutive equations (2.34) can be further simplified if we acknowledge the fact that two different observers in relative motion to each other should witness the same form of material response when one of them performs an experiment on a material, for example a tensile test. The translation of this observation into mathematical terms necessitates some notational effort. To this end, let O and O^* denote two different observers, where O remains fixed at the origin of an inertial cartesian system $\{\boldsymbol{e}_i\} \in \mathbb{E}^3_1, i = 1,..,3$ in the Euclidean vector space. The second observer O^* watches the first, who is performing the tensile test. In doing so, observer O^* is located at the origin of another cartesian system $\{\boldsymbol{e}^*_i\} \in \mathbb{E}^3_2$ which is in motion relative to the first. That is, the positions of the origins of the base systems in space differ by a time-dependent translation $\boldsymbol{c}(t)$ and the base vectors itself by virtue of a time-dependent rotation $\boldsymbol{e}^*_i(t) = \boldsymbol{\alpha}(t)\boldsymbol{e}_i$, where $\boldsymbol{\alpha}$ is an orthogonal tensor with $\det(\boldsymbol{\alpha}) = 1$. The base systems $\{\boldsymbol{e}_i\}$ and $\{\boldsymbol{e}^*_i\}$ are also referred to as the *reference frames* of the observers. We assume that both observers share the same reference configuration such that a material point P of continuum body B is identified via reference positions $\boldsymbol{X} = \boldsymbol{X}^* = R(B)$, see Figure 2.6. Furthermore, observers O and O^* record the deformation of material point P by spatial positions $\boldsymbol{x} = \boldsymbol{\varphi}(\boldsymbol{X},t)$ and $\boldsymbol{x}^* = \boldsymbol{\varphi}^*(\boldsymbol{X}^*,t^*)$, respectively, which are related by a vector transformation and a time shift according to

$$\boldsymbol{x}^* = \boldsymbol{\alpha}(t)\boldsymbol{x} + \boldsymbol{c}(t) \quad \text{and} \quad t^* = t - a, \quad a \in \mathbb{R}. \tag{2.35}$$

This transformation implies a *change of frame*, where observer O^* (who sees material point $R(P)$ at current location $\boldsymbol{x}^*$) located at the origin of his reference frame $\{\boldsymbol{e}^*_i\}$ has to move to the origin of the other reference frame $\{\boldsymbol{e}_i\}$ and rotate to see the same material point P. This change of frame is also known as the *active interpretation*. Relation (2.35) is also referred to as an *Euclidean transformation*.

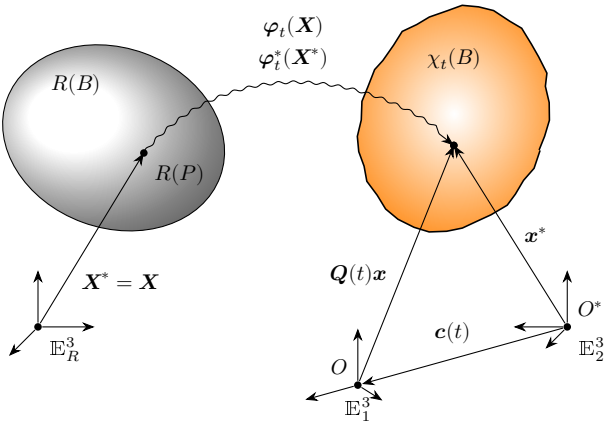

Figure 2.6.: Illustration of two different observers and a change in frame in terms of the *active interpretation*. Both observers share the same reference configuration $R(B)$ of continuum body B. Observer O^* is in relative motion with respect to observer O according to the Euclidean transformation (2.35).

As a starting point, we formally distinguish the constitutive relations of observer O^* from those of observer O (2.34) likewise by an additional asterisk, that is

$$\begin{aligned}
\psi^*(\boldsymbol{X}^*,t^*) &= \hat{\psi}^*(\boldsymbol{\varphi}^*(\boldsymbol{X}^*,t^*),\boldsymbol{F}^*(\boldsymbol{X}^*,t^*),\theta^*(\boldsymbol{X}^*,t^*),\mathrm{Grad}^*\theta^*(\boldsymbol{X}^*,t^*),\boldsymbol{\mathcal{E}}^*(\boldsymbol{X}^*,t^*),\boldsymbol{X}^*,t^*),\\
\boldsymbol{P}^*(\boldsymbol{X}^*,t^*) &= \hat{\boldsymbol{P}}^*(\boldsymbol{\varphi}^*(\boldsymbol{X}^*,t^*),\boldsymbol{F}^*(\boldsymbol{X}^*,t^*),\theta^*(\boldsymbol{X}^*,t^*),\mathrm{Grad}^*\theta^*(\boldsymbol{X}^*,t^*),\boldsymbol{\mathcal{E}}^*(\boldsymbol{X}^*,t^*),\boldsymbol{X}^*,t^*),\\
S^*(\boldsymbol{X}^*,t^*) &= \hat{S}^*(\boldsymbol{\varphi}^*(\boldsymbol{X}^*,t^*),\boldsymbol{F}^*(\boldsymbol{X}^*,t^*),\theta^*(\boldsymbol{X}^*,t^*),\mathrm{Grad}^*\theta^*(\boldsymbol{X}^*,t^*),\boldsymbol{\mathcal{E}}^*(\boldsymbol{X}^*,t^*),\boldsymbol{X}^*,t^*),\\
\boldsymbol{q}^*(\boldsymbol{X}^*,t^*) &= \hat{\boldsymbol{q}}^*(\boldsymbol{\varphi}^*(\boldsymbol{X}^*,t^*),\boldsymbol{F}^*(\boldsymbol{X}^*,t^*),\theta^*(\boldsymbol{X}^*,t^*),\mathrm{Grad}^*\theta^*(\boldsymbol{X}^*,t^*),\boldsymbol{\mathcal{E}}^*(\boldsymbol{X}^*,t^*),\boldsymbol{X}^*,t^*),\\
\dot{\boldsymbol{\mathcal{E}}}^*(\boldsymbol{X}^*,t^*) &= \hat{\boldsymbol{\mathcal{P}}}^*(\boldsymbol{\varphi}^*(\boldsymbol{X}^*,t^*),\boldsymbol{F}^*(\boldsymbol{X}^*,t^*),\theta^*(\boldsymbol{X}^*,t^*),\mathrm{Grad}^*\theta^*(\boldsymbol{X}^*,t^*),\boldsymbol{\mathcal{E}}^*(\boldsymbol{X}^*,t^*),\boldsymbol{X}^*,t^*).
\end{aligned} \tag{2.36}$$

Next, the so-called *principle of material frame-indifference* or *material objectivity* comes into play. It postulates that every representation of material properties should be independent of the frame of reference. Hence, the functionals should be the same, since they are describing the same material. This eventually boils down to the identities $\hat{\psi}^* = \hat{\psi}$, $\hat{\boldsymbol{P}}^* = \hat{\boldsymbol{P}}$, $\hat{S}^* = \hat{S}$, $\hat{\boldsymbol{q}}^* = \hat{\boldsymbol{q}}$, and $\hat{\boldsymbol{\mathcal{E}}}^* = \hat{\boldsymbol{\mathcal{E}}}$. We can therefore drop the corresponding asterisks in (2.36) and the response functions of observer O^* reduce to

$$\begin{aligned}
\psi^*(\boldsymbol{X}^*,t^*) &= \hat{\psi}(\boldsymbol{\varphi}^*(\boldsymbol{X}^*,t^*),\boldsymbol{F}^*(\boldsymbol{X}^*,t^*),\theta^*(\boldsymbol{X}^*,t^*),\mathrm{Grad}^*\theta^*(\boldsymbol{X}^*,t^*),\boldsymbol{\mathcal{E}}^*(\boldsymbol{X}^*,t^*),\boldsymbol{X}^*,t^*),\\
\boldsymbol{P}^*(\boldsymbol{X}^*,t^*) &= \hat{\boldsymbol{P}}(\boldsymbol{\varphi}^*(\boldsymbol{X}^*,t^*),\boldsymbol{F}^*(\boldsymbol{X}^*,t^*),\theta^*(\boldsymbol{X}^*,t^*),\mathrm{Grad}^*\theta^*(\boldsymbol{X}^*,t^*),\boldsymbol{\mathcal{E}}^*(\boldsymbol{X}^*,t^*),\boldsymbol{X}^*,t^*),\\
S^*(\boldsymbol{X}^*,t^*) &= \hat{S}(\boldsymbol{\varphi}^*(\boldsymbol{X}^*,t^*),\boldsymbol{F}^*(\boldsymbol{X}^*,t^*),\theta^*(\boldsymbol{X}^*,t^*),\mathrm{Grad}^*\theta^*(\boldsymbol{X}^*,t^*),\boldsymbol{\mathcal{E}}^*(\boldsymbol{X}^*,t^*),\boldsymbol{X}^*,t^*),\\
\boldsymbol{q}^*(\boldsymbol{X}^*,t^*) &= \hat{\boldsymbol{q}}(\boldsymbol{\varphi}^*(\boldsymbol{X}^*,t^*),\boldsymbol{F}^*(\boldsymbol{X}^*,t^*),\theta^*(\boldsymbol{X}^*,t^*),\mathrm{Grad}^*\theta^*(\boldsymbol{X}^*,t^*),\boldsymbol{\mathcal{E}}^*(\boldsymbol{X}^*,t^*),\boldsymbol{X}^*,t^*),\\
\dot{\boldsymbol{\mathcal{E}}}^*(\boldsymbol{X}^*,t^*) &= \hat{\boldsymbol{\mathcal{P}}}(\boldsymbol{\varphi}^*(\boldsymbol{X}^*,t^*),\boldsymbol{F}^*(\boldsymbol{X}^*,t^*),\theta^*(\boldsymbol{X}^*,t^*),\mathrm{Grad}^*\theta^*(\boldsymbol{X}^*,t^*),\boldsymbol{\mathcal{E}}^*(\boldsymbol{X}^*,t^*),\boldsymbol{X}^*,t^*).
\end{aligned} \tag{2.37}$$

Next, let us consider two special cases of the general observer transformation rule (2.35). The first one represents a rigid translation given by the choices $\boldsymbol{\alpha}(t^*) = \boldsymbol{I}$ and $\boldsymbol{c}(t^*) = -\boldsymbol{\varphi}(\boldsymbol{X}, t^*)$ as well as the time shift $a = 0$, implying $t^* = t$. In this case, the right-hand sides of (2.37) do not show any dependence on the motion, since $\boldsymbol{\varphi}^*(\boldsymbol{X}^*, t^*) = \boldsymbol{0}$, while the right-hand sides of constitutive equations (2.34) of observers O still do. The only remedy for this contradiction is to refrain from any direct motion dependency of the equations. Thus, for observer O we have

$$\begin{aligned}
\psi(\boldsymbol{X}, t) &= \hat{\psi}(\boldsymbol{F}(\boldsymbol{X}, t), \theta(\boldsymbol{X}, t), \mathrm{Grad}\theta(\boldsymbol{X}, t), \boldsymbol{\mathcal{E}}(\boldsymbol{X}, t), \boldsymbol{X}, t),\\
\boldsymbol{P}(\boldsymbol{X}, t) &= \hat{\boldsymbol{P}}(\boldsymbol{F}(\boldsymbol{X}, t), \theta(\boldsymbol{X}, t), \mathrm{Grad}\theta(\boldsymbol{X}, t), \boldsymbol{\mathcal{E}}(\boldsymbol{Y}, t), \boldsymbol{X}, t),\\
S(\boldsymbol{X}, t) &= \hat{S}(\boldsymbol{F}(\boldsymbol{X}, t), \theta(\boldsymbol{X}, t), \mathrm{Grad}\theta(\boldsymbol{X}, t), \boldsymbol{\mathcal{E}}(\boldsymbol{X}, t), \boldsymbol{X}, t),\\
\boldsymbol{q}(\boldsymbol{X}, t) &= \hat{\boldsymbol{q}}(\boldsymbol{F}(\boldsymbol{X}, t), \theta(\boldsymbol{X}, t), \mathrm{Grad}\theta(\boldsymbol{X}, t), \boldsymbol{\mathcal{E}}(\boldsymbol{X}, t), \boldsymbol{X}, t),\\
\dot{\boldsymbol{\mathcal{E}}}(\boldsymbol{X}, t) &= \hat{\boldsymbol{\mathcal{P}}}(\boldsymbol{F}(\boldsymbol{X}, t), \theta(\boldsymbol{X}, t), \mathrm{Grad}\theta(\boldsymbol{X}, t), \boldsymbol{\mathcal{E}}(\boldsymbol{X}, t), \boldsymbol{X}, t).
\end{aligned} \tag{2.38}$$

Accordingly, the constitutive functions of observer O^* reduce to

$$\begin{aligned}
\psi^*(\boldsymbol{X}^*, t^*) &= \hat{\psi}(\boldsymbol{F}^*(\boldsymbol{X}^*, t^*), \theta^*(\boldsymbol{X}^*, t^*), \mathrm{Grad}^*\theta^*(\boldsymbol{X}^*, t^*), \boldsymbol{\mathcal{E}}^*(\boldsymbol{X}^*, t^*), \boldsymbol{X}^*, t^*),\\
\boldsymbol{P}^*(\boldsymbol{X}^*, t^*) &= \hat{\boldsymbol{P}}(\boldsymbol{F}^*(\boldsymbol{X}^*, t^*), \theta^*(\boldsymbol{X}^*, t^*), \mathrm{Grad}^*\theta^*(\boldsymbol{X}^*, t^*), \boldsymbol{\mathcal{E}}^*(\boldsymbol{X}^*, t^*), \boldsymbol{X}^*, t^*),\\
S^*(\boldsymbol{X}^*, t^*) &= \hat{S}(\boldsymbol{F}^*(\boldsymbol{X}^*, t^*), \theta^*(\boldsymbol{X}^*, t^*), \mathrm{Grad}^*\theta^*(\boldsymbol{X}^*, t^*), \boldsymbol{\mathcal{E}}^*(\boldsymbol{X}^*, t^*), \boldsymbol{X}^*, t^*),\\
\boldsymbol{q}^*(\boldsymbol{X}^*, t^*) &= \hat{\boldsymbol{q}}(\boldsymbol{F}^*(\boldsymbol{X}^*, t^*), \theta^*(\boldsymbol{X}^*, t^*), \mathrm{Grad}^*\theta^*(\boldsymbol{X}^*, t^*), \boldsymbol{\mathcal{E}}^*(\boldsymbol{X}^*, t^*), \boldsymbol{X}^*, t^*),\\
\dot{\boldsymbol{\mathcal{E}}}^*(\boldsymbol{X}^*, t^*) &= \hat{\boldsymbol{\mathcal{P}}}(\boldsymbol{F}^*(\boldsymbol{X}^*, t^*), \theta^*(\boldsymbol{X}^*, t^*), \mathrm{Grad}^*\theta^*(\boldsymbol{X}^*, t^*), \boldsymbol{\mathcal{E}}^*(\boldsymbol{X}^*, t^*), \boldsymbol{X}^*, t^*).
\end{aligned} \tag{2.39}$$

The second case is given by the time shift $a = t$, $\boldsymbol{\alpha}(t^*) = \boldsymbol{I}$ and $\boldsymbol{c}(t^*) = \boldsymbol{0}$. In this situation the right-hand sides of (2.39) do not explicitly depend on time, $t^* = 0$, while the right-hand sides of (2.38) still do. Therefore, a direct time dependency of the response functions should be disregarded as well, leading to the general form

$$\begin{aligned}
\psi(\boldsymbol{X}, t) &= \hat{\psi}(\boldsymbol{F}(\boldsymbol{X}, t), \theta(\boldsymbol{X}, t), \mathrm{Grad}\theta(\boldsymbol{X}, t), \boldsymbol{\mathcal{E}}(\boldsymbol{X}, t), \boldsymbol{X}),\\
\boldsymbol{P}(\boldsymbol{X}, t) &= \hat{\boldsymbol{P}}(\boldsymbol{F}(\boldsymbol{X}, t), \theta(\boldsymbol{X}, t), \mathrm{Grad}\theta(\boldsymbol{X}, t), \boldsymbol{\mathcal{E}}(\boldsymbol{Y}, t), \boldsymbol{X}),\\
S(\boldsymbol{X}, t) &= \hat{S}(\boldsymbol{F}(\boldsymbol{X}, t), \theta(\boldsymbol{X}, t), \mathrm{Grad}\theta(\boldsymbol{X}, t), \boldsymbol{\mathcal{E}}(\boldsymbol{X}, t), \boldsymbol{X}),\\
\boldsymbol{q}(\boldsymbol{X}, t) &= \hat{\boldsymbol{q}}(\boldsymbol{F}(\boldsymbol{X}, t), \theta(\boldsymbol{X}, t), \mathrm{Grad}\theta(\boldsymbol{X}, t), \boldsymbol{\mathcal{E}}(\boldsymbol{X}, t), \boldsymbol{X}),\\
\dot{\boldsymbol{\mathcal{E}}}(\boldsymbol{X}, t) &= \hat{\boldsymbol{\mathcal{P}}}(\boldsymbol{F}(\boldsymbol{X}, t), \theta(\boldsymbol{X}, t), \mathrm{Grad}\theta(\boldsymbol{X}, t), \boldsymbol{\mathcal{E}}(\boldsymbol{X}, t), \boldsymbol{X}).
\end{aligned} \tag{2.40}$$

In summary, we find that constitutive equations (2.40) neither explicitly depend upon the motion nor on time, which is a consequence of the principle of material objectivity. Note that the evolution equation $(2.40)_5$ leads to internal variables $\boldsymbol{\mathcal{E}}(\boldsymbol{X}, t)$ which are functionals of the past histories of $\boldsymbol{F}(\boldsymbol{X}, t), \theta(\boldsymbol{X}, t)$ and $\mathrm{Grad}\theta(\boldsymbol{X}, t)$ only, so that the instantaneous response of the material will be elastic [65, p. 242]. Further note that the response functions derived so far are only necessary conditions for material objectivity. Additional restrictions are required to establish objective constitutive relations.

2.5.5. Further Objectivity Requirements

If we take account of the general transformation rules for *objective tensor fields* in our development of an objective thermomechanical constitutive framework, we will be able to establish further useful relations for the response functions (2.40) in case of different observers O and O^*. For example, the two-point stress tensor $\boldsymbol{P}(\boldsymbol{X},t)$ and the spatial heat flux $\boldsymbol{q}(\boldsymbol{X},t)$ are called objective in terms of the change of frame (2.35) if $\boldsymbol{P}^* = \boldsymbol{\alpha}(t)\boldsymbol{P}$ and $\boldsymbol{q}^* = \boldsymbol{\alpha}(t)\boldsymbol{q}$ holds, while the scalar quantities $S^* = S$ and $\psi^* = \psi$ are objective per definition [49, chap. 4]. We assume that the internal variables operate in the reference configuration and, therefore, are unaffected by a change of frame, $\boldsymbol{\mathcal{E}}^* = \boldsymbol{\mathcal{E}}$. Constitutive equations for both observers should be in line with these objectivity requirements and, therefore, equations (2.40) established for both observers applying to the same material should fulfill the relations (assuming zero time shift, that is $t^* = t$)

$$\begin{aligned}
\hat{\psi}(\boldsymbol{F}^*(t),\theta^*(t),\mathrm{Grad}^*\theta^*(t),\boldsymbol{\mathcal{E}}(t),\boldsymbol{X}^*) &= \hat{\psi}(\boldsymbol{F}(t),\theta(t),\mathrm{Grad}\theta(t),\boldsymbol{\mathcal{E}}(t),\boldsymbol{X}),\\
\hat{\boldsymbol{P}}(\boldsymbol{F}^*(t),\theta^*(t),\mathrm{Grad}^*\theta^*(t),\boldsymbol{\mathcal{E}}(t),\boldsymbol{X}^*) &= \boldsymbol{\alpha}(t)\hat{\boldsymbol{P}}(\boldsymbol{F}(t),\theta(t),\mathrm{Grad}\theta(t),\boldsymbol{\mathcal{E}}(t),\boldsymbol{X}),\\
\hat{S}(\boldsymbol{F}^*(t),\theta^*(t),\mathrm{Grad}^*\theta^*(t),\boldsymbol{\mathcal{E}}(t),\boldsymbol{X}^*) &= \hat{S}(\boldsymbol{F}(t),\theta(t),\mathrm{Grad}\theta(t),\boldsymbol{\mathcal{E}}(t),\boldsymbol{X}),\\
\hat{\boldsymbol{q}}(\boldsymbol{F}^*(t),\theta^*(t),\mathrm{Grad}^*\theta^*(t),\boldsymbol{\mathcal{E}}(t),\boldsymbol{X}^*) &= \boldsymbol{\alpha}(t)\hat{\boldsymbol{q}}(\boldsymbol{F}(t),\theta(t),\mathrm{Grad}\theta(t),\boldsymbol{\mathcal{E}}(t),\boldsymbol{X}),\\
\hat{\boldsymbol{\mathcal{P}}}(\boldsymbol{F}^*(t),\theta^*(t),\mathrm{Grad}^*\theta^*(t),\boldsymbol{\mathcal{E}}(t),\boldsymbol{X}^*) &= \hat{\boldsymbol{\mathcal{P}}}(\boldsymbol{F}(t),\theta(t),\mathrm{Grad}\theta(t),\boldsymbol{\mathcal{E}}(t),\boldsymbol{X}),
\end{aligned} \tag{2.41}$$

where the dependence on $\boldsymbol{X}^* = \boldsymbol{X}$ is understood. Furthermore, the Euclidean transformation (2.35) implies $\boldsymbol{F}^* = \boldsymbol{\alpha}(t)\boldsymbol{F}$. This transformation rule together with the scalar temperature field $\theta^* = \theta$ and $\mathrm{Grad}^*\theta^* = \mathrm{Grad}\theta$ for the temperature gradient yields

$$\begin{aligned}
\hat{\psi}(\boldsymbol{\alpha}(t)\boldsymbol{F}(t),\theta(t),\mathrm{Grad}\theta(t),\boldsymbol{\mathcal{E}}(t),\boldsymbol{X}) &= \hat{\psi}(\boldsymbol{F}(t),\theta(t),\mathrm{Grad}\theta(t),\boldsymbol{\mathcal{E}}(t),\boldsymbol{X}),\\
\hat{\boldsymbol{P}}(\boldsymbol{\alpha}(\tau)\boldsymbol{F}(t),\theta(t),\mathrm{Grad}\theta(t),\boldsymbol{\mathcal{E}}(t),\boldsymbol{X}) &= \boldsymbol{\alpha}(t)\hat{\boldsymbol{P}}(\boldsymbol{F}(t),\theta(t),\mathrm{Grad}\theta(t),\boldsymbol{\mathcal{E}}(t),\boldsymbol{X}),\\
\hat{S}(\boldsymbol{\alpha}(t)\boldsymbol{F}(t),\theta(t),\mathrm{Grad}\theta(t),\boldsymbol{\mathcal{E}}(t),\boldsymbol{X}) &= \hat{S}(\boldsymbol{F}(t),\theta(t),\mathrm{Grad}\theta(t),\boldsymbol{\mathcal{E}}(t),\boldsymbol{X}),\\
\hat{\boldsymbol{q}}(\boldsymbol{\alpha}(t)\boldsymbol{F}(t),\theta(t),\mathrm{Grad}\theta(t),\boldsymbol{\mathcal{E}}(t),\boldsymbol{X}) &= \boldsymbol{\alpha}(t)\hat{\boldsymbol{q}}(\boldsymbol{F}(t),\theta(t),\mathrm{Grad}\theta(t),\boldsymbol{\mathcal{E}}(t),\boldsymbol{X}),\\
\hat{\boldsymbol{\mathcal{P}}}(\boldsymbol{\alpha}(t)\boldsymbol{F}(t),\theta(t),\mathrm{Grad}\theta(t),\boldsymbol{\mathcal{E}}(t),\boldsymbol{X}) &= \hat{\boldsymbol{\mathcal{P}}}(\boldsymbol{F}(t),\theta(t),\mathrm{Grad}\theta(t),\boldsymbol{\mathcal{E}}(t),\boldsymbol{X}).
\end{aligned} \tag{2.42}$$

We refer to response functions satisfying relations (2.42) as *objective*. If, in addition, the explicit dependency on the reference position $\boldsymbol{X}$ is neglected, the material is said to be *homogeneous*. A further reduction is possible by taking the second law of thermodynamics into consideration, which imposes further restrictions on the constitutive equations (2.42).

2.6. Consequences of the Second Law

As already indicated above, the second law imposes further constraints on our constitutive framework. The process of finding reduced forms of (2.40) is called the *Coleman-Noll procedure* [62]. In the following, we will sketch out the basic steps. First, multiplication of (2.29) with the absolute temperature θ and substitution of (2.24) into the resulting equation yields the second law in terms of the specific Helmholtz energy $\psi(\boldsymbol{X},t)$,

$$\theta\gamma = \boldsymbol{P}\cdot\dot{\boldsymbol{F}} - \rho_0\dot{\theta}S - \rho_0\dot{\psi} - \frac{1}{\theta}(\mathrm{Grad}\theta)\cdot\boldsymbol{Q} \geq 0. \tag{2.43}$$

Next, we calculate the material time derivative of the Helmholtz energy function,

$$\dot{\psi} = \frac{\partial \hat{\psi}}{\partial \boldsymbol{F}} \cdot \dot{\boldsymbol{F}} + \frac{\partial \hat{\psi}}{\partial \theta}\dot{\theta} + \frac{\partial \hat{\psi}}{\partial \mathrm{Grad}\theta} \cdot (\mathrm{Grad}\theta)^{\cdot} + \frac{\partial \hat{\psi}}{\partial \boldsymbol{\mathcal{E}}} \cdot \hat{\boldsymbol{\mathcal{P}}}, \tag{2.44}$$

and insert this expression into the second law (2.43) to arrive at the inequality

$$\theta\gamma = \left(\boldsymbol{P} - \rho_0 \frac{\partial \hat{\psi}}{\partial \boldsymbol{F}}\right) \cdot \dot{\boldsymbol{F}} - \rho_0 \left(S + \frac{\partial \hat{\psi}}{\partial \theta}\theta\right)\dot{\theta} + \rho_0 \frac{\partial \hat{\psi}}{\partial \mathrm{Grad}\theta} \cdot (\mathrm{Grad}\theta)^{\cdot} - \rho_0 \frac{\partial \hat{\psi}}{\partial \boldsymbol{\mathcal{E}}} \cdot \hat{\boldsymbol{\mathcal{P}}} - \frac{1}{\theta}(\mathrm{Grad}\theta) \cdot \boldsymbol{Q} \geq 0. \tag{2.45}$$

This inequality has to be fulfilled for every $\dot{\boldsymbol{F}}$, $\dot{\theta}$ and $(\mathrm{Grad}\theta)^{\cdot}$ at all material points $\boldsymbol{X}$ of continuum body B at every instant of time t. This enables us to rewrite the constitutive relations in the form

$$\psi(\boldsymbol{X}, t) = \hat{\psi}(\boldsymbol{F}, \theta, \boldsymbol{\mathcal{E}}, \boldsymbol{X}), \quad \boldsymbol{P}(\boldsymbol{X}, t) = \rho_0 \frac{\partial \hat{\psi}}{\partial \boldsymbol{F}}(\boldsymbol{F}, \theta, \boldsymbol{\mathcal{E}}, \boldsymbol{X}), \quad S(\boldsymbol{X}, t) = -\frac{\partial \hat{\psi}}{\partial \theta}(\boldsymbol{F}, \theta, \boldsymbol{\mathcal{E}}, \boldsymbol{X}) \tag{2.46}$$

for the specific Helmholtz energy, the stresses and the specific entropy, respectively, followed by the remainder inequality

$$\mathcal{D}_{\mathrm{int}} - \frac{1}{\theta}(\mathrm{Grad}\theta) \cdot \boldsymbol{Q} \geq 0, \quad \text{where} \quad \mathcal{D}_{\mathrm{int}} = -\rho_0 \frac{\partial \hat{\psi}}{\partial \boldsymbol{\mathcal{E}}} \cdot \hat{\boldsymbol{\mathcal{P}}}(\boldsymbol{F}, \theta, \mathrm{Grad}\theta, \boldsymbol{\mathcal{E}}, \boldsymbol{X}). \tag{2.47}$$

As already indicated in Section 2.3, expression $(2.47)_1$ implies the dissipation inequality (2.30) if we assume that entropy production by conduction of heat must be non-negative. Now, by taking account of (2.46) and applying standard arguments[4] on relations (2.42) (see e.g. [66, p. 305]) we arrive at the following *objective* constitutive relations in terms of the family of generalized strain tensors (2.9) in the reference configuration

$$\begin{aligned} \psi(\boldsymbol{X}, t) &= \check{\psi}(\boldsymbol{\varepsilon}, \theta, \boldsymbol{\mathcal{E}}, \boldsymbol{X}), & \boldsymbol{\sigma}(\boldsymbol{X}, t) &= \rho_0 \frac{\partial \check{\psi}}{\partial \boldsymbol{\varepsilon}}(\boldsymbol{\varepsilon}, \theta, \boldsymbol{\mathcal{E}}, \boldsymbol{X}), \\ S(\boldsymbol{X}, t) &= -\frac{\partial \check{\psi}}{\partial \theta}(\boldsymbol{\varepsilon}, \theta, \boldsymbol{\mathcal{E}}, \boldsymbol{X}), & \dot{\boldsymbol{\mathcal{E}}}(\boldsymbol{X}, t) &= \boldsymbol{\mathcal{P}}(\boldsymbol{\varepsilon}, \theta, \mathrm{Grad}\theta, \boldsymbol{\mathcal{E}}, \boldsymbol{X}), \end{aligned} \tag{2.48}$$

where we call the symmetric second-order tensor $\boldsymbol{\sigma}$ the *generalized stress tensor* in the reference configuration dual to the strain tensor $\boldsymbol{\varepsilon}$. Finally, we introduce *Duhamel's law of heat conduction* in terms of the spatial second-order conductivity tensor $\boldsymbol{\lambda}(\boldsymbol{\varepsilon}, \theta, \boldsymbol{\mathcal{E}}, \boldsymbol{X})$ in the spatial and referential form,

$$\boldsymbol{q}(\boldsymbol{X}, t) = -\boldsymbol{\lambda}\mathrm{grad}\theta \qquad \text{and} \qquad \boldsymbol{Q}(\boldsymbol{X}, t) = -(\det \boldsymbol{F})\boldsymbol{F}^{-1}\boldsymbol{\lambda}\boldsymbol{F}^{T-1}\mathrm{Grad}\theta, \tag{2.49}$$

respectively. Reduced response functions (2.48) together with (2.49) form the basis for the material modeling of amorphous polymers through the glass transition region in the upcoming sections.

[4] The basic idea is to use the *polar decomposition* of the deformation gradient, $\boldsymbol{F} = \boldsymbol{R}\boldsymbol{U}$, where $\boldsymbol{R}$ is a proper orthogonal tensor and $\boldsymbol{U}$ is the *right stretch tensor*, and additionally by setting $\boldsymbol{\alpha} = \boldsymbol{R}^T$ in equation (2.42). As a result, the specific Helmholtz energy is given in terms of *material* strain tensors. Using different functional forms for the Helmholtz energy $\psi = \bar{\psi}(\boldsymbol{U}, \theta, \boldsymbol{\mathcal{E}}, \boldsymbol{X}) = \check{\psi}(\boldsymbol{\varepsilon}, \theta, \boldsymbol{\mathcal{E}}, \boldsymbol{X})$ eventually leads to equation (2.48).

3. Constitutive Modeling of Amorphous Polymers

Amorphous polymers feature some prominent material characteristics as a direct consequence of their special molecular constitution. Understanding the underlying microscopic aspects is vital in the constitutive modeling process. We therefore start with a general overview of the molecular nature of amorphous polymers and go on to discuss a very important property, the so-called glass transition phenomenon. Next, we continue with an outline of the superposition principles related to time-temperature-pressure equivalences. Since polymers are affected by physical aging, we devote a separate section to this topic. Special emphasis is put on polyvinyl butyral, an amorphous polymer of widespread use in civil engineering applications. Following these constitutive basics of polymeric systems, we eventually tackle the phenomenological material modeling process in terms of the internal variables approach introduced in the preceding chapter. We begin with the simplest thermoviscoelastic material law and finally develop a thermodynamically consistent constitutive extension to model amorphous polymers through the glass transition region assuming the thermorheological simplicity hypothesis. This constitutes the major contribution of this thesis.

3.1. General Aspects of Polymeric Materials

Polymers form a large class of materials whose distinguishing feature is their special chemical composition compared to other types of materials such as metals and ceramics. More precisely, polymers consist of long-chain *macromolecules*, which in turn are made up of thousands of smaller identical repeating units called *monomers*. While monomers are connected via *covalent bonds* ("primary bonds"), individual chains are additionally held together by comparatively weak interchain forces ("secondary bonds"), leading to some sort of entanglement network, see Figure 3.1. The different forms and sizes of the macromolecules making up the polymer as well as their spatial distribution have a great influence on the overall mechanical and thermal properties, such as strength, stiffness, toughness, moulding and annealing capabilities. The arrangements of atoms in a molecule chain and their spatial distribution are described by the terms *molecular configuration* and *molecular conformation*. The former describes those arrangements of atoms which can only be altered by breaking or reforming chemical bonds, whereas the latter are those arrangements of atoms which can be changed by rotation of chain segments around a single bond [67, p. 111]. Polymer resins are often mixed with certain additives, resulting in synthetic products known as industrial *plastics*. Additives modify and improve the properties of polymers according to their specific usage. Common additives include plasticizers, pigments, fillers, lubricants, extenders, antioxidants as well as heat and light stabilizers. Polymers belong to different categories and may be grouped as follows:

- either *thermosets* or *thermoplastics*, depending on the presence or absence of primary bonds between individual chains,
- the degree of crystallinity: either *amorphous* or *semi-crystalline* structures according to the molecular configuration,
- the chain size or their molecular weight distribution (a polymer with a *weight average molecular weight* of $10\,000\ \frac{\mathrm{g}}{\mathrm{mol}}$ is considered as low, while a so-called *high polymer* has, for example, a molecular weight of up to $200\,000\ \frac{\mathrm{g}}{\mathrm{mol}}$ or more),
- homopolymers, copolymers, terpolymers etc. according to the different types of monomers within a single chain,
- the degree of *polymerization*, that is the total number of monomers within a single chain molecule,
- whether the polymer is in a *glassy* or *rubbery* state at service temperature, or something in-between,
- their processing properties at elevated temperatures (melting or moulding capabilities),
- the type of application of the final product (e.g. adhesives, lubricants, computer housings, bumpers, fiber reinforced polymers, golf clubs, …).

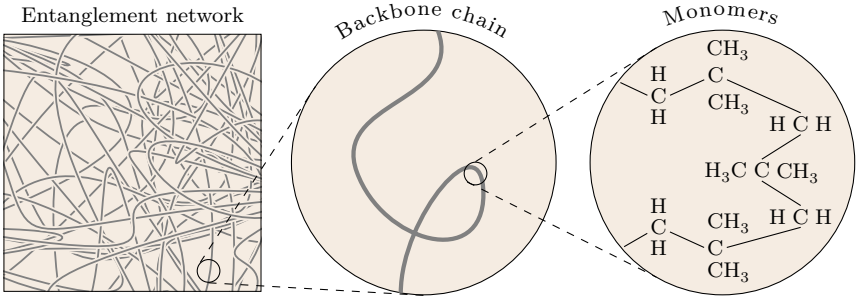

Figure 3.1.: Symbolic representation of an amorphous entanglement structure made up of many long-chain macromolecules, adapted from [68, p. 3]. The chains are held together by secondary bonds (van der Waals forces, hydrogen bonds, dipole-dipole interactions). The middle part depicts a single convoluted chain, which in turn consists of individual monomers.

As indicated above, the microscopic structure of polymers is quite complex, resulting in some remarkable macroscopic material properties. These have to be taken into account during the constitutive modeling process. Since polymers exhibit a marked time- and temperature-dependent material behavior, they are often modeled within the theory of thermoviscoelasticity. However, plastic deformations may also occur, as is the case for vulcanized rubber, for example. It is desirable at this point to familiarize the reader with some of the important thermoviscoelastic phenomena. These will be explained in the following sections.

3.1.1. The Glass Transition Phenomenon

Two different polymers may differ greatly in their structural appearance at room temperature. While one of them appears to be soft and rubbery, the other one seems to be

rather rigid and glassy. However, after heating the second polymer to a certain extent it will possibly transform and become similar to the first one. This type of transformation generally occurs within a narrow temperature interval, the so-called *glass transition region*[1]. At temperatures well below the transition region the polymer chain backbones are largely immobilized, which is why the bulk appears to be hard and stiff. Upon heating through the transition region, the polymer expands and the internal structure becomes more flexible. The thermal motion of individual molecular chains increases and the decrease of packing of the system eventually allows for short-range translational and rotational motions of the macromolecules relative to each other. These conformational changes result in an overall *viscous* material behavior (implying phenomena such as relaxation and creep), which characterizes the transition from the glassy to the rubbery state. Usually, the glass transition region is identified by a single temperature value, the *glass transition temperature*. The glass transition temperature strongly depends on the mobility of the polymeric chains. The mobility is influenced by several factors (for an in-depth discussion see [69, chap. 10]):

- the chemical composition, i.e. chain stiffness, side group effects and cross-linking of chains. Flexible groups in the chain and flexible side groups lower the glass transition, while covalent bonds between polymeric chains increase the transition temperature,
- strong intermolecular forces (secondary bonds between chains) shift the glass transition towards higher temperatures,
- increasing molecular weight increases also the glass transition temperature. However, upon a certain threshold no further increase will occur,
- plasticizers favor changes in the molecular conformation, leading to lower glass transition temperatures.

There exist different methods to determine a polymer's glass transition temperature. Dilatometric or calorimetric experiments are standard practice in the field of physical chemistry. Engineers, on the other hand, prefer so-called Dynamic Mechanical Thermal Analyses (DMTA for short). Accordingly, for one polymer there may be as many different glass transition temperatures in the literature as there are methods available (see also Table 3.1). Nevertheless, most often the values cover a specific range where the smallest and largest value give some indication of the bounds of the glass transition region[2].

Remark 10. *As indicated in the preceding section, material scientists distinguish between thermoplastics and thermosets. Both types are glass-like well below their specific transition temperature. However, the associated molecular interpretation is different: while thermoplastics appear rigid because of the many entanglements between individual macromolecules, thermosetting polymers comprise macromolecular chains hold together by covalent bonds [67, p. 196], thus hindering relative motion of neighboring chains.*

[1] As the name implies, the glass transition is characteristic for amorphous materials such as glasses, which happens at elevated temperatures, e.g. above 500 °C in case of soda lime silica glass. Other terms for glass transition region found in the literature are *α-transition* or *second-order transition*.

[2] Note that Ferry [68, p. 312] considers only dilatometric experiments as the appropriate means to determine the glass transition temperature (see also [67, p. 80]).

To give some impressions on the different thermoviscoelastic phenomena occuring during the glass transition, Figures 3.2 and 3.3 compile some experimental findings of both thermal and mechanical properties related to amorphous materials. Figure 3.2 shows the temperature dependence of the specific heat capacity *at constant pressure* as well as the specific volume of a polyvinyl butyral (PVB) sample [70]. Note that the curves represent measurements made upon heating of the sample from well below the glass transition temperature far into the rubbery regime. The curves of the specific heat are characteristic for amorphous polymers and display a steep rise between the glassy and the rubbery state, followed by a constant slope above the glass transition. From the curves of the specific volume we infer an improved mobility of molecular chains during heating through the glass transition region. The slope of the specific volume represents the coefficient of thermal expansion, which undergoes a more or less pronounced change during the transition, depending on the plasticizer content. As is evident, the plasticizer shifts the transition region towards lower temperatures and broadens the intervall. Both the thermal history of the sample and the heating rate play a crucial role and will significantly influence the outcome of the experiments. We will further investigate this in Part III of this thesis. Some mechanical characteristics in the glass transition region

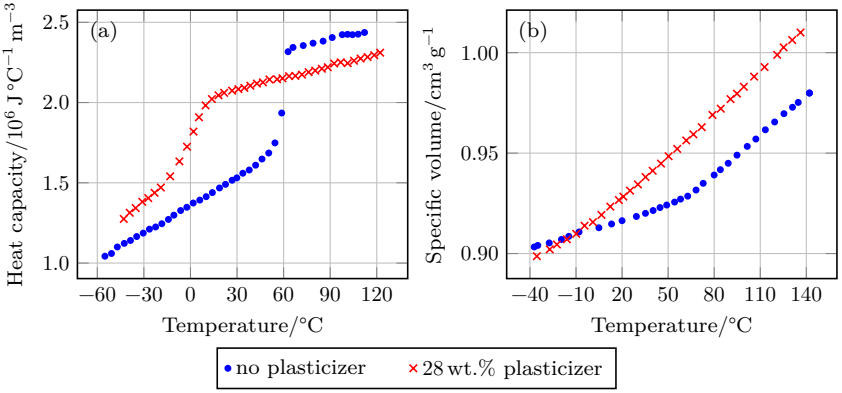

Figure 3.2.: Temperature dependence of the specific heat capacity at constant pressure (a) and the specific volume (b) using the example of polyvinyl butyral (Mowital® B 70 SFP) with different plasticizer content (triethylene glycol di-(2-ethyl butyrate)) [70]. As is evident, the plasticizer shifts the glass transition region towards lower temperatures and broadens the intervall. Note that the shapes of the curves and the location of the transition region also depend on the cooling and heating rate applied during the experiment.

are illustrated in Figure 3.3, again taking the example of PVB. On the left-hand side we see the temperature-dependent shear storage modulus determined by DMTA [17, p. 116]. The shear stiffness displays a marked drop by several orders of magnitude in passing from the glassy to the rubbery state. This explains the stiff and rigid appearance at temperatures well below the glass transition, in contrast to the soft and flexible structure associated with the rubbery regime. Notice that the glass transition region of the specific heat capacity shown in Figure 3.2 is located several degrees (about 15 °C) below the transition of the shear storage modulus. These discrepancies may stem from

different sources. First, different PVB products with varying plasticizer content were used to determine the thermal and mechanical properties[3]. Second, the curves of the specific heat capacity and the storage modulus are rate-dependent. Third, the curve of the storage modulus additionally depends on the frequency applied during the DMTA [17, p. 59]. Fourth, the differences may be associated with different stress and entropy relaxation mechanisms. Similar to the shear stiffness, the bulk behavior is also affected by changes through the glass transition. Nevertheless, the drop in bulk stiffness is much less pronounced as that in shear deformation. Since the glassy bulk and shear moduli are approximately of the same order of magnitude, the large difference in stiffness decrease results in an incompressible material behavior in the rubbery state. This is

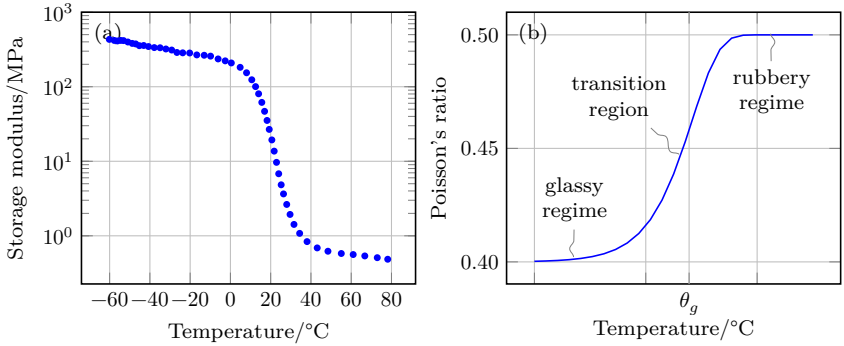

Figure 3.3.: Temperature dependence of the shear storage modulus G' of a polyvinyl butyral sample (Trosifol®) [17, p. 116] (a) and schematic representation of the temperature-dependent Poisson's ratio ν (b) (no data available). The shear modulus significantly decreases through the glass transition region by several orders of magnitude. The right diagram clearly indicates the incompressibility in the rubbery regime, which is in sharp contrast to the glassy state (θ_g denotes the glass transition temperature).

schematically sketched on the right-hand side of Figure 3.3 in form of Poisson's ratio. Reliable experimental data on the lateral contraction behavior of polyvinyl butyral are not available, which is why we assume a functional form similar to the other parameters (see e.g. [71] for experiments on polystyrene and poly(methyl methacrylate) and an in-depth discussion on Poisson's ratio in linear viscoelasticity). Vague hints on the magnitude of the glassy Poisson's ratio of PVB are found in [17, p. 130 f.]. Its value is likely to be somewhere between 0.3 and 0.4. The rubbery state is characterized by incompressibility and Poisson's ratio is close to 0.5. It should be emphasized at this point that linear viscoelastic theories do not allow for simple interconversion formulae of elastic constants known from linear elasticity. Instead, integral expressions interrelate the time-dependent material parameters (these may nevertheless be circumvented by algebraic relationships in the Laplace domain [71, 72]). Although the functional dependency of Poisson's ratio on temperature reveals some important thermoviscoelastic features of amorphous polymers, its direct use in the formulation of constitutive

[3]The lack of consistent experimental data on PVB combined with insufficient documentation of thermal histories renders the thermoviscoelastic material modeling of PVB quite difficult.

equations is quite limited, since stress-strain relations are rather defined in terms of compressive strength parameters than in lateral contraction data. Indeed, knowledge about the bulk response of polymeric materials is indispensable in establishing reliable thermoviscoelastic stress-strain constitutive relations, since volume relaxation highly influences configurational changes within the polymer, which in turn affects the viscous behavior in shear deformation. This is especially important to consider when performing DMTA's far below the glass transition temperature [73]. As indicated in [74], a derivation of bulk (relaxation and creep) properties from other viscoelastic parameters is questionable due to a lack of experimental accuracy. Instead, direct measurements of the bulk relaxation behavior becomes necessary.

In the above discussion we have already used terminology which is associated with time-dependent processes (such as relaxation and creep), though the main subject was to shed light on the influence of temperature on the material parameters near the glass transition region. However, in terms of amorphous polymers the effect of time and temperature shows some remarkable analogies and, therefore, time and temperature should actually be treated as (at least superficially) similar influences on the material response. We shall investigate this further in the following section.

3.1.2. Time-Temperature-Superposition Principle

The *time-temperature-superposition principle* expresses the experimental observation that a glassy polymer (i.e. far below the glass transition temperature) under long-term loading eventually deforms as much as the same polymer in its rubbery state (i.e. at elevated temperatures). Conversely, the same polymer in its rubbery state exhibits a stiff material response when subjected to a fast load application, that is a behavior rather associated with the glassy state. Thus, low temperatures are in a sense equivalent to long time durations (or low frequencies), while high temperatures correspond to short time intervals (or high frequencies) [68, chap. 11]. Put differently, the effect of time on the stiffness of an amorphous polymer is in some sense equivalent to that of temperature as described in the preceding section. This striking feature implies not only huge advantages when it comes to the experimental investigation into the time-dependent mechanical properties of polymers [67, chap. 7], but also in the formulation of thermoviscoelastic constitutive equations. Specifically, by introducing the positive, monotonically decreasing scalar variable $a(\theta, \theta_0)$ with respect to some reference temperature θ_0 such that $a(\theta_0, \theta_0) = 1$, the equivalence between time and temperature may be expressed by either one of the following relations

$$\xi(t) = \int_0^t \frac{1}{a(\theta(x), \theta_0)} dx, \qquad \text{or} \qquad \tau_i(\theta) = a(\theta, \theta_0)\tau_i(\theta_0), \quad i = 1, \dots, m. \tag{3.1}$$

The first equation is prevalent in theories where the current stresses are formulated as hereditary integrals in terms of the strain rate (for example in rational thermodynamics). Here, the quantity $\xi(t)$ is referred to as the *material* or *effective time*. The relaxation functions (the kernel functions in the hereditary integral) are functions of the material time defined by the *material clock model* $(3.1)_1$, where the so-called *shift factor*[4] $a(\theta, \theta_0)$ depends on the current temperature $\theta(t)$ and a fixed reference temperature θ_0. Thus,

[4] The reader though should be aware that in the literature the shift factor is sometimes defined as the inverse value of the one given here, or the natural logarithm of the inverse value, which may be the source of some confusion.

for a given instant of time t the constitutive equations are evaluated with respect to material time $\xi(t)$ rather than the actual time t. For example, in a one-dimensional setting the stresses at time t may be determined by the current values and the past history of strain and temperature as

$$\sigma(t) = \int_0^t \hat{E}(\xi(t) - \xi(\tau)) \frac{\partial}{\partial \tau}(\varepsilon(\tau) - \alpha(\theta(\tau) - \theta_0))d\tau, \quad \xi(t) - \xi(\tau) = \int_\tau^t \frac{1}{a(\theta(x), \theta_0)} dx. \tag{3.2}$$

Here, the relaxation function $\hat{E}(\xi)$ refers to the reference temperature θ_0[5]. The material constant α denotes the linear coefficient of thermal expansion. Note that material time and actual time coincide in case of isothermal processes. Thus, considering this special case, from the definition $a(\theta_0, \theta_0) = 1$ and $(3.2)_2$ we find that $\xi(t) - \xi(\tau) = t - \tau$ holds and the nonlinear relation $(3.2)_1$ reduces to the stresses known from linear viscoelasticity. For a more comprehensive treatment on the time-temperature-superposition principle with regard to integral constitutive relations we refer to the literature [39, 53, 67, 75, 76]. The second option $(3.1)_2$, on the other hand, is convenient in connection with stress-strain relations expressed in the form of rate equations or in terms of an internal variables approach. Here, m relaxation mechanisms describe the time-dependent material response, where the temperature dependence enters the equation by a shift of the relaxation times $\tau_i(\theta_0)$ corresponding to reference temperature θ_0. Since the shift factor is defined as a monotonically decreasing function with temperature, an increase in temperature lowers $a(\theta, \theta_0)$, resulting in smaller relaxation times (lower stiffness modulus or reduced viscosity) and vice versa. A possible rate equation for the stresses looks as follows

$$\dot{\sigma}(t) + \frac{1}{\tau(\theta(t))}\sigma(t) = E\left(\dot{\varepsilon}(t) - \alpha\dot{\theta}(t)\right), \quad \tau(\theta(t)) = a(\theta(t), \theta_0)\tau(\theta_0), \tag{3.3}$$

where the single ($m = 1$) temperature dependent relaxation time is determined by a shift of the reference relaxation time $\tau(\theta_0)$ and renders the problem nonlinear (note that the material parameter E is constant). While constitutive equation (3.3) is associated with the actual time t, the integral equation (3.2) additionally depends on the material time $\xi(t)$. Both the material clock model and the shift in relaxation times according to (3.1) are restricted to *thermorheologically simple materials*[6]. However, the integral type in its current form is somewhat more general, as the relaxation function $\hat{E}(\xi)$ may represent a continuous relaxation spectrum, possibly including an equilibrium value. In contrast, the differential form represents only one relaxation mechanism corresponding to a single Maxwell element. A straightforward generalization to a Maxwell model including an equilibrium value to represent solid-like behavior is nevertheless possible. Moreover, if the relaxation function $\hat{E}(\xi)$ is approximated by means of a Prony series, both variants get very similar and indeed become mathematically equivalent. From a numerical perspective, however, rate equations are rather easier to handle and the nested integral in the first approach seems quite complicated. For a deeper insight into the time-temperature-superposition principle with regard to rate equations using the internal variables approach see [56, 60]. The different shifting procedures resulting from the time-temperature-superposition principle are illustrated in Figure 3.4 for various thermal and mechanical properties. Note that the ideas introduced so far are

[5] In this special case the relaxation function $\hat{E}$ is the same with respect to strains ε and thermal strains $\alpha(\theta - \theta_0)$. In general, however, different relaxation mechanisms will govern the stress response [53, p. 80].

[6] For *thermorheological complex materials* the relaxation times no longer shift equally, see e.g. [77].

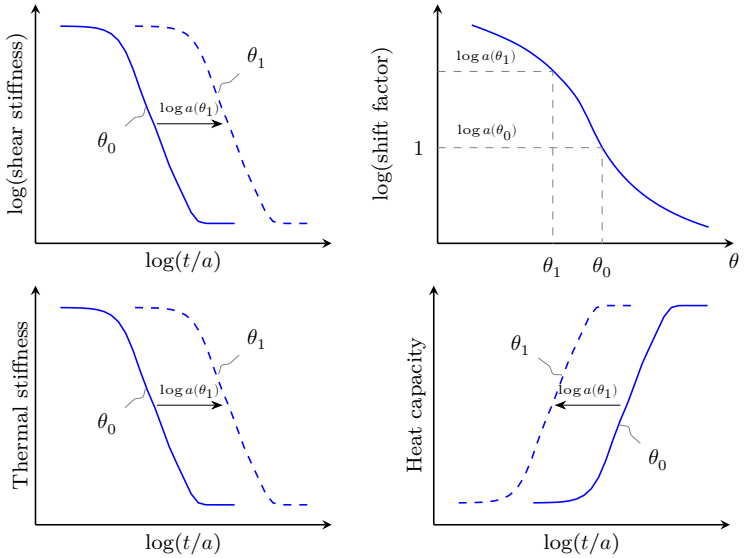

Figure 3.4.: Sketch of some consequences of the *time-temperature-superposition principle* for *thermorheologically simple materials*. The diagram at the top right shows the temperature-dependent shift factor. Remaining graphs represent various mechanical and thermal properties (called *master curves* in rheological circles). The relaxation functions at any temperature can be directly obtained from the corresponding master curve at reference temperature θ_0 through a horizontal shift on the *reduced* logarithmic time axis $\log(t/a)$.

restricted to *homogeneous* temperature distributions (temperature is allowed to vary in time only, not in space) and the overall problem statement is rather associated with a mechanical setting allowing for temperature induced stresses (though a fully coupled thermomechanical setting is conceivable if strains are also homogeneous). It is nevertheless possible to extend the approach discussed above to *nonconstant, nonuniform* temperature states $\theta(\boldsymbol{X}, t)$, which naturally stipulates the evaluation of the balance of energy (2.23) and the formulation of a heat flux constitutive relation (2.49).

We conclude this section with an important remark on the equivalence of time and temperature regarding amorphous polymers. The effect of time (or frequency) is quite similar to that of temperature, given the observed "transition region" of thermal and mechanical parameters with respect to time t. However, the transition from glasslike to rubberlike consistency due to time or frequency is nevertheless inherently different from the glass transition described in the preceding section [68, p. 353]. Put simply, a polymer above its glass transition temperature is still in its rubbery state, though it might respond glass-like under quick load application and vice versa.

3.1.3. Time-Pressure-Superposition Principle

While the time-temperature-superposition principle of polymeric systems has been studied quite extensively since the second half of the last century [78], the *time-pressure-superposition principle* appears as a rather unnoticed subject within the polymeric science community. This is due to the inherent difficulties related to experiments involving precise measurements in small volume changes of solids. However, all of the characteristics associated with time-temperature changes laid out in the preceding section are equally valid for polymeric materials under pressure loading [79], [68, chap. 11], [80, chap. 3]. Hence, analogous to equations (3.1) we may formulate a *stress clock* or pressure-dependent relaxation times as

$$\xi(t) = \int_0^t \frac{1}{a(\mathrm{tr}\boldsymbol{\sigma}(x), p_0)}\, dx, \qquad \text{or} \qquad \tau_i(\mathrm{tr}\boldsymbol{\sigma}) = a(\mathrm{tr}\boldsymbol{\sigma}, p_0)\tau_i(p_0), \quad i = 1, \dots, m, \tag{3.4}$$

where the pressure dependence of the shift factor is expressed through the first invariant of the stress tensor, $\mathrm{tr}\boldsymbol{\sigma}$, and p_0 signifies some defined reference pressure. Thus, all the diagrams in Figure 3.4 may be equally sketched by substituting all occurrences of temperature with pressure. The corresponding shift procedures then apply to constant temperature states. This pressure-dependent behavior results from the accompanied volume change and greatly influences the other viscoelastic properties as already outlined in Section 3.1.1. Ideally, to model amorphous polymers in a general thermodynamic framework, we require a shift factor which incorporates both influences. For a more thorough treatment of stress-dependent shift factors we refer to the literature [77, 79–81].

3.1.4. Physical Aging of Amorphous Polymers

An amorphous polymer cooled well below its glass transition temperature undergoes very slow and gradual internal changes over time and the polymer eventually tends asymptotically towards a state of thermodynamic equilibrium. However, this continuation of the glass forming process may take weeks, months or even years, depending on the degree of cooling into the glassy state. This experimental observation has far-reaching consequences on the overall material properties and its implications are collectively summarized by the term *physical aging* [82]. More specifically, the volume of a polymer quenched from above its glass transition temperature into the glassy regime is greater than its glassy equilibrium value and the thermal quench is thus accompanied by a long-term volumetric creep process[7]. Since the molecular motion of backbone chains is greatly influenced by the degree of packing of the system, physical aging will affect time-dependent mechanical processes such as shear and tensile relaxation even in the small-strain regime [73]. This experimental observation is illustrated in Figure 3.5. A tensile sample of polyvinyl chloride is quenched from above its glass transition temperature into the glassy state. The upper diagram schematically depicts a sequence of creep and recovery tests of the first four out of ten consecutive constant stress load applications. The horizontal axis reflects the elapsed time after the thermal quench (the aging time). The lower diagram shows the resultant tensile creep compliance (TCC) corresponding to ten load steps applied after different aging times as summarized in the

[7] Creep in the glassy regime is affiliated with side group motions [67, p. 257].

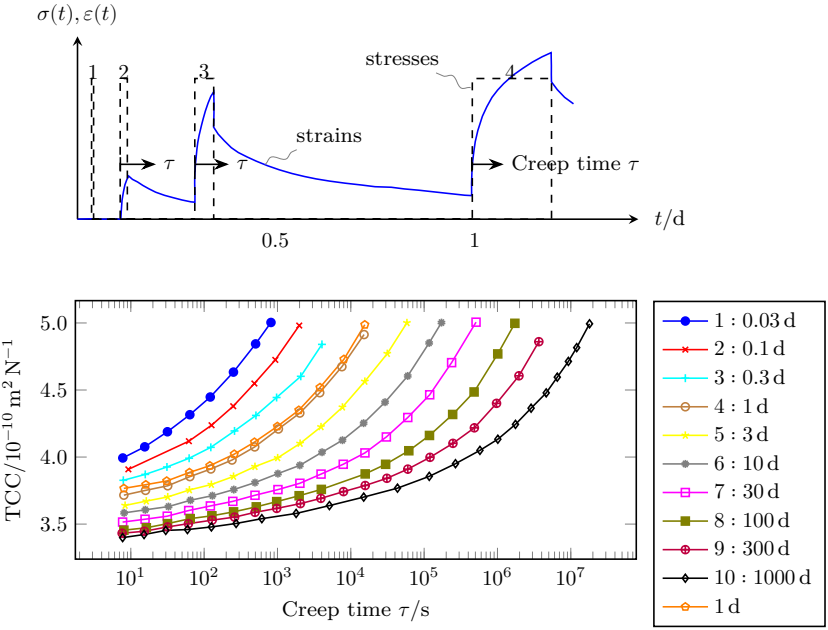

Figure 3.5.: Schematic representation of the effect of *physical aging* on the creep behavior of a *glassy* polymer, taken from [82]. The upper diagram shows part of the creep response due to the applied stress (load steps 5 to 10 left out). The lower diagram shows the resultant tensile creep compliance (TCC). Clearly, different aging times (1–10) have a significant influence on the outcome of creep experiments (see text for further information).

legend. Clearly, taking the example of the creep time $\tau = 1000\,\mathrm{s}$ indicates the differences in the measured TCC's as a direct consequence of physical aging. Furthermore, a separate measurement was performed where the first three load steps were omitted under otherwise equal conditions (curve ⊸). Despite the absence of the first three load steps, the curve nearly coincides (2 % deviation) with the corresponding curve of the first experiment (curve ⊸), implying that physical aging is unaffected by prior creep tests. It was further concluded that individual creep curves could be horizontally shifted and superimposed to form a single master curve (curve ⊸). Since the shape of the creep curves remain invariant with respect to aging, an increase in aging time increases all relaxation times by the same (shift) factor. Hence, physical aging affects relaxation times [82, p. 13]. This fact should be taken into account when using a material clock model according to equation (3.1). These observations again highlight the importance of volumetric relaxation phenomena in amorphous polymers, which is thus indispensable in the formulation of phenomenological constitutive equations within a thermomechanical context. Moreover, the knowledge of the aging behavior is critical when modeling the long-term material response of glassy polymers [82, p. 2]. The aging

phenomenon has motivated the development of the so-called *time-aging-superposition principle* [67, p. 265], analogous to the superposition principles introduced above. We conclude this section by recognizing the fact that, in addition to a temperature and stress (or strain) dependence of the shift factor, it should equally include history effects to properly take account of the physical aging phenomena described in this section.

3.2. Properties of Polyvinyl Butyral

Polyvinyl butyral (PVB for short) is an amorphous random *terpolymer* which consists of the three monomers vinyl acetate (VAc), vinyl alcohol (VA) and vinyl butyral[8]. Figure 3.6 depicts the structural formula of PVB resin. Its weight average molecular weight ranges from $40\,000\,\mathrm{g\,mol^{-1}}$ to $300\,000\,\mathrm{g\,mol^{-1}}$ [83, 84] and, therefore, belongs to the class of so-called *high polymers*. In addition, industrialized PVB contains certain amounts of plasticizer content ranging from between 15 wt.% to 30 wt.%, depending on the specific application. Popular plasticizers include, among others, dibutyl sebacate (DBS), triethylene glycol di-(2-ethyl hexanoate) or dihexyl adipate (DHA). As already mentioned above, the amount of plasticizer content has a dominant effect on the location and shape of the glass transition region, as illustrated in Figure 3.2 on page 34. While the transition temperature of PVB resin can be as high as 80 °C (depending on its VA content), the transition temperatures of plasticized PVB range from −1 °C to 30 °C, see Table 3.1. Besides an improved processability, plasticized PVB displays an increased adhesion to glass, which is of paramount importance for laminated safety glass applications. However, the introduction of plasticizer considerably complicates the constitutive modeling procedure. This is due to the fact that the glass transition region now falls within a temperature regime typically encountered in civil engineering applications and, therefore, has to be taken into account in the design process of structural engineers, see Figures 3.2 and 3.3 on page 34 and 35.

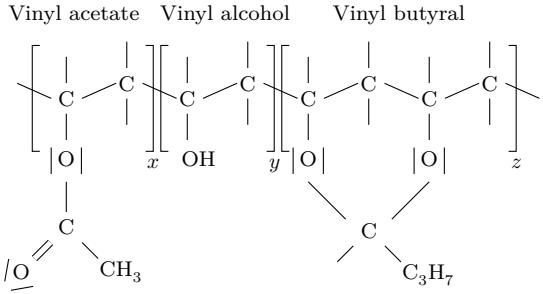

Figure 3.6.: Terpolymer structure of PVB resin consisting of the three monomers *vinyl acetate*, *vinyl alcohol* and *vinyl butyral*. The letters x, y and z imply that each monomer occurs randomly multiple times within a single chain, where the ratio $x : y : z$ equals approximately $2 : 22 : 76$, with slight deviations depending on the manufacturer, see [83, p. 94].

[8] The term *random* signifies the random arrangement of monomers, while the term *terpolymer* refers to three different constituents, in contrast to copolymers for example, whose macromolecules consist of two different types of monomers.

PVB is currently manufactured and sold by a number of companies including Eastman (Saflex®, Butvar®, Vanceva®), Kuraray (Trosifol®, Mowital®, SentryGlas®, Butacite®) and Sekisui (S-Lec®). Industrialized PVB is found in key sectors such as the automobile industry (automotive windshields), building trade (laminated safety and security glass) and partly in photovoltaic applications (sealing material). Its worldwide market size was estimated at more than 350 000 tons back in 2015 with an increasing trend prognosticated for upcoming years [83, 85].

Manufacturer	Product name	Plasticizer	Plast. cont. (in wt.%)	VA cont. (in mol%)	θ_g (in °C)	Method	Reference
Sekisui	S-Lec	Dibutyl sebacate	22	22	16	DSC[5]	[86]
Dupont	Butacite	Dibutyl sebacate	22	22	16	DSC	[86]
Monsanto	Saflex	Dibutyl sebacate	22	22	16	DSC	[86]
Mowital[1]	B 70 SFP	95-08-9[3]	28	18–22	−0.5	CM[6]	[70]
Mowital[1]	B 70 SFP	95-08-9[3]	28	18–22	−1	DM[7]	[70]
-	B XYSG	95-08-9[3]	31	-	0	DM	[87]
Kuraray Trosifol	PVB BG	DHA or 3G8[4]	25–30	18–22	27	DMTA[8]	[17]
-	standard PVB[2]	-	25–30[2]	18–22[2]	8	DMTA[9]	[19]
-	standard PVB[2]	-	25–30[2]	18–22[2]	(28)	DMTA[8]	[19]

[1] PVB resin (final plasticized product was selfmade)
[2] expected to be the same as the first three entries
[3] triethylene glycol-di-(2-ethylbutyrate)
[4] dihexyladipat (DHA) or triethylenglycol-di-2-ethylhexanoat (3G8)
[5] differential calorimetric scanning
[6] calorimetric measurement
[7] dilatometric measurement
[8] Dynamic Mechanical Thermal Analysis (peak in $\tan\delta$)
[9] Dynamic Mechanical Thermal Analysis (peak in E'')

Table 3.1.: Comparison of different PVB products. Different glass transition temperatures θ_g result from different plasticizer material and content as well as different procedures used to determine θ_g. From the data it is inferred that the glass transition of "standard" PVB spans a temperature range from −1 to 28 °C. Note, however, the glass transition region of the specific heat capacity of plasticized PVB shown in Figure 3.2 on page 34. Manufacturer names and products refer to the references cited and may not reflect the current industrial situation.

3.3. Modeling Small Strains and Small Temperature Changes

In this section, we start with the formulation of basic constitutive equations to describe isotropic thermoviscoelastic material behavior assuming small strains and small temperature changes. These equations adopt the internal variables approach as outlined in Section 2.4. Any finite thermoviscoelastic material law should reduce to this material formulation if the conditions $||\boldsymbol{\varepsilon}|| \ll 1$, $|\theta - \theta_0| \ll 1$, $|\dot{\theta}| \ll 1$, $||\dot{\boldsymbol{\varepsilon}}|| \ll 1$ and $||\mathrm{Grad}\theta|| \ll 1$ are met (θ_0 is a fixed reference temperature). Note, however, that the following constitutive relations are already nonlinear due to the influence of internal dissipation. Although this formulation is quite inadequate to model amorphous polymers through the glass transition region, it serves as a first step towards more elaborate theories as those discussed in Section 3.4. In the sequel, thermal and mechanical properties refer to reference temperature θ_0. Any dependence on an infinitesimal deviation from the reference temperature is necessarily neglected.

3.3.1. Constitutive Framework

The material model is fully defined in terms of the Helmholtz energy, evolution equations for the internal variables and a material law for the heat flux according to equations (2.48) and (2.49). We establish these below along with derived quantities and show the thermodynamic consistency with respect to the Clausius-Planck inequality (2.30). In what follows we assume a homogeneous material described by the set of functions

$$\begin{aligned}
\psi(\boldsymbol{X},t) &= \hat{\psi}(\boldsymbol{\varepsilon},\theta,\boldsymbol{\mathcal{E}}_1,\dots,\boldsymbol{\mathcal{E}}_m),\\
\boldsymbol{\sigma}(\boldsymbol{X},t) &= \hat{\boldsymbol{\sigma}}(\boldsymbol{\varepsilon},\theta,\boldsymbol{\mathcal{E}}_1,\dots,\boldsymbol{\mathcal{E}}_m),\\
S(\boldsymbol{X},t) &= \hat{S}(\boldsymbol{\varepsilon},\theta,\boldsymbol{\mathcal{E}}_1,\dots,\boldsymbol{\mathcal{E}}_m),\\
\boldsymbol{Q}(\boldsymbol{X},t) &= \hat{\boldsymbol{Q}}(\mathrm{Grad}\theta),\\
\dot{\boldsymbol{\mathcal{E}}}_l(\boldsymbol{X},t) &= \boldsymbol{\mathcal{P}}_l(\boldsymbol{\varepsilon},\theta,\boldsymbol{\mathcal{E}}_l), \qquad l = 1,\dots,m,
\end{aligned} \tag{3.5}$$

where we assume m independent relaxation mechanisms. This implies that the evolution of the lth internal variable $\boldsymbol{\mathcal{E}}_l(\boldsymbol{X},t)$ does not explicitly depend on the other internal variables. The strain tensor is simply given by the linear relation

$$\boldsymbol{\varepsilon}(\boldsymbol{X},t) := \frac{1}{2}\left(\mathrm{Grad}\boldsymbol{u} + (\mathrm{Grad}\boldsymbol{u})^T\right), \quad \text{where} \quad \mathrm{Grad}\boldsymbol{u}(\boldsymbol{X},t) = \frac{\partial \boldsymbol{u}}{\partial \boldsymbol{X}}(\boldsymbol{X},t). \tag{3.6}$$

Note that this material formulation trivially meets the objectivity requirements discussed in Section 2.5.5. In the sequel, we will drop the $(\hat{\bullet})$-notation for the sake of convenience.

3.3.2. Specification of the Helmholtz Energy

The *specific* Helmholtz energy $(3.5)_1$ is split into an *equilibrium* and a *transient* part as follows

$$\psi(\boldsymbol{X},t) = \psi_{\mathrm{eq}}(\boldsymbol{\varepsilon},\theta) + \psi_{\mathrm{tr}}(\boldsymbol{\varepsilon},\theta,\boldsymbol{\mathcal{E}}_1,\dots,\boldsymbol{\mathcal{E}}_m), \quad [\psi] = \frac{\mathrm{J}}{\mathrm{kg}}. \tag{3.7}$$

Here, the equilibrium Helmholtz energy only depends on the current strain $\boldsymbol{\varepsilon}(\boldsymbol{X},t)$ and the temperature $\theta(\boldsymbol{X},t)$, while the transient part additionally depends on the set of

internal variables $\boldsymbol{\mathcal{E}}_l(\boldsymbol{X},t)$ and should vanish when approaching thermodynamic equilibrium. The equilibrium part is given by

$$\psi_{\text{eq}}(\boldsymbol{X},t) = \frac{1}{2\rho_0}\psi_1(\text{tr}\boldsymbol{\varepsilon})^2 + \frac{1}{\rho_0}\psi_2(\text{dev}\boldsymbol{\varepsilon})\cdot(\text{dev}\boldsymbol{\varepsilon}) + \frac{1}{\rho_0}\psi_4(\text{tr}\boldsymbol{\varepsilon})(\theta-\theta_0) + \frac{1}{2\rho_0}\psi_5(\theta-\theta_0)^2. \quad (3.8)$$

The material parameters are summarized in Table 3.2. The transient part represents memory effects quantifying the deviation from thermodynamic equilibrium of the material. It is defined in terms of the bulk and shear Prony parameters K_l, α_l and G_l as

$$\psi_{\text{tr}}(\boldsymbol{X},t) = \frac{1}{2\rho_0}\sum_r K_r(\text{tr}\boldsymbol{\varepsilon} - \text{tr}\boldsymbol{\mathcal{E}}_r - 3\alpha_r(\theta-\theta_0))^2 + \frac{1}{\rho_0}\sum_r G_r(\text{dev}\boldsymbol{\varepsilon} - \text{dev}\boldsymbol{\mathcal{E}}_r)\cdot(\text{dev}\boldsymbol{\varepsilon} - \text{dev}\boldsymbol{\mathcal{E}}_r). \quad (3.9)$$

While the stiffness parameters K_r and G_r usually assume positive values, the *linear* thermal expansion coefficients α_r may be either positive or negative, depending on the material at hand (see also [88, p. 377 f.]). This is not immediately obvious. We will explain this circumstance in Section 3.3.9. Notice that the transient part contains internal variables $\boldsymbol{\mathcal{E}}_l(\boldsymbol{X},t)$, which necessitates the specification of additional evolution equations.

Parameter	Unit	Physical meaning
ρ_0	$\frac{\text{kg}}{\text{m}^3}$	Reference density ρ_0
ψ_1	$\frac{\text{N}}{\text{m}^2}$	Bulk modulus K_∞
ψ_2	$\frac{\text{N}}{\text{m}^2}$	Shear modulus G_∞
ψ_4	$\frac{\text{N}}{\text{m}^2\,\text{K}}$	Thermal stiffness $-3\alpha_\infty K_\infty$
ψ_5	$\frac{\text{J}}{\text{kg}\,\text{K}^2}$	Specific heat capacity $-\frac{c_\infty}{\theta_0} + \frac{1}{\rho_0}\sum_r 9\alpha_r^2 K_r$ ($\boldsymbol{\varepsilon} = const.$)

Table 3.2.: Summary of the material parameters for the *equilibrium* Helmholtz energy function (3.8). All values relate to the reference temperature θ_0. Note that the material requires the *constant deformation* heat capacity c_∞ and the equilibrium *linear* coefficient of thermal expansion α_∞. The "missing" material parameter $\boldsymbol{\psi_3} = \boldsymbol{0}$ representing initial stresses is not relevant at this point and will be included in the constitutive extension in Section 3.4.

3.3.3. Evolution Equations of the Internal Variables

In the same way as with the strain tensor (2.12) we split the internal variables and their rates into their volumetric and deviatoric parts as

$$\boldsymbol{\mathcal{E}}_l(\boldsymbol{X},t) = \frac{1}{3}(\text{tr}\boldsymbol{\mathcal{E}}_l)\boldsymbol{I} + \text{dev}\boldsymbol{\mathcal{E}}_l, \quad \Rightarrow \quad \dot{\boldsymbol{\mathcal{E}}}_l(\boldsymbol{X},t) = \frac{1}{3}(\text{tr}\dot{\boldsymbol{\mathcal{E}}}_l)\boldsymbol{I} + \text{dev}\dot{\boldsymbol{\mathcal{E}}}_l, \quad [\boldsymbol{\mathcal{E}}_l] = \frac{\text{m}}{\text{m}}, \quad (3.10)$$

where $l = 1, \dots, m$. Now, the evolution of the volumetric and deviatoric internal variables are governed by the following rate equations [61, p. 338],

$$\begin{aligned} \text{tr}\dot{\boldsymbol{\mathcal{E}}}_l(\boldsymbol{X},t) &= \frac{1}{\tau_l^K}(\text{tr}\boldsymbol{\varepsilon} - \text{tr}\boldsymbol{\mathcal{E}}_l - 3\alpha_l(\theta-\theta_0)), & \tau_l^K &= \frac{\eta_l^K}{K_l}, \\ \text{dev}\dot{\boldsymbol{\mathcal{E}}}_l(\boldsymbol{X},t) &= \frac{1}{\tau_l^G}(\text{dev}\boldsymbol{\varepsilon} - \text{dev}\boldsymbol{\mathcal{E}}_l), & \tau_l^G &= \frac{\eta_l^G}{G_l}. \end{aligned} \quad (3.11)$$

These are motivated by the kinematics of the Maxwell model shown in Figure 3.7. Thus, the set of internal variables represent symmetric second-order strain-valued tensors characterizing the current deformation of the dashpots. The relaxation times τ_l^K and τ_l^G being affiliated with viscous bulk and shear deformation possibly assume different values. They depend on the bulk and shear viscosities η_l^K and η_l^G. Notice that only the bulk part in $(3.11)_1$ is affected by variations in temperature. Further note that the deviatoric part $(3.11)_3$ constitutes five independent equations. Since the material is affected by internal dissipation, we have to check for thermomechanical consistency.

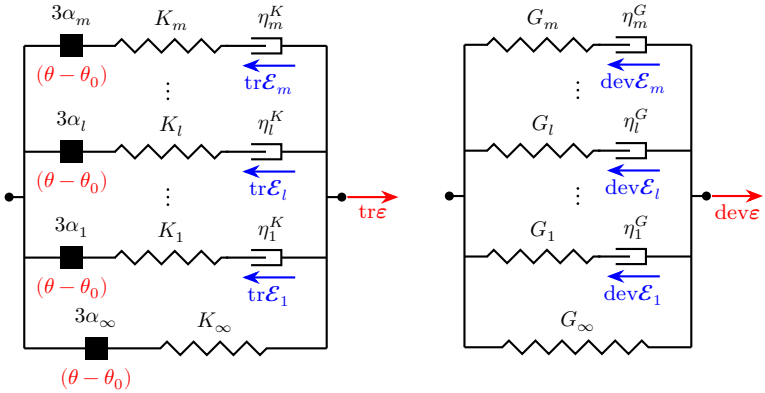

Figure 3.7.: Maxwell model representation of the viscous bulk and shear deformation assuming m independent relaxation mechanisms. Only the bulk part is affected by variations in temperature. The *constant* material parameters K_l, G_l, η_l^K, η_l^G and α_l as well as equilibrium values K_∞, G_∞ and α_∞ refer to reference temperature θ_0. The equilibrium part eventually renders the material solid-like.

3.3.4. Dissipation Inequality — Thermomechanical Consistency

The constitutive framework is thermodynamically consistent when the internal dissipation $(2.47)_2$ is non-negative,

$$\mathcal{D}_{\mathrm{int}}(\boldsymbol{X},t) = -\sum_r \rho_0 \frac{\partial \psi}{\partial \boldsymbol{\mathcal{E}}_r}(\boldsymbol{\varepsilon},\theta,\boldsymbol{\mathcal{E}}_1,\dots,\boldsymbol{\mathcal{E}}_m)\cdot\boldsymbol{\mathcal{P}}_r(\boldsymbol{\varepsilon},\theta,\boldsymbol{\mathcal{E}}_r) \geq 0, \quad [\mathcal{D}_{\mathrm{int}}] = \frac{\mathrm{W}}{\mathrm{m}^3}. \tag{3.12}$$

Invoking the chain rule in calculating the partial derivatives of the transient Helmholtz energy (3.9) and taking advantage of the volumetric-deviatoric split (3.10) yields

$$\mathcal{D}_{\mathrm{int}} = \sum_r \left[\underbrace{\frac{K_r}{\tau_r^K}}_{\geq 0} \underbrace{\left(\mathrm{tr}\boldsymbol{\varepsilon} - \mathrm{tr}\boldsymbol{\mathcal{E}}_r - 3\alpha_r(\theta-\theta_0)\right)^2}_{\geq 0} + \underbrace{\frac{2G_r}{\tau_r^G}}_{\geq 0} \underbrace{\left(\mathrm{dev}\boldsymbol{\varepsilon} - \mathrm{dev}\boldsymbol{\mathcal{E}}_r\right)\cdot\left(\mathrm{dev}\boldsymbol{\varepsilon} - \mathrm{dev}\boldsymbol{\mathcal{E}}_r\right)}_{\geq 0} \right] \geq 0. \tag{3.13}$$

Since this inequality holds for every thermodynamic process at every instant of time t, the constitutive model is in accordance with the second law of thermodynamics.

Note, however, that we have assumed positive entropy production in terms of heat conduction by using a simple constitutive law for the heat flux (see below). Further note the nonlinearity of the internal dissipation.

3.3.5. Specification of the Heat Flux

We assume that Duhamel's law of heat conduction (2.49) with constant conductivity $\lambda > 0$ under thermal isotropy holds,

$$\boldsymbol{Q}(\boldsymbol{X}, t) = -\lambda \mathrm{Grad}\theta(\boldsymbol{X}, t). \tag{3.14}$$

This classic assumption is quite often found in the literature and is known as *Fourier's law of heat conduction* [49, p. 269]. Since the deformations are small, the difference between spatial and referential heat flux becomes negligible. Note that the condition

$$-\frac{1}{\theta(\boldsymbol{X}, t)}(\mathrm{Grad}\theta(\boldsymbol{X}, t)) \cdot \boldsymbol{Q}(\boldsymbol{X}, t) \geq 0 \tag{3.15}$$

from the remainder inequality $(2.47)_1$ holds trivially in case of (3.14). This is necessary when we want to show thermomechanical consistency by positive dissipation $\mathcal{D}_{\mathrm{int}} \geq 0$.

3.3.6. Structural Thermoviscoelastic Heating

In anticipation of the balance of energy in upcoming sections we need to introduce a further quantity called *structural thermoviscoelastic heating* $\mathcal{H}_{\mathrm{in}}(\boldsymbol{X}, t)$. It is defined in terms of the partial derivative of the Helmholtz energy $(3.5)_1$ with respect to temperature and the internal variables as

$$\mathcal{H}_{\mathrm{in}}(\boldsymbol{X}, t) = -\rho_0 \theta_0 \sum_r \frac{\partial^2 \psi}{\partial \boldsymbol{\mathcal{E}}_r \partial \theta}(\boldsymbol{\varepsilon}, \theta, \boldsymbol{\mathcal{E}}_1, \dots, \boldsymbol{\mathcal{E}}_m) \cdot \boldsymbol{\mathcal{P}}_r(\boldsymbol{\varepsilon}, \theta, \boldsymbol{\mathcal{E}}_r), \quad [\mathcal{H}_{\mathrm{in}}] = \frac{\mathrm{W}}{\mathrm{m}^3}. \tag{3.16}$$

Analogously to the internal dissipation we apply the chain rule in calculating the partial derivatives of the transient Helmholtz energy (3.9) and make use of the volumetric-deviatoric split (3.10). This leads to

$$\mathcal{H}_{\mathrm{in}}(\boldsymbol{X}, t) = -\sum_r \theta_0 \frac{3\alpha_r K_r}{\tau_r^K}(\mathrm{tr}\boldsymbol{\varepsilon} - \mathrm{tr}\boldsymbol{\mathcal{E}}_r - 3\alpha_r(\theta - \theta_0)). \tag{3.17}$$

Note that structural thermoviscoelastic heating in the current framework is only governed by volumetric deformations.

3.3.7. Stress and Thermal Stress Tensor

The stresses $(3.5)_2$ are derived from the Helmholtz energy according to equation $(2.48)_2$. They are split into *equilibrium stresses* and (transient) *overstresses* as follows

$$\boldsymbol{\sigma}(\boldsymbol{X}, t) = \rho_0 \frac{\partial \psi}{\partial \boldsymbol{\varepsilon}}(\boldsymbol{\varepsilon}, \theta, \boldsymbol{\mathcal{E}}_1, \dots, \boldsymbol{\mathcal{E}}_m) = \boldsymbol{\sigma}_{\mathrm{eq}}(\boldsymbol{\varepsilon}, \theta) + \boldsymbol{\sigma}_{\mathrm{tr}}(\boldsymbol{\varepsilon}, \theta, \boldsymbol{\mathcal{E}}_1, \dots, \boldsymbol{\mathcal{E}}_m), \quad [\boldsymbol{\sigma}] = \frac{\mathrm{N}}{\mathrm{m}^2}. \tag{3.18}$$

The equilibrium part only depends on the current strain $\boldsymbol{\varepsilon}(\boldsymbol{X}, t)$ and temperature $\theta(\boldsymbol{X}, t)$,

$$\boldsymbol{\sigma}_{\mathrm{eq}}(\boldsymbol{X}, t) = (\psi_1(\mathrm{tr}\boldsymbol{\varepsilon}) + \psi_4(\theta - \theta_0))\boldsymbol{I} + 2\psi_2(\mathrm{dev}\boldsymbol{\varepsilon}), \tag{3.19}$$

while the transient part additionally depends on the set of internal variables $\boldsymbol{\mathcal{E}}_l(\boldsymbol{X},t)$ and should vanish when approaching thermodynamic equilibrium,

$$\boldsymbol{\sigma}_{\mathrm{tr}}(\boldsymbol{X},t)=\sum_r K_r(\mathrm{tr}\boldsymbol{\varepsilon}-\mathrm{tr}\boldsymbol{\mathcal{E}}_r-3\alpha_r(\theta-\theta_0))\boldsymbol{I}+\sum_r 2G_r(\mathrm{dev}\boldsymbol{\varepsilon}-\mathrm{dev}\boldsymbol{\mathcal{E}}_r). \tag{3.20}$$

Finally, we calculate the thermal stresses as the partial derivative of the stress tensor with respect to temperature,

$$\boldsymbol{M}(\boldsymbol{X},t)=\frac{\partial\boldsymbol{\sigma}}{\partial\theta}(\boldsymbol{\varepsilon},\theta,\boldsymbol{\mathcal{E}}_1,\dots,\boldsymbol{\mathcal{E}}_m)=\psi_4\boldsymbol{I}-\sum_r 3\alpha_r K_r\boldsymbol{I},\quad [\boldsymbol{M}]=\frac{\mathrm{N}}{\mathrm{m}^2\,\mathrm{K}}. \tag{3.21}$$

Although equation (3.21) might suggest that the thermal stresses are constant, this is not at all the case. It is implicitly dependent on current time t through the internal variables $\boldsymbol{\mathcal{E}}_l(\boldsymbol{X},t)$. This becomes clear by transforming the stresses (3.18) into a hereditary integral expression (see equation (3.30) for the hydrostatic part) and subsequent differentiation with respect to temperature $\theta(\boldsymbol{X},t)$ [60, p. 91 ff.]. The thermal stresses will enter the balance of energy in later sections.

3.3.8. Specific Entropy and Heat Capacity

The *specific* entropy $(3.5)_3$ follows from the Helmholtz energy through the derivative $(2.48)_2$. The usual split into *equilibrium entropy* and *transient entropy* is given by

$$S(\boldsymbol{X},t)=-\frac{\partial\psi}{\partial\theta}(\boldsymbol{\varepsilon},\theta,\boldsymbol{\mathcal{E}}_1,\dots,\boldsymbol{\mathcal{E}}_m)=S_{\mathrm{eq}}(\boldsymbol{\varepsilon},\theta)+S_{\mathrm{tr}}(\boldsymbol{\varepsilon},\theta,\boldsymbol{\mathcal{E}}_1,\dots,\boldsymbol{\mathcal{E}}_m),\quad [S]=\frac{\mathrm{J}}{\mathrm{kg\,K}}. \tag{3.22}$$

Here, the equilibrium entropy simply reads

$$S_{\mathrm{eq}}(\boldsymbol{X},t)=-\frac{1}{\rho_0}\psi_4(\mathrm{tr}\boldsymbol{\varepsilon})-\frac{1}{\rho_0}\psi_5(\theta-\theta_0), \tag{3.23}$$

while the transient entropy assumes the form

$$S_{\mathrm{tr}}(\boldsymbol{X},t)=\frac{1}{\rho_0}\sum_r 3\alpha_r K_r(\mathrm{tr}\boldsymbol{\varepsilon}-\mathrm{tr}\boldsymbol{\mathcal{E}}_r-3\alpha_r(\theta-\theta_0)). \tag{3.24}$$

Notice the similarity between equation (3.24) and the (hydrostatic) overstresses (3.20). Besides the constant reference density ρ_0, they only differ by the constant factors α_r. However, this huge resemblance of the relaxation mechanisms of stresses and entropy poses a severe restriction on the constitutive model and is, therefore, inadequate to model real amorphous polymers. We complete the set of constitutive equations by specifying the (constant deformation) *specific heat capacity* as

$$c(\boldsymbol{X},t)=-\theta_0\frac{\partial^2\psi}{\partial\theta^2}(\boldsymbol{\varepsilon},\theta,\boldsymbol{\mathcal{E}}_1,\dots,\boldsymbol{\mathcal{E}}_m)=-\frac{1}{\rho_0}\psi_5\theta_0-\frac{1}{\rho_0}\sum_r 9\alpha_r^2K_r\theta_0\geq 0,\quad [c]=\frac{\mathrm{J}}{\mathrm{kg\,K}}. \tag{3.25}$$

The specific heat capacity is a positive scalar quantity which is required for the balance of energy. As with the thermal stresses (3.21), the specific heat is not a constant in this material formulation. It is implicitly dependent on current time t through the internal variables $\boldsymbol{\mathcal{E}}_l(\boldsymbol{X},t)$. This becomes clear by transforming the entropy (3.22) into a hereditary integral expression (see equation (3.31)) and subsequent differentiation with respect to temperature $\theta(\boldsymbol{X},t)$ [60, p. 91 ff.]. In the next section we discuss some general properties of the material model and give a brief comparison to rational thermodynamics.

3.3.9. Some Remarks on the Material Model

As pointed out in Section 3.3.2 the linear coefficients of thermal expansion α_r in the bulk evolution equation $(3.11)_1$ may either be positive or negative. We explain this by the following gedankenexperiment. After an infinitely fast temperature jump $\Delta\theta = \theta - \theta_0$ under constant reference pressure the stresses $\boldsymbol{\sigma}(\boldsymbol{X}, t)$ should vanish irrespective of time t. Thus, from equation (3.18) it follows that

$$\left(K_\infty + \sum_r K_r\right)(\mathrm{tr}\boldsymbol{\varepsilon}) - \left(3\alpha_\infty K_\infty + \sum_r 3\alpha_r K_r(\theta - \theta_0)\right)(\theta - \theta_0) - \sum_r K_r(\mathrm{tr}\boldsymbol{\mathcal{E}}_r) = 0. \quad (3.26)$$

Immediately after the change in temperature the internal variables are still zero, that is $\mathrm{tr}\boldsymbol{\mathcal{E}}_l(\boldsymbol{X}, t = 0^+) = 0$, and the volumetric strain follows from condition (3.26),

$$\mathrm{tr}\boldsymbol{\varepsilon}(\boldsymbol{X}, t = 0^+) = \frac{3\alpha_\infty K_\infty + \sum_r 3\alpha_r K_r}{K_\infty + \sum_r K_r}(\theta - \theta_0). \quad (3.27)$$

On the other hand, when equilibrium is reached the rate of the internal variables vanish, $\dot{\boldsymbol{\mathcal{E}}}_l(\boldsymbol{X}, t = \infty) = 0$. Thus, from the evolution equation $(3.11)_1$ we derive the m equilibrium values $\mathrm{tr}\boldsymbol{\mathcal{E}}_l(\boldsymbol{X}, t = \infty) = \mathrm{tr}\boldsymbol{\varepsilon} - 3\alpha_l(\theta - \theta_0)$. Substituting these expressions into the zero-stress condition (3.26) yields the equilibrium strain

$$\mathrm{tr}\boldsymbol{\varepsilon}(\boldsymbol{X}, t = \infty) = 3\alpha_\infty(\theta - \theta_0). \quad (3.28)$$

To simplify matters, we choose only one relaxation mechanism and set $K_1 = K_\infty$. From experimental observations we know that the sample will creep towards its equilibrium value (3.28) as time passes. This is illustrated in Figure 3.8 together with different choices of material parameter α_1. If we choose $\alpha_1 = 0$, the start value resulting from the temperature jump becomes $\mathrm{tr}\boldsymbol{\varepsilon}(\boldsymbol{X}, t = 0^+) = \frac{3}{2}\alpha_\infty(\theta - \theta_0)$, see equation (3.27). The sign of material parameter α_1 determines whether the new creep curve lies above or below this one. Thus, in contrast to the other Prony parameters, the α_r values are not necessarily positive.

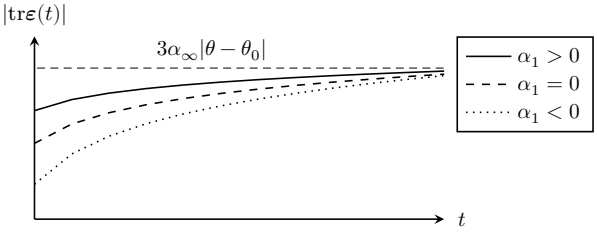

Figure 3.8.: Qualitative creep curves after an infinitely fast temperature jump. Only one relaxation mechanism is active ($m = 1$). Material parameter α_1 in equation $(3.11)_1$ may be either positive or negative. The shape of the creep curve depends on *both* material parameters α_l and K_l.

To finish this section, we briefly compare the material model with corresponding constitutive equations derived from rational thermodynamics [53]. To this end, we solve

evolution equation $(3.11)_1$ with the integrating factor method. This results in an analytical expression for the spherical part of the internal variables,

$$\begin{aligned}\mathrm{tr}\boldsymbol{\mathcal{E}}_l(t) &= \int_0^t \frac{1}{\tau_l} e^{-\frac{t-x}{\tau_l}} \left(\mathrm{tr}\boldsymbol{\varepsilon}(x) - 3\alpha_l(\theta(x)-\theta_0)\right)dx, \\ &= \mathrm{tr}\boldsymbol{\varepsilon}(t) - 3\alpha_r(\theta(t)-\theta_0) - \int_0^t e^{-\frac{t-x}{\tau_l}} \frac{\partial \mathrm{tr}\boldsymbol{\varepsilon}}{\partial x}(x)dx + \int_0^t 3\alpha_l e^{-\frac{t-x}{\tau_l}} \frac{\partial \theta}{\partial x}(x)dx,\end{aligned} \tag{3.29}$$

where the dependence on referential position $\boldsymbol{X}$ has been left out for the sake of readability and where we further assume initial conditions $\mathrm{tr}\boldsymbol{\varepsilon}(\boldsymbol{X}, t=0) = 0$ and $\theta(\boldsymbol{X}, t=0) = \theta_0$. Substitution of (3.29) into the expressions for the stresses (3.18) and the entropy (3.22) leads to

$$\frac{1}{3}\mathrm{tr}\boldsymbol{\sigma}(t) = \psi_1(\mathrm{tr}\boldsymbol{\varepsilon}) + \psi_4(\theta-\theta_0) + \int_0^t \sum_r K_r e^{-\frac{t-x}{\tau_r}} \frac{\partial \mathrm{tr}\boldsymbol{\varepsilon}}{\partial x} dx - \int_0^t \sum_r 3\alpha_r K_r e^{-\frac{t-x}{\tau_r}} \frac{\partial \theta}{\partial x} dx \tag{3.30}$$

for the first invariant of the stresses and, correspondingly, for the entropy

$$\rho_0 S(t) = -\psi_4(\mathrm{tr}\boldsymbol{\varepsilon}) - \psi_5(\theta-\theta_0) + \int_0^t \sum_r 3\alpha_r K_r e^{-\frac{t-x}{\tau_r}} \frac{\partial \mathrm{tr}\boldsymbol{\varepsilon}}{\partial x} dx - \int_0^t \sum_r 9\alpha_r^2 K_r e^{-\frac{t-x}{\tau_r}} \frac{\partial \theta}{\partial x} dx. \tag{3.31}$$

In comparing these equations with corresponding stress and entropy relations found in the theory of rational thermodynamics [53, p. 80] we recognize some similarities if we also assume the isotropic case for the literature expressions (they are given for anisotropy). One major difference is that the literature values do not assume discrete relaxation spectra. However, for practical applications the relaxation functions in the rational thermodynamics setting will usually be approximated by finite Prony series. What is even more restrictive in the last equation derived here is that the relaxation function in the second integral is already fixed by the parameters α_r and K_r, which also appear in the second integral of equation (3.30) representing thermal stress relaxation. This is in sharp contrast with the relaxation function derived from rational thermodynamics, which is independent of the thermal stress relaxation. We conclude that the internal variables approach introduced here is too restrictive and necessitates the use of more than one internal variable to account for differences in the stress and entropy relaxation phenomena. Moreover, the experimental observations discussed in Section 3.1 such as temperature-dependent material parameters and physical aging are equally not reproducible with the constitutive framework introduced above. Hence, a constitutive extension that factors in the various phenomena relating to amorphous polymers becomes necessary.

3.4. Modeling Moderate Strains and Large Temperature Changes

In this section, we continue the constitutive modeling process to describe isotropic thermoviscoelastic material behavior under moderate strains and large temperature changes. More specifically, we assume that the conditions $||\boldsymbol{\varepsilon}|| \leq 15\,\%$ and $|\theta - \theta_0| \leq 75\,°\mathrm{C}$ hold, where $\boldsymbol{\varepsilon}$ are the engineering strains, and restrict ourselves to sufficiently *slow* processes[9].

[9] We cannot give a precise quantification since this requires further experimental testing and validation. The highest engineering strain rate considered during validation was $||\dot{\boldsymbol{\varepsilon}}|| = 0.1\,\mathrm{s}^{-1}$ though.

The following constitutive equations adopt the internal variables approach as outlined in Section 2.4 and are suitable to model amorphous polymers through the glass transition region. In the sequel, material parameters depend on the strains, temperature and internal variables through the relaxation times to incorporate the various phenomena discussed in Section 3.1. We refer to [11] for a detailed compilation of the complex nonlinear behavior of amorphous polymers at small and large strains.

3.4.1. Constitutive Framework

The material model is fully defined in terms of the Helmholtz energy, evolution equations for the internal variables and a material law for the heat flux according to equations (2.48) and (2.49). We establish these below along with derived quantities and discuss the thermodynamic consistency with respect to the Clausius-Planck inequality (2.30). In what follows we assume a homogeneous material described by the set of functions

$$\begin{aligned}
\psi(\boldsymbol{X},t) &= \hat{\psi}(\boldsymbol{H},\theta,\boldsymbol{\mathcal{Z}}_i,\zeta_i,\chi_i),\\
\boldsymbol{\sigma}(\boldsymbol{X},t) &= \hat{\boldsymbol{\sigma}}(\boldsymbol{H},\theta,\boldsymbol{\mathcal{Z}}_i,\zeta_i),\\
S(\boldsymbol{X},t) &= \hat{S}(\boldsymbol{H},\theta,\boldsymbol{\mathcal{Z}}_i,\zeta_i,\chi_i),\\
\boldsymbol{Q}(\boldsymbol{X},t) &= \hat{\boldsymbol{Q}}(\mathrm{Grad}\theta),\\
\dot{\boldsymbol{\mathcal{Z}}}_l(\boldsymbol{X},t) &= \boldsymbol{\mathcal{A}}_l(\boldsymbol{H},\theta,\boldsymbol{\mathcal{Z}}_i,\zeta_i,\chi_i),\\
\dot{\zeta}_l(\boldsymbol{X},t) &= \mathcal{B}_l(\boldsymbol{H},\theta,\boldsymbol{\mathcal{Z}}_i,\zeta_i,\chi_i),\\
\dot{\chi}_l(\boldsymbol{X},t) &= \mathcal{C}_l(\boldsymbol{H},\theta,\boldsymbol{\mathcal{Z}}_i,\zeta_i,\chi_i), \qquad i,l=1,\dots,m,
\end{aligned} \tag{3.32}$$

where we assume m coupled relaxation mechanisms. Here, the internal variables $\boldsymbol{\mathcal{Z}}_l(\boldsymbol{X},t)$ represent symmetric second-order tensors. In contrast, internal variables $\zeta_l(\boldsymbol{X},t)$ and $\chi_l(\boldsymbol{X},t)$ are scalar-valued quantities. The strain tensor is derived from the family of generalized strain tensors (2.9), where we choose $k=0$ for the logarithmic strain

$$\boldsymbol{H}(\boldsymbol{X},t) := \frac{1}{2}\ln(\boldsymbol{C}), \text{ where } \boldsymbol{C}(\boldsymbol{X},t) = \boldsymbol{F}^{\mathrm{T}}(\boldsymbol{X},t)\boldsymbol{F}(\boldsymbol{X},t). \tag{3.33}$$

The choice of the logarithmic or true strain is critical in this material formulation to correctly reproduce volumetric deformations (compare Remark 2 on page 12), since the shift function is sensitive to changes in the dilatation of the polymer. Note that constitutive relations (3.32) meet the objectivity requirements discussed in Section 2.5.5, since scalar-valued internal variables are objective per definition. In the sequel, we will drop the $\hat{(\bullet)}$-signs of the functions to alleviate the notation.

3.4.2. Specification of the Helmholtz Energy

The *specific* Helmholtz energy $(3.32)_1$ is split into an *equilibrium* and a *transient* part as follows

$$\psi(\boldsymbol{X},t) = \psi_{\mathrm{eq}}(\boldsymbol{H},\theta) + \psi_{\mathrm{tr}}(\boldsymbol{H},\theta,\boldsymbol{\mathcal{Z}}_i,\zeta_i,\chi_i), \quad [\psi] = \frac{\mathrm{J}}{\mathrm{kg}}. \tag{3.34}$$

Here, the equilibrium Helmholtz energy only depends on the current strain $\boldsymbol{H}(\boldsymbol{X},t)$ and the temperature $\theta(\boldsymbol{X},t)$, while the transient part additionally depends on the set of

internal variables $\boldsymbol{\mathcal{Z}}_l(\boldsymbol{X},t)$, $\zeta_l(\boldsymbol{X},t)$ and $\chi_l(\boldsymbol{X},t)$ and should vanish when approaching thermodynamic equilibrium. The equilibrium part is defined as

$$\begin{aligned}\psi_{\text{eq}} = \psi_{\text{eq}}^{\text{ref}} - S_{\text{eq}}^{\text{ref}}(\theta-\theta_0) + \frac{1}{2\rho_0}\psi_1(\text{tr}\boldsymbol{H})^2 + \frac{1}{\rho_0}\psi_2(\text{dev}\boldsymbol{H})\cdot(\text{dev}\boldsymbol{H}) + \frac{1}{\rho_0}\boldsymbol{\psi_3}\cdot\boldsymbol{H} \\ + \frac{1}{\rho_0}\psi_4(\text{tr}\boldsymbol{H})(\theta-\theta_0) + \frac{1}{\rho_0}\psi_5\theta_0\left(\theta\ln\left(\frac{\theta}{\theta_0}\right)-(\theta-\theta_0)\right) \\ + \frac{1}{2\rho_0}\psi_6(\text{tr}\boldsymbol{H})^2(\theta-\theta_0) + \frac{1}{2\rho_0}\psi_7(\text{tr}\boldsymbol{H})(\theta-\theta_0)^2 \\ + \frac{1}{\rho_0}\psi_8\theta_0\left(\theta\ln\left(\frac{\theta}{\theta_0}\right)-(\theta-\theta_0)-\frac{1}{2\theta_0}(\theta-\theta_0)^2\right).\end{aligned} \tag{3.35}$$

While some terms are either strain- or temperature-dependent, others are mixed terms containing both influences. In general, pure strain terms relate to equilibrium stresses, while purely temperature-dependent terms determine the equilibrium entropy and specific heat capacity. For the most part, the expression for the equilibrium Helmholtz energy represents a Taylor series expansion with respect to the reference state, containing only terms up to the third order. Only the *calorimetric* part (characterized by material parameters ψ_5 and ψ_8) has been chosen in such a way that it reflects the equilibrium specific heat capacity in accordance with experimental findings. The meanings of the different material parameters required for the equilibrium part $\psi_{\text{eq}}(\boldsymbol{H},t)$ are summarized in Table 3.3. Here, all values refer to the reference temperature θ_0.

Parameter	Unit	Physical meaning
ρ_0	$\frac{\text{kg}}{\text{m}^3}$	Reference density
$\psi_{\text{eq}}^{\text{ref}}$	$\frac{\text{J}}{\text{kg}}$	Reference Helmholtz energy
$S_{\text{eq}}^{\text{ref}}$	$\frac{\text{J}}{\text{kg K}}$	Reference entropy
ψ_1	$\frac{\text{N}}{\text{m}^2}$	Bulk modulus K_∞
ψ_2	$\frac{\text{N}}{\text{m}^2}$	Shear modulus G_∞
$\boldsymbol{\psi_3}$	$\frac{\text{N}}{\text{m}^2}$	Initial stresses $\boldsymbol{\sigma}(\boldsymbol{X},t=0)$
ψ_4	$\frac{\text{N}}{\text{m}^2\,\text{K}}$	Thermal stiffness $-3\alpha_\infty K_\infty$
ψ_5	$\frac{\text{J}}{\text{m}^3\,\text{K}^2}$	Heat capacity $-\frac{c_\infty}{\theta_0}+\frac{1}{\rho_0}\sum_r 9\alpha_r^2 K_r$ ($\boldsymbol{H}=const.$)
ψ_6	$\frac{\text{N}}{\text{m}^2\,\text{K}}$	Change of bulk modulus w.r.t. temperature $\frac{\partial K_\infty}{\partial\theta}$
ψ_7	$\frac{\text{N}}{\text{m}^2\,\text{K}^2}$	Change of the CTE w.r.t. temperature (see Section 3.4.10)
ψ_8	$\frac{\text{J}}{\text{m}^3\,\text{K}^2}$	Change of heat capacity w.r.t. temperature $\frac{\partial c_\infty}{\partial\theta}$

Table 3.3.: Summary of the *rubbery* material parameters for the *equilibrium* Helmholtz energy function (3.35). All values relate to the reference temperature θ_0. Note that the material requires the *constant deformation* heat capacity c_∞ and the equilibrium *linear* coefficient of thermal expansion α_∞ (CTE for short). For a graphical visualization of the various model inputs see Figure 3.11 on page 70.

The transient part, on the other hand, is defined in terms of the bulk and shear Prony parameters K_l, α_l, β_l and G_l, respectively, and four additional non-constant prefactor

functions Ψ_K, Ψ_α, Ψ_β and Ψ_G. It is given by the expression

$$\begin{aligned}\psi_{\text{tr}} = &\frac{1}{2\rho_0}\Psi_K(\theta)\sum_r K_r(\text{tr}\boldsymbol{H} - \text{tr}\boldsymbol{\mathcal{Z}}_r)^2 \\ &- \frac{1}{\rho_0}\Psi_\alpha(\text{tr}\boldsymbol{H},\theta)\sum_r K_r(\text{tr}\boldsymbol{H} - \text{tr}\boldsymbol{\mathcal{Z}}_r)(3\alpha_r(\theta-\theta_0)+\zeta_r) \\ &+ \frac{1}{2\rho_0}\Psi_\beta(\theta)\sum_r K_r(3\beta_r(\theta-\theta_0)+\chi_r)^2 \\ &+ \frac{1}{\rho_0}\Psi_G(\theta)\sum_r G_r\,(\text{dev}\boldsymbol{H} - \text{dev}\boldsymbol{\mathcal{Z}}_r)\cdot(\text{dev}\boldsymbol{H} - \text{dev}\boldsymbol{\mathcal{Z}}_r)\,.\end{aligned} \tag{3.36}$$

The transient Helmholtz energy is governed by four different relaxation mechanisms. The first relates to hydrostatic stress relaxation and is determined by the evolution of internal variables $\text{tr}\boldsymbol{\mathcal{Z}}_l(\boldsymbol{X},t)$. The second additionally depends on the scalar quantities $\zeta_l(\boldsymbol{X},t)$ and characterizes both thermal stress and entropy relaxation. The third mechanism described by internal variables $\chi_l(\boldsymbol{X},t)$ relates to the relaxation of the entropy and the specific heat capacity due to a change in temperature. Finally, the last relaxing term depending on internal variables $\text{dev}\boldsymbol{\mathcal{Z}}_l(\boldsymbol{X},t)$ is attributed to shear stress relaxation. Following relations between glassy (index "g") and equilibrium material parameters hold: $\sum_r K_r = K_\text{g} - K_\infty$, $\sum_r G_r = G_g - G_\infty$, $\sum_r \alpha_r K_r = \alpha_\text{g} K_\text{g} - \alpha_\infty K_\infty$ and $\alpha_r \leq 0, \beta_r \leq 0$. Thus, the Prony parameters define the transition from glassy to equilibrium consistency. While the stiffness parameters K_l and G_l usually assume positive values, the other coefficients pertaining to thermal stress and entropy relaxation, α_l and β_l, are negative. This is a direct consequence of experimental observations on amorphous polymers and becomes more clear in Section 6.1 of the modeling and simulation Part III. Another explanation is given in terms of the dissipation inequality, see Remark 15 on page 58. Next, we specify the prefactor functions,

$$\begin{aligned}\Psi_K(\theta) &= 1 + \tilde{C}_1(\theta-\theta_0) \geq 0, \\ \Psi_\alpha(\text{tr}\boldsymbol{H},\theta) &= 1 + \tilde{C}_2(\theta-\theta_0) + \tilde{C}_3(\text{tr}\boldsymbol{H}) \geq 0, \\ \Psi_\beta(\theta) &= 1 + \tilde{C}_4(\theta-\theta_0) + \frac{1}{2}\tilde{C}_5(\theta-\theta_0)^2 \geq 0, \\ \Psi_G(\theta) &= 1 + \tilde{C}_6(\theta-\theta_0) \geq 0.\end{aligned} \tag{3.37}$$

They depend on the glassy material parameters $\tilde{C}_i$, $i = 1,\dots,6$. The interpretation of these parameters is summarized in Table 3.4 and illustrated in Figure 3.11 on page 70. The positivity requirement of the functions is necessary to guaranty thermodynamic consistency (see Section 3.4.4). Notice that the Helmholtz energy is fully defined in terms of equilibrium (rubbery) and transient (glassy) material parameters. All of the required material data can be extracted from independent experiments on the same polymer. On the thermal side these are dilatometric and calorimetric experiments. The Prony parameters G_l, on the other hand, correspond exclusively to the theory of linear viscoelasticity and are generally determined by Dynamic Mechanical Thermal Analyses (DMTA) in the small strain regime. This is a particularly attractive feature of the nonlinear thermoviscoelastic material formulation for thermorheologically simple materials in terms of the internal variables approach. Note that the introduction of internal variables $\boldsymbol{\mathcal{Z}}_l(\boldsymbol{X},t)$, $\zeta_l(\boldsymbol{X},t)$ and $\chi_l(\boldsymbol{X},t)$ in the transient part of the Helmholtz energy necessitates the specification of additional evolution equations.

Parameter	Unit	Physical meaning
K_l	$\frac{\mathrm{N}}{\mathrm{m}^2}$	Prony parameters for hydrostatic stress relaxation
α_l	$\frac{1}{\mathrm{K}}$	Prony parameters for thermal stress relaxation
β_l	$\frac{1}{\mathrm{K}}$	Prony parameters for entropy relaxation
G_l	$\frac{\mathrm{N}}{\mathrm{m}^2}$	Prony parameters for shear stress relaxation
$\tilde{C}_1$	$\frac{1}{\mathrm{K}}$	Related to the temperature variation of K_g
$\tilde{C}_2$	$\frac{1}{\mathrm{K}}$	Related to the temperature variation of α_g
$\tilde{C}_3$	1	Related to the strain variation of K_g
$\tilde{C}_4$	$\frac{1}{\mathrm{K}}$	Related to the temperature variation of c_g
$\tilde{C}_5$	$\frac{1}{\mathrm{K}^2}$	Related to the temperature variation of c_g
$\tilde{C}_6$	$\frac{1}{\mathrm{K}}$	Related to the temperature variation of G_g
C_1	1	First WLF constant, see Section 3.4.9

Table 3.4.: Summary of the *glassy* material parameters required for the *transient* Helmholtz energy function (3.36). For analytical expressions of the various parameters and a graphical representation we refer to Section 3.4.10.

3.4.3. Evolution Equations of the Internal Variables

As outlined in Section 3.3.9 we have to extend the set of internal variables to allow for different stress and entropy relaxation mechanisms. To this end, we define the following set of evolution equations,

$$\begin{aligned}
\dot{\boldsymbol{\mathcal{Z}}}_l(\boldsymbol{X},t) &= \boldsymbol{\mathcal{A}}_l(\boldsymbol{H},\theta,\boldsymbol{\mathcal{Z}}_i,\zeta_i,\chi_i), \qquad [\boldsymbol{\mathcal{Z}}_l] = \frac{\mathrm{m}}{\mathrm{m}},\\
\dot{\zeta}_l(\boldsymbol{X},t) &= \mathcal{B}_l(\boldsymbol{H},\theta,\boldsymbol{\mathcal{Z}}_i,\zeta_i,\chi_i), \qquad [\zeta_l] = \frac{\mathrm{m}}{\mathrm{m}},\\
\dot{\chi}_l(\boldsymbol{X},t) &= \mathcal{C}_l(\boldsymbol{H},\theta,\boldsymbol{\mathcal{Z}}_i,\zeta_i,\chi_i), \qquad [\chi_l] = \frac{\mathrm{m}}{\mathrm{m}},
\end{aligned} \tag{3.38}$$

where $i,l = 1,\dots,m$. Here, internal variables $\boldsymbol{\mathcal{Z}}_l(\boldsymbol{X},t)$ represent second-order strain-valued tensors which account for (mechanical) *hydrostatic* and *shear stress relaxation*, respectively. They are conveniently split into their volumetric and deviatoric parts in the same way as the strain tensor (2.12) as

$$\boldsymbol{\mathcal{Z}}_l(\boldsymbol{X},t) = \frac{1}{3}(\mathrm{tr}\boldsymbol{\mathcal{Z}}_l)\boldsymbol{I} + \mathrm{dev}\boldsymbol{\mathcal{Z}}_l \quad \Rightarrow \quad \dot{\boldsymbol{\mathcal{Z}}}_l(\boldsymbol{X},t) = \frac{1}{3}(\mathrm{tr}\dot{\boldsymbol{\mathcal{Z}}}_l)\boldsymbol{I} + \mathrm{dev}\dot{\boldsymbol{\mathcal{Z}}}_l, \quad l = 1,\dots,m. \tag{3.39}$$

Now, the evolution of the volumetric and deviatoric internal variables are governed by the following nonlinear rate equations

$$\begin{aligned}
\mathrm{tr}\dot{\boldsymbol{\mathcal{Z}}}_l(\boldsymbol{X},t) &= \frac{1}{a(\boldsymbol{H},\theta,\boldsymbol{\mathcal{Z}}_i,\zeta_i,\chi_i)\tau_l^K}(\mathrm{tr}\boldsymbol{H} - \mathrm{tr}\boldsymbol{\mathcal{Z}}_l), \qquad \tau_l^K = \frac{\eta_l^K}{K_l},\\
\mathrm{dev}\dot{\boldsymbol{\mathcal{Z}}}_l(\boldsymbol{X},t) &= \frac{1}{a(\boldsymbol{H},\theta,\boldsymbol{\mathcal{Z}}_i,\zeta_i,\chi_i)\tau_l^G}\left(\mathrm{dev}\boldsymbol{H} - \mathrm{dev}\boldsymbol{\mathcal{Z}}_l\right), \qquad \tau_l^G = \frac{\eta_l^G}{G_l}.
\end{aligned} \tag{3.40}$$

The constant material parameters τ_l^K, η_l^K and τ_l^G, η_l^G correspond to reference temperature θ_0. Both equations show some similarities with their linear counterparts (3.11).

However, besides the purely mechanical association their evolution is governed by a shift factor $a(\boldsymbol{H}, \theta, \boldsymbol{\mathcal{Z}}_i, \zeta_i, \chi_i)$ which depends not only on the current strain and temperature, but also on the internal variables. The same applies to the bulk and shear viscosities. They are related through the equations

$$\begin{aligned} \hat{\tau}_l^K(\boldsymbol{H}, \theta, \boldsymbol{\mathcal{Z}}_i, \zeta_i, \chi_i) &= a(\boldsymbol{H}, \theta, \boldsymbol{\mathcal{Z}}_i, \zeta_i, \chi_i)\tau_l^K = \frac{\hat{\eta}_l^K(\boldsymbol{H}, \theta, \boldsymbol{\mathcal{Z}}_i, \zeta_i, \chi_i)}{\Psi_K(\theta)K_l}, \\ \hat{\tau}_l^G(\boldsymbol{H}, \theta, \boldsymbol{\mathcal{Z}}_i, \zeta_i, \chi_i) &= a(\boldsymbol{H}, \theta, \boldsymbol{\mathcal{Z}}_i, \zeta_i, \chi_i)\tau_l^G = \frac{\hat{\eta}_l^G(\boldsymbol{H}, \theta, \boldsymbol{\mathcal{Z}}_i, \zeta_i, \chi_i)}{\Psi_G(\theta)G_l}. \end{aligned} \tag{3.41}$$

This is necessary to integrate the various material characteristics of amorphous polymers described in Section 3.1 into the constitutive model. The second type of internal variables $(3.38)_2$ are scalar-valued quantities associated with *thermal stress relaxation*. Their evolution is governed by the nonlinear equation

$$\dot{\zeta}_l(\boldsymbol{X}, t) = -\frac{1}{a(\boldsymbol{H}, \theta, \boldsymbol{\mathcal{Z}}_i, \zeta_i, \chi_i)\tau_l^K}(3\alpha_l(\theta - \theta_0) + \zeta_l). \tag{3.42}$$

The third evolution equation for the internal variables $(3.38)_3$ differs only in the material parameters β_l from the preceding one. It relates to *entropy relaxation* and is defined by the nonlinear equation

$$\dot{\chi}_l(\boldsymbol{X}, t) = -\frac{1}{a(\boldsymbol{H}, \theta, \boldsymbol{\mathcal{Z}}_i, \zeta_i, \chi_i)\tau_l^K}(3\beta_l(\theta - \theta_0) + \chi_l). \tag{3.43}$$

The different relaxation mechanisms described by the four evolution equations are illustrated in Figure 3.9 in terms of four *coupled* Maxwell models.

Remark 11. *To get a better understanding of the evolution equations and the physical motivation, let us take a closer look at the shear related viscous flow described by evolution equation* $(3.40)_2$ *and recast it into the following set of equations,*

$$\hat{\eta}_l^G(\theta)\left(\mathrm{dev}\dot{\boldsymbol{\mathcal{Z}}}_l\right) = \hat{G}_l(\theta)(\mathrm{dev}\boldsymbol{H} - \mathrm{dev}\boldsymbol{\mathcal{Z}}_l), \tag{3.44}$$

$$a(\theta) = \frac{\hat{\tau}_l^G(\theta)}{\tau_l^G} = \frac{\hat{\eta}_l^G(\theta)}{\eta_l^G}\frac{G_l}{\hat{G}_l(\theta)}, \tag{3.45}$$

$$\hat{G}_l(\theta) = \Psi_G(\theta)G_l, \tag{3.46}$$

where we have considerably simplified the model by considering only temperature dependence. Now, for the special choice $\tilde{C}_6 = \frac{1}{\theta_0}$ *of the shear related material parameter the prefactor function* $(3.37)_4$ *is equal to* $\Psi_G(\theta) = \frac{\theta}{\theta_0}$ *If we substitute this expression into equation* (3.46) *and combine it with the shift factor* (3.45) *we get*

$$a(\theta) = \frac{\hat{\eta}_l^G(\theta)}{\eta_l^G}\frac{\theta_0}{\theta}. \tag{3.47}$$

A similar expression for the shift factor is found in [89, p. 184] in terms of the time-temperature-superposition principle (we have neglected the change in density). Thus, the prefactor function $\Psi_G(\theta)$ *is associated with the so-called vertical shift [67, p. 241] (the same applies to all other prefactor functions* (3.37)*).*

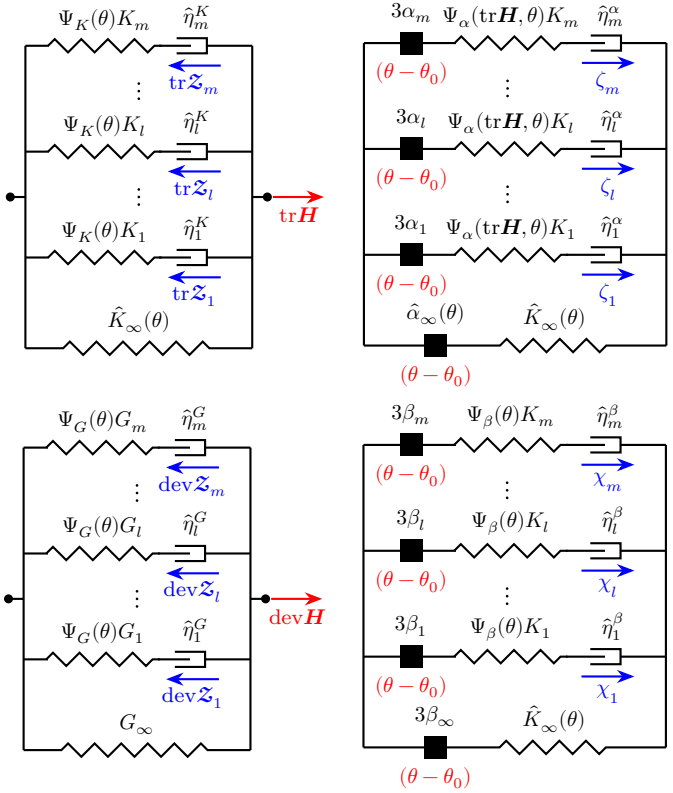

Figure 3.9.: Maxwell model representation of four *coupled* relaxation mechanisms corresponding to evolution equations (3.40), (3.42) and (3.43). Above: hydrostatic stress and thermal stress relaxation, below: shear stress and entropy relaxation. Each type consists of m different relaxation mechanisms. Individual bulk and shear viscosities are functions of current strain, temperature and internal variables, resulting in the coupling of all four models.

Remark 12. *From the special case $\alpha_l = \beta_l$ for all $l = 1, \dots, m$ we infer from evolution equations (3.42) and (3.43) that $\zeta_l(\boldsymbol{X}, t) = \chi_l(\boldsymbol{X}, t)$, assuming identical initial conditions. Furthermore, we set $\tilde{C}_i = 0$ for all $i = 1, \dots, 6$ and define $\mathrm{tr}\boldsymbol{\mathcal{E}}_l := \mathrm{tr}\boldsymbol{\mathcal{Z}}_l + \zeta_l$ as well as $\mathrm{dev}\boldsymbol{\mathcal{E}}_l := \mathrm{dev}\boldsymbol{\mathcal{Z}}_l$ and use a shift factor $a(\theta)$ which only depends on the current temperature $\theta(t)$. If, in addition, we develop the equilibrium Helmholtz energy (3.35) into a Taylor series expansion which contains only terms up to the second order and use the linearized strain tensor $\boldsymbol{\varepsilon}(\boldsymbol{X}, t)$ instead of its logarithmic counterpart, then we obtain the material model described in [60, Section 7]. Finally, we linearize the evolution equations (3.40), (3.42) and (3.43), implying $a \equiv 1$, and we eventually arrive at the material model described in Section 3.3 for the case of small strains and small*

temperature changes.

Remark 13. *It is possible to modify the last two evolution equations in order to simplify the parameter identification process. We demonstrate this by the example of equation (3.43). To this end, we substitute $\chi_l(\boldsymbol{X},t)$ with $3\beta_l\chi_l(\boldsymbol{X},t)$ and obtain the new evolution equation*

$$\dot{\chi}_l(\boldsymbol{X},t) = \frac{1}{a(\boldsymbol{H},\theta,\boldsymbol{\mathcal{Z}}_i,\zeta_i,\chi_i)\tau_l^K}(\theta-\theta_0-\chi_l), \tag{3.48}$$

instead of equation (3.43). Notice that the character of internal variables $\chi_l(\boldsymbol{X},t)$ now corresponds to a temperature. Next, we include the change in the transient Helmholtz energy (3.36),

$$\begin{aligned}\psi_{\mathrm{tr}} = &\frac{1}{2\rho_0}\Psi_K(\theta)\sum_r K_r(\mathrm{tr}\boldsymbol{H}-\mathrm{tr}\boldsymbol{\mathcal{Z}}_r)^2\\ &-\frac{1}{\rho_0}\Psi_\alpha(\mathrm{tr}\boldsymbol{H},\theta)\sum_r K_r(\mathrm{tr}\boldsymbol{H}-\mathrm{tr}\boldsymbol{\mathcal{Z}}_r)(3\alpha_r(\theta-\theta_0)+\zeta_r)\\ &+\frac{1}{2\rho_0}\Psi_\beta(\theta)\sum_r B_r(\theta-\theta_0-\chi_r)^2\\ &+\frac{1}{\rho_0}\Psi_G(\theta)\sum_r G_r\left(\mathrm{dev}\boldsymbol{H}-\mathrm{dev}\boldsymbol{\mathcal{Z}}_r\right)\cdot\left(\mathrm{dev}\boldsymbol{H}-\mathrm{dev}\boldsymbol{\mathcal{Z}}_r\right),\end{aligned} \tag{3.49}$$

where $B_r := 9K_r\beta_r^2$. Here, the choice of Prony parameters B_r in the third sum is more straightforward than that of the β_r's in equation (3.36), which have to be adjusted to the bulk parameters K_r. As a consequence, the identification of parameters during validation becomes much more convenient.

Remark 14. *The evolution equations introduced above use Prony parameters to model the different mechanical and thermal relaxation phenomena observed in amorphous polymers. In contrast, some authors prefer hyperbolic functions to model the glass transition [15]. However, such models are generally applied to pure shear deformation and do not take account of the various effects of physical aging.*

Since the material is affected by internal dissipation, we have to check for thermomechanical consistency.

3.4.4. Dissipation Inequality — Thermomechanical Consistency

The constitutive framework is thermodynamically consistent when the internal dissipation $(2.47)_2$ is non-negative,

$$\mathcal{D}_{\mathrm{int}}(\boldsymbol{X},t) = -\rho_0\sum_r\left[\frac{\partial\psi}{\partial\boldsymbol{\mathcal{Z}}_r}\cdot\dot{\boldsymbol{\mathcal{Z}}}_r+\frac{\partial\psi}{\partial\zeta_r}\dot{\zeta}_r+\frac{\partial\psi}{\partial\chi_r}\dot{\chi}_r\right]\geq 0,\quad [\mathcal{D}_{\mathrm{int}}]=\frac{\mathrm{W}}{\mathrm{m}^3}. \tag{3.50}$$

Invoking the chain rule in calculating the partial derivatives of the transient Helmholtz energy (3.36) and taking advantage of the volumetric-deviatoric split (3.39) yields

$$\begin{aligned}\mathcal{D}_{\text{int}}(\boldsymbol{X},t) = &\sum_r \underbrace{\frac{\Psi_K(\theta)K_r}{a(\boldsymbol{H},\theta,\boldsymbol{\mathcal{Z}}_i,\zeta_i,\chi_i)\tau_r^K}}_{\geq 0} \underbrace{\left(\text{tr}\boldsymbol{H}-\text{tr}\boldsymbol{\mathcal{Z}}_r\right)^2}_{\geq 0} \\ &+\sum_r \underbrace{\frac{\Psi_G(\theta)2G_r}{a(\boldsymbol{H},\theta,\boldsymbol{\mathcal{Z}}_i,\zeta_i,\chi_i)\tau_r^G}}_{\geq 0} \underbrace{\left(\text{dev}\boldsymbol{H}-\text{dev}\boldsymbol{\mathcal{Z}}_r\right)\cdot\left(\text{dev}\boldsymbol{H}-\text{dev}\boldsymbol{\mathcal{Z}}_r\right)}_{\geq 0} \\ &-\sum_r \underbrace{\frac{2\Psi_\alpha(\text{tr}\boldsymbol{H},\theta)K_r}{a(\boldsymbol{H},\theta,\boldsymbol{\mathcal{Z}}_i,\zeta_i,\chi_i)\tau_r^K}}_{\geq 0} \left(\text{tr}\boldsymbol{H}-\text{tr}\boldsymbol{\mathcal{Z}}_r\right)\left(3\alpha_r(\theta-\theta_0)+\zeta_r\right) \\ &+\sum_r \underbrace{\frac{\Psi_\beta(\theta)K_r}{a(\boldsymbol{H},\theta,\boldsymbol{\mathcal{Z}}_i,\zeta_i,\chi_i)\tau_r^K}}_{\geq 0} \underbrace{\left(3\beta_r(\theta-\theta_0)+\chi_r\right)^2}_{\geq 0},\end{aligned} \tag{3.51}$$

where we have used the positivity conditions of the prefactor functions (3.37). Now, inequality (3.50) has to hold for every thermodynamic process at every instant of time t in order that the constitutive model is in accordance with the second law of thermodynamics (again we assume positive entropy production by heat conduction). We see from the dissipation function (3.51) that only the mixed terms may cause problems. However, during extensive validation of the material model on four polymeric systems as described in Part III we did not encounter a single case where the dissipation inequality was violated, though our simulations encompassed a wide range of temperature intervals and moderate strain levels. We are therefore confident that the set of constitutive equations produce physically meaningful results when modeling amorphous polymers through the glass transition region. Note, however, that we have assumed positive entropy production in terms of heat conduction by using a simple constitutive law for the heat flux (see the following section).

Remark 15. *A physical motivation to choose negative linear coefficients of thermal expansion α_l stems from the form of the dissipation function and the following thought experiment: immediately after an infinitely fast temperature jump $\Delta\theta = \theta - \theta_0 > 0$ all internal variables are still zero. The temperature jump is accompanied by an instantaneous elastic dilatation. Thus, immediately after the positive change in temperature the volumetric strains are positive,* $\text{tr}\boldsymbol{H} > 0$. *Therefore, in order that the third sum in the dissipation (3.51) be positive the coefficients of thermal expansion α_l need necessarily be negative. Analogous reasoning applies to an infinitely fast quench $\Delta\theta = \theta - \theta_0 < 0$.*

3.4.5. Specification of the Heat Flux

We assume that Duhamel's law of heat conduction (2.49) with constant conductivity $\lambda > 0$ under thermal isotropy holds,

$$\boldsymbol{q}(\boldsymbol{X},t) = -\lambda\text{grad}\theta(\boldsymbol{X},t) \quad \Leftrightarrow \quad \boldsymbol{Q}(\boldsymbol{X},t) = -(\det\boldsymbol{F})\lambda\boldsymbol{C}^{-1}\text{Grad}\theta(\boldsymbol{X},t). \tag{3.52}$$

This classic assumption is quite often found in the literature and is known as *Fourier's law of heat conduction* [49, p. 269]. Note that the condition

$$-\frac{1}{\theta(\boldsymbol{X},t)}\left(\text{Grad}\theta(\boldsymbol{X},t)\right)\cdot\boldsymbol{Q}(\boldsymbol{X},t) \geq 0 \tag{3.53}$$

from the remainder inequality $(2.47)_1$ holds trivially in case of (3.52). This is necessary when we want to show thermomechanical consistency by positive dissipation $\mathcal{D}_{\text{int}} \geq 0$. Further note that the assumption of a constant thermal conductivity is only of limited validity. Measurements on amorphous polymers [90] clearly indicate a temperature dependence of the thermal conductivity, sometimes characterized by a peak within the glass transition region.

3.4.6. Structural Thermoviscoelastic Heating

In anticipation of the balance of energy in upcoming sections we need to introduce a further quantity called *structural thermoviscoelastic heating* $\mathcal{H}_{\text{in}}(\boldsymbol{X}, t)$. It is defined in terms of the partial derivative of the Helmholtz energy $(3.32)_1$ with respect to temperature and the internal variables as

$$\mathcal{H}_{\text{in}}(\boldsymbol{X}, t) = -\rho_0 \theta \sum_r \left[\frac{\partial^2 \psi}{\partial \boldsymbol{\mathcal{Z}}_r \partial \theta} \cdot \dot{\boldsymbol{\mathcal{Z}}}_r + \frac{\partial^2 \psi}{\partial \zeta_r \partial \theta} \dot{\zeta}_r + \frac{\partial^2 \psi}{\partial \chi_r \partial \theta} \dot{\chi}_r \right], \quad [\mathcal{H}_{\text{in}}] = \frac{\text{W}}{\text{m}^3}. \tag{3.54}$$

Analogously to the internal dissipation we apply the chain rule in calculating the partial derivatives of the transient Helmholtz energy (3.36) and make use of the volumetric-deviatoric split (3.39). This leads to

$$\begin{aligned}
\mathcal{H}_{\text{in}} = & \sum_r \frac{\theta}{a(\boldsymbol{H}, \theta, \boldsymbol{\mathcal{Z}}_i, \zeta_i, \chi_i) \tau_r^K} \frac{\partial \Psi_K(\theta)}{\partial \theta} K_r (\text{tr}\boldsymbol{H} - \text{tr}\boldsymbol{\mathcal{Z}}_r)^2 \\
& - \sum_r \frac{2\theta}{a(\boldsymbol{H}, \theta, \boldsymbol{\mathcal{Z}}_i, \zeta_i, \chi_i) \tau_r^K} \frac{\partial \Psi_\alpha(\text{tr}\boldsymbol{H}, \theta)}{\partial \theta} K_r (3\alpha_r(\theta - \theta_0) + \zeta_r)(\text{tr}\boldsymbol{H} - \text{tr}\boldsymbol{\mathcal{Z}}_r) \\
& - \sum_r \frac{\theta \Psi_\alpha(\text{tr}\boldsymbol{H}, \theta)}{a(\boldsymbol{H}, \theta, \boldsymbol{\mathcal{Z}}_i, \zeta_i, \chi_i) \tau_r^K} 3\alpha_r K_r (\text{tr}\boldsymbol{H} - \text{tr}\boldsymbol{\mathcal{Z}}_r) \\
& + \sum_r \frac{\theta}{a(\boldsymbol{H}, \theta, \boldsymbol{\mathcal{Z}}_i, \zeta_i, \chi_i) \tau_r^K} \frac{\partial \Psi_\beta(\theta)}{\partial \theta} K_r (3\beta_r(\theta - \theta_0) + \chi_r)^2 \\
& + \sum_r \frac{\theta \Psi_\beta(\theta)}{a(\boldsymbol{H}, \theta, \boldsymbol{\mathcal{Z}}_i, \zeta_i, \chi_i) \tau_r^K} 3\beta_r K_r (3\beta_r(\theta - \theta_0) + \chi_r) \\
& + \sum_r \frac{\theta}{a(\boldsymbol{H}, \theta, \boldsymbol{\mathcal{Z}}_i, \zeta_i, \chi_i) \tau_r^G} \frac{\partial \Psi_G(\theta)}{\partial \theta} 2G_r (\text{dev}\boldsymbol{H} - \text{dev}\boldsymbol{\mathcal{Z}}_r) \cdot (\text{dev}\boldsymbol{H} - \text{dev}\boldsymbol{\mathcal{Z}}_r).
\end{aligned} \tag{3.55}$$

Note that structural thermoviscoelastic heating in the current framework is governed by both volumetric and shear deformation.

3.4.7. Stress and Thermal Stress Tensor

The stresses $(3.32)_2$ are derived from the Helmholtz energy according to equation $(2.48)_2$ and form the thermodynamic conjugate to the Hencky strain (3.33). They are split into *equilibrium stresses* and (transient) *overstresses* as follows

$$\boldsymbol{\sigma}(\boldsymbol{X}, t) = \rho_0 \frac{\partial \psi}{\partial \boldsymbol{H}}(\boldsymbol{H}, \theta, \boldsymbol{\mathcal{Z}}_i, \zeta_i) = \boldsymbol{\sigma}_{\text{eq}}(\boldsymbol{H}, \theta) + \boldsymbol{\sigma}_{\text{tr}}(\boldsymbol{H}, \theta, \boldsymbol{\mathcal{Z}}_i, \zeta_i), \quad [\boldsymbol{\sigma}] = \frac{\text{N}}{\text{m}^2}. \tag{3.56}$$

The equilibrium part only depends on the current strain $\boldsymbol{H}(\boldsymbol{X},t)$ and the temperature $\theta(\boldsymbol{X},t)$,

$$\boldsymbol{\sigma}_{\mathrm{eq}} = \boldsymbol{\psi_3} + \left(\psi_1(\mathrm{tr}\boldsymbol{H}) + \psi_4(\theta-\theta_0) + \psi_6(\mathrm{tr}\boldsymbol{H})(\theta-\theta_0) + \frac{1}{2}\psi_7(\theta-\theta_0)^2\right)\boldsymbol{I} + 2\psi_2(\mathrm{dev}\boldsymbol{H}), \quad (3.57)$$

while the transient part additionally depends on the set of internal variables $\boldsymbol{\mathcal{Z}}_l(\boldsymbol{X},t)$ and $\zeta_l(\boldsymbol{X},t)$ and should vanish when approaching thermodynamic equilibrium,

$$\begin{aligned}\boldsymbol{\sigma}_{\mathrm{tr}} = \sum_r \Bigg[&\Psi_K(\theta) K_r(\mathrm{tr}\boldsymbol{H} - \mathrm{tr}\boldsymbol{\mathcal{Z}}_r) - \frac{\partial \Psi_\alpha(\mathrm{tr}\boldsymbol{H},\theta)}{\partial \mathrm{tr}\boldsymbol{H}} K_r(\mathrm{tr}\boldsymbol{H} - \mathrm{tr}\boldsymbol{\mathcal{Z}}_r)(3\alpha_r(\theta-\theta_0) + \zeta_r) \\ &- \Psi_\alpha(\mathrm{tr}\boldsymbol{H},\theta) K_r(3\alpha_r(\theta-\theta_0) + \zeta_r)\Bigg]\boldsymbol{I} + \sum_r \Psi_G(\theta) 2G_r\left(\mathrm{dev}\boldsymbol{H} - \mathrm{dev}\boldsymbol{\mathcal{Z}}_r\right).\end{aligned} \quad (3.58)$$

Finally, we calculate the thermal stresses as the partial derivative of the stress tensor with respect to temperature. The thermal stresses are likewise split into *equilibrium* and *thermal overstresses*,

$$\boldsymbol{M}(\boldsymbol{X},t) = \frac{\partial \boldsymbol{\sigma}}{\partial \theta}(\boldsymbol{H},\theta,\boldsymbol{\mathcal{Z}}_i,\zeta_i) = \boldsymbol{M}_{\mathrm{eq}}(\boldsymbol{H},\theta) + \boldsymbol{M}_{\mathrm{tr}}(\boldsymbol{H},\theta,\boldsymbol{\mathcal{Z}}_i,\zeta_i), \quad [\boldsymbol{M}] = \frac{\mathrm{N}}{\mathrm{m}^2\,\mathrm{K}}. \quad (3.59)$$

The equilibrium part reads

$$\boldsymbol{M}_{\mathrm{eq}} = (\psi_4 + \psi_6(\mathrm{tr}\boldsymbol{H}) + \psi_7(\theta-\theta_0))\boldsymbol{I}. \quad (3.60)$$

The transient thermal stresses take on the form

$$\begin{aligned}\boldsymbol{M}_{\mathrm{tr}} = \sum_r \Bigg[&\frac{\partial \Psi_K(\theta)}{\partial \theta} K_r(\mathrm{tr}\boldsymbol{H} - \mathrm{tr}\boldsymbol{\mathcal{Z}}_r) - \frac{\partial \Psi_\alpha(\mathrm{tr}\boldsymbol{H},\theta)}{\partial \mathrm{tr}\boldsymbol{H}} 3\alpha_r K_r(\mathrm{tr}\boldsymbol{H} - \mathrm{tr}\boldsymbol{\mathcal{Z}}_r) \\ &- 3\alpha_r K_r \Psi_\alpha(\mathrm{tr}\boldsymbol{H},\theta) - \frac{\partial \Psi_\alpha(\mathrm{tr}\boldsymbol{H},\theta)}{\partial \theta} K_r(3\alpha_r(\theta-\theta_0) + \zeta_r)\Bigg]\boldsymbol{I} \\ &+ \frac{\partial \Psi_G(\theta)}{\partial \theta} \sum_r 2G_r\left(\mathrm{dev}\boldsymbol{H} - \mathrm{dev}\boldsymbol{\mathcal{Z}}_r\right).\end{aligned} \quad (3.61)$$

The thermal stresses will enter the balance of energy in later sections.

3.4.8. Specific Entropy and Heat Capacity

The *specific* entropy $(3.32)_3$ follows from the Helmholtz energy through the derivative $(2.48)_3$ on page 29. The usual split into *equilibrium entropy* and *transient entropy* is given by

$$S(\boldsymbol{X},t) = -\frac{\partial \psi}{\partial \theta}(\boldsymbol{H},\theta,\boldsymbol{\mathcal{Z}}_i,\zeta_i,\chi_i) = S_{\mathrm{eq}}(\boldsymbol{H},\theta) + S_{\mathrm{tr}}(\boldsymbol{H},\theta,\boldsymbol{\mathcal{Z}}_i,\zeta_i,\chi_i), \quad [S] = \frac{\mathrm{J}}{\mathrm{kg}\,\mathrm{K}}. \quad (3.62)$$

Here, the equilibrium entropy simply reads

$$\begin{aligned}S_{\mathrm{eq}} = S_{\mathrm{eq}}^{\mathrm{ref}} &- \frac{1}{\rho_0}\psi_4(\mathrm{tr}\boldsymbol{H}) - \frac{1}{\rho_0}\psi_5\theta_0 \ln\left(\frac{\theta}{\theta_0}\right) - \frac{1}{2\rho_0}\psi_6(\mathrm{tr}\boldsymbol{H})^2 \\ &- \frac{1}{\rho_0}\psi_7(\mathrm{tr}\boldsymbol{H})(\theta-\theta_0) - \frac{1}{\rho_0}\psi_8\left(\theta_0 \ln\left(\frac{\theta}{\theta_0}\right) - (\theta-\theta_0)\right),\end{aligned} \quad (3.63)$$

while the transient entropy assumes the more complicated form

$$\begin{aligned} S_{\mathrm{tr}} = \frac{1}{\rho_0}\sum_r \Big[& 3\alpha_r K_r \Psi_\alpha(\mathrm{tr}\boldsymbol{H},\theta)(\mathrm{tr}\boldsymbol{H} - \mathrm{tr}\boldsymbol{\mathcal{Z}}_r) - 3\beta_r K_r \Psi_\beta(\theta)(3\beta_r(\theta-\theta_0)+\chi_r) \\ & + \frac{\partial \Psi_\alpha(\mathrm{tr}\boldsymbol{H},\theta)}{\partial\theta} K_r(\mathrm{tr}\boldsymbol{H} - \mathrm{tr}\boldsymbol{\mathcal{Z}}_r)(3\alpha_r(\theta-\theta_0)+\zeta_r) \\ & - \frac{1}{2}\frac{\partial \Psi_\beta(\theta)}{\partial\theta} K_r(3\beta_r(\theta-\theta_0)+\chi_r)^2 - \frac{1}{2}\frac{\partial \Psi_K(\theta)}{\partial\theta} K_r(\mathrm{tr}\boldsymbol{H} - \mathrm{tr}\boldsymbol{\mathcal{Z}}_r)^2 \\ & - \frac{\partial \Psi_G(\theta)}{\partial\theta} G_r\,(\mathrm{dev}\boldsymbol{H} - \mathrm{dev}\boldsymbol{\mathcal{Z}}_r)\cdot(\mathrm{dev}\boldsymbol{H} - \mathrm{dev}\boldsymbol{\mathcal{Z}}_r)\Big]. \end{aligned} \tag{3.64}$$

Notice the difference between equation (3.64) and the overstresses (3.58), which is in sharp contrast to the material model described in Section 3.3. This results from the second term in the above equation, since the overstresses do not depend on internal variables $\chi_l(\boldsymbol{X},t)$, allowing for different stress and entropy relaxations. We complete the set of constitutive equations by specifying the (constant deformation) *specific heat capacity* as

$$c(\boldsymbol{X},t) = -\theta\frac{\partial^2\psi}{\partial\theta^2}(\boldsymbol{H},\theta,\boldsymbol{\mathcal{Z}}_i,\chi_i) = c_{\mathrm{eq}}(\boldsymbol{H},\theta) + c_{\mathrm{tr}}(\boldsymbol{H},\theta,\boldsymbol{\mathcal{Z}}_i,\chi_i) \geq 0, \quad [c] = \frac{\mathrm{J}}{\mathrm{kg\,K}}. \tag{3.65}$$

The equilibrium specific heat depends on the current strain and temperature values according to

$$c_{\mathrm{eq}} = -\frac{1}{\rho_0}\psi_5\theta_0 - \frac{1}{\rho_0}\psi_7(\mathrm{tr}\boldsymbol{H})\theta + \frac{1}{\rho_0}\psi_8(\theta-\theta_0). \tag{3.66}$$

The linear temperature dependence in this equation reflects the behavior of the specific heat capacity in the rubbery regime of amorphous polymers, see Figure 3.2 on page 34. Now it becomes clear why we have chosen the special form of the temperature-dependent terms in the equilibrium Helmholtz energy (3.35). They are a direct consequence of integrating equation (3.65) twice with respect to temperature. Finally, the transient part of the specific heat is given by

$$\begin{aligned} c_{\mathrm{tr}} = \frac{1}{\rho_0}\sum_r \Big[& 6\alpha_r K_r \frac{\partial \Psi_\alpha(\mathrm{tr}\boldsymbol{H},\theta)}{\partial\theta}\theta(\mathrm{tr}\boldsymbol{H} - \mathrm{tr}\boldsymbol{\mathcal{Z}}_r) - \frac{1}{2}\frac{\partial^2 \Psi_\beta(\theta)}{\partial\theta^2}\theta K_r(3\beta_r(\theta-\theta_0)+\chi_r)^2 \\ & - 6\beta_r K_r \frac{\partial \Psi_\beta(\theta)}{\partial\theta}\theta(3\beta_r(\theta-\theta_0)+\chi_r) - 9\beta_r^2 K_r \Psi_\beta(\theta)\theta\Big]. \end{aligned} \tag{3.67}$$

The specific heat capacity at constant deformation is a positive scalar quantity which is required for the balance of energy. The only thing which is still missing is an appropriate specification of the shift factor.

3.4.9. Specification of the Thermoviscoelastic Shift Factor

The shift factor is a key ingredient of the thermoviscoelastic material model since it determines many essential behavioral characteristics of the material response. As mentioned in Section 3, the shift factor may depend on the temperature, stresses, strains (or volume) and the internal variables to account for the various superposition principles

deduced from experimental observations on amorphous polymers. Other influences such as moisture effects are conceivable to form part of the material clock[10]. Accordingly, there exist different material clock models in the literature, including stress clocks [79, 81], strain clocks [91], volume clocks [92, 93], entropy clocks [94] and potential internal energy clocks [39, 40], depending on the nature of the shift factor (see [39, 75] for a thorough discussion of different clock models). Especially the *potential internal energy clock model* seems promising to capture a wide range of material characteristics observed on glassy polymers, including stress, volume and entalpy relaxation, physical aging as well as yield in both tension and compression[11]. Thus, we will adopt this approach in the sequel. To fix ideas, we define the shift factor in terms of the *potential internal energy* U_{p} as follows [39]

$$\log a(\boldsymbol{X}, t) = C_1 \left(\frac{U_{\mathrm{p}}^{\mathrm{ref}}}{U_{\mathrm{p}}(\boldsymbol{H}, \theta, \boldsymbol{\mathcal{Z}}_i, \zeta_i, \chi_i)} - 1 \right), \tag{3.68}$$

where C_1 is the first WLF constant [95] and $U_{\mathrm{p}}^{\mathrm{ref}} = U_{\mathrm{p}}(\boldsymbol{0}, \theta_0, \boldsymbol{0}, 0, 0)$ is related to the second WLF constant C_2. Notice the strong resemblance in shape of the shift factor (3.68) with the famous WLF equation [68, p. 303],

$$\log a_{\mathrm{WLF}}(\theta) = -\frac{C_1(\theta - \theta_0)}{C_2 + \theta - \theta_0} = C_1 \left(\frac{C_2}{C_2 + \theta - \theta_0} - 1 \right). \tag{3.69}$$

The derivation of the potential internal energy in terms of the internal variables approach adopted here closely follows the rational thermodynamics framework introduced in [39]. First, we calculate the *specific internal energy* by means of the Legendre transformation

$$U(\boldsymbol{X}, t) = \psi(\boldsymbol{X}, t) + \theta(\boldsymbol{X}, t) S(\boldsymbol{X}, t), \quad [U] = \frac{\mathrm{J}}{\mathrm{kg}}, \tag{3.70}$$

with the specific Helmholtz energy (3.34) and the specific entropy (3.62) already defined in preceding sections. Next, we split the internal energy into *equilibrium* and *transient internal energy* contributions,

$$U(\boldsymbol{X}, t) = U_{\mathrm{eq}}(\boldsymbol{H}, \theta) + U_{\mathrm{tr}}(\boldsymbol{H}, \theta, \boldsymbol{\mathcal{Z}}_i, \zeta_i, \chi_i). \tag{3.71}$$

[10] As outlined in Section 3.1.2, the term *material clock* is rather associated with hereditary integral constitutive relations, which are based on a *material time*, see equation $(3.1)_1$. Note, however, that the internal variables approach introduced here uses evolution equations which are defined in terms of actual time t only.

[11] Note that all of these nonlinear effects already occur in the small strain regime [11].

The equilibrium part reads

$$\begin{aligned}
U_{\mathrm{eq}} = U_{\mathrm{eq}}^{\mathrm{ref}} &+ \frac{1}{2\rho_0}\psi_1(\mathrm{tr}\boldsymbol{H})^2 + \frac{1}{\rho_0}\psi_2(\mathrm{dev}\boldsymbol{H})\cdot(\mathrm{dev}\boldsymbol{H}) + \frac{1}{\rho_0}\boldsymbol{\psi_3}\cdot\boldsymbol{H} + \frac{1}{\rho_0}\psi_4(\mathrm{tr}\boldsymbol{H})(\theta-\theta_0) \\
&+ \frac{1}{\rho_0}\psi_5\theta_0\left(\theta\ln\left(\frac{\theta}{\theta_0}\right) - (\theta-\theta_0)\right) + \frac{1}{2\rho_0}\psi_6(\mathrm{tr}\boldsymbol{H})^2(\theta-\theta_0) \\
&+ \frac{1}{2\rho_0}\psi_7(\mathrm{tr}\boldsymbol{H})(\theta-\theta_0)^2 + \frac{1}{2\rho_0}\psi_8\theta_0\left(\theta\ln\left(\frac{\theta}{\theta_0}\right) - (\theta-\theta_0) - \frac{1}{2\theta_0}(\theta-\theta_0)^2\right) \\
&- \frac{1}{\rho_0}\psi_4(\mathrm{tr}\boldsymbol{H})\theta - \frac{1}{\rho_0}\psi_5\theta_0\ln\left(\frac{\theta}{\theta_0}\right)\theta - \frac{1}{2\rho_0}\psi_6(\mathrm{tr}\boldsymbol{H})^2\theta - \frac{1}{\rho_0}\psi_7(\mathrm{tr}\boldsymbol{H})(\theta-\theta_0)\theta \\
&- \frac{1}{\rho_0}\psi_8\left(\theta_0\ln\left(\frac{\theta}{\theta_0}\right) - (\theta-\theta_0)\right)\theta,
\end{aligned} \tag{3.72}$$

where $U_{\mathrm{eq}}^{\mathrm{ref}} = \psi_{\mathrm{eq}}^{\mathrm{ref}} + \theta_0 S_{\mathrm{eq}}^{\mathrm{ref}}$. The transient part vanishes when thermodynamic equilibrium is reached and is given by the expression

$$\begin{aligned}
U_{\mathrm{tr}} = &\frac{1}{\rho_0}\Psi_\alpha(\mathrm{tr}\boldsymbol{H},\theta)\sum_r 3\alpha_r K_r(\mathrm{tr}\boldsymbol{H} - \mathrm{tr}\boldsymbol{\mathcal{Z}}_r)\theta - \frac{1}{\rho_0}\Psi_\beta(\theta)\sum_r 3\beta_r K_r(3\beta_r(\theta-\theta_0)+\chi_r)\theta \\
&- \frac{1}{\rho_0}\left(\Psi_\alpha(\mathrm{tr}\boldsymbol{H},\theta) - \frac{\partial\Psi_\alpha(\mathrm{tr}\boldsymbol{H},\theta)}{\partial\theta}\theta\right)\sum_r K_r(\mathrm{tr}\boldsymbol{H} - \mathrm{tr}\boldsymbol{\mathcal{Z}}_r)(3\alpha_r(\theta-\theta_0)+\zeta_r) \\
&+ \frac{1}{2\rho_0}\left(\Psi_K(\theta) - \frac{\partial\Psi_K(\theta)}{\partial\theta}\theta\right)\sum_r K_r(\mathrm{tr}\boldsymbol{H} - \mathrm{tr}\boldsymbol{\mathcal{Z}}_r)^2 \\
&+ \frac{1}{2\rho_0}\left(\Psi_\beta(\theta) - \frac{\partial\Psi_\beta(\theta)}{\partial\theta}\theta\right)\sum_r K_r(3\beta_r(\theta-\theta_0)+\chi_r)^2 \\
&+ \frac{1}{\rho_0}\left(\Psi_G(\theta) - \frac{\partial\Psi_G(\theta)}{\partial\theta}\theta\right)\sum_r G_r(\mathrm{dev}\boldsymbol{H} - \mathrm{dev}\boldsymbol{\mathcal{Z}}_r)\cdot(\mathrm{dev}\boldsymbol{H} - \mathrm{dev}\boldsymbol{\mathcal{Z}}_r).
\end{aligned} \tag{3.73}$$

Next, we determine the potential internal energy $U_{\mathrm{p}}(\boldsymbol{X},t)$. In doing so, we perform the usual split into equilibrium and transient parts,

$$U_{\mathrm{p}}(\boldsymbol{X},t) = U_{\mathrm{p,eq}}(\boldsymbol{X},t) + U_{\mathrm{p,tr}}(\boldsymbol{X},t) = U_{\mathrm{p,eq}}(\boldsymbol{X},t) + U_{\mathrm{tr}}(\boldsymbol{X},t). \tag{3.74}$$

Here, the transient contribution of the potential internal energy is equal to the transient internal energy $U_{\mathrm{tr}}(\boldsymbol{X},t)$, which represents molecular configurational rearrangements and is, therefore, not accompanied by changes in temperature (temperature changes are only attributed to changes in *kinetic energy*). The next stage lies in the determination of the equilibrium potential internal energy $U_{\mathrm{p,eq}}(\boldsymbol{X},t)$. From Figure 3.10 we infer that it is just the difference between the equilibrium internal energy $U_{\mathrm{eq}}(\boldsymbol{X},t)$ and the kinetic energy. Since there exists no procedure to determine the exact form of the equilibrium part, we have to use approximate measures. To this end, we conduct three thought experiments. The first one consists of an infinitely fast thermal quench at constant deformation. Because the volume is kept constant, the potential internal energy in this fictitious experiment does not change. Therefore, the change in kinetic energy equals

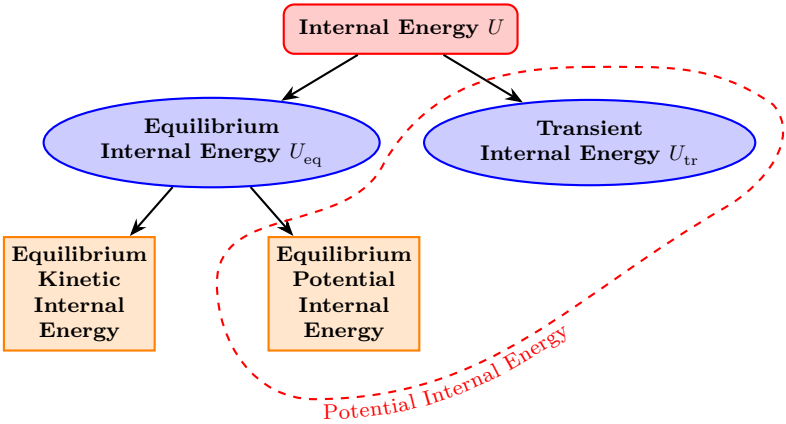

Figure 3.10.: Illustration of different contributions to the potential internal energy U_{p}.

the change in internal energy $U(\boldsymbol{X},t)$. As a result, we can calculate the change in the equilibrium potential internal energy $U_{\mathrm{p,eq}}(\boldsymbol{X},t)$ after the infinitely fast quench as the difference between the change in equilibrium internal energy $U_{\mathrm{eq}}(\boldsymbol{X},t)$ and the change in internal energy $U(\boldsymbol{X},t)$. For the change in equilibrium internal energy we have

$$\begin{aligned}
&U_{\mathrm{eq}}(\boldsymbol{H}=\boldsymbol{0},\theta)-U_{\mathrm{eq}}^{\mathrm{ref}}\\
&=\frac{1}{\rho_0}\psi_5\theta_0\left(\theta\ln\left(\frac{\theta}{\theta_0}\right)-(\theta-\theta_0)\right)+\frac{1}{2\rho_0}\psi_8\theta_0\left(\theta\ln\left(\frac{\theta}{\theta_0}\right)-(\theta-\theta_0)-\frac{1}{2\theta_0}(\theta-\theta_0)^2\right)\\
&\quad-\theta\left[\frac{1}{\rho_0}\psi_5\theta_0\ln\left(\frac{\theta}{\theta_0}\right)+\frac{1}{\rho_0}\psi_8\left(\theta_0\ln\left(\frac{\theta}{\theta_0}\right)-(\theta-\theta_0)\right)\right].
\end{aligned}\tag{3.75}$$

The kinetic energy change (due to an *instantaneous* isochoric quench, that is all internal variables are still zero), which equals the change in internal energy $U(\boldsymbol{X},t)$, leads to

$$\begin{aligned}
&U^{\mathrm{quench}}(\boldsymbol{H}=\boldsymbol{0},\theta,\boldsymbol{\mathcal{Z}}_i=\boldsymbol{0},\zeta_i=0,\chi_i=0)-U_{\mathrm{eq}}^{\mathrm{ref}}\\
&=U_{\mathrm{eq}}(\boldsymbol{H}=\boldsymbol{0},\theta)+U_{\mathrm{tr}}(\boldsymbol{H}=\boldsymbol{0},\theta,\boldsymbol{\mathcal{Z}}_i=\boldsymbol{0},\zeta_i=0,\chi_i=0)-U_{\mathrm{eq}}^{\mathrm{ref}}\\
&=\frac{1}{\rho_0}\psi_5\theta_0\left(\theta\ln\left(\frac{\theta}{\theta_0}\right)-(\theta-\theta_0)\right)+\frac{1}{2\rho_0}\psi_8\theta_0\left(\theta\ln\left(\frac{\theta}{\theta_0}\right)-(\theta-\theta_0)-\frac{1}{2\theta_0}(\theta-\theta_0)^2\right)\\
&\quad-\theta\left[\frac{1}{\rho_0}\psi_5\theta_0\ln\left(\frac{\theta}{\theta_0}\right)+\frac{1}{\rho_0}\psi_8\left(\theta_0\ln\left(\frac{\theta}{\theta_0}\right)-(\theta-\theta_0)\right)\right]\\
&\quad-\frac{1}{\rho_0}\Psi_\beta(\theta)\sum_r 9\beta_r^2K_r(\theta-\theta_0)\theta+\frac{1}{2\rho_0}\left(\Psi_\beta(\theta)-\frac{\partial\Psi_\beta(\theta)}{\partial\theta}\theta\right)\sum_r 9\beta_r^2K_r(\theta-\theta_0)^2.
\end{aligned}\tag{3.76}$$

Now we can determine the difference between equations (3.75) and (3.76) to obtain the change of the equilibrated part of the potential internal energy as follows

$$\begin{aligned}
&\Delta U_{\mathrm{p,eq}}(\boldsymbol{X},t)(\boldsymbol{H}=\boldsymbol{0},\theta,\boldsymbol{\mathcal{Z}}_i=\boldsymbol{0},\zeta_i=0,\chi_i=0)\\
&=U_{\mathrm{eq}}(\boldsymbol{H}=\boldsymbol{0},\theta)-U^{\mathrm{quench}}(\boldsymbol{H}=\boldsymbol{0},\theta,\boldsymbol{\mathcal{Z}}_i=\boldsymbol{0},\zeta_i=0,\chi_i=0)\\
&=\frac{1}{\rho_0}\Psi_\beta(\theta)\sum_r 9\beta_r^2K_r(\theta-\theta_0)\theta-\frac{1}{2\rho_0}\left(\Psi_\beta(\theta)-\frac{\partial\Psi_\beta(\theta)}{\partial\theta}\theta\right)\sum_r 9\beta_r^2K_r(\theta-\theta_0)^2.
\end{aligned}\tag{3.77}$$

The second thought experiment consists of an infinitely fast deformation at constant reference temperature θ_0. Since the temperature is kept constant, there is no change in kinetic energy and the change in equilibrium potential internal energy $U_{\mathrm{p,eq}}(\boldsymbol{X},t)$ is just the change in equilibrium internal energy $U_{\mathrm{eq}}(\boldsymbol{X},t)$, see Figure 3.10. Thus, we have

$$\begin{aligned}
&\Delta U_{\mathrm{p,eq}}(\mathrm{tr}\boldsymbol{H},\theta=\theta_0)=U_{\mathrm{eq}}(\mathrm{tr}\boldsymbol{H},\theta=\theta_0)-U_{\mathrm{eq}}^{\mathrm{ref}}\\
&=\frac{1}{2\rho_0}\psi_1(\mathrm{tr}\boldsymbol{H})^2+\frac{1}{\rho_0}\psi_2(\mathrm{dev}\boldsymbol{H})\cdot(\mathrm{dev}\boldsymbol{H})+\frac{1}{\rho_0}\boldsymbol{\psi_3}\cdot\boldsymbol{H}-\frac{1}{\rho_0}\psi_4(\mathrm{tr}\boldsymbol{H})\theta_0-\frac{1}{2\rho_0}\psi_6(\mathrm{tr}\boldsymbol{H})^2\theta_0.
\end{aligned}\tag{3.78}$$

The third and last experiment is a combination of the former two, that is an infinitely fast quench combined with a prescribed instantaneous deformation. The resulting expression should contain expressions (3.77) and (3.78) and, in addition, mixed terms representing changes in volume, shape and temperature. The prefactors for these mixed terms should be limited by the equilibrium and the glassy values. Since [39, p. 4592] prefers the glassy parameters after extensive validation of four different polymer systems, we also opt for these values and the resulting equilibrium potential internal energy reads

$$\begin{aligned}
&U_{\mathrm{p,eq}}(\mathrm{tr}\boldsymbol{H},\theta)\\
&=U_{\mathrm{p}}^{\mathrm{ref}}+\frac{1}{2\rho_0}\psi_1(\mathrm{tr}\boldsymbol{H})^2+\frac{1}{\rho_0}\psi_2(\mathrm{dev}\boldsymbol{H})\cdot(\mathrm{dev}\boldsymbol{H})+\frac{1}{\rho_0}\boldsymbol{\psi_3}\cdot\boldsymbol{H}\\
&\quad-\frac{1}{\rho_0}\Psi_\alpha(\mathrm{tr}\boldsymbol{H},\theta)\sum_r 3\alpha_rK_r(\mathrm{tr}\boldsymbol{H})\theta-\frac{1}{2\rho_0}\left(\Psi_K(\theta)-\frac{\partial\Psi_K(\theta)}{\partial\theta}\theta-1\right)\sum_r K_r(\mathrm{tr}\boldsymbol{H})^2\\
&\quad+\frac{1}{\rho_0}\Psi_\beta(\theta)\sum_r 9\beta_r^2K_r(\theta-\theta_0)\theta-\frac{1}{2\rho_0}\left(\Psi_\beta(\theta)-\frac{\partial\Psi_\beta(\theta)}{\partial\theta}\theta\right)\sum_r 9\beta_r^2K_r(\theta-\theta_0)^2\\
&\quad+\frac{1}{\rho_0}\left(\Psi_\alpha(\mathrm{tr}\boldsymbol{H},\theta)-\frac{\partial\Psi_\alpha(\mathrm{tr}\boldsymbol{H},\theta)}{\partial\theta}\theta\right)\sum_r 3\alpha_rK_r(\mathrm{tr}\boldsymbol{H})(\theta-\theta_0),
\end{aligned}\tag{3.79}$$

where $U_{\mathrm{p}}^{\mathrm{ref}}=U_{\mathrm{eq}}^{\mathrm{ref}}$. Note that equation (3.79) reduces exactly to expression (3.77) if the deformation is kept constant during the quench, $\boldsymbol{H}(\boldsymbol{X},t)=\boldsymbol{0}$, and reduces approximately to expression (3.78) when the temperature is kept constant during deformation, $\theta(\boldsymbol{X},t)=\theta_0$, due to the mixed term assumption. Finally, the potential internal energy $U_{\mathrm{p}}(\boldsymbol{X},t)$ is given as the sum of the equilibrium and the transient contributions according

to equation (3.74) as

$$
\begin{aligned}
U_{\mathrm{p}} = U_{\mathrm{p}}^{\mathrm{ref}} &+ \frac{1}{2\rho_0}\psi_1(\mathrm{tr}\boldsymbol{H})^2 + \frac{1}{\rho_0}\psi_2(\mathrm{dev}\boldsymbol{H})\cdot(\mathrm{dev}\boldsymbol{H}) + \frac{1}{\rho_0}\boldsymbol{\psi_3}\cdot\boldsymbol{H} + \frac{1}{2\rho_0}\sum_r K_r(\mathrm{tr}\boldsymbol{H})^2 \\
&- \frac{1}{\rho_0}\Psi_\alpha(\mathrm{tr}\boldsymbol{H},\theta)\sum_r 3\alpha_r K_r(\mathrm{tr}\boldsymbol{\mathcal{Z}}_r)\theta_0 - \frac{1}{\rho_0}\Psi_\beta(\theta)\sum_r 3\beta_r K_r\chi_r\theta_0 \\
&- \frac{1}{\rho_0}\frac{\partial\Psi_\alpha(\mathrm{tr}\boldsymbol{H},\theta)}{\partial\theta}\theta\sum_r 3\alpha_r K_r(\theta-\theta_0)(\mathrm{tr}\boldsymbol{\mathcal{Z}}_r) - \frac{1}{\rho_0}\frac{\partial\Psi_\beta(\theta)}{\partial\theta}\theta\sum_r 3\beta_r K_r(\theta-\theta_0)\chi_r \\
&- \frac{1}{\rho_0}\left(\Psi_\alpha(\mathrm{tr}\boldsymbol{H},\theta) - \frac{\partial\Psi_\alpha(\mathrm{tr}\boldsymbol{H},\theta)}{\partial\theta}\theta\right)\sum_r K_r(\mathrm{tr}\boldsymbol{H}-\mathrm{tr}\boldsymbol{\mathcal{Z}}_r)\zeta_r \\
&- \frac{1}{\rho_0}\left(\Psi_K(\theta) - \frac{\partial\Psi_K(\theta)}{\partial\theta}\theta\right)\sum_r K_r(\mathrm{tr}\boldsymbol{H})(\mathrm{tr}\boldsymbol{\mathcal{Z}}_r) \\
&+ \frac{1}{2\rho_0}\left(\Psi_K(\theta) - \frac{\partial\Psi_K(\theta)}{\partial\theta}\theta\right)\sum_r K_r(\mathrm{tr}\boldsymbol{\mathcal{Z}}_r)^2 \\
&+ \frac{1}{2\rho_0}\left(\Psi_\beta(\theta) - \frac{\partial\Psi_\beta(\theta)}{\partial\theta}\theta\right)\sum_r K_r(\chi_r)^2 \\
&+ \frac{1}{\rho_0}\left(\Psi_G(\theta) - \frac{\partial\Psi_G(\theta)}{\partial\theta}\theta\right)\sum_r G_r(\mathrm{dev}\boldsymbol{H}-\mathrm{dev}\boldsymbol{\mathcal{Z}}_r)\cdot(\mathrm{dev}\boldsymbol{H}-\mathrm{dev}\boldsymbol{\mathcal{Z}}_r),
\end{aligned}
\tag{3.80}
$$

where $U_{\mathrm{p}}^{\mathrm{ref}} = U_{\mathrm{eq}}^{\mathrm{ref}}$. This equation for the potential internal energy completes the definition of the thermoviscoelastic shift factor (3.68). Most of the relaxing terms do not contribute significantly to the potential internal energy. However, there are two expressions which deserve special attention. The first one highlighted represents the viscoelastic entropic contribution to the potential internal energy (*entropy clock model*), since it stems from the transient part of the specific entropy, see equation (3.64). These terms are associated with physical aging and enthalpy relaxation effects which are observed when the polymer is cooled well below its glass transition temperature. The characteristic "leveling-off" of the shift factor in the glassy regime is attributed to these two terms. Indeed, even if the temperature is held constant in the glassy regime, the internal variables $\boldsymbol{\mathcal{Z}}_l$ and χ_l continue to change and converge (slowly) towards their equilibrium values, causing the shift factor in turn to relax towards its equilibrium response. Hence, physical aging is naturally predicted. The second expression, on the other hand, corresponds to a *stress clock* and is critical when deformation changes the shape of the polymer in the glassy state (for example during tensile tests at low temperatures). In general, the internal variables develop very slowly in the glassy state. However, this term will cause an increase in the potential internal energy during deviatoric deformation, which is accompanied by a decrease in the shift factor (3.68). Thus, the relaxation times decrease equally. The consequence is yield-like behavior in tension, compression and shear, which is in accordance with experimental observations [68, p. 483]. We refer to [39, 40] for an in-depth discussion of the potential internal energy clock model. In the next section we give further details on the different material parameters required for the constitutive formulation.

Remark 16. *The second term highlighted in equation (3.80) may be altered to resemble stress clock approaches found in the literature [39, p. 4593]. This can lead to improved predictions during the validation process. Specifically, we have modified this expression as follows,*

$$\begin{aligned} U_{\mathrm{p}} = \ldots &+ \frac{2}{\rho_0} \sum_r G_r \left(\mathrm{dev}\boldsymbol{H} - \mathrm{dev}\boldsymbol{\mathcal{Z}}_r\right) \cdot \left(\mathrm{dev}\boldsymbol{H}\right) \\ &- \frac{1}{\rho_0 (G_g - G_\infty)} \left(\sum_r G_r \left(\mathrm{dev}\boldsymbol{H} - \mathrm{dev}\boldsymbol{\mathcal{Z}}_r\right) \right) \cdot \left(\sum_r G_r \left(\mathrm{dev}\boldsymbol{H} - \mathrm{dev}\boldsymbol{\mathcal{Z}}_r\right) \right), \end{aligned} \tag{3.81}$$

where $G_g - G_\infty = \sum_r G_r$ is the difference between the glassy and the rubbery shear modulus. This corresponds to a mixture of the viscoelastic strains with the current strain state. The potential internal energy with the modified expression 3.81 for the transient shear contribution will be used for the simulations in Part III of this thesis.

3.4.10. Derivation of some Material Parameters

In this section, we provide further information on the different material parameters required for the Helmholtz energy (3.34). First, we give a detailed derivation of the equilibrium parameter ψ_7. As a first approximation, this parameter may be inferred from experimental data on the coefficient of thermal expansion and the equilibrium bulk modulus. The derivation follows a simple heating experiment. To this end, we assume small strains, which serves as a reasonable approach to estimate the unknown parameter. In the isotropic case the value $3\alpha_\infty$ is roughly equal to the *cubic* coefficient of thermal expansion. Since we deal with equilibrium (rubbery) values, the following derivation relates to the temperature range above the glass transition, that is $\theta > \theta_{\mathrm{g}}$. In what follows we use the definition of the cubic coefficient of thermal expansion and approximate it through a first-order Taylor series expansion,

$$\frac{1}{v}\frac{dv}{d\theta} \approx 3\hat{\alpha}_\infty(\theta) \approx 3\alpha_\infty + 3\frac{\partial \alpha_\infty}{\partial \theta}(\theta - \theta_0), \tag{3.82}$$

where v is the current volume. Integration within the entropic elastic (rubbery) region yields

$$\int_V^v \frac{1}{\bar{v}} d\bar{v} = \int_{\theta_0}^{\theta} 3\alpha_\infty + 3\frac{\partial \alpha_\infty}{\partial \theta}(\bar{\theta} - \theta_0) d\bar{\theta} \quad \Rightarrow \quad \ln \frac{v}{V} = 3\alpha_\infty(\theta - \theta_0) + \frac{3}{2}\frac{\partial \alpha_\infty}{\partial \theta}(\theta - \theta_0)^2, \tag{3.83}$$

where V designates the referential volume. Since we assume small strains, we can use the following volumetric approximation

$$\ln \frac{v}{V} = \ln\left(\frac{\Delta V}{V} + 1\right) \approx \frac{\Delta V}{V} \approx \mathrm{tr}\boldsymbol{\varepsilon}. \tag{3.84}$$

Now, the derivation of ψ_7 is based on a simple heating experiment under constant pressure. When the expansion is assumed to be stress-free it follows from the equilibrium stresses (3.57) that

$$\boldsymbol{\sigma}_{\mathrm{eq}}(\boldsymbol{\varepsilon}, \theta) = \boldsymbol{0} \quad \Rightarrow \quad (\psi_1 + \psi_6(\theta - \theta_0))(\mathrm{tr}\boldsymbol{\varepsilon}) + \left(\psi_4 + \frac{1}{2}\psi_7(\theta - \theta_0)\right)(\theta - \theta_0) = 0. \tag{3.85}$$

Next, by combining equations (3.83) and (3.84), equation (3.85) becomes

$$(\psi_1 + \psi_6(\theta - \theta_0))\left(3\alpha_\infty + \frac{3}{2}\frac{\partial \alpha_\infty}{\partial \theta}(\theta - \theta_0)\right) + \psi_4 + \frac{1}{2}\psi_7(\theta - \theta_0) = 0. \tag{3.86}$$

Differentiation with respect to temperature yields

$$3\alpha_\infty \psi_6 + (\psi_1 + 2\psi_6(\theta - \theta_0))\frac{3}{2}\frac{\partial \alpha_\infty}{\partial \theta} + \frac{1}{2}\psi_7 = 0, \tag{3.87}$$

which is solved for the temperature derivative of the equilibrium *linear* coefficient of thermal expansion

$$\frac{\partial \alpha_\infty}{\partial \theta} = -\frac{2\alpha_\infty \psi_6 + \frac{1}{3}\psi_7}{\psi_1 + 2\psi_6(\theta - \theta_0)}. \tag{3.88}$$

A reasonable assumption is that the temperature dependence in the denominator of equation (3.88) is of minor importance. Thus, simple transformation of above equation leads to an expression for material parameter ψ_7, that is

$$\psi_7 = -3(\psi_1 + 2\psi_6(\theta - \theta_0))\frac{\partial \alpha_\infty}{\partial \theta} - 6\alpha_\infty \psi_6 \approx -3\psi_1 \frac{\partial \alpha_\infty}{\partial \theta} - 6\alpha_\infty \psi_6. \tag{3.89}$$

Therefore, as a first approximation, material parameter ψ_7 may be inferred from experimental data relating to the equilibrium coefficient of thermal expansion α_∞ and the temperature dependence of the equilibrium compression modulus (via parameter ψ_6).

Next, we try to approximate glassy material parameter $\tilde{C}_2$. In contrast to the thought experiment above the derivation is now based on a simple cooling experiment. To this end, we perform an infinitely fast thermal quench $\Delta\theta = \theta - \theta_0 < 0$ into the glassy state. In doing so, we have to substitute the equilibrium coefficient of thermal expansion in equation $(3.83)_2$ with its glassy counterpart. In this case, the thermal contraction (3.84) becomes

$$\mathrm{tr}\boldsymbol{\varepsilon} = 3\alpha_\mathrm{g}(\theta - \theta_0) + \frac{3}{2}\frac{\partial \alpha_\mathrm{g}}{\partial \theta}(\theta - \theta_0)^2. \tag{3.90}$$

Since we have to consider the (initial) transient stresses under this infinitely fast quench assumption, the zero-stress condition $\mathrm{tr}\boldsymbol{\sigma}(\boldsymbol{\varepsilon}, \theta, \mathbf{0}, 0, 0) = 0$ yields

$$\begin{aligned}&\left(\psi_1 + \sum_r K_r + \left(\psi_6 + \tilde{C}_1 \sum_r K_r\right)(\theta - \theta_0)\right)(\mathrm{tr}\boldsymbol{\varepsilon}) \\ &+ \left(\psi_4 - \sum_r 3\alpha_r K_r + \left(\frac{1}{2}\psi_7 - \tilde{C}_2 \sum_r 3\alpha_r K_r\right)(\theta - \theta_0)\right)(\theta - \theta_0) = 0,\end{aligned} \tag{3.91}$$

where we have assumed that material parameter $\tilde{C}_3 = 0$, see Table 3.5. Since the following manipulations are basically the same as for equilibrium parameter ψ_7 above, we cut short and directly provide the resulting expression

$$\tilde{C}_2 = \frac{\frac{1}{3}\psi_7 + 2\alpha_\mathrm{g}\left(\psi_6 + \tilde{C}_1 \sum_r K_r\right) + \left(\psi_1 + \sum_r K_r\right)\frac{\partial \alpha_\mathrm{g}}{\partial \theta}}{2\sum_r \alpha_r K_r}. \tag{3.92}$$

We do not know for a similar procedure to derive analytical expressions for the glassy parameters $\tilde{C}_4$ and $\tilde{C}_5$. Such a procedure would require an isentropic temperature

change, for example under adiabatic conditions. However, since an infinitely fast thermal quench is accompanied by internal dissipation $\mathcal{D}_{\mathrm{int}}(\boldsymbol{X}, t)$, there will equally be a change in entropy $S(\boldsymbol{X}, t)$ [48, p. 172]. Nevertheless, these parameters may be inferred from calorimetric measurements. The glassy parameters for the prefactor functions (3.37) are summarized in Table 3.5. Finally, we provide some graphical interpretation

Parameter	Value
$\tilde{C}_1$	$\left(\frac{\partial K_{\mathrm{g}}}{\partial \theta} - \frac{\partial K_{\infty}}{\partial \theta}\right) / \left(K_{\mathrm{g}} - K_{\infty}\right)$
$\tilde{C}_2$	$\left(K_{\mathrm{g}} \frac{\partial \alpha_{\mathrm{g}}}{\partial \theta} - K_{\infty} \frac{\partial \alpha_{\infty}}{\partial \theta} + 2\alpha_{\mathrm{g}} \frac{\partial K_{\mathrm{g}}}{\partial \theta} - 2\alpha_{\infty} \frac{\partial K_{\infty}}{\partial \theta}\right) / \left(2 \sum_r \alpha_r K_r\right)$
$\tilde{C}_3$	0
$\tilde{C}_4$	(extracted from calorimetric measurements)
$\tilde{C}_5$	(extracted from calorimetric measurements)
$\tilde{C}_6$	$\left(\frac{\partial G_g}{\partial \theta} - \frac{\partial G_{\infty}}{\partial \theta}\right) / \left(G_g - G_{\infty}\right)$

Table 3.5.: Summary of approximate values for the *glassy* material parameters $\tilde{C}_1$ to $\tilde{C}_6$ from equation (3.37) under the assumption of an infinitely fast thermal quench. For the parameters $\tilde{C}_4$ and $\tilde{C}_5$ relating to entropy relaxation no analytical expressions could be derived.

of the material parameters required for the thermoviscoelastic material model. They are summarized in Figure 3.11.

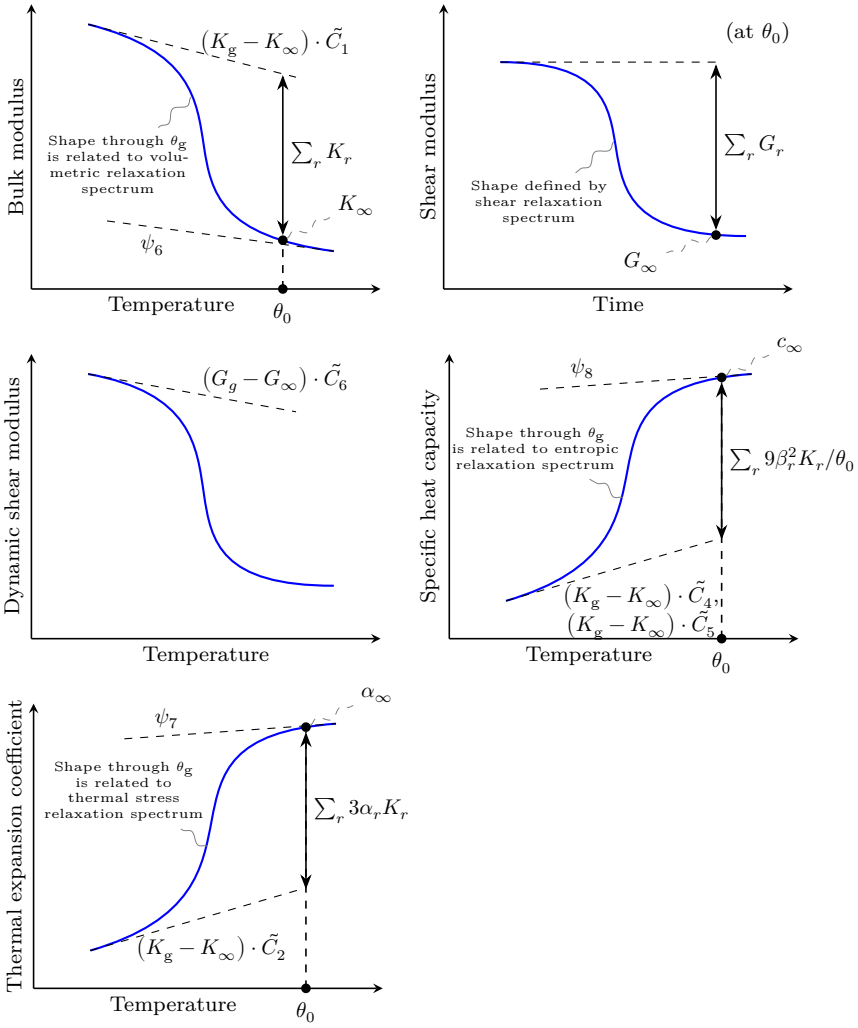

Figure 3.11.: Illustration of the physical significance of certain material input data required for the Helmholtz energy (3.34). θ_g denotes the glass transition temperature. Parameters such as ψ_8 in the lower diagram on the right represent the slope of the dashed line. For analytical expressions of the equilibrium values see Table 3.3 on page 52. For the glassy parameters we refer to Table 3.5.

3.4.11. Comparison with Rational Thermodynamics

In the final section of this chapter we give a brief comparison between the material model based on the internal variables approach developed above and the closely related formulation within the framework of rational thermodynamics [39]. Table 3.6 summarizes some important aspects concerning the analytical description and the numerical treatment of both formulations. The latter will be covered in detail in Part II of this thesis. See also [96, p. 86] and [49, p. 295] for a critical comparison of the internal variables approach and rational thermodynamics in general.

	Internal Variables Approach	**Rational Thermodynamics**
Verification of thermodynamical consistency	*easy to show through internal dissipation*	*difficult to show, not provided in derivation*
Derivation of stresses, entropy etc. from potential	*straightforward through partial differentiation*	*difficult, implying multiple integration by parts operations*
Extensibility (e.g. damage effects)	*with relative ease by adding further internal variables*	*difficult due to the integral formulation*
Numerical integration	*Runge-Kutta methods with integrated step size control, multi-step methods*	*Newton-Cotes formulas, Gauss integration*
Storage requirements	*increased due to the many internal variables*	*reduced, depending on the time integration scheme*
Parameter identification	*difficult due to the many Prony parameters*	*easy, using stretched exponential relaxation functions (requires huge storage capacity though), alternatively using Prony series*

Table 3.6.: Comparison of the material formulation based on the internal variables approach developed in this thesis and the rational thermodynamics framework covered in [39].

Part II.

Algorithmic Framework

4. The Global Picture: Solution Algorithms

In this chapter, we discuss numerical solution strategies to solve transient problems in the context of finite thermoviscoelasticity assuming quasistatic processes. Following the method of vertical lines, we start with the spatial discretization using the finite element method and subsequently apply temporal discretization schemes in the form of implicit Runge-Kutta methods, see Figure 4.1. The focus is primarily on the global set of equations resulting from the assembling process of individual element contributions. This is an appropriate choice if we seek to implement time integration schemes into existing finite element software. The resultant coupled system of equations is treated as a monolithic entity[1]. The final section briefly outlines automatic time-stepping procedures, which are of paramount importance for solving highly transient initial boundary value problems. We have extended the in-house FEM software `FEAP` *with a new interface which enables the solution of thermomechanically coupled problems in combination with powerful automatic time-stepping control mechanisms.*

4.1. Spatial Discretization with the Finite Element Method

In this section, we develop a finite element model for the nonlinear thermomechanical behavior of solid continuum bodies assuming quasistatic processes. Starting point are the local (strong) forms of the balance principles, which are readily transformed into equivalent variational (weak) formulations. Next, space-continuous fields will be replaced with their discrete counterparts by approximating displacements and temperatures over a finite element. This is in line with the principle of local action discussed in Section 2.5.3 [54, p. 200]. In doing so, we apply Lagrangian interpolation functions for the unknown fields and stick to the standard isoparametric concept [54, p. 139]. After the spatial discretization follows the assembling process of individual element contributions, which eventually yields the space-discrete-time-continuous initial boundary value problem in the context of finite thermoviscoelasticity. It is important to emphasize, however, that the finite element formulation rests on a different strain type than the material formulation in the preceding section. Specifically, by setting $k = 2$ in the family of generalized strain tensors (2.9) on page 11 we obtain the *Green-Lagrange strain*

$$\boldsymbol{E}(\boldsymbol{X},t) := \frac{1}{2}\left(\boldsymbol{C}-\boldsymbol{I}\right), \text{ where } \boldsymbol{C}(\boldsymbol{X},t) = \boldsymbol{F}^{\mathrm{T}}(\boldsymbol{X},t)\boldsymbol{F}(\boldsymbol{X},t). \tag{4.1}$$

The Green-Lagrange strain along with the second Piola-Kirchhoff stresses as their thermodynamic conjugate form the basis for the upcoming finite element formulation.

[1] For an in-depth discussion on different algorithmic solution strategies for coupled problems we refer to [97–100].

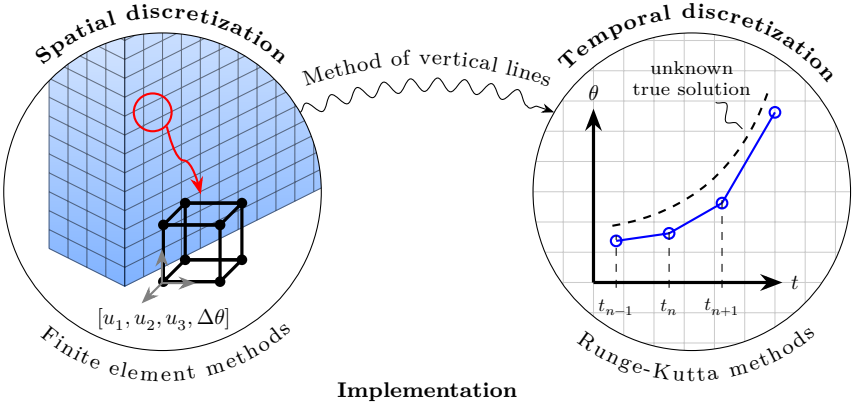

Implementation

```
1  ! Local variables
2  integer :: nodes, steps
3
4  real(8) :: time, error
5  real(8) :: step_size
6
7  ! Start calculations
8  call init(time, step_size, error)
```

Fortran, FEAP

Figure 4.1.: Workflow for the numerical solution of transient initial boundary value problems. According to the *method of vertical lines*, we begin with the spatial discretization using *finite elements*, followed by the temporal discretization in terms of *implicit Runge-Kutta methods*. Finally, the set of equations derived on paper is translated into a high-level programming language such as *Fortran* to conduct simulations on a computer using the FEM software FEAP.

4.1.1. Variational Formulation of the Balance Equations

We start with the derivation of the *variational* or *weak formulations* of the balance equations. To this end, let the spaces of *test functions* be defined by

$$\begin{aligned} \mathcal{V}_{\boldsymbol{u}} &= \{\delta\boldsymbol{u} : \Omega \to \mathbb{E}^3,\ \delta\boldsymbol{u}(\boldsymbol{X}) = \boldsymbol{0}\ \forall\ \boldsymbol{X} \in \partial\Omega_{\boldsymbol{u}}\}, \\ \mathcal{V}_{\theta} &= \{\delta\theta : \Omega \to \mathbb{R},\ \delta\theta(\boldsymbol{X}) = 0\ \forall\ \boldsymbol{X} \in \partial\Omega_{\theta}\}, \end{aligned} \tag{4.2}$$

where $\Omega = R(B)$ is the reference configuration of continuum body B and $\partial\Omega_{\boldsymbol{u}} \subseteq \partial\Omega$, $\partial\Omega_{\theta} \subseteq \partial\Omega$. In the sequel, we shall restrict ourselves to quasistatic conditions, that is $\ddot{\boldsymbol{\varphi}}(\boldsymbol{X}, t) = \boldsymbol{0}$. In this case the balance of linear momentum (2.19) reads

$$\mathrm{Div}(\boldsymbol{P}) + \boldsymbol{B} = \boldsymbol{0}, \quad \text{where} \quad \boldsymbol{P}(\boldsymbol{X}, t) = \boldsymbol{F}(\boldsymbol{X}, t)\boldsymbol{S}(\boldsymbol{X}, t). \tag{4.3}$$

Here, the so-called *second Piola-Kirchhoff stress tensor* $\boldsymbol{S}(\boldsymbol{X}, t)$ represents the thermodynamic conjugate to the Green-Lagrange strain $\boldsymbol{E}(\boldsymbol{X}, t)$. Next, by multiplying above equation with the virtual displacement $\delta\boldsymbol{u}(\boldsymbol{X}) \in \mathcal{V}_{\boldsymbol{u}}$ followed by an integration over the domain of continuum body B leads to

$$0 = -\int_{\Omega} (\mathrm{Div}(\boldsymbol{F}\boldsymbol{S}) + \boldsymbol{B}) \cdot \delta\boldsymbol{u}\, dV \quad \forall\, \delta\boldsymbol{u} \in \mathcal{V}_{\boldsymbol{u}}, \tag{4.4}$$

where the minus sign is in anticipation of the weak form of the balance of energy. By making use of the relations $\boldsymbol{P} = \boldsymbol{F}\boldsymbol{S}$ and $\boldsymbol{P} \cdot \delta\boldsymbol{F} = \boldsymbol{S} \cdot \delta\boldsymbol{E}$ as well as the divergence theorem yields

$$0 = g^{\boldsymbol{u}}(t, \boldsymbol{u}, \theta, \boldsymbol{\mathcal{E}}_1, \dots, \boldsymbol{\mathcal{E}}_m, \delta\boldsymbol{u}) := -\int_{\Omega} \delta\boldsymbol{E} \cdot \boldsymbol{S} - \delta\boldsymbol{u} \cdot \boldsymbol{B}\, dV + \int_{\partial\Omega^{\boldsymbol{T}}} \delta\boldsymbol{u} \cdot \boldsymbol{T}\, dA, \tag{4.5}$$

where $\partial\Omega^{\boldsymbol{T}} \subseteq \Omega$ and $\partial\Omega^{\boldsymbol{T}} \cap \partial\Omega_{\boldsymbol{u}} = \emptyset$. Here, $g^{\boldsymbol{u}}$ denotes the weak form of the balance of linear momentum and forms the first part of the finite element framework. Note that the dependence on the internal variables $\boldsymbol{\mathcal{E}}_l(\boldsymbol{X}, t)$[2] stems from the constitutive relation for the stress tensor. The same procedure is now repeated for the balance of energy. Since the main interest is on the evolution of the temperature $\theta(\boldsymbol{X}, t)$, we start with the first law of thermodynamics in *temperature form* [48, p. 360], that is

$$\rho_0 c\dot{\theta} = R - \mathrm{Div}\boldsymbol{Q} - \mathcal{H}_{\mathrm{e}} - \mathcal{H}_{\mathrm{in}} + \mathcal{D}_{\mathrm{int}}, \quad \text{where} \quad \mathcal{H}_{\mathrm{e}} := -\rho_0 \theta \frac{\partial \boldsymbol{S}}{\partial \theta} \cdot \dot{\boldsymbol{E}}. \tag{4.6}$$

The scalar quantity $\mathcal{H}_{\mathrm{e}}(\boldsymbol{X}, t)$ is a thermoelastic coupling effect called *structural thermoelastic heating* ("Gough-Joule effect"). Multiplication of above equation with the virtual temperature $\delta\theta(\boldsymbol{X}) \in \mathcal{V}_\theta$ followed by an integration over the reference configuration of continuum body B gives

$$0 = \int_{\Omega} (\rho_0 c\dot{\theta} - R + \mathrm{Div}\boldsymbol{Q} + \mathcal{H}_{\mathrm{e}} + \mathcal{H}_{\mathrm{in}} - \mathcal{D}_{\mathrm{int}}) \delta\theta\, dV. \tag{4.7}$$

Straightforward application of the divergence theorem on the term containing the heat flux $\boldsymbol{Q}(\boldsymbol{X}, t)$ results in an additional integral over the boundary,

$$\begin{aligned} 0 = g^{\theta}(t, \boldsymbol{u}, \theta, \dot{\boldsymbol{u}}, \dot{\theta}, \boldsymbol{\mathcal{E}}_1, \dots, \boldsymbol{\mathcal{E}}_m, \delta\theta) := &-\int_{\Omega} \delta\theta(\rho_0 c\dot{\theta} - R + \mathcal{H}_{\mathrm{e}} + \mathcal{H}_{\mathrm{in}} - \mathcal{D}_{\mathrm{int}}) - \mathrm{Grad}\delta\theta \cdot \boldsymbol{Q}\, dV \\ &- \int_{\partial\Omega^{\boldsymbol{Q}}} \delta\theta \boldsymbol{Q} \cdot \boldsymbol{N}\, dA, \end{aligned} \tag{4.8}$$

where $\partial\Omega^{\boldsymbol{Q}} \subseteq \Omega$ and $\partial\Omega^{\boldsymbol{Q}} \cap \partial\Omega_{\theta} = \emptyset$. Here, g^{θ} denotes the *weak form of the balance of energy* and forms the second part of the finite element framework. Notice that the thermal weak formulation additionally depends on the rates $\dot{\boldsymbol{u}}(\boldsymbol{X}, t)$ and $\dot{\theta}(\boldsymbol{X}, t)$, where the former dependence follows from the influence of structural thermoelastic heating $(4.6)_2$. While the material formulation in Section 3.4 bases upon the Hencky strain $\boldsymbol{H}(\boldsymbol{X}, t)$, the variational formulation of the balance equations is given in terms of the Green-Lagrange strain $\boldsymbol{E}(\boldsymbol{X}, t)$. Consequently, we have to transform constitutive quantities between the finite element and the material interface. However, we will not delve into the technical details and instead refer to the literature[3] [47, 101].

[2] In the sequel, the symbol $\boldsymbol{\mathcal{E}}_l$ accounts for the various internal variables whose evolution is governed by the constitutive equations (3.38) defined on page 54.

[3] The references only consider the purely mechanical continuum theory, while the thermomechanical extension considered here requires further transformations related to the thermal quantities appearing in equation (4.8). Nevertheless, the transformation rules are essentially the same.

Remark 17. *The question arises whether we could use the Hencky strain in the variational formulation, rather than the Green-Lagrange strain, given that* $\boldsymbol{P} \cdot \delta \boldsymbol{F} = \boldsymbol{\sigma} \cdot \delta \boldsymbol{H}$ *in equation (4.5), in order to spare some computational overhead. The problem with this approach lies in the linearization of the weak form, which requires the calculation of the derivatives of kinematic quantities such as the strain variation* $\delta \boldsymbol{H}(\boldsymbol{X})$*. These calculations are quite involved, since the components of the Hencky strain tensor likely refer to the eigenbasis (2.14), while the linearization is performed with respect to the displacements* $\boldsymbol{u}(\boldsymbol{X}, t)$ *in the cartesian coordinate system. Moreover, since the element displacements are defined in terms of the element nodes, these calculations relate to the innermost loop construct in finite element codes and, therefore, are prohibitively costly to perform. Instead, the stresses and material tangent should be transformed [101]. Those calculations merely refer to the outermost loop over the integration points.*

4.1.2. Space-Discrete-Time-Continuous Balance Equations

With the continuous variational formulations (4.5) and (4.8) at hand, we can now proceed with the spatial discretization of continuum body B. To this end, we identify $\mathcal{Z}$ global nodes $\boldsymbol{Y}_K \in \Omega^h$, $K = 1, \dots, \mathcal{Z}$, in the reference configuration $\Omega = R(B)$ of continuum body B and approximate the region Ω by a finite number of non-overlapping subdomains Ω_e called *finite elements*, that is $\Omega \approx \Omega^h = \cup_e \Omega_e$. Each element is characterized by three defining properties. First, a set of nodal points $\boldsymbol{X}_I \in \Omega_e$, $I = 1, \dots, nel$, defining the element geometry. Second, a set of polynomial shape functions $N_I(\boldsymbol{X})$. Third, degrees of freedom $(u_{1,I}, u_{2,I}, u_{3,I}, \Delta\theta_I)$ attached to each element node. The first three degrees of freedom represent translational motions, while the fourth is the deviation of the absolute temperature from a reference temperature. The finite elements will eventually be assembled by mapping each nodal point $\boldsymbol{X}_I \in \Omega_e$ onto a corresponding global point $\boldsymbol{Y}_K \in \Omega^h$. The assembled region Ω^h is also called the *discretization* of the reference configuration. Geometry, displacements and temperature are interpolated over the finite element with respect to the nodal values using Lagrangian shape functions,

$$\begin{aligned} \boldsymbol{X}^h(\xi, \eta, \zeta, t) &= \sum_{I=1}^{nel} N_I(\xi, \eta, \zeta) \boldsymbol{X}_I(t), \\ \boldsymbol{u}^h(\xi, \eta, \zeta, t) &= \sum_{I=1}^{nel} N_I(\xi, \eta, \zeta) \boldsymbol{u}_I(t), \\ \theta^h(\xi, \eta, \zeta, t) &= \sum_{I=1}^{nel} N_I(\xi, \eta, \zeta) \theta_I(t). \end{aligned} \tag{4.9}$$

Approximations (4.9) correspond to the *isoparametric concept*, where geometry, element displacements and temperatures share the same type of shape functions and each physical point $\boldsymbol{X}^h \in \Omega_e$ is identified through the bijective *isoparametric map*

$$F : \begin{cases} [-1, 1]^3 \to \Omega_e \subseteq \Omega^h, \\ (\xi, \eta, \zeta) \mapsto \boldsymbol{X}^h = F(\xi, \eta, \zeta), \end{cases} \quad \text{where} \quad F(\xi, \eta, \zeta) := \sum_{I=1}^{nel} N_I(\xi, \eta, \zeta) \boldsymbol{X}_I. \tag{4.10}$$

Material time derivatives and derived kinematic quantities such as element strains $\boldsymbol{E}^h(\boldsymbol{X},t)$ follow in a straightforward manner from these approximations,

$$\begin{aligned}
\dot{\boldsymbol{u}}^h(\xi,\eta,\zeta,t) &= \sum_{I=1}^{nel} N_I(\xi,\eta,\zeta)\dot{\boldsymbol{u}}_I(t), & \dot{\theta}^h(\xi,\eta,\zeta,t) &= \sum_{I=1}^{nel} N_I(\xi,\eta,\zeta)\dot{\theta}_I(t),\\
\frac{\partial \boldsymbol{u}^h}{\partial \boldsymbol{X}}(\xi,\eta,\zeta,t) &= \sum_{I=1}^{nel} \boldsymbol{u}_I(t)\otimes\frac{\partial N_I}{\partial \boldsymbol{X}}(\xi,\eta,\zeta), & \frac{\partial \theta}{\partial \boldsymbol{X}}(\xi,\eta,\zeta,t) &= \sum_{I=1}^{nel} \frac{\partial N_I}{\partial \boldsymbol{X}}\theta_I(t),\\
\boldsymbol{F}^h(\xi,\eta,\zeta,t) &= \boldsymbol{I}+\frac{\partial \boldsymbol{u}^h}{\partial \boldsymbol{X}}(\xi,\eta,\zeta,t), & \boldsymbol{E}^h(\xi,\eta,\zeta,t) &= \frac{1}{2}\left(\left(\boldsymbol{F}^h\right)^T\boldsymbol{F}^h-\boldsymbol{I}\right).
\end{aligned} \tag{4.11}$$

Here, the gradients of the shape functions in the third and fourth equation follow from (4.9) and the inverse F^{-1} of the isoparametric map (4.10). In an analogous fashion we approximate the test functions as

$$\delta\boldsymbol{u}^h(\xi,\eta,\zeta) = \sum_{I=1}^{nel} N_I(\xi,\eta,\zeta)\delta\boldsymbol{u}_I, \qquad \delta\theta^h(\xi,\eta,\zeta) = \sum_{I=1}^{nel} N_I(\xi,\eta,\zeta)\delta\theta_I. \tag{4.12}$$

This is called the *Bubnov-Galerkin method*, because above approximations contain the same shape functions as equations (4.9). Note, however, that the test functions do not explicitly depend on time according to definition (4.2). They rather relate to a *fixed* instant of time [102, p. 419]. Next, we approximate the weak form of the balance of linear momentum (4.5) by summing up the contributions of each finite element in the discretized domain,

$$0 = g^{\boldsymbol{u}}(t,\boldsymbol{u},\theta,\boldsymbol{\mathcal{E}}_1,\dots,\boldsymbol{\mathcal{E}}_m,\delta\boldsymbol{u}) \approx \sum_{e=1}^{\mathcal{N}} g_e^{\boldsymbol{u}}\left(t,\boldsymbol{u}^h,\theta^h,\boldsymbol{\mathcal{E}}_1^h,\dots,\boldsymbol{\mathcal{E}}_m^h,\delta\boldsymbol{u}^h\right), \tag{4.13}$$

where individual element contributions are given by

$$g_e^{\boldsymbol{u}}(t,\boldsymbol{u}^h,\theta^h,\boldsymbol{\mathcal{E}}_1^h,\dots,\boldsymbol{\mathcal{E}}_m^h,\delta\boldsymbol{u}^h) = -\int_{\Omega_e}\delta\boldsymbol{E}^h\cdot\boldsymbol{S}^h-\delta\boldsymbol{u}^h\cdot\boldsymbol{B}^h\,dV+\int_{\partial\Omega_e^{\boldsymbol{T}}}\delta\boldsymbol{u}^h\cdot\boldsymbol{T}^h\,dA. \tag{4.14}$$

The same procedure for the thermal weak form (4.8) yields

$$0 = g^{\theta}(t,\boldsymbol{u},\theta,\dot{\boldsymbol{u}},\dot{\theta},\boldsymbol{\mathcal{E}}_1,\dots,\boldsymbol{\mathcal{E}}_m,\delta\theta) \approx \sum_{e=1}^{\mathcal{N}} g_e^{\theta}(t,\boldsymbol{u}^h,\theta^h,\dot{\boldsymbol{u}}^h,\dot{\theta}^h,\boldsymbol{\mathcal{E}}_1^h,\dots,\boldsymbol{\mathcal{E}}_m^h,\delta\theta^h), \tag{4.15}$$

where the variational formulation for a single element reads

$$\begin{aligned}
g_e^{\theta}\left(t,\boldsymbol{u}^h,\theta^h,\dot{\boldsymbol{u}}^h,\dot{\theta}^h,\boldsymbol{\mathcal{E}}_1^h,\dots,\boldsymbol{\mathcal{E}}_m^h,\delta\theta^h\right) = &-\int_{\Omega_e}\delta\theta^h(\rho_0 c\dot{\theta}^h-R^h+\mathcal{H}_{\mathrm{e}}^h+\mathcal{H}_{\mathrm{in}}^h-\mathcal{D}_{\mathrm{int}}^h)\,dV\\
&+\int_{\Omega_e}\mathrm{Grad}\delta\theta^h\cdot\boldsymbol{Q}^h\,dV-\int_{\partial\Omega_e^{\boldsymbol{Q}}}\delta\theta\boldsymbol{Q}^h\cdot\boldsymbol{N}^h\,dA.
\end{aligned} \tag{4.16}$$

Notice that, after spatial integration of equations (4.14) and (4.16), resulting expressions still depend on time t, but no longer on referential position $\boldsymbol{X}^h\in\Omega_e$. In view of the

FEM interpolations (4.11) and (4.12) the element-discrete weak formulations (4.14) and (4.16) are reformulated in a concise vector notation. For the mechanical part this yields

$$g_e^{\boldsymbol{u}}\left(t,\boldsymbol{u}^h,\theta^h,\boldsymbol{\mathcal{E}}_1^h,\dots,\boldsymbol{\mathcal{E}}_m^h,\delta\boldsymbol{u}^h\right)=-\sum_{I=1}^{nel}\delta\boldsymbol{u}_I\cdot(\boldsymbol{f}_I^{\boldsymbol{u}\mathrm{i}}-\boldsymbol{f}_I^{\boldsymbol{u}\mathrm{e}}),\tag{4.17}$$

with the internal and external force vectors according to

$$\boldsymbol{f}^{\boldsymbol{u}\mathrm{i}}_{I(3\times1)}=\int_{\Omega_e}\boldsymbol{B}_I^T\boldsymbol{S}^h\,dV\quad(\text{in N})\quad\text{and}\quad\boldsymbol{f}^{\boldsymbol{u}\mathrm{e}}_{I(3\times1)}=\int_{\Omega_e}N_I\boldsymbol{B}^h\,dV+\int_{\partial\Omega_e^{\boldsymbol{T}}}N_I\boldsymbol{T}^h\,dA\quad(\text{in N}).\tag{4.18}$$

The $\boldsymbol{B}_I(\xi,\eta,\zeta)$-matrices occurring in the internal force vector resulting from the variation of element strains $(4.11)_6$ are standard FEM-related quantities that can be found in any textbook on nonlinear finite element methods, for example [103, p. 124]. On the other hand, the shorthand notation for the thermal part is given by the expression

$$g_e^{\theta}\left(t,\boldsymbol{u}^h,\theta^h,\dot{\boldsymbol{u}}^h,\dot\theta^h,\boldsymbol{\mathcal{E}}_1^h,\dots,\boldsymbol{\mathcal{E}}_m^h,\delta\theta^h\right)=-\sum_{I=1}^{nel}\delta\theta_I\left[\sum_{K=1}^{nel}\left(d_{IK}^{\theta\theta}\dot\theta_K+\boldsymbol{d}_{IK}^{\theta\boldsymbol{u}}\dot{\boldsymbol{u}}_K\right)-(f_I^{\theta\mathrm{i}}-f_I^{\theta\mathrm{e}})\right],\tag{4.19}$$

with the internal and external flux according to

$$\begin{aligned}f^{\theta\mathrm{i}}_{I(1\times1)}&=\int_{\Omega_e}-\boldsymbol{g}_I^T\cdot\boldsymbol{Q}^h+N_I(\mathcal{H}^h_{\mathrm{in}}-\mathcal{D}^h_{\mathrm{int}})\,dV\quad(\text{in W}),\\ f^{\theta\mathrm{e}}_{I(1\times1)}&=\int_{\Omega_e}N_IR^h\,dV-\int_{\partial\Omega_e^{\boldsymbol{Q}}}N_I\boldsymbol{Q}^h\cdot\boldsymbol{N}^h\,dA\quad(\text{in W}),\end{aligned}\tag{4.20}$$

and matrix-like representations for the capacitance and the structural thermoelastic heating

$$\begin{aligned}d^{\theta\theta}_{IK(1\times1)}&=\int_{\Omega_e}N_IN_K\rho_0c\,dV\quad(\text{in J/K}),\\ \boldsymbol{d}^{\theta\boldsymbol{u}}_{IK(1\times3)}&=-\int_{\Omega_e}N_I\theta^h\boldsymbol{M}^h\boldsymbol{B}_K\,dV\quad(\text{in N}).\end{aligned}\tag{4.21}$$

The last expression contains the thermal stress tensor $\boldsymbol{M}(\boldsymbol{X},t)$ defined by equation (3.59) on page 60. The vectors $\boldsymbol{g}_I(\xi,\eta,\zeta)=\frac{\partial N_I}{\partial\boldsymbol{X}}$ in equation $(4.20)_1$ are the thermal counterparts of the $\boldsymbol{B}_I(\xi,\eta,\zeta)$-matrices in the element-related semi-discrete balance of linear momentum. Although we have developed concise notation for the weak formulations through equations (4.17) and (4.19), we can still get rid of the summation notation over element nodes by assembling each finite element contribution using *global* matrix-vector notation. The summation notation is closer to the finite element implementation. However, the formal time integration is best performed using global expressions. We derive these in the following section.

4.1.3. Semi-discretized Initial Boundary Value Problem

Since we are interested in a concise notation of the variational formulation in order to set the stage for the temporal integration in upcoming sections, the following steps aim at a clean matrix-vector notation. To fix ideas, we rewrite the element-wise semi-discrete balance principles (4.17) and (4.19) by taking account of nonzero but otherwise arbitrary virtual quantities, $\delta\theta_I \neq 0$ and $\delta\boldsymbol{u}_I \neq \boldsymbol{0}$, and arrive at

$$\underbrace{\begin{bmatrix} \boldsymbol{d}_e^{\theta\theta} & \boldsymbol{d}_e^{\theta\boldsymbol{u}} \\ \boldsymbol{0} & \boldsymbol{0} \end{bmatrix}}_{\boldsymbol{d}_e} \underbrace{\begin{bmatrix} \dot{\boldsymbol{v}}_e^{\theta} \\ \dot{\boldsymbol{v}}_e^{\boldsymbol{u}} \end{bmatrix}}_{\dot{\boldsymbol{v}}_e} = - \underbrace{\begin{bmatrix} \boldsymbol{f}_e^{\theta\mathrm{i}} - \boldsymbol{f}_e^{\theta\mathrm{e}} \\ \boldsymbol{f}_e^{\boldsymbol{u}\mathrm{i}} - \boldsymbol{f}_e^{\boldsymbol{u}\mathrm{e}} \end{bmatrix}}_{\boldsymbol{f}_e^{\mathrm{i}} - \boldsymbol{f}_e^{\mathrm{e}}}, \tag{4.22}$$

with the element displacement and temperature vectors ($N = nel$)

$$\boldsymbol{v}^{\boldsymbol{u}}_{\mathrm{e}(3N\times 1)} = \begin{bmatrix} \boldsymbol{u}_1 \\ \vdots \\ \boldsymbol{u}_I \\ \vdots \\ \boldsymbol{u}_N \end{bmatrix}, \qquad \boldsymbol{v}^{\theta}_{\mathrm{e}(N\times 1)} = \begin{bmatrix} \theta_1 \\ \vdots \\ \theta_I \\ \vdots \\ \theta_N \end{bmatrix}, \tag{4.23}$$

the element flux and force vectors ($N = nel$),

$$\boldsymbol{f}^{\theta\mathrm{i}}_{\mathrm{e}(N\times 1)} = \begin{bmatrix} f_1^{\theta\mathrm{i}} \\ \vdots \\ f_I^{\theta\mathrm{i}} \\ \vdots \\ f_N^{\theta\mathrm{i}} \end{bmatrix}, \quad \boldsymbol{f}^{\theta\mathrm{e}}_{\mathrm{e}(N\times 1)} = \begin{bmatrix} f_1^{\theta\mathrm{e}} \\ \vdots \\ f_I^{\theta\mathrm{e}} \\ \vdots \\ f_N^{\theta\mathrm{e}} \end{bmatrix}, \quad \boldsymbol{f}^{\boldsymbol{u}\mathrm{i}}_{e(3N\times 1)} = \begin{bmatrix} \boldsymbol{f}_1^{\boldsymbol{u}\mathrm{i}} \\ \vdots \\ \boldsymbol{f}_I^{\boldsymbol{u}\mathrm{i}} \\ \vdots \\ \boldsymbol{f}_N^{\boldsymbol{u}\mathrm{i}} \end{bmatrix}, \quad \boldsymbol{f}^{\boldsymbol{u}\mathrm{e}}_{e(3N\times 1)} = \begin{bmatrix} \boldsymbol{f}_1^{\boldsymbol{u}\mathrm{e}} \\ \vdots \\ \boldsymbol{f}_I^{\boldsymbol{u}\mathrm{e}} \\ \vdots \\ \boldsymbol{f}_N^{\boldsymbol{u}\mathrm{e}} \end{bmatrix}, \tag{4.24}$$

as well as capacitance and structural thermoelastic heating matrices ($N = nel$)

$$\boldsymbol{d}^{\theta\theta}_{e(N\times N)} = \begin{bmatrix} d_{11}^{\theta\theta} & \cdots & d_{1N}^{\theta\theta} \\ & \ddots & \\ \vdots & d_{IK}^{\theta\theta} & \vdots \\ & \ddots & \\ d_{N1}^{\theta\theta} & \cdots & d_{NN}^{\theta\theta} \end{bmatrix}, \quad \boldsymbol{d}^{\theta\boldsymbol{u}}_{e(N\times 3N)} = \begin{bmatrix} \boldsymbol{d}_{11}^{\theta\boldsymbol{u}} & \cdots & \boldsymbol{d}_{1N}^{\theta\boldsymbol{u}} \\ & \ddots & \\ \vdots & \boldsymbol{d}_{IK}^{\theta\boldsymbol{u}} & \vdots \\ & \ddots & \\ \boldsymbol{d}_{N1}^{\theta\boldsymbol{u}} & \cdots & \boldsymbol{d}_{NN}^{\theta\boldsymbol{u}} \end{bmatrix}. \tag{4.25}$$

Next, we assemble individual element equations (4.22) by mapping each nodal point $\boldsymbol{X}_I \in \Omega_e$ onto corresponding global nodes $\boldsymbol{Y}_K \in \Omega^h$ of the finite element mesh and arrive at the global equation system

$$\underbrace{\begin{bmatrix} \mathsf{D}^{\theta\theta} & \mathsf{D}^{\theta\boldsymbol{u}} \\ \mathsf{0} & \mathsf{0} \end{bmatrix}}_{\mathsf{D}} \underbrace{\begin{bmatrix} \dot{\mathsf{V}}^{\theta} \\ \dot{\mathsf{V}}^{\boldsymbol{u}} \end{bmatrix}}_{\dot{\mathsf{V}}} = - \underbrace{\begin{bmatrix} \mathsf{F}^{\theta} \\ \mathsf{F}^{\boldsymbol{u}} \end{bmatrix}}_{\mathsf{F}}, \quad \text{where} \quad \begin{bmatrix} \mathsf{F}^{\theta} \\ \mathsf{F}^{\boldsymbol{u}} \end{bmatrix} = \begin{bmatrix} \mathsf{F}^{\theta}_{\mathrm{i}} - \mathsf{F}^{\theta}_{\mathrm{e}} \\ \mathsf{F}^{\boldsymbol{u}}_{\mathrm{i}} - \mathsf{F}^{\boldsymbol{u}}_{\mathrm{e}} \end{bmatrix}, \tag{4.26}$$

with the global flux and force vectors, global temperature and displacement vectors as well as global capacitance and structural thermoelastic heating matrices given by

$$\begin{aligned} \mathsf{F}^{\theta} &= \mathop{\mathsf{A}}_{e=1}^{\mathcal{N}} [\boldsymbol{f}_e^{\theta\mathrm{i}} - \boldsymbol{f}_e^{\theta\mathrm{e}}], & \mathsf{F}^{\boldsymbol{u}} &= \mathop{\mathsf{A}}_{e=1}^{\mathcal{N}} [\boldsymbol{f}_e^{\boldsymbol{u}\mathrm{i}} - \boldsymbol{f}_e^{\boldsymbol{u}\mathrm{e}}], \\ \mathsf{V}^{\theta} &= \mathop{\mathsf{A}}_{e=1}^{\mathcal{N}} \boldsymbol{v}_e^{\theta}, & \mathsf{V}^{\boldsymbol{u}} &= \mathop{\mathsf{A}}_{e=1}^{\mathcal{N}} \boldsymbol{v}_e^{\boldsymbol{u}}, \\ \mathsf{D}^{\theta\theta} &= \mathop{\mathsf{A}}_{e=1}^{\mathcal{N}} \boldsymbol{d}_e^{\theta\theta}, & \mathsf{D}^{\theta\boldsymbol{u}} &= \mathop{\mathsf{A}}_{e=1}^{\mathcal{N}} \boldsymbol{d}_e^{\theta\boldsymbol{u}}. \end{aligned} \tag{4.27}$$

Finally, the global semi-discretized balance relations are completed with evolution equations for the internal variables as well as initial and boundary conditions to get a precise mathematical problem statement, see Table 4.1. There exist several possibilities as to the numerical time integration of the initial boundary value problem and the general algorithmic treatment of the differential algebraic system of equations [98, 99, 104]. In what follows, the coupled problem is treated as a monolithic entity which is integrated by Runge-Kutta methods.

Semi-discretized initial boundary value problem:

$$\begin{aligned} \mathbf{D}(\mathbf{V}(t),\mathbf{E}(t))\dot{\mathbf{V}}(t) &= -\mathbf{F}(t,\mathbf{V}(t),\mathbf{E}(t),\boldsymbol{\Lambda}(t)),\\ \dot{\mathbf{E}}(t) &= \mathbf{P}(\mathbf{V}(t),\mathbf{E}(t)),\\ \mathbf{0} &= \mathbf{M}\mathbf{V}(t)-\bar{\mathbf{V}}(t). \end{aligned} \tag{4.28}$$

Initial conditions:

$$\mathbf{V}(t_0)=\mathbf{V}_0,\quad \mathbf{E}(t_0)=\mathbf{E}_0,\quad \boldsymbol{\Lambda}(t_0)=\boldsymbol{\Lambda}_0. \tag{4.29}$$

Boundary conditions:

$$\mathbf{V}_b(t)=\bar{\mathbf{V}}(t)\ \forall\, \boldsymbol{X}^h\in\partial\Omega^h_{\boldsymbol{u}}\quad\text{and}\quad \mathbf{F}_e(t)=\bar{\mathbf{F}}(t)\ \forall\, \boldsymbol{X}^h\in\partial\Omega^h_{\boldsymbol{T}}. \tag{4.30}$$

Table 4.1.: Semi-discretized initial boundary value problem to model amorphous polymers through the glass transition region. Equations $(4.28)_1$ represent the global balance equations with *singular* damping matrix $\mathbf{D}(t)$. Equations $(4.28)_2$ and $(4.28)_3$ are evolution equations for the internal variables $\mathbf{E}(t)$ and the prescribed boundary conditions, respectively. The Lagrange multipliers $\boldsymbol{\Lambda}(t)$ represent unknown reaction forces and flux resulting from prescribed displacement and temperature values at the boundary. $\mathbf{M}$ is a filter matrix containing only zeros and ones.

Remark 18. *The balance equations* $(4.28)_1$ *additionally depend on Lagrange multipliers which account for unknown reaction forces and flux. These, however, only occur at global nodes with prescribed displacements or temperature values. If, for example, we assume that global node* $\boldsymbol{Y}_I\in\partial\Omega^h_\theta$ *is assigned a prescribed temperature and* $\boldsymbol{Y}_K\in\partial\Omega^h_{\boldsymbol{u}}$ *a prescribed displacement, the global thermal and mechanical right-hand side vectors* $\mathbf{F}^\theta$ *and* $\mathbf{F}^{\boldsymbol{u}}$ *in equation* (4.26) *look as follows*

$$\mathbf{F}^\theta=\begin{bmatrix} \vdots & & \vdots\\ \mathbf{F}^\theta_{\mathrm{i},I-1} & - & \mathbf{F}^\theta_{\mathrm{e},I-1}\\ \mathbf{F}^\theta_{\mathrm{i},I} & + & \boldsymbol{\lambda}_I\\ \mathbf{F}^\theta_{\mathrm{i},I+1} & - & \mathbf{F}^\theta_{\mathrm{e},I+1}\\ \vdots & & \vdots \end{bmatrix}\quad\text{and}\quad \mathbf{F}^{\boldsymbol{u}}=\begin{bmatrix} \vdots & & \vdots\\ \mathbf{F}^{\boldsymbol{u}}_{\mathrm{i},K-1} & - & \mathbf{F}^{\boldsymbol{u}}_{\mathrm{e},K-1}\\ \mathbf{F}^{\boldsymbol{u}}_{\mathrm{i},K} & + & \boldsymbol{\lambda}_K\\ \mathbf{F}^{\boldsymbol{u}}_{\mathrm{i},K+1} & - & \mathbf{F}^{\boldsymbol{u}}_{\mathrm{e},K+1}\\ \vdots & & \vdots \end{bmatrix}. \tag{4.31}$$

Thus, only entries relating to prescribed boundary conditions contain Lagrange multipliers. Unknown degrees of freedom remain unaffected.

Remark 19. *The global vector of internal variables* $\mathbf{E}(t)$ *in equation* $(4.28)_2$ *formally contains all internal variables of each finite element at every integration point. The*

assembling process starting from an arbitrary integration point to the entire global vector is depicted in the scheme below

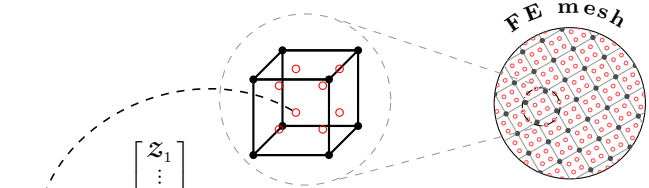

$$\boldsymbol{\mathcal{E}}_{gp,(8m\times 1)} = \begin{bmatrix} \boldsymbol{\mathcal{Z}}_1 \\ \vdots \\ \boldsymbol{\mathcal{Z}}_m \\ \zeta_1 \\ \vdots \\ \zeta_m \\ \chi_1 \\ \vdots \\ \chi_m \end{bmatrix}, \qquad \boldsymbol{e}_{((8m\cdot GP)\times 1)} = \begin{bmatrix} \boldsymbol{\mathcal{E}}_1 \\ \vdots \\ \boldsymbol{\mathcal{E}}_{gp} \\ \vdots \\ \boldsymbol{\mathcal{E}}_{GP} \end{bmatrix}, \qquad \mathbf{E}_{((8m\cdot GP\cdot \mathcal{N})\times 1)} = \begin{bmatrix} \boldsymbol{e}_1 \\ \vdots \\ \boldsymbol{e}_e \\ \vdots \\ \boldsymbol{e}_{\mathcal{N}} \end{bmatrix}, \tag{4.32}$$

where GP denotes the total number of integration points of a finite element.

4.2. Temporal Discretization with DIRK Methods

This section deals with the global algorithm for the time integration of the semi-discretized initial boundary value problem summarized in Table 4.1. In mathematical terms, this type of problem represents a (semi-explicit) *differential-algebraic system of equations* (DAE) of index 1. The differential part consists of the semi-discrete balance of energy and the evolution equations of the internal variables. The semi-discrete balance of linear momentum together with the boundary conditions make up the algebraic part. These are also called *constraint conditions*. Since the DAE system is of index 1, only one differentiation step is required to transform the problem into the underlying system of ordinary differential equations (ODE). In the following sections, we give a short introduction to *diagonally implicit Runge-Kutta methods* (DIRK), followed by detailed steps on the linearization of the nonlinear space-time-discrete DAE system. Finally, we derive the effective system of equations which enables us to translate the global time integration algorithm into high-level computer code.

4.2.1. A Short Introduction to DIRK Methods

Runge-Kutta methods have originally been conceived to solve systems of ordinary differential equations of the form

$$\dot{\boldsymbol{y}}(t) = \boldsymbol{f}(\boldsymbol{y}(t), t), \quad \boldsymbol{y}_0 = \boldsymbol{y}(t_0), \quad t \geq t_0. \tag{4.33}$$

To this end, the continuous time interval $\mathcal{T} \subseteq \mathbb{R}^+$ is first subdivided into a finite number of discrete points in time, $\mathcal{T} = \cup_{n=0}^{N}[t_n, t_{n+1}]$. Next, the attention is given to the isolated time interval $[t_n, t_{n+1}]$ with time step size $\Delta t_n := t_{n+1} - \Delta t_n > 0$. As is typical for one-step methods, the numerical solution $\boldsymbol{y}_n \approx \boldsymbol{y}(t_n)$ at time t_n serves as the starting point to calculate the approximate solution $\boldsymbol{y}_{n+1}$ at time t_{n+1}. In principle, for (diagonally implicit) Runge-Kutta methods there exist two different but equivalent schemes in the

mathematical literature to do so. The first type takes the stage values (displacements, temperatures and internal variables in our specific case) as the unknown quantities, that is

$$\begin{aligned} \boldsymbol{y}_{n+1} &= \boldsymbol{y}_n + \Delta t_n \sum_{i=1}^{s} b_i \, \boldsymbol{f}(t_n + c_i \Delta t_n, \boldsymbol{y}_{n+c_i}), \\ \boldsymbol{y}_{n+c_i} &= \boldsymbol{y}_n + \Delta t_n \sum_{j=1}^{i} a_{ij} \, \boldsymbol{f}(t_n + c_j \Delta t_n, \boldsymbol{y}_{n+c_j}), \qquad i = 1, \dots, s. \end{aligned} \tag{4.34}$$

Thus, the numerical solution at time t_{n+1} is given as a linear combination of function $\boldsymbol{f}$ evaluated with respect to different *stage solutions* $\boldsymbol{y}_{n+c_i}$ with appropriate scheme weights b_i and nodes c_i. The stage solutions in turn have to be determined by solving the generally nonlinear system of equations $(4.34)_2$ with stage weights a_{ij}. The second approach, on the other hand, takes the velocities as the primary unknowns and corresponds to the formulas

$$\begin{aligned} \boldsymbol{y}_{n+1} &= \boldsymbol{y}_n + \Delta t_n \sum_{i=1}^{s} b_i \, \dot{\boldsymbol{y}}_{n+c_i}, \\ \dot{\boldsymbol{y}}_{n+c_i} &= \boldsymbol{f}\left(t_n + c_j \Delta t_n, \boldsymbol{y}_n + \Delta t_n \sum_{j=1}^{i} a_{ij} \, \dot{\boldsymbol{y}}_{n+c_j} \right), \qquad i = 1, \dots, s. \end{aligned} \tag{4.35}$$

The scheme parameters of Runge-Kutta methods are often summarized in so-called *Butcher arrays*, see Table 4.2. In case of DIRK methods the upper triangular matrix is zero and the implicit character of the integration method results from nonzero diagonal elements. Mathematicians choose the scheme parameters such that the method fulfills certain convergence and stability criteria. Naturally, one always has to consider a trade-off between high order of convergence and good stability properties. Adding further stages usually improves both characteristics, but the computational costs increase as well.

c_1	a_{11}	0	0	0
c_2	a_{21}	a_{22}	0	0
c_3	a_{21}	a_{32}	a_{33}	0
c_4	a_{41}	a_{42}	a_{43}	a_{44}
1	b_1	b_2	b_3	b_4

c_1	a_{11}	0	0	0
c_2	a_{21}	a_{22}	0	0
c_3	a_{21}	a_{32}	a_{33}	0
1	b_1	b_2	b_3	b_4
1	b_1	b_2	b_3	b_4

0	0	0	0	0
c_2	a_{21}	a_{22}	0	0
c_3	a_{21}	a_{32}	a_{33}	0
1	b_1	b_2	b_3	b_4
1	b_1	b_2	b_3	b_4

Table 4.2.: Typical Butcher arrays for the class of diagonally implicit Runge-Kutta (DIRK) methods. The first scheme is the most general. The second type represents so-called *stiffly-accurate* DIRK methods, where the parameters of the last stage are equal to the scheme weights. The third variant is an *explicit stiffly-accurate* DIRK method. Here, the solution of the first stage is simply given by the solution of the previous time step.

Strictly speaking, above formulas only apply to systems of ODE's (4.33). An extension to DAE systems of index 1 is nevertheless possible by invoking either the so-called *ε-embedding method* ("direct approach") or the *state space form method* ("indirect approach") [104, chap. 6]. However, a more straightforward procedure for the time discretization in the special case of DIRK methods is feasible by using the formulas relating to ODE's [105] and we will stick to this approach in the sequel. As mentioned earlier, both forms are equivalent, but the first set of formulas (4.34) is closer to typical FEM codes, which generally solve for unknown stage values rather than rates. Hence,

we adopt this approach and reformulate it to be in line with the notation used in preceding sections[4],

$$\begin{aligned} \mathbf{V}_{n+1} &= \mathbf{V}_n + \Delta t_n \sum_{i=1}^{s} b_i \dot{\mathbf{V}}_{n+c_i}, & \mathbf{V}_{n+c_i} &= \mathbf{V}_n + \Delta t_n \sum_{j=1}^{i} a_{ij} \dot{\mathbf{V}}_{n+c_j}, \\ \mathbf{E}_{n+1} &= \mathbf{E}_n + \Delta t_n \sum_{i=1}^{s} b_i \dot{\mathbf{E}}_{n+c_i}, & \mathbf{E}_{n+c_i} &= \mathbf{E}_n + \Delta t_n \sum_{j=1}^{i} a_{ij} \dot{\mathbf{E}}_{n+c_j}, \end{aligned} \tag{4.36}$$

where $i = 1, \dots, s$. From the equations on the right we can extract the velocities of the ith stage,

$$\left.\begin{aligned} \dot{\mathbf{V}}_{n+c_i} &= \frac{\mathbf{V}_{n+c_i} - \mathbf{V}_n}{a_{ii}\Delta t_n} - \frac{1}{a_{ii}} \sum_{j=1}^{i-1} a_{ij} \dot{\mathbf{V}}_{n+c_j}, \\ \dot{\mathbf{E}}_{n+c_i} &= \frac{\mathbf{E}_{n+c_i} - \mathbf{E}_n}{a_{ii}\Delta t_n} - \frac{1}{a_{ii}} \sum_{j=1}^{i-1} a_{ij} \dot{\mathbf{E}}_{n+c_j}, \end{aligned}\right\} \quad i = 1, \dots, s, \tag{4.37}$$

which will eventually enter the semi-discrete DAE system defined in Table 4.1 to yield the corresponding space-time-discrete version summarized in Table 4.3. Note, however, that this derivation rather works with DIRK methods. Fully implicit Runge-Kutta methods (FIRK) would require the inverse of the coefficient matrix a_{ij} to derive similar algebraic relations for the velocities, since all stages are interdependent. Nonetheless, FIRK methods produce large systems of equations, which render them impractical for common FEM applications. DIRK methods, on the other hand, allow for a sequential evaluation of individual stages rather than one huge implicit system. In the next section we seek for an iterative solution procedure to solve the nonlinear DAE system.

Remark 20. *One problem associated with the solution of stiff ODE's using Runge-Kutta methods is related to the phenomenon of order reduction [106–108]. That is, the theoretical results on the convergence order of a Runge-Kutta method may fail for very stiff problems. This empirical observation directly translates to DAE's, which may be seen as the limit case of very stiff ODE's. Things get worse when the ODE system stems from the spatial discretization of initial boundary values problems [109]. The degree of order reduction depends on the type of problem being integrated, the type of boundary condition being applied and the spatial smoothness of the solution [109, p. 39]. As [106, 110] pointed out, stiffly-accurate Runge-Kutta methods are less affected by order reduction. These methods should always be preferred for very stiff problems.*

4.2.2. Linearization of the Space-Time-Discrete DAE System

In order to implement diagonally implicit Runge-Kutta methods into typical FEM software, we resort to iterative procedures such as the Newton-Raphson method to solve the nonlinear system of differential-algebraic equations given in Table 4.3. There are generally two distinct approaches to do so [105, 111]. The first approach applies the Newton-Raphson method to the entire DAE system and uses order reduction techniques [112] such as static condensation to eliminate constitutive equations from the global system of equations. The second approach, on the other hand, is based on the *implicit*

[4] Actually, these formulas seem like a mixture of both, since, for example, equation $(4.36)_1$ resembles $(4.35)_1$, while equation $(4.36)_2$ is similar to $(4.34)_2$. However, we still seek for the solution of unknown stage solutions rather than velocities.

Space-time-discrete initial boundary value problem:

$$\left.\begin{aligned} \mathbf{D}\left(\mathbf{V}_{n+c_i}, \mathbf{E}_{n+c_i}\right)\dot{\mathbf{V}}_{n+c_i} &= -\mathbf{F}\left(t_{n+c_i}, \mathbf{V}_{n+c_i}, \mathbf{E}_{n+c_i}, \mathbf{\Lambda}_{n+c_i}\right), \\ \dot{\mathbf{E}}_{n+c_i} &= \mathbf{P}\left(\mathbf{V}_{n+c_i}, \mathbf{E}_{n+c_i}\right), \\ \mathbf{0} &= \mathbf{M}\mathbf{V}_{n+c_i} - \bar{\mathbf{V}}_{n+c_i}, \end{aligned}\right\} \quad i = 1, \dots, s. \tag{4.38}$$

Initial conditions:

$$\mathbf{V}(t_n) = \mathbf{V}_n, \qquad \mathbf{E}(t_n) = \mathbf{E}_n, \qquad \mathbf{\Lambda}(t_n) = \mathbf{\Lambda}_n. \tag{4.39}$$

Boundary conditions:

$$\begin{aligned} \mathbf{V}_b\left(t_{n+c_i}\right) &= \bar{\mathbf{V}}\left(t_{n+c_i}\right) \;\; \forall\, \boldsymbol{X}^h \in \partial\Omega^h_{\boldsymbol{u}} \quad \text{and} \\ \mathbf{F}_e\left(t_{n+c_i}\right) &= \bar{\mathbf{F}}\left(t_{n+c_i}\right) \;\; \forall\, \boldsymbol{X}^h \in \partial\Omega^h_{\boldsymbol{T}}. \end{aligned} \tag{4.40}$$

Table 4.3.: Space-time-discrete initial boundary value problem in terms of an s-stage DIRK method. Equation $(4.38)_1$ represent the discrete global balance equations with *singular* damping matrix $\mathbf{D}_{n+c_i}$. Equations $(4.38)_2$ and $(4.38)_3$ are evolution equations for the internal variables $\mathbf{E}_{n+c_i}$ and the prescribed boundary conditions, respectively. The rate vectors in the first two equations are given by expressions (4.37).

function theorem and uses the *state space form* mentioned earlier. Here, the unknown internal variables are replaced by a functional relationship in the neighborhood of the solution of (4.28). This additionally requires the application of the DIRK scheme on the (local) integration point level resulting in a nested iterative solution procedure (also known as the "Multilevel Newton method"). The second approach is usually applied in common FEM codes, but we opt for the first in order to spare the local iterations. The inherent drawback of this technique is that the internal variables need to be updated at each integration point after each global iteration, see [111] for an in-depth discussion. We begin with the linearization of the discrete balance equations.

Linearization of the Discrete Balance Equations

Insertion of the displacement and temperature rates $(4.37)_1$ into the space-time-discrete balance equations $(4.38)_1$ yields

$$\begin{aligned} \mathbf{0} &= \mathbf{D}\left(\mathbf{V}_{n+c_i}, \mathbf{E}_{n+c_i}\right)\dot{\mathbf{V}}_{n+c_i} + \mathbf{F}\left(t_{n+c_i}, \mathbf{V}_{n+c_i}, \mathbf{E}_{n+c_i}, \mathbf{\Lambda}_{n+c_i}\right) \\ &= \mathbf{D}\left(\mathbf{V}_{n+c_i}, \mathbf{E}_{n+c_i}\right)\left(\frac{\mathbf{V}_{n+c_i} - \mathbf{V}_n}{a_{ii}\Delta t_n} - \frac{1}{a_{ii}}\sum_{j=1}^{i-1} a_{ij}\dot{\mathbf{V}}_{n+c_j}\right) + \mathbf{F}\left(t_{n+c_i}, \mathbf{V}_{n+c_i}, \mathbf{E}_{n+c_i}, \mathbf{\Lambda}_{n+c_i}\right) \\ &=: \mathbf{G}\left(t_{n+c_i}, \mathbf{V}_{n+c_i}, \mathbf{E}_{n+c_i}, \mathbf{\Lambda}_{n+c_i}\right), \qquad i = 1, \dots, s, \end{aligned} \tag{4.41}$$

where $\mathbf{G}_{n+c_i}$ is the global residual of the balance equations. Next, by iterating from time step t_n to stage node $t_n + c_i\Delta t_n$ of the ith stage, we obtain the stage solution

$\mathbf{V}_{n+c_i}$. The current iteration in the linearization of the residual $\mathbf{G}_{n+c_i}$ is indicated by superscripts $(\bullet)^j$ as

$$\begin{aligned}\mathbf{0} &= \mathbf{G}\left(t_{n+c_i}, \mathbf{V}^{j+1}_{n+c_i}, \mathbf{E}^{j+1}_{n+c_i}, \boldsymbol{\Lambda}^{j+1}_{n+c_i}\right)\\ &= \mathbf{G}\left(t_{n+c_i}, \mathbf{V}^{j}_{n+c_i} + \Delta\mathbf{V}^{j}_{n+c_i}, \mathbf{E}^{j}_{n+c_i} + \Delta\mathbf{E}^{j}_{n+c_i}, \boldsymbol{\Lambda}^{j}_{n+c_i} + \Delta\boldsymbol{\Lambda}^{j}_{n+c_i}\right)\\ &\approx \mathbf{G}^j_{n+c_i} + \frac{\partial \mathbf{G}^j_{n+c_i}}{\partial \mathbf{V}_{n+c_i}}\Delta\mathbf{V}^j_{n+c_i} + \frac{\partial \mathbf{G}^j_{n+c_i}}{\partial \mathbf{E}_{n+c_i}}\Delta\mathbf{E}^j_{n+c_i} + \frac{\partial \mathbf{G}^j_{n+c_i}}{\partial \boldsymbol{\Lambda}_{n+c_i}}\Delta\boldsymbol{\Lambda}^j_{n+c_i}.\end{aligned} \tag{4.42}$$

Thus, we arrive at an incremental version of the global balance relations,

$$\frac{\partial \mathbf{G}^j_{n+c_i}}{\partial \mathbf{V}_{n+c_i}}\Delta\mathbf{V}^j_{n+c_i} - \frac{\partial \mathbf{G}^j_{n+c_i}}{\partial \mathbf{E}_{n+c_i}}\Delta\mathbf{E}^j_{n+c_i} - \frac{\partial \mathbf{G}^j_{n+c_i}}{\partial \boldsymbol{\Lambda}_{n+c_i}}\Delta\boldsymbol{\Lambda}^j_{n+c_i} = -\mathbf{G}^j_{n+c_i}, \tag{4.43}$$

where the partial derivatives follow from the global residual (4.41),

$$\begin{aligned}\frac{\partial \mathbf{G}^j_{n+c_i}}{\partial \mathbf{V}_{n+c_i}} &= \frac{1}{a_{ii}\Delta t_n}\mathbf{D}^j_{n+c_i} + \frac{\partial \mathbf{F}^j_{n+c_i}}{\partial \mathbf{V}_{n+c_i}} + \frac{\partial \mathbf{D}^j_{n+c_i}}{\partial \mathbf{V}_{n+c_i}}\dot{\mathbf{V}}^j_{n+c_i},\\ \frac{\partial \mathbf{G}^j_{n+c_i}}{\partial \mathbf{E}_{n+c_i}} &= \frac{\partial \mathbf{F}^j_{n+c_i}}{\partial \mathbf{E}_{n+c_i}} + \frac{\partial \mathbf{D}^j_{n+c_i}}{\partial \mathbf{E}_{n+c_i}}\dot{\mathbf{V}}^j_{n+c_i},\\ \frac{\partial \mathbf{G}^j_{n+c_i}}{\partial \boldsymbol{\Lambda}_{n+c_i}} &= \frac{\partial \mathbf{F}^j_{n+c_i}}{\partial \boldsymbol{\Lambda}_{n+c_i}}.\end{aligned} \tag{4.44}$$

The update of global displacement and temperature values after each iteration reads

$$\mathbf{V}^{j+1}_{n+c_i} = \mathbf{V}^j_{n+c_i} + \Delta\mathbf{V}^j_{n+c_i}, \qquad \mathbf{V}^0_{n+c_i} = \mathbf{V}_n \quad (n \geq 0). \tag{4.45}$$

Next, we continue in the same manner with the evolution equations of the internal variables.

Linearization of the Constitutive Equations

Insertion of the rate approximations for the internal variables $(4.37)_2$ into the space-time-discrete constitutive equations $(4.38)_2$ yields

$$\begin{aligned}\mathbf{0} = \dot{\mathbf{E}}\left(t_{n+c_i}\right) - \mathbf{P}\left(\mathbf{V}_{n+c_i}, \mathbf{E}_{n+c_i}\right) &= \frac{\mathbf{E}_{n+c_i} - \mathbf{E}_n}{a_{ii}\Delta t_n} - \frac{1}{a_{ii}}\sum_{j=1}^{i-1} a_{ij}\dot{\mathbf{E}}_{n+c_j} - \mathbf{P}\left(\mathbf{V}_{n+c_i}, \mathbf{E}_{n+c_i}\right)\\ &=: \mathbf{L}\left(\mathbf{V}_{n+c_i}, \mathbf{E}_{n+c_i}\right), \qquad i = 1, \dots, s,\end{aligned} \tag{4.46}$$

where $\mathbf{L}_{n+c_i}$ denotes the residual of the constitutive equations. Next, we iterate from time step t_n to stage node $t_n + c_i\Delta t_n$ to obtain the stage solutions for the internal variables $\mathbf{E}_{n+c_i}$. As per usual, superscripts $(\bullet)^j$ indicate the current iteration in the linearization of the residual $\mathbf{L}_{n+c_i}$,

$$\begin{aligned}\mathbf{0} = \mathbf{L}\left(\mathbf{V}^{j+1}_{n+c_i}, \mathbf{E}^{j+1}_{n+c_i}\right) &= \mathbf{L}\left(\mathbf{V}^{j}_{n+c_i} + \Delta\mathbf{V}^{j}_{n+c_i}, \mathbf{E}^{j}_{n+c_i} + \Delta\mathbf{E}^{j}_{n+c_i}\right)\\ &\approx \mathbf{L}^j_{n+c_i} + \frac{\partial \mathbf{L}^j_{n+c_i}}{\partial \mathbf{V}_{n+c_i}}\Delta\mathbf{V}^j_{n+c_i} + \frac{\partial \mathbf{L}^j_{n+c_i}}{\partial \mathbf{E}_{n+c_i}}\Delta\mathbf{E}^j_{n+c_i}.\end{aligned} \tag{4.47}$$

Thus, we arrive at an incremental version for the constitutive relations of the internal variables,

$$\frac{\partial \mathbf{L}^j_{n+c_i}}{\partial \mathbf{V}_{n+c_i}} \Delta \mathbf{V}^j_{n+c_i} + \frac{\partial \mathbf{L}^j_{n+c_i}}{\partial \mathbf{E}_{n+c_i}} \Delta \mathbf{E}^j_{n+c_i} = -\mathbf{L}^j_{n+c_i}. \tag{4.48}$$

The partial derivatives are not required at this point, since the evolution equations will soon be eliminated by applying model order reduction techniques. Their calculation is therefore postponed to Section 5.2. As before, after each global iteration follows the mandatory update of all internal variables,

$$\mathbf{E}^{j+1}_{n+c_i} = \mathbf{E}^j_{n+c_i} + \Delta \mathbf{E}^j_{n+c_i}, \qquad \mathbf{E}^0_{n+c_i} = \mathbf{E}_n \quad (n \geq 0). \tag{4.49}$$

Finally, the boundary conditions will be linearized.

Linearization of the Boundary Conditions

First, we define the global residual for the space-time-discrete boundary condition $(4.38)_3$,

$$\mathbf{0} = \mathbf{M}\mathbf{V}_{n+c_i} - \bar{\mathbf{V}}_{n+c_i} =: \mathbf{B}(t_{n+c_i}, \mathbf{V}_{n+c_i}), \qquad i = 1, \dots, s. \tag{4.50}$$

The linearization of the residual follows in the usual manner using the superscript notation,

$$\mathbf{0} \approx \mathbf{B}(t_{n+c_i}, \mathbf{V}^{j+1}_{n+c_i}) = \mathbf{B}(t_{n+c_i}, \mathbf{V}^j_{n+c_i} + \Delta \mathbf{V}^j_{n+c_i}) \approx \mathbf{B}^j_{n+c_i} + \frac{\partial \mathbf{B}^j_{n+c_i}}{\partial \mathbf{V}_{n+c_i}} \Delta \mathbf{V}^j_{n+c_i}. \tag{4.51}$$

Now, the incremental version of the boundary conditions is given in terms of the filter matrix $\mathbf{M}$ by partial differentiation of (4.50), that is

$$\frac{\partial \mathbf{B}^j_{n+c_i}}{\partial \mathbf{V}_{n+c_i}} \Delta \mathbf{V}^j_{n+c_i} = -\mathbf{B}^j_{n+c_i}, \quad \text{where} \quad \frac{\partial \mathbf{B}^j_{n+c_i}}{\partial \mathbf{V}_{n+c_i}} = \mathbf{M}. \tag{4.52}$$

Updating the boundary conditions is only necessary in the first iteration, since the increments are already known beforehand. Nevertheless, we keep to the same notation as usual,

$$\mathbf{B}^{j+1}_{n+c_i} = \mathbf{B}^j_{n+c_i} + \Delta \mathbf{B}^j_{n+c_i}, \qquad \mathbf{B}^0_{n+c_i} = \mathbf{B}_n \quad (n \geq 0). \tag{4.53}$$

In the next stage, we collect all three linearizations to establish the global Newton-Raphson scheme.

Global Newton-Raphson Algorithm

Summarizing equations (4.43), (4.48) and $(4.52)_1$ yields the inremental version of the global DAE system to iterate from time step t_n to the ith stage node $t_n + c_i \Delta t_n$ using

$$\begin{bmatrix} \frac{\partial \mathbf{G}}{\partial \mathbf{V}} & \frac{\partial \mathbf{G}}{\partial \mathbf{E}} & \frac{\partial \mathbf{G}}{\partial \mathbf{\Lambda}} \\ \frac{\partial \mathbf{L}}{\partial \mathbf{V}} & \frac{\partial \mathbf{L}}{\partial \mathbf{E}} & \mathbf{0} \\ \frac{\partial \mathbf{B}}{\partial \mathbf{V}} & \mathbf{0} & \mathbf{0} \end{bmatrix}^j_{n+c_i} \begin{bmatrix} \Delta \mathbf{V} \\ \Delta \mathbf{E} \\ \Delta \mathbf{\Lambda} \end{bmatrix}^j_{n+c_i} = - \begin{bmatrix} \mathbf{G} \\ \mathbf{L} \\ \mathbf{B} \end{bmatrix}^j_{n+c_i}, \qquad i = 1, \dots, s. \tag{4.54}$$

After solving the linear system of equations for the jth iteration follows the update of all quantities using the formulas

$$\mathbf{V}_{n+c_i}^{j+1} = \mathbf{V}_{n+c_i}^{j} + \Delta\mathbf{V}_{n+c_i}^{j}, \quad \mathbf{E}_{n+c_i}^{j+1} = \mathbf{E}_{n+c_i}^{j} + \Delta\mathbf{E}_{n+c_i}^{j}, \quad \boldsymbol{\Lambda}_{n+c_i}^{j+1} = \boldsymbol{\Lambda}_{n+c_i}^{j} + \Delta\boldsymbol{\Lambda}_{n+c_i}^{j}. \tag{4.55}$$

In accordance with the typical structure of FEM codes, it is convenient to distinguish between *primary* unknowns, that is global displacements, temperatures and reaction forces and flux, as well as *secondary* unknowns, represented by the internal variables. Generally, the latter are evaluated at (local) integration point level. Thus, in the sequel we will eliminate the secondary unknowns from the system of equations (4.54) by means of model order reduction techniques [112] and thereby derive the effective system of equations.

4.2.3. Static Condensation and Effective System of Equations

Invoking the linearized equation for the global vector of internal variables (4.48) enables us to determine the increments $\Delta\mathbf{E}$ of the jth iteration in terms of the residual $\mathbf{L}$ and the increments of primary unknowns $\Delta\mathbf{V}$ as

$$\Delta\mathbf{E}_{n+c_i}^{j} = -\left[\frac{\partial\mathbf{L}_{n+c_i}^{j}}{\partial\mathbf{E}_{n+c_i}}\right]^{-1}\left(\mathbf{L}_{n+c_i}^{j} + \frac{\partial\mathbf{L}_{n+c_i}^{j}}{\partial\mathbf{V}_{n+c_i}}\Delta\mathbf{V}_{n+c_i}^{j}\right), \quad i = 1, \dots, s. \tag{4.56}$$

Substitution of above expression into the iterative procedure (4.54) to reduce the global system such that it contains only primary unknowns and unknown reaction forces and flux yields

$$\begin{bmatrix} \frac{\partial\mathbf{G}}{\partial\mathbf{V}} - \frac{\partial\mathbf{G}}{\partial\mathbf{E}}\left[\frac{\partial\mathbf{L}}{\partial\mathbf{E}}\right]^{-1}\frac{\partial\mathbf{L}}{\partial\mathbf{V}} & \frac{\partial\mathbf{G}}{\partial\boldsymbol{\Lambda}} \\ \frac{\partial\mathbf{B}}{\partial\mathbf{V}} & \mathbf{0} \end{bmatrix}_{n+c_i}^{j} \begin{bmatrix}\Delta\mathbf{V} \\ \Delta\boldsymbol{\Lambda}\end{bmatrix}_{n+c_i}^{j} = \begin{bmatrix} -\mathbf{G} + \frac{\partial\mathbf{G}}{\partial\mathbf{E}}\left[\frac{\partial\mathbf{L}}{\partial\mathbf{E}}\right]^{-1}\mathbf{L} \\ -\mathbf{B} \end{bmatrix}_{n+c_i}^{j}. \tag{4.57}$$

It is convenient to shorten the notation by defining $\mathbf{K} := \frac{\partial\mathbf{G}}{\partial\mathbf{V}} - \frac{\partial\mathbf{G}}{\partial\mathbf{E}}\left[\frac{\partial\mathbf{L}}{\partial\mathbf{E}}\right]^{-1}\frac{\partial\mathbf{L}}{\partial\mathbf{V}}$ for the upper left part of the matrix and $\mathbf{R} := -\mathbf{G} + \frac{\partial\mathbf{G}}{\partial\mathbf{E}}\left[\frac{\partial\mathbf{L}}{\partial\mathbf{E}}\right]^{-1}\mathbf{L}$ for the residual. Furthermore, we make use of the derivative $(4.52)_2$ and the fact that $\mathbf{M}^T = \frac{\partial\mathbf{G}}{\partial\boldsymbol{\Lambda}}$, since Lagrange multipliers (reaction forces and flux) only occur in those equations which are subject to prescribed boundary conditions, see also Remark 18 on page 81. Using these abbreviations results in the compact form

$$\begin{bmatrix}\mathbf{K} & \mathbf{M}^T \\ \mathbf{M} & \mathbf{0}\end{bmatrix}_{n+c_i}^{j} \begin{bmatrix}\Delta\mathbf{V} \\ \Delta\boldsymbol{\Lambda}\end{bmatrix}_{n+c_i}^{j} = -\begin{bmatrix}\mathbf{R} \\ \mathbf{B}\end{bmatrix}_{n+c_i}^{j}. \tag{4.58}$$

To obtain the effective system of equations containing only the unknown quantities requires a split into free and fixed degrees of freedom. To this end, the global vector of primary unknowns is formally partitioned into the vector of unknowns $\mathbf{U}$ and prescribed values $\mathbf{V}_\mathrm{p}$. Consequently, the filter matrix $\mathbf{M}$ assumes the simple form shown below

$$\mathbf{V} = \begin{bmatrix}\mathbf{U} \\ \mathbf{V}_\mathrm{p}\end{bmatrix} \quad \Rightarrow \quad \mathbf{M} = [\mathbf{0} \;\; \mathbf{1}]. \tag{4.59}$$

Substitution of the partitioned vector and the filter matrix into the system of equations (4.58) gives

$$\begin{bmatrix} \mathbf{K}_{\text{eff}} & \mathbf{K}_{\text{up}} & \mathbf{0} \\ \mathbf{K}_{\text{pu}} & \mathbf{K}_{\text{pp}} & \mathbf{1} \\ \mathbf{0} & \mathbf{1} & \mathbf{0} \end{bmatrix}^{j}_{n+c_i} \begin{bmatrix} \Delta\mathbf{U} \\ \Delta\mathbf{V}_{\text{p}} \\ \Delta\boldsymbol{\Lambda} \end{bmatrix}^{j}_{n+c_i} = - \begin{bmatrix} \mathbf{R}_{\text{eff}} \\ \mathbf{R}_{\text{p}} \\ \mathbf{B} \end{bmatrix}^{j}_{n+c_i}. \tag{4.60}$$

Above expression contains submatrices and subvectors of matrix $\mathbf{K}$ and $\mathbf{R}$, respectively, corresponding to the partition (4.59). Now, in the *first* iteration ($j = 0$) at time step t_{n+c_i} we usually set $\mathbf{V}^0_{\text{p},n+c_i} = \bar{\mathbf{V}}(t_n) = \bar{\mathbf{V}}_n$ according to the specified boundary conditions (4.40). Then, from equation $(4.60)_3$ and the definition (4.50) as well as equation $(4.60)_1$, it follows that

$$\Delta\mathbf{V}^0_{\text{p},n+c_i} = \bar{\mathbf{V}}(t_{n+c_i}) - \bar{\mathbf{V}}_n = \bar{\mathbf{V}}_{n+c_i} - \bar{\mathbf{V}}_n, \tag{4.61}$$

$$\mathbf{K}^0_{\text{eff},n+c_i}\Delta\mathbf{U}^0_{n+c_i} = -\mathbf{R}^0_{\text{eff},n+c_i} - \mathbf{K}^0_{\text{up},n+c_i}\Delta\mathbf{V}^0_{\text{p},n+c_i}. \tag{4.62}$$

On the other hand, for *subsequent* iterations ($j \geq 1$) we set $\mathbf{V}^j_{\text{p},n+c_i} = \bar{\mathbf{V}}(t_{n+c_i}) = \bar{\mathbf{V}}_{n+c_i}$ (prescribed nodal values). In this case the system of equations (4.60) reduces to

$$\begin{aligned} \Delta\mathbf{V}^j_{\text{p},n+c_i} &= \mathbf{0}, \\ \mathbf{K}^j_{\text{eff},n+c_i}\Delta\mathbf{U}^j_{n+c_i} &= -\mathbf{R}^j_{\text{eff},n+c_i}, \\ \mathbf{K}^j_{\text{pu},n+c_i}\Delta\mathbf{U}^j_{n+c_i} + \Delta\boldsymbol{\Lambda}^j_{n+c_i} &= -\mathbf{R}^j_{\text{p},n+c_i} = -\boldsymbol{\Lambda}^j_{n+c_i} - \mathbf{F}^{\text{i}}_{n+c_i}. \end{aligned} \tag{4.63}$$

Clearly, when the solution has converged the left hand side of $(4.63)_3$ vanishes, resulting in the reaction forces and flux $\boldsymbol{\Lambda}_{n+c_i} = -\mathbf{F}^{\text{i}}_{n+c_i}$. The second equation, on the other hand, corresponds to the *effective system of equations*,

$$\left.\begin{aligned} \mathbf{K}^j_{\text{eff},n+c_i}\Delta\mathbf{U}^j_{n+c_i} &= -\mathbf{R}^j_{\text{eff},n+c_i}, \\ \mathbf{U}^{j+1}_{n+c_i} &= \mathbf{U}^j_{n+c_i} + \Delta\mathbf{U}^j_{n+c_i}, \\ \mathbf{U}^0_{n+c_i} &= \mathbf{U}_n, \end{aligned}\right\} \quad i = 1, \dots, s. \tag{4.64}$$

Here, the *effective stiffness matrix* and the *effective residual vector* for the time step $t_{n+c_i}, i = 1, \dots, s$, and the jth iteration follow from the definition of the matrix $\mathbf{K}$ and the vector $\mathbf{R}$ in equation (4.58) and the derivatives (4.44), leading to

$$\begin{aligned} \mathbf{K}^j_{\text{eff},n+c_i} &= \left[\frac{1}{a_{ii}\Delta t_n}\mathbf{D} + \frac{\partial\mathbf{F}}{\partial\mathbf{V}} + \frac{\partial\mathbf{D}}{\partial\mathbf{V}}\dot{\mathbf{V}} - \left(\frac{\partial\mathbf{F}}{\partial\mathbf{E}} + \frac{\partial\mathbf{D}}{\partial\mathbf{E}}\dot{\mathbf{V}}\right)\left[\frac{\partial\mathbf{L}}{\partial\mathbf{E}}\right]^{-1}\frac{\partial\mathbf{L}}{\partial\mathbf{V}}\right]^{j}_{n+c_i}, \\ \mathbf{R}^j_{\text{eff},n+c_i} &= \left[\mathbf{F} + \mathbf{D}\dot{\mathbf{V}} - \left(\frac{\partial\mathbf{F}}{\partial\mathbf{E}} + \frac{\partial\mathbf{D}}{\partial\mathbf{E}}\dot{\mathbf{V}}\right)\left[\frac{\partial\mathbf{L}}{\partial\mathbf{E}}\right]^{-1}\mathbf{L}\right]^{j}_{n+c_i}. \end{aligned} \tag{4.65}$$

The unsymmetric effective stiffness matrix is also called the *global iteration matrix* (or *matrix pencil* in mathematical terms). Notice that the time step size Δt_n directly affects the iteration matrix and, therefore, the condition of the linear system of equations. Further note that the effective stiffness matrix is the same as in the Multilevel Newton scheme, but the effective residual is not. It contains extra terms steming from the residual $\mathbf{L}$ of the internal variables. These are eventually calculated at (local) integration

point level, which implies the solution of a linear system of equations[5]. This circumvents local iterations in case of nonlinear constitutive relations. The drawback of this approach is that local updates of internal variables $(4.55)_2$ after each global iteration become necessary. We have implemented several DIRK schemes into the finite element program `FEAP`, ranging from first to fourth order of convergence with differing stability properties, see Table 4.4. Some of them include an explicit first stage, which increases the order of consistency by one at no additional cost. Some of the DIRK variants feature an embedded method as a cheap error estimator for automatic step size control. This will be discussed in the following section.

4.3. Adaptive Step Size Controller

The numerical solution of transient initial boundary value problems demands the application of automatic time-stepping procedures. There are several reasons supporting this, for example:

- the time step size should be as large as possible for simulation times spanning long duration and at the same time as small as necessary to keep to the accuracy requirements,
- it is preferable to spare the additional effort stemming from manual readjustments of the time step size, especially when this happens on top of manual mesh refinement procedures usually implied by FEM computations,
- the solution may exhibit strong variations in its properties, requiring drastic step size changes,
- the evolution of the temperature and the internal variables should be controlled in such a way that one can at least estimate the resulting time integration error to produce reasonable numerical results,
- stiff computations rely on implicit methods, which implies an iterative solution process of nonlinear equations. The convergence rate of such iterations is affected by the step size, and step size changes entail matrix factorizations [116],
- to obtain an improved quality of the numerical solution in terms of better smoothness achieved by smoother step size changes as well as increased computational stability [116].

In what follows, we begin with the classical approach to automatic time-stepping. Afterwards, we supplement more rigorous approaches using control theoretic aspects. These do not receive by far the attention they deserve compared with the classical approach. However, an in-depth discussion of the underlying control theory is beyond this thesis. Instead, we refer to the literature cited below.

4.3.1. The Classical Approach

Runge-Kutta methods are often furnished with another set of scheme weights $\tilde{b}_i$ to allow for an efficient error estimation in order to adjust the step size automatically. The new scheme weights imply an *embedded method* with a different order of consistency than the base method and, therefore, provides a simple means to estimate the integration

[5] This is only indicated symbolically using the inverse function $[\bullet]^{-1}$ in equation (4.65).

Method	Stages	Variant	Stage order	Order of convergence	Stability				Stiffly-accurate	Embedded time-stepping	Reference
					A	B	BN	L			
Radau-IIA	1	SDIRK	1	1	✓	✓	✓	✓	✓		
RK-Gauss	1	SDIRK	1	1	✓	✓					
Lobatto-IIIA	2	ESDIRK	2	2	✓				✓		
4	2	SDIRK	1	3	✓			✓			[109, p. 73]
5	2	SDIRK	1	2	✓			✓	✓	✓	[109, p. 72]
ESDIRK12	2	ESDIRK	1	1(2)	✓(✓)	✓(✗)	✓(✗)	✓(✗)	✓(✗)	✓	[113, p. 11]
7	3	SDIRK	1	3	✓	✓		✓	✓	✓	[109, p. 77]
8	3	SDIRK	1	4	✓			✓			[109, p. 78]
9	3	EDIRK	2	3	✓	✓			✓		[109, p. 70]
ESDIRK23	3	ESDIRK	2	2(3)	✓(✗)			✓(✗)	✓(✗)	✓	[113, p. 13]
DIRK2PR	3	SDIRK	1	2(3)	✓(✓)			✓(✓)	✓(✓)	✓	[114, p. 13]
12	4	EDIRK	2	4	✓				✓		[109, p. 70]
ESDIRK34	4	ESDIRK	2	3(4)	✓(✗)			✓(✗)	✓(✗)	✓	[113, p. 16]
14	4	SDIRK	2	3	✓			✓	✓	✓	[109, p. 82]

Table 4.4.: Summary of different DIRK variants implemented in the in-house FEM code `FEAP` to solve initial boundary value problems. SDIRK stands for *singly diagonally implicit Runge-Kutta method*, an additional E refers to an explicit first stage. Parenthesized values pertain to the error estimator. Order of convergence and stability properties apply to classic (non-stiff) ODE theories. *Stiffly-accurate* methods should be preferred in FEM codes, since they are not overly affected by order reduction in case of stiff problems, see Remark 20. The highest order of consistency of an s-stage SDIRK method is $s+1$ [115, p. 247]. The highest stage-order of an ESDIRK method is at most 2 [106, p. 1124]. The highest order of convergence of a four-stage, stiffly-accurate, L-stable SDIRK method is 3.

error during a time step [117, p. 198],[118, p. 165]. Specifically, we assume the base method

$$\boldsymbol{y}_{n+1} = \boldsymbol{y}_n + \Delta t_n \sum_{i=1}^{s} b_i \, \boldsymbol{f}\left(t_n + c_i \Delta t_n, \boldsymbol{y}_{n+c_i}\right) \quad \text{and} \quad ||\boldsymbol{y}_{n+1} - \boldsymbol{y}(t_{n+1})|| = \mathcal{O}\left(\Delta t_n^{p+1}\right), \tag{4.66}$$

is of order p, while the embedded method shall be of order q, that is

$$\tilde{\boldsymbol{y}}_{n+1} = \boldsymbol{y}_n + \Delta t_n \sum_{i=1}^{s} \tilde{b}_i \, \boldsymbol{f}\left(t_n + c_i \Delta t_n, \boldsymbol{y}_{n+c_i}\right) \quad \text{and} \quad ||\tilde{\boldsymbol{y}}_{n+1} - \boldsymbol{y}(t_{n+1})|| = \mathcal{O}\left(\Delta t_n^{q+1}\right). \tag{4.67}$$

Hence, we can estimate the *local truncation error* from $(4.66)_1$ and $(4.67)_1$ simply as

$$\widehat{\boldsymbol{e}}_{n+1} \approx \tilde{\boldsymbol{y}}_{n+1} - \boldsymbol{y}_{n+1} = \Delta t_n \sum_{i=1}^{s} (\tilde{b}_i - b_i) \, \boldsymbol{f}\left(t_n + c_i \Delta t_n, \boldsymbol{y}_{n+c_i}\right). \tag{4.68}$$

On the other hand, by using an appropriate norm for the local error and assuming $q > p$, from $(4.66)_2$, $(4.67)_2$ and the triangle inequality it follows that

$$||\widehat{\boldsymbol{e}}_{n+1}|| \approx ||\tilde{\boldsymbol{y}}_{n+1} - \boldsymbol{y}_{n+1}|| = \mathcal{O}\left(\Delta t_n^{p+1}\right). \tag{4.69}$$

Having equations (4.68) and (4.69) at hand, we can readily estimate the local truncation error. Moreover, since the stage solutions $\boldsymbol{y}_{n+c_i}$ are already known, this comes practically at no cost. Thus, specifying prescribed *absolute* and *relative error tolerances* ϵ_a and ϵ_r for the local error (4.69) allows for the calculation of the new time step size,

$$\left.\begin{aligned} ||\tilde{\boldsymbol{y}}_{n+1} - \boldsymbol{y}_{n+1}|| &= C \Delta t_n^{p+1} \\ ||\widehat{\boldsymbol{e}}_{new}|| \approx C \Delta t_{new}^{p+1} &\stackrel{!}{=} \epsilon_a + \epsilon_r ||\hat{\boldsymbol{y}}_n|| \end{aligned}\right\} \quad \Rightarrow \quad \Delta t_{new} = \Delta t_n \left(\frac{\epsilon_a + \epsilon_r ||\boldsymbol{y}_n||}{||\tilde{\boldsymbol{y}}_{n+1} - \boldsymbol{y}_{n+1}||} \right)^{\frac{1}{p+1}}. \tag{4.70}$$

In general, it is possible to control two different error types,

$$r_{n+1} = \begin{cases} ||\widehat{\boldsymbol{e}}_{n+1}||, & \textit{error per step (EPS)}, \\ ||\widehat{\boldsymbol{e}}_{n+1}||/\Delta t_n, & \textit{error per unit step (EPUS)}. \end{cases} \tag{4.71}$$

Notice that equation (4.70) corresponds to the error per step approach[6]. In our thermoviscoelastic setting we have calculated local errors of the primary unknowns, internal variables and reaction forces and flux,

$$\begin{aligned} \hat{u}_I &:= \tilde{u}_{I,n+1} - u_{I,n+1}, & \hat{\theta}_I &:= \tilde{\theta}_{I,n+1} - \theta_{I,n+1}, \\ \hat{\mathcal{E}}_i &:= \tilde{\mathcal{E}}_{I,n+1} - \mathcal{E}_{I,n+1}, & \hat{\lambda}_I &:= \tilde{\lambda}_{I,n+1} - \lambda_{I,n+1}. \end{aligned} \tag{4.72}$$

The calculation of local errors (4.72) is carried out according to equation (4.68). They eventually enter the *mixed absolute-relative norms* [119] given by

$$\begin{aligned} ||\hat{\mathbf{U}}_{n+1}|| &:= \sqrt{\frac{1}{n_{\boldsymbol{u}}} \sum_{I=1}^{n_{\boldsymbol{u}}} \left(\frac{\hat{u}_I}{\epsilon_r |u_{I,n}| + \epsilon_a} \right)^2 + \frac{1}{n_\theta} \sum_{I=1}^{n_\theta} \left(\frac{\hat{\theta}_I}{\epsilon_r |\theta_{I,n}| + \epsilon_a} \right)^2}, \\ ||\hat{\mathbf{E}}_{n+1}|| &:= \max_{I=1,\dots,n_\varepsilon} \left| \frac{\hat{\mathcal{E}}_I}{\epsilon_r |\mathcal{E}_{I,n}| + \epsilon_a} \right|, \quad ||\hat{\mathbf{\Lambda}}_{n+1}|| := \max_{I=1,\dots,n_\lambda} \left| \frac{\hat{\lambda}_I}{\epsilon_r |\lambda_{I,n}| + \epsilon_a} \right|, \end{aligned} \tag{4.73}$$

[6] In choosing the error per unit step, the exponent in equation (4.70) on the right-hand side should be replaced by $\frac{1}{p}$.

where $n_{\boldsymbol{u}}$ and n_θ are, respectively, the number of active (nonprescribed) displacement and thermal degrees of freedom, $n_{\mathcal{E}} = 8{\cdot}\mathcal{N}{\cdot}GP{\cdot}m$ is the total number of internal variables and n_λ is the number of reaction forces and flux at prescribed Dirichlet boundary conditions. The new step size then follows from [118, p. 168]

$$\Delta t_{new} = \Delta t_n \cdot \begin{cases} \max\left(f_{\min}, f_{\text{safety}}/e_{\text{m}}^{1/p+1}\right), & \text{if } e_{\text{m}} > 1, \\ \min\left(f_{\max}, f_{\text{safety}}/e_{\text{m}}^{1/p+1}\right), & \text{if } e_{\text{m}} \leq 1. \end{cases} \tag{4.74}$$

Here $e_{\text{m}} := \max\left(||\hat{\mathbf{U}}_{n+1}||, ||\hat{\mathbf{E}}_{n+1}||, ||\hat{\boldsymbol{\Lambda}}_{n+1}||\right)$, the safety factor $0.8 < f_{\text{safety}} < 0.9$ prevents oscillations in the time step size and the factors $0.2 < f_{\min} < 0.5$ and $2 < f_{\max} < 3$ damp extreme step size changes. Note that the absolute-relative error norms (4.73) used for estimating the new step size (4.74) replace the term in parentheses on the right-hand side of equation (4.70). Formulas (4.70) and (4.74) are, however, rather heuristic and more rigorous step size controllers based on *feedback control* have been developed [116, 120, 121]. We briefly discuss two of them in the following sections.

4.3.2. I-Controller — First Order Adaptivity

A first improvement of the heuristic step size controller (4.70) follows from well-defined control theoretical aspects in the form of a discrete-time *integral controller* (I controller for short). Based on the error-per-step approach $(4.71)_1$ it is given by the formula [116, p. 288]

$$\Delta t_{new} = \Delta t_n \left(\frac{\epsilon_a + \epsilon_r||\boldsymbol{y}_n||}{||\tilde{\boldsymbol{y}}_{n+1} - \boldsymbol{y}_{n+1}||}\right)^{k_1}, \quad \text{where } (p+1)k_1 \in (0,1) \tag{4.75}$$

and p is the order of the DIRK method. The condition on the right corresponds to a slow, smooth control of the integration process. The exponent k_1 is known as the *integral gain* in control theory. If we were to choose $(p+1)k_1 = 1$, that is outside of the specified interval in equation (4.75), we obtain the classical controller from the previous section. This behavior is also called *deadbeat control*.

4.3.3. Predictive Error Controller — Second Order Adaptivity

Another control theory based adaptive time-stepping mechanism is the *proportional integral controller* (PI controller for short). It is given by the formula

$$\Delta t_{new} = \frac{\Delta t_n}{\Delta t_{n-1}} \left(\frac{\epsilon_a + \epsilon_r||\boldsymbol{y}_n||}{||\tilde{\boldsymbol{y}}_{n+1} - \boldsymbol{y}_{n+1}||}\right)^{\frac{k_2}{p+1}} \left(\frac{||\tilde{\boldsymbol{y}}_n - \boldsymbol{y}_{n-1}||}{||\tilde{\boldsymbol{y}}_{n+1} - \boldsymbol{y}_{n+1}||}\right)^{\frac{k_1}{p+1}} \Delta t_n \tag{4.76}$$

in terms of the EPS approach $(4.71)_1$. Above formula is also known as a *second-order predictive controller*. In contrast to the I-controller it contains two control parameters, k_1 and k_2, also known as *proportional* and *integral gains*, respectively. According to [121, p. 512] a good choice is $k_1 = 1$ and $k_2 = 1$, which corresponds to deadbeat control. The Fortran code for the predictive controller is shown in Figure 4.2. For further information on error-control strategies see also [109, p. 46].

```
1  if (err_norm > 1.d0) then                ! Reject current step.
2    if (.not. step_accepted) then          ! Repeated step rejection.
3
4      min_q = 0.1d0                        ! Set stage order of DIRK or Rosenbrock method.
5      if (edirk) min_q = 2.d0              ! Explicit first stage.
6
7      ! Estimate reduced order of Runge–Kutta method.
8      q_est = max(min_q, log(err_norm/err_rej)/log(dt/dt_rej))
9      q_est = min(q_est, q)
10     dt_new = dt*max(f_min, f_safety*err_norm**(-1.d0/q_est))
11   else
12     dt_new = dt*max(f_min, f_safety*err_norm**(-1.d0/q))    ! See equation (4.70).
13   end if
14
15   dt_rej = dt
16   err_rej = err_norm
17
18   first_after_rejection = .true.
19   step_accepted = .false.
20   nr = nr + 1                            ! Increment number of rejected steps.
21 else                                     ! Accepted current step.
22   if (first_time_step .or. first_after_rejection) then
23     dt_new = dt*min(f_max, f_safety*err_norm**(-1.d0/q))    ! See equation (4.70).
24   else                                   ! Use predictive controller.
25     aux1 = min(f_max, f_safety*err_norm**(-k2/q))
26     aux2 = min(f_max, f_safety*(err_norm/err_acc)**(-k1/q))
27
28     dt_new = dt/dt_acc*aux1*aux2*dt     ! See equation (4.76).
29   end if
30
31   dt_acc = dt
32   err_acc = err_norm
33
34   step_accepted = .true.
35   first_after_rejection = .false.
36 end if
```

Figure 4.2.: Fortran code fragment implementing the *predictive controller* in the FEM software `FEAP`, adapted from [121, p. 511].

5. The Local Picture: Finite Element and Material Implementation

This chapter deals with the finite element and material implementation in the context of nonlinear thermoviscoelasticity assuming quasistatic processes. To this end, a complete finite element formalism is derived. This entails the specification of the element stiffness matrix and the element residual vector, which consist of mechanical and thermal contributions as well as influences stemming from the evolution of the internal variables. These are calculated on integration point level, providing a close link to the consistent derivation of the material tangent in terms of the constitutive model developed in Section 3.4. Following the general algorithmic structure laid out in the preceding chapter, all equations are closely related to DIRK time integration schemes. We have extended the in-house FEM program `FEAP` *with a nonlinear coupled thermomechanical element and a material interface to model amorphous polymers during nonisothermal processes through the glass transition region.*

5.1. Element Stiffness and Residual for DIRK Methods

In this section, we take a closer look at the balance of linear momentum and the balance of energy of an individual finite element. This allows to gain further insight into the implementation details and the connection to the material interface. In the pages to follow, all element quantities are given in Voigt notation unless stated otherwise. All equations relate to the ith stage of a DIRK integrator and are, therefore, evaluated at time $t_{n+c_i}, i = 1, \dots, s$, where s denotes the number of stages of the DIRK method. Each nodal point has three translational and one thermal degree of freedom. The latter describes deviations of the absolute temperature $\theta(\boldsymbol{X}, t)$ from the constant reference temperature θ_0. Most of the time we drop the element related superscript $(\bullet)^h$ for the sake of notational convenience.

5.1.1. Space-Time-Discrete Equation of Motion

We begin with the space-time-discrete version of the balance of linear momentum $(4.22)_2$ on page 80. Accordingly, internal and external element nodal forces are balanced during calculation of the ith Runge-Kutta stage at time t_{n+c_i},

$$\mathbf{0} = -\left(\boldsymbol{f}^{\boldsymbol{u}\mathrm{i}}_{I,n+c_i} - \boldsymbol{f}^{\boldsymbol{u}\mathrm{e}}_{I,n+c_i} \right), \quad I = 1, \dots, nel. \tag{5.1}$$

The nodal force vectors (4.18) are repeated below without the time index $(\bullet)_{n+c_i}$,

$$\boldsymbol{f}^{\boldsymbol{u}\mathrm{i}}_{I(3\times1)} = \int_{\Omega^h} \boldsymbol{B}_I^T \boldsymbol{S}^h \, dV \quad \text{and} \quad \boldsymbol{f}^{\boldsymbol{u}\mathrm{e}}_{I(3\times1)} = \int_{\Omega^h} N_I \boldsymbol{B}^h \, dV + \int_{\partial\Omega^{\boldsymbol{T}}_e} N_I \boldsymbol{T}^h \, dA. \tag{5.2}$$

The linearization process already described in Section 4.2.2 is now repeated with the focus on (local) element quantities. First, we linearize the residual (5.1) with respect to the displacements

$$\frac{\partial \boldsymbol{f}_I^{\boldsymbol{u}\mathrm{i}}}{\partial \boldsymbol{u}} \Delta \boldsymbol{u} := \frac{d}{d\alpha} \left[\boldsymbol{f}_I^{\boldsymbol{u}\mathrm{i}}(\boldsymbol{u} + \alpha \Delta \boldsymbol{u}, \theta, \boldsymbol{\mathcal{E}}) \right] \Big|_{\alpha=0} = \sum_{K=1}^{nel} \int_{\Omega^h} \mathbf{G}_{IK} + \boldsymbol{B}_I^T \frac{\partial \boldsymbol{S}}{\partial \boldsymbol{E}} \boldsymbol{B}_K \, dV \Delta \boldsymbol{u}_K. \tag{5.3}$$

Here, the vector $\boldsymbol{\mathcal{E}}(\boldsymbol{X}, t)$ represents the internal variables of a finite element, see equation (4.32) on page 82, and the geometrical part is given by the expression

$$\mathbf{G}_{IK} = g_{IK} \boldsymbol{I}, \quad g_{IK} = \frac{1}{2} \left(\frac{\partial N_I}{\partial \boldsymbol{X}} \otimes \frac{\partial N_K}{\partial \boldsymbol{X}} + \frac{\partial N_K}{\partial \boldsymbol{X}} \otimes \frac{\partial N_I}{\partial \boldsymbol{X}} \right) \cdot \boldsymbol{S} = \mathrm{Grad} N_I \cdot (\boldsymbol{S} \, \mathrm{Grad} N_K), \tag{5.4}$$

with the stresses $\boldsymbol{S}(\boldsymbol{X}, t)$ in tensor notation. Next, we linearize the element residual with respect to the temperature $\theta(\boldsymbol{X}, t)$. The resulting equation yields

$$\frac{\partial \boldsymbol{f}_I^{\boldsymbol{u}\mathrm{i}}}{\partial \theta} \Delta \theta := \frac{d}{d\alpha} \left[\boldsymbol{f}_I^{\boldsymbol{u}\mathrm{i}}(\boldsymbol{u}, \theta + \alpha \Delta \theta, \boldsymbol{\mathcal{E}}) \right] \Big|_{\alpha=0} = \sum_{K=1}^{nel} \int_{\Omega^h} \boldsymbol{B}_I^T \frac{\partial \boldsymbol{S}}{\partial \theta} N_K \, dV \Delta \theta_K. \tag{5.5}$$

Finally, the change with respect to the internal variables $\boldsymbol{\mathcal{E}}(\boldsymbol{X}, t)$ gives

$$\frac{\partial \boldsymbol{f}_I^{\boldsymbol{u}\mathrm{i}}}{\partial \boldsymbol{\mathcal{E}}} \Delta \boldsymbol{\mathcal{E}} := \frac{d}{d\alpha} \left[\boldsymbol{f}_I^{\boldsymbol{u}\mathrm{i}}(\boldsymbol{u}, \theta, \boldsymbol{\mathcal{E}} + \alpha \Delta \boldsymbol{\mathcal{E}}) \right] \Big|_{\alpha=0} = \int_{\Omega^h} \boldsymbol{B}_I^T \frac{\partial \boldsymbol{S}}{\partial \boldsymbol{\mathcal{E}}} \Delta \boldsymbol{\mathcal{E}} \, dV. \tag{5.6}$$

Here, the increment $\Delta \boldsymbol{\mathcal{E}}(\boldsymbol{X}, t)$ of the internal variables follows from the global relation (4.56) on page 88. Since the update is calculated at integration point level, the corresponding local equation reads

$$\begin{aligned} \Delta \boldsymbol{\mathcal{E}} &= - \left[\frac{\partial \boldsymbol{L}}{\partial \boldsymbol{\mathcal{E}}} \right]^{-1} \left(\boldsymbol{L} + \frac{\partial \boldsymbol{L}}{\partial \boldsymbol{u}} \Delta \boldsymbol{u} + \frac{\partial \boldsymbol{L}}{\partial \theta} \Delta \theta \right) = - \left[\frac{\partial \boldsymbol{L}}{\partial \boldsymbol{\mathcal{E}}} \right]^{-1} \left(\boldsymbol{L} + \frac{\partial \boldsymbol{L}}{\partial \boldsymbol{E}} \frac{\partial \boldsymbol{E}}{\partial \boldsymbol{u}} \Delta \boldsymbol{u} + \frac{\partial \boldsymbol{L}}{\partial \theta} \Delta \theta \right) \\ &= - \left[\frac{\partial \boldsymbol{L}}{\partial \boldsymbol{\mathcal{E}}} \right]^{-1} \left(\boldsymbol{L} + \frac{\partial \boldsymbol{L}}{\partial \boldsymbol{E}} \sum_{K=1}^{nel} \boldsymbol{B}_K \Delta \boldsymbol{u}_K + \frac{\partial \boldsymbol{L}}{\partial \theta} \sum_{K=1}^{nel} N_K \Delta \theta_K \right), \end{aligned} \tag{5.7}$$

where we have inserted the expressions $\Delta \boldsymbol{E} = \sum_{K=1}^{nel} \boldsymbol{B}_K \Delta \boldsymbol{u}_K$ and $\Delta \theta = \sum_{K=1}^{nel} N_K \Delta \theta_K$ for the increments of the element strain and temperature values. Next, we substitute above equation into the linearized internal force vector (5.6). In doing so, we separate terms which belong to the element stiffness matrix and the element force vector. Thus, the contribution of the internal variables on the nodal element forces reads

$$\boldsymbol{f}_{I\underset{(3\times1)}{}}^{\boldsymbol{u}\boldsymbol{\mathcal{E}}} = \int_{\Omega^h} \underbrace{\boldsymbol{B}_I^T}_{(3\times6)} \underbrace{\frac{\partial \boldsymbol{S}^h}{\partial \boldsymbol{\mathcal{E}}}}_{(6\times8m)} \underbrace{\left[\frac{\partial \boldsymbol{L}^h}{\partial \boldsymbol{\mathcal{E}}} \right]^{-1}}_{(8m\times8m)} \underbrace{\boldsymbol{L}^h}_{(8m\times1)} \, dV, \tag{5.8}$$

where the size of individual quantities is indicated by underbraces (remember that m designates the number of Maxwell elements). The element stiffness, on the other hand,

contains the standard expression known from purely mechanical theories[1],

$$\boldsymbol{k}^{\boldsymbol{uu}}_{IK(3\times3)} = \int_{\Omega^h} \underbrace{\mathbf{G}_{IK}}_{(3\times3)} + \underbrace{\boldsymbol{B}^T_I}_{(3\times6)} \left[\underbrace{\frac{\partial \boldsymbol{S}^h}{\partial \boldsymbol{E}^h}}_{(6\times6)} - \underbrace{\frac{\partial \boldsymbol{S}^h}{\partial \boldsymbol{\mathcal{E}}}}_{(6\times8m)} \underbrace{\left[\frac{\partial \boldsymbol{L}^h}{\partial \boldsymbol{\mathcal{E}}}\right]^{-1}}_{(8m\times8m)} \underbrace{\frac{\partial \boldsymbol{L}^h}{\partial \boldsymbol{E}^h}}_{(8m\times6)} \right] \underbrace{\boldsymbol{B}_K}_{(6\times3)} \, dV, \tag{5.9}$$

as well as a coupling term resulting from the thermal stresses,

$$\boldsymbol{k}^{\boldsymbol{u}\theta}_{IK(3\times1)} = \int_{\Omega^h} \underbrace{\boldsymbol{B}^T_I}_{(3\times6)} \left[\underbrace{\frac{\partial \boldsymbol{S}^h}{\partial \theta^h}}_{(6\times1)} - \underbrace{\frac{\partial \boldsymbol{S}^h}{\partial \boldsymbol{\mathcal{E}}}}_{(6\times8m)} \underbrace{\left[\frac{\partial \boldsymbol{L}^h}{\partial \boldsymbol{\mathcal{E}}}\right]^{-1}}_{(8m\times8m)} \underbrace{\frac{\partial \boldsymbol{L}^h}{\partial \theta^h}}_{(8m\times1)} \right] N_K \, dV. \tag{5.10}$$

They correspond to their global counterpart (4.65) on page 89 excluding the damping terms, since these only relate to the balance of energy. In summary, the linearized linear momentum of a finite element follows from equations (5.2), (5.8) as well as the element matrices (5.9) and (5.10) to

$$\sum_{K=1}^{nel} \left(\boldsymbol{k}^{\boldsymbol{uu}}_{IK} \Delta \boldsymbol{u}_K + \boldsymbol{k}^{\boldsymbol{u}\theta}_{IK} \Delta \theta_K \right) = - \left(\boldsymbol{f}^{\boldsymbol{u}\mathrm{i}}_I - \boldsymbol{f}^{\boldsymbol{u}\mathcal{E}}_I - \boldsymbol{f}^{\boldsymbol{u}\mathrm{e}}_I \right), \quad I = 1, \dots, nel. \tag{5.11}$$

If we drop the summation notation in favor of an equivalent matrix multiplication we arrive at

$$\boldsymbol{k}^{\boldsymbol{uu}}_e \Delta \boldsymbol{v}^{\boldsymbol{u}}_e + \boldsymbol{k}^{\boldsymbol{u}\theta}_e \Delta \boldsymbol{v}^{\theta}_e = - \boldsymbol{f}^{\boldsymbol{u}\mathrm{i}}_e + \boldsymbol{f}^{\boldsymbol{u}\mathcal{E}}_e + \boldsymbol{f}^{\boldsymbol{u}\mathrm{e}}_e \quad \text{at time } t_{n+c_i} \text{ with } i = 1, \dots, s. \tag{5.12}$$

The local system of equations given above corresponds to the mechanical part of the global equation $(4.64)_1$ on page 89. In the next section we proceed in the same manner with the balance of energy of a finite element.

Remark 21. *A difficulty arises from the fact that element and material formulations are based on different types of strain. Indeed, the element stiffness matrix and load vector are both defined in terms of the Green-Lagrange strain $\boldsymbol{E}(\boldsymbol{X}, t)$ and the thermodynamic conjugate stresses $\boldsymbol{S}(\boldsymbol{X}, t)$. On the other hand, the constitutive framework introduced in Section 3.4 bases upon the Hencky strain $\boldsymbol{H}(\boldsymbol{X}, t)$ and its conjugate stresses $\boldsymbol{\sigma}(\boldsymbol{X}, t)$. Thus, transformations for the second and fourth order tensors in equations $(5.2)_1$, (5.8), (5.9) and (5.10) become necessary (see also Remark 17 on page 77). For a thorough explanation of the transformation rules involved we refer to [101]. Note, however, that the same transformations are also required for the thermal quantities in the following section.*

Remark 22. *Equations (5.8), (5.9) and (5.10) already indicate that we have to solve a linear system of equations with multiple right-hand sides at each integration point in order to correctly establish the element stiffness matrices and the residual vectors [111],*

$$\left[\frac{\partial \boldsymbol{L}}{\partial \boldsymbol{\mathcal{E}}} \right] [\mathbf{y} \,|\, \mathbf{Y} \,|\, \mathbf{z}] = \left[\boldsymbol{L} \,\middle|\, \frac{\partial \boldsymbol{L}}{\partial \boldsymbol{E}} \,\middle|\, \frac{\partial \boldsymbol{L}}{\partial \theta} \right]. \tag{5.13}$$

After determination of the solutions $\mathbf{y}$, $\mathbf{Y}$ and $\mathbf{z}$ these should be saved in the history fields for later reuse when updating the internal variables $\boldsymbol{\mathcal{E}}(\boldsymbol{X}, t)$. This is necessary after each global iteration (see also Section 5.2.2 on page 107).

[1] In case of the constitutive model described in Section 3.3, the term within squared brackets follows from the stress relation (3.18) and the evolution equations (3.11), which eventually resolves to a constant value. In general, however, no analytical expression exists. Thus, the calculation of the stiffness matrix generally necessitates the solution of a linear system of equations, as indicated by the inverse matrix $[\bullet]^{-1}$ in equation (5.9).

5.1.2. Space-Time-Discrete Equation of Energy

The same procedure used in the preceding section is now repeated for the space-time-discrete version of the equation of energy $(4.22)_1$ on page 80. Accordingly, the internal and external element nodal flux are balanced during calculation of the ith Runge-Kutta stage at time t_{n+c_i},

$$0 = -\sum_{J=1}^{nel} \left(d^{\theta\theta}_{IJ,n+c_i} \dot{\theta}_{J,n+c_i} + d^{\theta\boldsymbol{u}}_{IJ,n+c_i} \dot{\boldsymbol{u}}_{J,n+c_i} \right) - \left(f^{\theta \mathrm{i}}_{I,n+c_i} - f^{\theta \mathrm{e}}_{I,n+c_i} \right), \quad I = 1, \dots, nel, \tag{5.14}$$

where element nodal displacement and temperature rates follow from their global counterparts (4.37) on page 84,

$$\begin{aligned} \dot{\boldsymbol{u}}_{J,n+c_i} &= \frac{\boldsymbol{u}_{J,n+c_i} - \boldsymbol{u}_{J,n}}{a_{ii}\Delta t_n} - \frac{1}{a_{ii}} \sum_{j=1}^{i-1} a_{ij} \dot{\boldsymbol{u}}_{J,n+c_j}, \\ \dot{\theta}_{J,n+c_i} &= \frac{\theta_{J,n+c_i} - \theta_{J,n}}{a_{ii}\Delta t_n} - \frac{1}{a_{ii}} \sum_{j=1}^{i-1} a_{ij} \dot{\theta}_{J,n+c_j}. \end{aligned} \tag{5.15}$$

The element nodal flux quantities (4.20) from page 79 are repeated below without the time index,

$$\begin{aligned} f^{\theta \mathrm{i}}_{I(1\times 1)} &= \int_{\Omega^h} -\boldsymbol{g}_I^T \cdot \boldsymbol{Q}^h + N_I \left(\mathcal{H}^h_{\mathrm{in}} - \mathcal{D}^h_{\mathrm{int}} \right) dV, \\ f^{\theta \mathrm{e}}_{I(1\times 1)} &= \int_{\Omega^h} N_I R^h \, dV - \int_{\partial\Omega^h_e} N_I \boldsymbol{Q}^h \cdot \boldsymbol{N}^h \, dA. \end{aligned} \tag{5.16}$$

In contrast to the balance of linear momentum, we have to take account of the element damping matrices. Their nodal contributions are given as

$$d^{\theta\theta}_{IJ(1\times 1)} = \int_{\Omega^h} N_I N_J \rho_0 c \, dV \quad \text{and} \quad d^{\theta\boldsymbol{u}}_{IJ(1\times 3)} = -\int_{\Omega^h} N_I \theta^h \boldsymbol{M}^h \boldsymbol{B}_J \, dV. \tag{5.17}$$

The first term represents the element nodal capacitance, while the second corresponds to the structural thermoelastic heating of an element node ("Gough-Joule effect"). Having these quantities at hand enables us to continue the linearization process in the same manner as with the element-discrete linear momentum in the preceding section. Thus, linearization of the residual (5.14) with respect to the displacements yields an expression for the element nodal flux,

$$\begin{aligned} \frac{\partial f^{\theta \mathrm{i}}_I}{\partial \boldsymbol{u}} \Delta\boldsymbol{u} &:= \frac{d}{d\alpha} \left[f^{\theta \mathrm{i}}_I (\boldsymbol{u} + \alpha\Delta\boldsymbol{u}, \theta, \boldsymbol{\mathcal{E}}) \right] \Big|_{\alpha=0} \\ &= \sum_{K=1}^{nel} \int_{\Omega^h} N_I \left[\frac{\partial \mathcal{H}_{\mathrm{in}}}{\partial \boldsymbol{E}} - \frac{\partial \mathcal{D}_{\mathrm{int}}}{\partial \boldsymbol{E}} \right] \boldsymbol{B}_K \\ &\quad - (\det \boldsymbol{F}) \boldsymbol{g}_I \cdot \big(\left(\boldsymbol{F}^{-1} \boldsymbol{\lambda} \boldsymbol{F}^{T-1} \mathrm{Grad}\theta \right) \cdot \boldsymbol{g}_K \big) \boldsymbol{F}^{-1} \\ &\quad - \left(\boldsymbol{F}^{-1} \boldsymbol{\lambda} \boldsymbol{F}^{T-1} \mathrm{Grad}\theta \right) \otimes \left(\boldsymbol{F}^{T-1} \boldsymbol{g}_K \right) \\ &\quad + \left(\boldsymbol{F}^{-1} \boldsymbol{\lambda} \boldsymbol{F}^{T-1} \boldsymbol{g}_K \right) \otimes \left(\boldsymbol{F}^{T-1} \mathrm{Grad}\theta \right) dV \Delta\boldsymbol{u}_K. \end{aligned} \tag{5.18}$$

The last three terms follow from the change of the referential heat flux $\boldsymbol{Q}(\boldsymbol{X},t)$ with respect to the displacements $\boldsymbol{u}(\boldsymbol{X},t)$, see equation $(2.49)_2$ on page 29. Notice, however, that above equation rests on the simplifying assumption of a constant thermal conductivity $\boldsymbol{\lambda}$. As explained in Section 3.4.5, the conductivity generally depends upon the displacements, the temperature and all internal variables. Linearization of the damping terms gives

$$\begin{aligned}\sum_{J=1}^{nel}\frac{\partial}{\partial \boldsymbol{u}}\left(d_{IJ}^{\theta\theta}\dot{\theta}_J+d_{IJ}^{\theta\boldsymbol{u}}\dot{\boldsymbol{u}}_J\right)\Delta\boldsymbol{u} &:= \sum_{J=1}^{nel}\frac{d}{d\alpha}\left[\left(d_{IJ}^{\theta\theta}\dot{\theta}_J+d_{IJ}^{\theta\boldsymbol{u}}\dot{\boldsymbol{u}}_J\right)(\boldsymbol{u}+\alpha\Delta\boldsymbol{u},\theta,\boldsymbol{\mathcal{E}})\right]\Big|_{\alpha=0}\\ &= \sum_{K=1}^{nel}\int_{\Omega^h}N_I\left[\rho_0\frac{\partial c}{\partial \boldsymbol{E}}\dot{\theta}-\frac{1}{a_{ii}\Delta t_n}\theta\boldsymbol{M}-\theta\dot{\boldsymbol{E}}\cdot\frac{\partial \boldsymbol{M}}{\partial \boldsymbol{E}}\right]\boldsymbol{B}_K\,dV\Delta\boldsymbol{u}_K.\end{aligned} \tag{5.19}$$

Note that the rate terms correspond to the DIRK approximations (5.15), since all equations derived here relate to the instant of time t_{n+c_i}. This is also the reason for the additional term including the scheme weights a_{ij} and the time step size Δt_n in the above expression, which results from the derivation with respect to the displacements of equations $(5.17)_2$ and $(5.15)_1$. Next, we linearize the element residual (5.14) with respect to temperature $\theta(\boldsymbol{X},t)$. For the nodal flux we get (again assuming constant $\boldsymbol{\lambda}$)

$$\begin{aligned}\frac{\partial f_I^{\theta\mathrm{i}}}{\partial\theta}\Delta\theta &:= \frac{d}{d\alpha}\left[f_I^{\theta\mathrm{i}}(\boldsymbol{u},\theta+\alpha\Delta\theta,\boldsymbol{\mathcal{E}})\right]\Big|_{\alpha=0}\\ &= \sum_{K=1}^{nel}\int_{\Omega^h}N_I\left[\frac{\partial\mathcal{H}_{\mathrm{in}}^h}{\partial\theta^h}-\frac{\partial\mathcal{D}_{\mathrm{int}}^h}{\partial\theta^h}\right]N_K+(\det\boldsymbol{F})\boldsymbol{g}_I\cdot\left(\boldsymbol{F}^{-1}\boldsymbol{\lambda}\boldsymbol{F}^{T-1}\boldsymbol{g}_K\right)\,dV\Delta\theta_K,\end{aligned} \tag{5.20}$$

while the damping terms yield

$$\begin{aligned}\sum_{J=1}^{nel}\frac{\partial}{\partial\theta}\left(d_{IJ}^{\theta\theta}\dot{\theta}_J+d_{IJ}^{\theta\boldsymbol{u}}\dot{\boldsymbol{u}}_J\right)\Delta\theta &:= \sum_{J=1}^{nel}\frac{d}{d\alpha}\left[\left(d_{IJ}^{\theta\theta}\dot{\theta}_J+d_{IJ}^{\theta\boldsymbol{u}}\dot{\boldsymbol{u}}_J\right)(\boldsymbol{u},\theta+\alpha\Delta\theta,\boldsymbol{\mathcal{E}})\right]\Big|_{\alpha=0}\\ &= \sum_{K=1}^{nel}\int_{\Omega^h}N_I\Big[\frac{1}{a_{ii}\Delta t_n}\rho_0 c+\rho_0\frac{\partial c}{\partial\theta}\dot{\theta}\\ &\qquad -\dot{\boldsymbol{E}}\cdot\left(\boldsymbol{M}+\theta\frac{\partial\boldsymbol{M}}{\partial\theta}\right)\Big]N_K\,dV\Delta\theta_K.\end{aligned} \tag{5.21}$$

Finally, we calculate the change with respect to internal variables $\boldsymbol{\mathcal{E}}(\boldsymbol{X},t)$. The element nodal flux gives

$$\frac{\partial f_I^{\theta\mathrm{i}}}{\partial\boldsymbol{\mathcal{E}}}\Delta\boldsymbol{\mathcal{E}} := \frac{d}{d\alpha}\left[f_I^{\theta\mathrm{i}}(\boldsymbol{u},\theta,\boldsymbol{\mathcal{E}}+\alpha\Delta\boldsymbol{\mathcal{E}})\right]\Big|_{\alpha=0} = \int_{\Omega^h}N_I\left[\frac{\partial\mathcal{H}_{\mathrm{in}}}{\partial\boldsymbol{\mathcal{E}}}-\frac{\partial\mathcal{D}_{\mathrm{int}}}{\partial\boldsymbol{\mathcal{E}}}\right]\Delta\boldsymbol{\mathcal{E}}\,dV, \tag{5.22}$$

while the damping terms result in the expression

$$\begin{aligned}\sum_{J=1}^{nel}\frac{\partial}{\partial\boldsymbol{\mathcal{E}}}\left(d_{IJ}^{\theta\theta}\dot{\theta}_J+d_{IJ}^{\theta}\dot{\boldsymbol{u}}_J\right)\Delta\boldsymbol{\mathcal{E}} &:= \frac{d}{d\alpha}\left[\left(d_{IJ}^{\theta\theta}\dot{\theta}_J+d_{IJ}^{\theta}\dot{\boldsymbol{u}}_J\right)(\boldsymbol{u},\theta,\boldsymbol{\mathcal{E}}+\alpha\Delta\boldsymbol{\mathcal{E}})\right]\Big|_{\alpha=0}\\ &= \int_{\Omega^h}N_I\left[\rho_0\frac{\partial c}{\partial\boldsymbol{\mathcal{E}}}\dot{\theta}-\theta\dot{\boldsymbol{E}}\cdot\frac{\partial\boldsymbol{M}}{\partial\boldsymbol{\mathcal{E}}}\right]\Delta\boldsymbol{\mathcal{E}}\,dV.\end{aligned} \tag{5.23}$$

Similar to the element-discrete balance of linear momentum in the preceding section, the increments $\Delta\boldsymbol{\mathcal{E}}(\boldsymbol{X},t)$ of the internal variables $(5.7)_2$ are substituted into equations (5.22) and (5.23) followed by a separation into terms belonging to the element stiffness and the residual. As a result, the contribution of the internal variables on the element nodal flux reads

$$f^{\theta\mathcal{E}}_{I(1\times1)} = \int_{\Omega^h} N_I \Big(\underbrace{\frac{\partial \mathcal{H}^h_{\text{in}}}{\partial \boldsymbol{\mathcal{E}}}}_{(1\times 8m)} - \underbrace{\frac{\partial \mathcal{D}^h_{\text{int}}}{\partial \boldsymbol{\mathcal{E}}}}_{(1\times 8m)} + \rho_0 \dot{\theta}^h \underbrace{\frac{\partial c^h}{\partial \boldsymbol{\mathcal{E}}}}_{(1\times 8m)} - \theta^h \underbrace{\dot{\boldsymbol{E}}^h}_{(6\times1)} \cdot \underbrace{\frac{\partial \boldsymbol{M}^h}{\partial \boldsymbol{\mathcal{E}}}}_{(6\times 8m)} \Big) \underbrace{\Big[\frac{\partial \boldsymbol{L}^h}{\partial \boldsymbol{\mathcal{E}}}\Big]^{-1}}_{(8m\times 8m)} \underbrace{\boldsymbol{L}^h}_{(8m\times1)} \, dV. \tag{5.24}$$

The element (thermal) stiffness, on the other hand, consists of two parts, which in turn are made up of several contributions. For the first part we get

$$k^{\theta\theta}_{IK(1\times1)} = k_1 + k_2 + k_3 + k_4 + k_5 + k_6 + k_7. \tag{5.25}$$

The first term is due to the derivative of the temperature rate $(5.15)_2$, while the second term relates to the classical *conductivity matrix*. The remaining terms stem from the temperature dependency of the thermodynamic quantities, namely the specific heat capacity $c(\boldsymbol{X},t)$, stresses $\boldsymbol{\sigma}(\boldsymbol{X},t)$ and thermal stresses $\boldsymbol{M}(\boldsymbol{X},t)$, structural viscous heating $\mathcal{H}_{\text{in}}(\boldsymbol{X},t)$ and internal dissipation $\mathcal{D}_{\text{int}}(\boldsymbol{X},t)$. These are summarized below,

$$\begin{aligned}
k_1 &= \int_{\Omega^h} N_I \frac{1}{a_{ii}\Delta t_n} \rho_0 c^h N_K \, dV, \\
k_2 &= \int_{\Omega^h} (\det \boldsymbol{F}) \boldsymbol{g}_I \cdot \big(\boldsymbol{F}^{-1} \boldsymbol{\lambda} \boldsymbol{F}^{T-1} \boldsymbol{g}_K \big) \, dV, \\
k_3 &= \int_{\Omega^h} N_I \dot{\theta}^h \Big[\underbrace{\frac{\partial c^h}{\partial \theta^h}}_{(1\times1)} - \underbrace{\frac{\partial c^h}{\partial \boldsymbol{\mathcal{E}}}}_{(1\times 8m)} \underbrace{\Big[\frac{\partial \boldsymbol{L}^h}{\partial \boldsymbol{\mathcal{E}}}\Big]^{-1}}_{(8m\times 8m)} \underbrace{\frac{\partial \boldsymbol{L}^h}{\partial \theta^h}}_{(8m\times1)} \Big] N_K \rho_0 \, dV, \\
k_4 &= \int_{\Omega^h} -N_I \theta^h \underbrace{\dot{\boldsymbol{E}}^h}_{(6\times1)} \cdot \Big[\underbrace{\frac{\partial \boldsymbol{M}^h}{\partial \theta^h}}_{(6\times1)} - \underbrace{\frac{\partial \boldsymbol{M}^h}{\partial \boldsymbol{\mathcal{E}}}}_{(6\times 8m)} \underbrace{\Big[\frac{\partial \boldsymbol{L}^h}{\partial \boldsymbol{\mathcal{E}}}\Big]^{-1}}_{(8m\times 8m)} \underbrace{\frac{\partial \boldsymbol{L}^h}{\partial \theta^h}}_{(8m\times1)} \Big] N_K \, dV, \\
k_5 &= \int_{\Omega^h} N_I \Big[\underbrace{\frac{\partial \mathcal{H}^h_{\text{in}}}{\partial \theta^h}}_{(1\times1)} - \underbrace{\frac{\partial \mathcal{H}^h_{\text{in}}}{\partial \boldsymbol{\mathcal{E}}}}_{(1\times 8m)} \underbrace{\Big[\frac{\partial \boldsymbol{L}^h}{\partial \boldsymbol{\mathcal{E}}}\Big]^{-1}}_{(8m\times 8m)} \underbrace{\frac{\partial \boldsymbol{L}^h}{\partial \theta^h}}_{(8m\times1)} \Big] N_K \, dV, \\
k_6 &= \int_{\Omega^h} -N_I \Big[\underbrace{\frac{\partial \mathcal{D}^h_{\text{int}}}{\partial \theta^h}}_{(1\times1)} - \underbrace{\frac{\partial \mathcal{D}^h_{\text{int}}}{\partial \boldsymbol{\mathcal{E}}}}_{(1\times 8m)} \underbrace{\Big[\frac{\partial \boldsymbol{L}^h}{\partial \boldsymbol{\mathcal{E}}}\Big]^{-1}}_{(8m\times 8m)} \underbrace{\frac{\partial \boldsymbol{L}^h}{\partial \theta^h}}_{(8m\times1)} \Big] N_K \, dV, \\
k_7 &= \int_{\Omega^h} -N_I \underbrace{\dot{\boldsymbol{E}}^h}_{(6\times1)} \cdot \underbrace{\boldsymbol{M}^h}_{(6\times1)} N_K \, dV.
\end{aligned} \tag{5.26}$$

Here, also indirect influences of temperature changes through the internal variables $\boldsymbol{\mathcal{E}}(\boldsymbol{X},t)$ enter the stiffness matrix. The second part is a mixed term taking account of coupling effects stemming from the strain dependency of the thermodynamic quantities,

$$\boldsymbol{k}^{\theta\boldsymbol{u}}_{IK(1\times3)} = \boldsymbol{k}_1 + \boldsymbol{k}_2 + \boldsymbol{k}_3 + \boldsymbol{k}_4 + \boldsymbol{k}_5 + \boldsymbol{k}_6. \tag{5.27}$$

The different contributions are listed below,

$$
\begin{aligned}
\boldsymbol{k}_1 &= \int_{\Omega^h} -N_I \frac{1}{a_{ii}\Delta t_n}\theta \underbrace{\boldsymbol{M}^h}_{(1\times 6)} \underbrace{\boldsymbol{B}_K}_{(6\times 3)}\, dV,\\
\boldsymbol{k}_2 &= \int_{\Omega^h} -(\det\boldsymbol{F})\boldsymbol{g}_I \cdot \big((\boldsymbol{F}^{-1}\boldsymbol{\lambda}\boldsymbol{F}^{T-1}\mathrm{Grad}\theta)\cdot \boldsymbol{g}_K \big)\, \boldsymbol{F}^{-1}\\
&\qquad - \big(\boldsymbol{F}^{-1}\boldsymbol{\lambda}\boldsymbol{F}^{T-1}\mathrm{Grad}\theta\big)\otimes\big(\boldsymbol{F}^{T-1}\boldsymbol{g}_K\big)\\
&\qquad + \big(\boldsymbol{F}^{-1}\boldsymbol{\lambda}\boldsymbol{F}^{T-1}\boldsymbol{g}_K\big)\otimes\big(\boldsymbol{F}^{T-1}\mathrm{Grad}\theta\big)\, dV,\\
\boldsymbol{k}_3 &= \int_{\Omega^h} N_I\dot{\theta}^h \Bigg[\underbrace{\frac{\partial c^h}{\partial \boldsymbol{E}^h}}_{(1\times 6)} - \underbrace{\frac{\partial c^h}{\partial \boldsymbol{\mathcal{E}}}}_{(1\times 8m)} \underbrace{\left[\frac{\partial \boldsymbol{L}^h}{\partial \boldsymbol{\mathcal{E}}}\right]^{-1}}_{(8m\times 8m)} \underbrace{\frac{\partial \boldsymbol{L}^h}{\partial \boldsymbol{E}^h}}_{(8m\times 6)} \Bigg] \underbrace{\boldsymbol{B}_K}_{(6\times 3)} \rho_0\, dV,\\
\boldsymbol{k}_4 &= \int_{\Omega^h} -N_I\theta^h \underbrace{\dot{\boldsymbol{E}}^h}_{(6\times 1)} \cdot \Bigg[\underbrace{\frac{\partial \boldsymbol{M}^h}{\partial \boldsymbol{E}^h}}_{(6\times 6)} - \underbrace{\frac{\partial \boldsymbol{M}^h}{\partial \boldsymbol{\mathcal{E}}}}_{(6\times 8m)} \underbrace{\left[\frac{\partial \boldsymbol{L}^h}{\partial \boldsymbol{\mathcal{E}}}\right]^{-1}}_{(8m\times 8m)} \underbrace{\frac{\partial \boldsymbol{L}^h}{\partial \boldsymbol{E}^h}}_{(8m\times 6)} \Bigg] \underbrace{\boldsymbol{B}_K}_{(6\times 3)} dV,\\
\boldsymbol{k}_5 &= \int_{\Omega^h} N_I \Bigg[\underbrace{\frac{\partial \mathcal{H}^h_{\text{in}}}{\partial \boldsymbol{E}^h}}_{(1\times 6)} - \underbrace{\frac{\partial \mathcal{H}^h_{\text{in}}}{\partial \boldsymbol{\mathcal{E}}}}_{(1\times 8m)} \underbrace{\left[\frac{\partial \boldsymbol{L}^h}{\partial \boldsymbol{\mathcal{E}}}\right]^{-1}}_{(8m\times 8m)} \underbrace{\frac{\partial \boldsymbol{L}^h}{\partial \boldsymbol{E}^h}}_{(8m\times 6)} \Bigg] \underbrace{\boldsymbol{B}_K}_{(6\times 3)} dV,\\
\boldsymbol{k}_6 &= \int_{\Omega^h} -N_I \Bigg[\underbrace{\frac{\partial \mathcal{D}^h_{\text{int}}}{\partial \boldsymbol{E}^h}}_{(1\times 6)} - \underbrace{\frac{\partial \mathcal{D}^h_{\text{int}}}{\partial \boldsymbol{\mathcal{E}}}}_{(1\times 8m)} \underbrace{\left[\frac{\partial \boldsymbol{L}^h}{\partial \boldsymbol{\mathcal{E}}}\right]^{-1}}_{(8m\times 8m)} \underbrace{\frac{\partial \boldsymbol{L}^h}{\partial \boldsymbol{E}^h}}_{(8m\times 6)} \Bigg] \underbrace{\boldsymbol{B}_K}_{(6\times 3)} dV.
\end{aligned}
\tag{5.28}
$$

In summary, the linearized balance of energy of a finite element follows from equations (5.16), (5.24) as well as the element matrices (5.25) and (5.27) to

$$
\sum_{K=1}^{nel} \left(k^{\theta\theta}_{IK}\Delta\theta_K + \boldsymbol{k}^{\theta\boldsymbol{u}}_{IK}\Delta\boldsymbol{u}_K\right) = -\left(f^{\theta\mathrm{i}}_I - f^{\theta\mathcal{E}}_I - f^{\theta\mathrm{e}}_I\right), \quad I = 1,\dots,nel. \tag{5.29}
$$

Dropping the summation notation in favor of an equivalent matrix multiplication yields

$$
\boldsymbol{k}^{\theta\theta}_e\Delta\boldsymbol{v}^\theta_e + \boldsymbol{k}^{\theta\boldsymbol{u}}_e\Delta\boldsymbol{v}^\theta_e = -\boldsymbol{f}^{\theta\mathrm{i}}_e + \boldsymbol{f}^{\theta\mathcal{E}}_e + \boldsymbol{f}^{\theta\mathrm{e}}_e. \tag{5.30}
$$

The local system of equations corresponds to the thermal part of the global equation $(4.64)_1$ on page 89. In the next section we give a summary of all the element quantities derived so far.

Remark 23. *Above equations include underbraces indicating the different sizes of matrix and vector quantities. In terms of the constitutive model derived in Section 3.4 there are six independent components for the internal variables $\boldsymbol{\mathcal{Z}}(\boldsymbol{X},t)$ as well as two scalars $\zeta(\boldsymbol{X},t)$ and $\chi(\boldsymbol{X},t)$ for a total number of m relaxation mechanisms. As mentioned in Remark 22, the nonlinear material model requires the solution of a linear system of equations at each integration point. In order to reduce the computational costs, it is recommended to implement the constitutive routine in principal axes. In this case, the number of entries reduces from $8m$ to $5m$ and the storage of the history arrays required to save the internal variables reduces as well. This is especially advantageous in case of multistage DIRK methods (see also Section 5.2.3).*

5.1.3. Summary of Element Quantities

Having the linearized element-discrete balance equations (5.12) and (5.30) at hand, we can summarize them to form a local system of equations similar to its global counterpart (4.64) on page 89. For the ith stage solution at instant of time $t_{n+c_i}, i = 1, \dots, m$ it reads

$$\begin{bmatrix} \boldsymbol{k}_e^{\boldsymbol{uu}} & \boldsymbol{k}_e^{\boldsymbol{u}\theta} \\ \boldsymbol{k}_e^{\theta\boldsymbol{u}} & \boldsymbol{k}_e^{\theta\theta} \end{bmatrix} \begin{bmatrix} \Delta \boldsymbol{v}_e^{\boldsymbol{u}} \\ \Delta \boldsymbol{v}_e^{\theta} \end{bmatrix} = - \begin{bmatrix} \boldsymbol{f}_e^{\boldsymbol{u}\mathrm{i}} - \boldsymbol{f}_e^{\boldsymbol{u}\mathcal{E}} - \boldsymbol{f}_e^{\boldsymbol{u}\mathrm{e}} \\ \boldsymbol{f}_e^{\theta\mathrm{i}} - \boldsymbol{f}_e^{\theta\mathcal{E}} - \boldsymbol{f}_e^{\theta\mathrm{e}} \end{bmatrix}. \tag{5.31}$$

The nodal displacements and temperatures are summarized in the vectors ($N = nel$)

$$\boldsymbol{v}^{\boldsymbol{u}}_{e(3N\times 1)} = \begin{bmatrix} \boldsymbol{u}_1 \\ \vdots \\ \boldsymbol{u}_I \\ \vdots \\ \boldsymbol{u}_N \end{bmatrix}, \qquad \boldsymbol{v}^{\theta}_{e(N\times 1)} = \begin{bmatrix} \theta_1 \\ \vdots \\ \theta_I \\ \vdots \\ \theta_N \end{bmatrix}. \tag{5.32}$$

In addition, the element residual consists of three terms which are given on the right-hand side of equation (5.31),

$$\begin{aligned} \boldsymbol{f}^{\boldsymbol{u}\mathrm{i}}_{e(3N\times 1)} &= \begin{bmatrix} \boldsymbol{f}_1^{\boldsymbol{u}\mathrm{i}} \\ \vdots \\ \boldsymbol{f}_I^{\boldsymbol{u}\mathrm{i}} \\ \vdots \\ \boldsymbol{f}_N^{\boldsymbol{u}\mathrm{i}} \end{bmatrix}, \qquad \boldsymbol{f}^{\boldsymbol{u}\mathrm{e}}_{e(3N\times 1)} = \begin{bmatrix} \boldsymbol{f}_1^{\boldsymbol{u}\mathrm{e}} \\ \vdots \\ \boldsymbol{f}_I^{\boldsymbol{u}\mathrm{e}} \\ \vdots \\ \boldsymbol{f}_N^{\boldsymbol{u}\mathrm{e}} \end{bmatrix}, \qquad \boldsymbol{f}^{\boldsymbol{u}\mathcal{E}}_{e(3N\times 1)} = \begin{bmatrix} \boldsymbol{f}_1^{\boldsymbol{u}\mathcal{E}} \\ \vdots \\ \boldsymbol{f}_I^{\boldsymbol{u}\mathcal{E}} \\ \vdots \\ \boldsymbol{f}_N^{\boldsymbol{u}\mathcal{E}} \end{bmatrix}, \\ \boldsymbol{f}^{\theta\mathrm{i}}_{e(N\times 1)} &= \begin{bmatrix} f_1^{\theta\mathrm{i}} \\ \vdots \\ f_I^{\theta\mathrm{i}} \\ \vdots \\ f_N^{\theta\mathrm{i}} \end{bmatrix}, \qquad \boldsymbol{f}^{\theta\mathrm{e}}_{e(N\times 1)} = \begin{bmatrix} f_1^{\theta\mathrm{e}} \\ \vdots \\ f_I^{\theta\mathrm{e}} \\ \vdots \\ f_N^{\theta\mathrm{e}} \end{bmatrix}, \qquad \boldsymbol{f}^{\theta\mathcal{E}}_{e(N\times 1)} = \begin{bmatrix} f_1^{\theta\mathcal{E}} \\ \vdots \\ f_I^{\theta\mathcal{E}} \\ \vdots \\ f_N^{\theta\mathcal{E}} \end{bmatrix}. \end{aligned} \tag{5.33}$$

Here, the vectors on the right stem from the influence of the internal variables $\boldsymbol{\mathcal{E}}(\boldsymbol{X}, t)$. The four stiffness contributions read

$$\begin{aligned} \boldsymbol{k}^{\boldsymbol{uu}}_{e(3N\times 3N)} &= \begin{bmatrix} \boldsymbol{k}_{11}^{\boldsymbol{uu}} & \cdots & \boldsymbol{k}_{1N}^{\boldsymbol{uu}} \\ & \ddots & \\ \vdots & \boldsymbol{k}_{IK}^{\boldsymbol{uu}} & \vdots \\ & \ddots & \\ \boldsymbol{k}_{N1}^{\boldsymbol{uu}} & \cdots & \boldsymbol{k}_{NN}^{\boldsymbol{uu}} \end{bmatrix}, \qquad \boldsymbol{k}^{\boldsymbol{u}\theta}_{e(3N\times N)} = \begin{bmatrix} \boldsymbol{k}_{11}^{\boldsymbol{u}\theta} & \cdots & \boldsymbol{k}_{1N}^{\boldsymbol{u}\theta} \\ & \ddots & \\ \vdots & \boldsymbol{k}_{IK}^{\boldsymbol{u}\theta} & \vdots \\ & \ddots & \\ \boldsymbol{k}_{N1}^{\boldsymbol{u}\theta} & \cdots & \boldsymbol{k}_{NN}^{\boldsymbol{u}\theta} \end{bmatrix}, \\ \boldsymbol{k}^{\theta\theta}_{e(N\times N)} &= \begin{bmatrix} k_{11}^{\theta\theta} & \cdots & k_{1N}^{\theta\theta} \\ & \ddots & \\ \vdots & k_{IK}^{\theta\theta} & \vdots \\ & \ddots & \\ k_{N1}^{\theta\theta} & \cdots & k_{NN}^{\theta\theta} \end{bmatrix}, \qquad \boldsymbol{k}^{\theta\boldsymbol{u}}_{e(N\times 3N)} = \begin{bmatrix} \boldsymbol{k}_{11}^{\theta\boldsymbol{u}} & \cdots & \boldsymbol{k}_{1N}^{\theta\boldsymbol{u}} \\ & \ddots & \\ \vdots & \boldsymbol{k}_{IK}^{\theta\boldsymbol{u}} & \vdots \\ & \ddots & \\ \boldsymbol{k}_{N1}^{\theta\boldsymbol{u}} & \cdots & \boldsymbol{k}_{NN}^{\theta\boldsymbol{u}} \end{bmatrix}. \end{aligned} \tag{5.34}$$

Finally, we assemble contributions from all elements to obtain the global vectors

$$\begin{aligned} \mathsf{F}^{\boldsymbol{u}} &= \mathop{\mathsf{A}}_{e=1}^{\mathcal{N}} \left[\boldsymbol{f}_e^{\boldsymbol{u}\mathrm{i}} - \boldsymbol{f}_e^{\boldsymbol{u}\mathcal{E}} - \boldsymbol{f}_e^{\boldsymbol{u}\mathrm{e}} \right], & \mathsf{F}^{\theta} &= \mathop{\mathsf{A}}_{e=1}^{\mathcal{N}} \left[\boldsymbol{f}_e^{\theta\mathrm{i}} - \boldsymbol{f}_e^{\theta\mathcal{E}} - \boldsymbol{f}_e^{\theta\mathrm{e}} \right], \\ \mathsf{V}^{\boldsymbol{u}} &= \mathop{\mathsf{A}}_{e=1}^{\mathcal{N}} \boldsymbol{v}_e^{\boldsymbol{u}}, & \mathsf{V}^{\theta} &= \mathop{\mathsf{A}}_{e=1}^{\mathcal{N}} \boldsymbol{v}_e^{\theta} \end{aligned} \tag{5.35}$$

and global matrices

$$\mathsf{K}^{\boldsymbol{uu}} = \mathop{\mathsf{A}}_{e=1}^{\mathcal{N}} \boldsymbol{k}_e^{\boldsymbol{uu}}, \qquad \mathsf{K}^{\boldsymbol{u}\theta} = \mathop{\mathsf{A}}_{e=1}^{\mathcal{N}} \boldsymbol{k}_e^{\boldsymbol{u}\theta}, \qquad \mathsf{K}^{\theta\boldsymbol{u}} = \mathop{\mathsf{A}}_{e=1}^{\mathcal{N}} \boldsymbol{k}_e^{\theta\boldsymbol{u}}, \qquad \mathsf{K}^{\theta\theta} = \mathop{\mathsf{A}}_{e=1}^{\mathcal{N}} \boldsymbol{k}_e^{\theta\theta}. \tag{5.36}$$

By canceling columns and rows which pertain to prescribed Dirichlet boundary conditions in the above matrices, we arrive at the effective stiffness matrix $(4.65)_1$ given on page 89.

5.2. Material Evaluation for Finite Thermoviscoelasticity

Up to now we have discussed the global solution algorithms and gave detailed information on the finite element implementation. The aim of this section is to step down on integration point level to provide the quantities relevant to the implementation of the constitutive equations presented in Section 3.4. More precisely, the focus is on the determination of the *consistent material tangent*, that is the calculation of partial derivatives of material variables such as stresses and specific heat capacity in terms of the chosen time integrator. However, it serves no purpose to lay out all quantities. Instead, only a restricted set of equations will be derived here to illustrate the general procedure. Remaining equations are summarized in Appendix A. The update of the internal variables happens at local integration point level and deserves special attention, since it forms an essential part in the overall algorithmic solution strategy. Thus, a separate section is devoted to this topic. Finally, we give some general details concerning the material implementation and the problems involved.

5.2.1. Derivation of the Material Tangent

Influence of the First Evolution Equation

According to equation (5.7) we need the partial derivatives of the local residual $\boldsymbol{L}(\boldsymbol{X}, t)$, which forms part of the element stiffness matrices and element vectors in equations (5.12) and (5.30). This comprises the influence of all three evolution equations (3.38) on page 54. The general procedure is demonstrated below for the internal variables $\boldsymbol{\mathcal{Z}}_l(\boldsymbol{X}, t)$, the residual of which is defined by $(l, k = 1, \dots, m)$

$$\boldsymbol{\mathcal{R}}_l(t) := \dot{\boldsymbol{\mathcal{Z}}}_l(t) - \boldsymbol{\mathcal{A}}_l \left(\boldsymbol{H}(t), \theta(t), \boldsymbol{\mathcal{Z}}_k(t), \zeta_k(t), \chi_k(t) \right). \tag{5.37}$$

In Voigt notation above equation becomes

$$\boldsymbol{\mathcal{R}}^h_{l(6\times1)} = \dot{\boldsymbol{\mathcal{Z}}}^h_l - \boldsymbol{\mathcal{A}}_l \left(t, \boldsymbol{H}^h, \theta^h, \boldsymbol{\mathcal{Z}}^h_k, \zeta^h_k, \chi^h_k \right), \tag{5.38}$$

which is conveniently split into its volumetric and deviatoric parts

$$\boldsymbol{\mathcal{R}}^h_{l,n+c_i} = \frac{1}{3} \left(\mathrm{tr} \boldsymbol{\mathcal{R}}^h_{l,n+c_i} \right) \boldsymbol{I} + \mathrm{dev} \boldsymbol{\mathcal{R}}^h_{l,n+c_i}. \tag{5.39}$$

The residual of the volumetric contribution in terms of the DIRK velocities $(4.37)_2$ reads

$$\begin{aligned}\mathrm{tr}\boldsymbol{\mathcal{R}}^h_{l,n+c_i} &= \mathrm{tr}\dot{\boldsymbol{\mathcal{Z}}}^h_{l,n+c_i} - \mathrm{tr}\boldsymbol{\mathcal{A}}_{l,n+c_i},\\ &= \frac{\mathrm{tr}\boldsymbol{\mathcal{Z}}^h_{l,n+c_i} - \mathrm{tr}\boldsymbol{\mathcal{Z}}^h_{l,n}}{a_{ii}\Delta t_n} - \frac{1}{a_{ii}}\sum_{j=1}^{i-1} a_{ij}\mathrm{tr}\dot{\boldsymbol{\mathcal{Z}}}^h_{l,n+c_j}\\ &\quad - \frac{1}{a\left(\boldsymbol{H}^h,\theta^h,\boldsymbol{\mathcal{Z}}^h_k,\zeta^h_k,\chi^h_k\right)\tau^K_l}\left(\mathrm{tr}\boldsymbol{H}^h_{n+c_i} - \mathrm{tr}\boldsymbol{\mathcal{Z}}^h_{l,n+c_i}\right),\end{aligned} \tag{5.40}$$

while the deviatoric residual takes on the form

$$\begin{aligned}\mathrm{dev}\boldsymbol{\mathcal{R}}^h_{l,n+c_i} &= \mathrm{dev}\dot{\boldsymbol{\mathcal{Z}}}^h_{l,n+c_i} - \mathrm{dev}\boldsymbol{\mathcal{A}}_{l,n+c_i},\\ &= \frac{\mathrm{dev}\boldsymbol{\mathcal{Z}}^h_{l,n+c_i} - \mathrm{dev}\boldsymbol{\mathcal{Z}}^h_{l,n}}{a_{ii}\Delta t_n} - \frac{1}{a_{ii}}\sum_{j=1}^{i-1} a_{ij}\mathrm{dev}\dot{\boldsymbol{\mathcal{Z}}}^h_{l,n+c_j}\\ &\quad - \frac{1}{a\left(\boldsymbol{H}^h,\theta^h,\boldsymbol{\mathcal{Z}}^h_k,\zeta^h_k,\chi^h_k\right)\tau^G_l}\left(\mathrm{dev}\boldsymbol{H}^h_{n+c_i} - \mathrm{dev}\boldsymbol{\mathcal{Z}}^h_{l,n+c_i}\right).\end{aligned} \tag{5.41}$$

Application of the chain rule to calculate the change with respect to internal variables $\boldsymbol{\mathcal{Z}}_r(\boldsymbol{X},t)$ yields

$$\begin{aligned}\frac{\partial\boldsymbol{\mathcal{R}}^h_{l,n+c_i}}{\partial\boldsymbol{\mathcal{Z}}^h_{r,n+c_i}} &= \frac{\partial\boldsymbol{\mathcal{R}}^h_{l,n+c_i}}{\partial\mathrm{tr}\boldsymbol{\mathcal{R}}^h_{l,n+c_i}}\frac{\partial\mathrm{tr}\boldsymbol{\mathcal{R}}^h_{l,n+c_i}}{\partial\boldsymbol{\mathcal{Z}}^h_{r,n+c_i}} + \frac{\partial\boldsymbol{\mathcal{R}}^h_{l,n+c_i}}{\partial\mathrm{dev}\boldsymbol{\mathcal{R}}^h_{l,n+c_i}}\frac{\partial\mathrm{dev}\boldsymbol{\mathcal{R}}^h_{l,n+c_i}}{\partial\boldsymbol{\mathcal{Z}}^h_{r,n+c_i}}\\ &= \frac{1}{3}\boldsymbol{I}\otimes\frac{\partial\mathrm{tr}\boldsymbol{\mathcal{R}}^h_{l,n+c_i}}{\partial\boldsymbol{\mathcal{Z}}^h_{r,n+c_i}} + \frac{\partial\mathrm{dev}\boldsymbol{\mathcal{R}}^h_{l,n+c_i}}{\partial\boldsymbol{\mathcal{Z}}^h_{r,n+c_i}}.\end{aligned} \tag{5.42}$$

The first term is given without the time subscript as

$$\begin{aligned}\frac{1}{3}\boldsymbol{I}\otimes\frac{\partial\mathrm{tr}\boldsymbol{\mathcal{R}}^h_l}{\partial\boldsymbol{\mathcal{Z}}^h_r} &= \frac{1}{3}\left(\frac{1}{a_{ii}\Delta t_n} + \frac{1}{a\tau^K_l}\right)\delta_{lr}\boldsymbol{I}\otimes\boldsymbol{I} + \frac{1}{3a^2\tau^K_l}\left(\mathrm{tr}\boldsymbol{H}^h - \mathrm{tr}\boldsymbol{\mathcal{Z}}^h_l\right)\frac{\partial a}{\partial\mathrm{tr}\boldsymbol{\mathcal{Z}}^h_r}\boldsymbol{I}\otimes\boldsymbol{I}\\ &\quad + \frac{1}{3a^2\tau^K_l}\left(\mathrm{tr}\boldsymbol{H}^h - \mathrm{tr}\boldsymbol{\mathcal{Z}}^h_l\right)\boldsymbol{I}\otimes\left(\mathrm{dev}\frac{\partial a}{\partial\mathrm{dev}\boldsymbol{\mathcal{Z}}^h_r}\right),\end{aligned} \tag{5.43}$$

while the second term reads

$$\begin{aligned}\frac{\partial\mathrm{dev}\boldsymbol{\mathcal{R}}^h_l}{\partial\boldsymbol{\mathcal{Z}}^h_r} &= \left(\frac{1}{a_{ii}\Delta t_n} + \frac{1}{a\tau^G_l}\right)\delta_{lr}\left(\mathbb{1} - \frac{1}{3}\boldsymbol{I}\otimes\boldsymbol{I}\right) + \frac{1}{a^2\tau^G_l}\frac{\partial a}{\partial\mathrm{tr}\boldsymbol{\mathcal{Z}}^h_r}\left(\mathrm{dev}\boldsymbol{H}^h - \mathrm{dev}\boldsymbol{\mathcal{Z}}^h_l\right)\otimes\boldsymbol{I}\\ &\quad + \frac{1}{a^2\tau^G_l}\left(\mathrm{dev}\boldsymbol{H}^h - \mathrm{dev}\boldsymbol{\mathcal{Z}}^h_l\right)\otimes\left(\mathrm{dev}\frac{\partial a}{\partial\mathrm{dev}\boldsymbol{\mathcal{Z}}^h_r}\right).\end{aligned} \tag{5.44}$$

In a similar fashion the partial derivatives with respect to the remaining internal variables $\zeta_r(\boldsymbol{X},t)$ and $\chi_r(\boldsymbol{X},t)$ give

$$\begin{aligned}\frac{\partial \boldsymbol{\mathcal{R}}_l^h}{\partial \zeta_r^h} &= \frac{1}{3a^2\tau_l^K}\left(\mathrm{tr}\boldsymbol{H}^h - \mathrm{tr}\boldsymbol{\mathcal{Z}}_l^h\right)\frac{\partial a}{\partial \zeta_r^h}\boldsymbol{I} + \frac{1}{a^2\tau_l^G}\left(\mathrm{dev}\boldsymbol{H}^h - \mathrm{dev}\boldsymbol{\mathcal{Z}}_l^h\right)\frac{\partial a}{\partial \zeta_r^h},\\ \frac{\partial \boldsymbol{\mathcal{R}}_l^h}{\partial \chi_r^h} &= \frac{1}{3a^2\tau_l^K}\left(\mathrm{tr}\boldsymbol{H}^h - \mathrm{tr}\boldsymbol{\mathcal{Z}}_l^h\right)\frac{\partial a}{\partial \chi_r^h}\boldsymbol{I} + \frac{1}{a^2\tau_l^G}\left(\mathrm{dev}\boldsymbol{H}^h - \mathrm{dev}\boldsymbol{\mathcal{Z}}_l^h\right)\frac{\partial a}{\partial \chi_r^h}.\end{aligned} \tag{5.45}$$

Finally, we calculate the partial derivatives with respect to the strain $\boldsymbol{H}(\boldsymbol{X},t)$ and the temperature $\theta(\boldsymbol{X},t)$. Application of the chain rule results in

$$\begin{aligned}\frac{\partial \boldsymbol{\mathcal{R}}_{l,n+c_i}^h}{\partial \boldsymbol{H}_{n+c_i}^h} &= \frac{\partial \boldsymbol{\mathcal{R}}_{l,n+c_i}^h}{\partial \mathrm{tr}\boldsymbol{\mathcal{R}}_{l,n+c_i}^h}\frac{\partial \mathrm{tr}\boldsymbol{\mathcal{R}}_{l,n+c_i}^h}{\partial \boldsymbol{H}_{n+c_i}^h} + \frac{\partial \boldsymbol{\mathcal{R}}_{l,n+c_i}^h}{\partial \mathrm{dev}\boldsymbol{\mathcal{R}}_{l,n+c_i}^h}\frac{\partial \mathrm{dev}\boldsymbol{\mathcal{R}}_{l,n+c_i}^h}{\partial \boldsymbol{H}_{n+c_i}^h}\\ &= \frac{1}{3}\boldsymbol{I}\otimes\frac{\partial \mathrm{tr}\boldsymbol{\mathcal{R}}_{l,n+c_i}^h}{\partial \boldsymbol{H}_{n+c_i}^h} + \frac{\partial \mathrm{dev}\boldsymbol{\mathcal{R}}_{l,n+c_i}^h}{\partial \boldsymbol{H}_{n+c_i}^h},\end{aligned} \tag{5.46}$$

with the volumetric part (again dropping the time indices)

$$\begin{aligned}\frac{1}{3}\boldsymbol{I}\otimes\frac{\partial \mathrm{tr}\boldsymbol{\mathcal{R}}_l^h}{\partial \boldsymbol{H}^h} = &-\frac{1}{3a\tau_l^K}\boldsymbol{I}\otimes\boldsymbol{I} + \frac{1}{3a^2\tau_l^K}\left(\mathrm{tr}\boldsymbol{H} - \mathrm{tr}\boldsymbol{\mathcal{Z}}_l^h\right)\frac{\partial a}{\partial \mathrm{tr}\boldsymbol{H}^h}\boldsymbol{I}\otimes\boldsymbol{I}\\ &+ \frac{1}{3a^2\tau_l^K}\left(\mathrm{tr}\boldsymbol{H}^h - \mathrm{tr}\boldsymbol{\mathcal{Z}}_l^h\right)\boldsymbol{I}\otimes\left(\mathrm{dev}\frac{\partial a}{\partial \mathrm{dev}\boldsymbol{H}^h}\right)\end{aligned} \tag{5.47}$$

and the deviatoric part

$$\begin{aligned}\frac{\partial \mathrm{dev}\boldsymbol{\mathcal{R}}_l^h}{\partial \boldsymbol{H}^h} = &-\frac{1}{a\tau_l^G}\left(\mathbb{1} - \frac{1}{3}\boldsymbol{I}\otimes\boldsymbol{I}\right) + \frac{1}{a^2\tau_l^G}\frac{\partial a}{\partial \mathrm{tr}\boldsymbol{H}^h}\left(\mathrm{dev}\boldsymbol{H}^h - \mathrm{dev}\boldsymbol{\mathcal{Z}}_l^h\right)\otimes\boldsymbol{I}\\ &+ \frac{1}{a^2\tau_l^G}\left(\mathrm{dev}\boldsymbol{H}^h - \mathrm{dev}\boldsymbol{\mathcal{Z}}_l^h\right)\otimes\left(\mathrm{dev}\frac{\partial a}{\partial \mathrm{dev}\boldsymbol{H}^h}\right).\end{aligned} \tag{5.48}$$

The temperature derivative is given by

$$\frac{\partial \boldsymbol{\mathcal{R}}_l^h}{\partial \theta^h} = \frac{1}{3a^2\tau_l^K}\left(\mathrm{tr}\boldsymbol{H}^h - \mathrm{tr}\boldsymbol{\mathcal{Z}}_l^h\right)\frac{\partial a}{\partial \theta^h}\boldsymbol{I} + \frac{1}{a^2\tau_l^G}\frac{\partial a}{\partial \theta^h}\left(\mathrm{dev}\boldsymbol{H}^h - \mathrm{dev}\boldsymbol{\mathcal{Z}}_l^h\right). \tag{5.49}$$

The same procedure is necessary for the other evolution equations and the remaining thermodynamic quantities. A second example follows in terms of the stresses $\boldsymbol{\sigma}(\boldsymbol{X},t)$.

Influence of the Stresses and Thermal Stresses

The stress tensor (3.56) is defined on page 59. Its partial derivative with respect to the internal variables $\boldsymbol{\mathcal{Z}}_l(\boldsymbol{X},t)$ and $\zeta_l(\boldsymbol{X},t)$ reads

$$\begin{aligned}\frac{\partial \boldsymbol{\sigma}^h}{\partial \boldsymbol{\mathcal{Z}}_l^h} &= -\Psi_K\left(\theta^h\right)K_l\boldsymbol{I}\otimes\boldsymbol{I} - 2\Psi_G\left(\theta^h\right)G_l\left(\mathbb{1} - \frac{1}{3}\boldsymbol{I}\otimes\boldsymbol{I}\right)\\ &\quad + \frac{\partial \Psi_\alpha\left(\mathrm{tr}\boldsymbol{H}^h,\theta^h\right)}{\partial \mathrm{tr}\boldsymbol{H}^h}\left(3\alpha_l\left(\theta^h - \theta_0\right) + \zeta_l^h\right)K_l\boldsymbol{I}\otimes\boldsymbol{I},\\ \frac{\partial \boldsymbol{\sigma}^h}{\partial \zeta_l^h} &= -\left(\Psi_\alpha\left(\mathrm{tr}\boldsymbol{H}^h,\theta^h\right) + \frac{\partial \Psi_\alpha\left(\mathrm{tr}\boldsymbol{H}^h,\theta^h\right)}{\partial \mathrm{tr}\boldsymbol{H}^h}\left(\mathrm{tr}\boldsymbol{H}^h - \mathrm{tr}\boldsymbol{\mathcal{Z}}_l^h\right)\right)K_l\boldsymbol{I},\end{aligned} \tag{5.50}$$

where we have dropped the time subscript $(\bullet)_{n+c_i}$ to alleviate the notation. The change with respect to the strain $\boldsymbol{H}(\boldsymbol{X},t)$ is split into an equilibrium and a transient part,

$$\frac{\partial \boldsymbol{\sigma}^h_{n+c_i}}{\partial \boldsymbol{H}^h_{n+c_i}} = \frac{\partial \boldsymbol{\sigma}^h_{\mathrm{eq,n+c_i}}}{\partial \boldsymbol{H}^h_{n+c_i}} + \frac{\partial \boldsymbol{\sigma}^h_{\mathrm{tr,n+c_i}}}{\partial \boldsymbol{H}^h_{n+c_i}}. \tag{5.51}$$

These are given by the expressions

$$\begin{aligned}
\frac{\partial \boldsymbol{\sigma}^h_{\mathrm{eq}}}{\partial \boldsymbol{H}^h} &= \left(\psi_1 + \psi_6\left(\theta^h - \theta_0\right)\right)\boldsymbol{I}\otimes\boldsymbol{I} + 2\psi_2\left(\mathbb{1} - \frac{1}{3}\boldsymbol{I}\otimes\boldsymbol{I}\right), \\
\frac{\partial \boldsymbol{\sigma}^h_{\mathrm{tr}}}{\partial \boldsymbol{H}^h} &= \sum_r \left(\Psi_K\left(\theta^h\right)K_r - \frac{\partial \Psi_\alpha\left(\mathrm{tr}\boldsymbol{H}^h, \theta^h\right)}{\partial \mathrm{tr}\boldsymbol{H}^h} 2K_r\left(3\alpha_r\left(\theta^h - \theta_0\right) + \zeta^h_r\right)\right)\boldsymbol{I}\otimes\boldsymbol{I} \\
&\quad + \sum_r 2G_r\Psi_G\left(\theta^h\right)\left(\mathbb{1} - \frac{1}{3}\boldsymbol{I}\otimes\boldsymbol{I}\right).
\end{aligned} \tag{5.52}$$

The partial derivative with respect to the temperature $\theta(\boldsymbol{X},t)$ yields the thermal stress tensor

$$\frac{\partial \boldsymbol{\sigma}^h_{n+c_i}}{\partial \theta^h_{n+c_i}} = \boldsymbol{M}^h_{n+c_i} = \frac{\partial \boldsymbol{\sigma}^h_{\mathrm{eq,n+c_i}}}{\partial \theta^h_{n+c_i}} + \frac{\partial \boldsymbol{\sigma}^h_{\mathrm{tr,n+c_i}}}{\partial \theta^h_{n+c_i}}. \tag{5.53}$$

The equilibrium part results in

$$\frac{\partial \boldsymbol{\sigma}^h_{\mathrm{eq}}}{\partial \theta^h} = \left(\psi_4 + \psi_6(\mathrm{tr}\boldsymbol{H}^h) + \psi_7\left(\theta^h - \theta_0\right)\right)\boldsymbol{I}, \tag{5.54}$$

while the transient part is given by

$$\begin{aligned}
\frac{\partial \boldsymbol{\sigma}^h_{\mathrm{tr}}}{\partial \theta^h} &= \sum_r \left[\frac{\partial \Psi_K\left(\theta^h\right)}{\partial \theta^h}K_r\left(\mathrm{tr}\boldsymbol{H}^h - \mathrm{tr}\boldsymbol{\mathcal{Z}}^h_r\right) - \frac{\partial \Psi_\alpha\left(\mathrm{tr}\boldsymbol{H}^h, \theta^h\right)}{\partial \mathrm{tr}\boldsymbol{H}^h}3\alpha_r K_r\left(\mathrm{tr}\boldsymbol{H}^h - \mathrm{tr}\boldsymbol{\mathcal{Z}}^h_r\right)\right. \\
&\quad \left. - \frac{\partial \Psi_\alpha\left(\mathrm{tr}\boldsymbol{H}^h, \theta^h\right)}{\partial \theta^h}K_r\left(3\alpha_r\left(\theta^h - \theta_0\right) + \zeta^h_r\right) - 3\alpha_r K_r\Psi_\alpha\left(\mathrm{tr}\boldsymbol{H}^h, \theta^h\right)\right]\boldsymbol{I} \\
&\quad + \sum_r \frac{\partial \Psi_G\left(\theta^h\right)}{\partial \theta^h}2G_r\left(\mathrm{dev}\boldsymbol{H}^h - \mathrm{dev}\boldsymbol{\mathcal{Z}}^h_r\right).
\end{aligned} \tag{5.55}$$

Next, we calculate the derivatives of the thermal stress tensor. Its change with respect to the internal variables $\boldsymbol{\mathcal{Z}}_l(\boldsymbol{X},t)$ leads to

$$\frac{\partial \boldsymbol{M}^h}{\partial \boldsymbol{\mathcal{Z}}^h_l} = \left(-\frac{\partial \Psi_K\left(\theta^h\right)}{\partial \theta^h}K_l + 3\alpha_l K_l\frac{\partial \Psi_\alpha\left(\mathrm{tr}\boldsymbol{H}^h, \theta^h\right)}{\partial \mathrm{tr}\boldsymbol{H}^h}\right)\boldsymbol{I}\otimes\boldsymbol{I} - \frac{\partial \Psi_G\left(\theta^h\right)}{\partial \theta^h}2G_l\left(\mathbb{1} - \frac{1}{3}\boldsymbol{I}\otimes\boldsymbol{I}\right). \tag{5.56}$$

The derivative with respect to the remaining internal variable $\zeta_l(\boldsymbol{X},t)$ read

$$\frac{\partial \boldsymbol{M}^h}{\partial \zeta^h_l} = -K_l\frac{\partial \Psi_\alpha\left(\mathrm{tr}\boldsymbol{H}^h, \theta^h\right)}{\partial \theta^h}\boldsymbol{I}. \tag{5.57}$$

Finally, we calculated the change in terms of the strain $\boldsymbol{H}(\boldsymbol{X},t)$ and the temperature $\theta(\boldsymbol{X},t)$. The former is conveniently split into its equilibrium and transient part,

$$\frac{\partial \boldsymbol{M}^h}{\partial \boldsymbol{H}^h} = \frac{\partial \boldsymbol{M}^h_{\mathrm{eq}}}{\partial \boldsymbol{H}^h} + \frac{\partial \boldsymbol{M}^h_{\mathrm{tr}}}{\partial \boldsymbol{H}^h}. \tag{5.58}$$

The equilibrium term is simply given by

$$\frac{\partial \boldsymbol{M}^h_{\mathrm{eq}}}{\partial \boldsymbol{H}^h} = \psi_6 \boldsymbol{I}\otimes\boldsymbol{I}, \tag{5.59}$$

while the transient part assumes a more complicated expression,

$$\begin{aligned}\frac{\partial \boldsymbol{M}^h_{\mathrm{tr}}}{\partial \boldsymbol{H}^h} = \sum_r \left(\frac{\partial \Psi_K\left(\theta^h\right)}{\partial \theta^h} K_r - \frac{\partial \Psi_\alpha\left(\mathrm{tr}\boldsymbol{H}^h, \theta^h\right)}{\partial \mathrm{tr}\boldsymbol{H}^h} 6\alpha_r K_r \right) \boldsymbol{I}\otimes\boldsymbol{I} \\ + \sum_r \frac{\partial \Psi_G\left(\theta^h\right)}{\partial \theta^h} 2G_r \left(\mathbb{1} - \frac{1}{3}\boldsymbol{I}\otimes\boldsymbol{I} \right).\end{aligned} \tag{5.60}$$

The change in temperature of the thermal stress tensor $\boldsymbol{M}(\boldsymbol{X},t)$ finally results in

$$\frac{\partial \boldsymbol{M}^h}{\partial \theta^h} = \psi_7 \boldsymbol{I} - \sum_r 6\alpha_r K_r \frac{\partial \Psi_\alpha\left(\mathrm{tr}\boldsymbol{H}^h, \theta^h\right)}{\partial \theta^h} \boldsymbol{I}. \tag{5.61}$$

The same procedure is applied to the remaining internal variables, the internal dissipation, structural viscous heating, specific heat capacity and the thermoviscoelastic shift factor. Resulting equations are summarized in Appendix A.

5.2.2. Update of the Internal Variables

Since the update of the internal variables $\boldsymbol{\mathcal{E}}(\boldsymbol{X},t)$ is essential for the correct application of the algorithm, it is worthwhile to take a closer look at the steps involved. Equation (5.7) already reflects the basic procedure, but we shall provide further detail in order to prevent erroneous evaluations of the $\boldsymbol{B}$-matrices and highlight some difficulties relating to strain transformations between the element and the material interface. The update usually takes place at local integration point level after each global iteration in terms of the strain and temperature increments $\Delta\boldsymbol{H}(\boldsymbol{X},t)$ and $\Delta\theta(\boldsymbol{X},t)$, the former being more complicated to handle. By using part of the expression in parentheses of equation $(5.7)_3$ at time t_{n+c_i} for the jth iteration and applying the chain rule twice yields $(l = 1, \ldots, m)$

$$\begin{aligned}\frac{\partial \boldsymbol{L}^j_{l,n+c_i}}{\partial \boldsymbol{u}_{n+c_i}} \Delta\boldsymbol{u}^j_{n+c_i} + \frac{\partial \boldsymbol{L}^j_{l,n+c_i}}{\partial \theta_{n+c_i}} \Delta\theta^j_{n+c_i} &= \frac{\partial \boldsymbol{L}^j_{l,n+c_i}}{\partial \boldsymbol{E}_{n+c_i}} \frac{\partial \boldsymbol{E}^j_{n+c_i}}{\partial \boldsymbol{u}_{n+c_i}} \Delta\boldsymbol{u}^j_{n+c_i} + \frac{\partial \boldsymbol{L}^j_{n+c_i}}{\partial \theta_{n+c_i}} \Delta\theta^j_{n+c_i} \\ &= \frac{\partial \boldsymbol{L}^j_{l,n+c_i}}{\partial \boldsymbol{H}_{n+c_i}} \frac{\partial \boldsymbol{H}^j_{n+c_i}}{\partial \boldsymbol{E}_{n+c_i}} \Delta\boldsymbol{E}^j_{n+c_i} + \frac{\partial \boldsymbol{L}^j_{l,n+c_i}}{\partial \theta_{n+c_i}} \Delta\theta^j_{n+c_i}, \\ &= \frac{\partial \boldsymbol{L}^j_{l,n+c_i}}{\partial \boldsymbol{H}_{n+c_i}} \mathbb{P}^j_{n+c_i} \Delta\boldsymbol{E}^j_{n+c_i} + \frac{\partial \boldsymbol{L}^j_{l,n+c_i}}{\partial \theta_{n+c_i}} \Delta\theta^j_{n+c_i},\end{aligned} \tag{5.62}$$

where the matrix $\mathbb{P} := \frac{\partial \boldsymbol{H}}{\partial \boldsymbol{E}}$ is the transformation matrix defined in [101] (equation $(6)_2$ in the reference). This enables us to calculate the increments $\Delta\boldsymbol{H}(\boldsymbol{X},t)$ of the Hencky strain using the formula

$$\Delta\boldsymbol{H}^{j}_{n+c_i} = \mathbb{P}^{j}_{n+c_i}\Delta\boldsymbol{E}^{j}_{n+c_i} = \mathbb{P}^{j}_{n+c_i}\sum_{I=1}^{nel}\boldsymbol{B}^{j}_{I,n+c_i}\Delta\boldsymbol{u}^{j}_{I,n+c_i}, \quad i = 1,\dots,s. \tag{5.63}$$

Notice that the evaluation of the $\boldsymbol{B}$- and $\mathbb{P}$-matrices corresponds to the displacements $\boldsymbol{u}^{j}_{n+c_i}$ *before* the current iteration. Having the increments of the Hencky strains (5.63) at hand, we can now calculate those of the internal variables as $(r = 1,\dots,m)$

$$\Delta\boldsymbol{\mathcal{E}}^{j}_{r,n+c_i} = -\left[\frac{\partial \boldsymbol{L}^{j}_{l,n+c_i}}{\partial \boldsymbol{\mathcal{E}}_{r,n+c_i}}\right]^{-1}\left[\boldsymbol{L}^{j}_{l,n+c_i} + \frac{\partial \boldsymbol{L}^{j}_{l,n+c_i}}{\partial \boldsymbol{H}_{n+c_i}}\Delta\boldsymbol{H}^{j}_{n+c_i} + \frac{\partial \boldsymbol{L}^{j}_{l,n+c_i}}{\partial \theta_{n+c_i}}\Delta\theta^{j}_{n+c_i}\right]. \tag{5.64}$$

Certainly, the inverse matrix is always interpreted as symbolic notation to represent the linear system of equations and is never determined explicitly. Instead, it is recommended to use the solutions known from previous calculations of the element stiffness matrix and the residual vector (see Remark 22 on page 97). Thus, the solution of the linear system of equations with multiple right-hand sides should be saved beforehand in the history fields for direct reuse when updating the internal variables using the formula

$$\boldsymbol{\mathcal{E}}^{j+1}_{r,n+c_i} = \boldsymbol{\mathcal{E}}^{j}_{r,n+c_i} + \Delta\boldsymbol{\mathcal{E}}^{j}_{r,n+c_i}, \quad r = 1,\dots,m. \tag{5.65}$$

5.2.3. Some Implementation Details

Problems Arising From Ill-Conditioned Matrices

In general, Prony series include a wide spectrum of relaxation times to properly account for the complex viscous material behavior of amorphous polymers. However, large differences in these time scales may result in very ill-conditioned local matrices $\frac{\partial \boldsymbol{L}}{\partial \boldsymbol{\mathcal{E}}}$ appearing in equation (5.13), which are required for the update of the internal variables $\boldsymbol{\mathcal{E}}(\boldsymbol{X},t)$ after each global iteration. A problem resulting from minor inaccuracies in the calculation of the internal variables occurs during the calculation of the internal dissipation $\mathcal{D}_{\text{int}}(\boldsymbol{X},t)$ and the structural viscous heating $\mathcal{H}_{\text{in}}(\boldsymbol{X},t)$ in the following global iteration. These quantities are determined according to equation (3.51) on page 58 and (3.55) on page 59, respectively. As is evident, the relaxation times appear in the denominator of these expressions. For very small values induced by a small shift factor in the rubbery regime the fractions become very large (for example in the order of 10^{15}). Normally, the expressions in parentheses should vanish, since very small relaxation times imply an *instantaneous* quasi-elastic response of the corresponding relaxation mechanism. However, due to the limited accuracy of floating point operations the expressions within parentheses in the equations of the internal dissipation and the structural thermoviscoelastic heating are close to but still unequal zero, causing small errors which eventually destabilize the entire algorithm. As a remedy, it is recommended to compare the current time step size with the shifted relaxation time and to consider the corresponding relaxation mechanism only when the ratio $\frac{a\tau}{\Delta t_n}$ is greater than a prescribed tolerance, for example 10^{-6}. Otherwise, the relaxation mechanism should be considered as quasi-elastic, which relaxes instantaneously and, therefore, does not contribute to the material stiffness.

Storage Requirements in Case of Multistage Methods

The material formulation based on Prony parameters implies a large quantity of internal variables, which increases with the number m of relaxation mechanisms used. Furthermore, in case of an s-stage DIRK method the velocities of *all* stages have to be saved, since the solution of the current stage depends on the values of preceding stages. The local error estimation for the adaptive step size controller likewise requires the velocities of all internal variable for every stage. In order to get an impression on the required storage requirements, consider the example listed in Table 5.1. The table

$\boldsymbol{\mathcal{E}}_n$	$8 \times m$
$\boldsymbol{\mathcal{E}}_{n+1}$	$8 \times m$
$\dot{\boldsymbol{\mathcal{E}}}_{n+c_i}$	$8 \times m \times s$
$\left[\frac{\partial \boldsymbol{L}}{\partial \boldsymbol{\mathcal{E}}}\right]^{-1} \boldsymbol{L}$	$8 \times m$
$\left[\frac{\partial \boldsymbol{L}}{\partial \boldsymbol{\mathcal{E}}}\right]^{-1} \frac{\partial \boldsymbol{L}}{\partial \boldsymbol{H}}$	$48 \times m$
$\left[\frac{\partial \boldsymbol{L}}{\partial \boldsymbol{\mathcal{E}}}\right]^{-1} \frac{\partial \boldsymbol{L}}{\partial \theta}$	$8 \times m$
$\sum$	$= 8 \times m \times (10 + s)$

$\mathcal{N}$	Storage (in MB) vs. Number of stages			
	$s = 1$	$s = 2$	$s = 3$	$s = 4$
10^1	1.1264	1.2288	1.3312	1.4336
10^2	11.264	12.288	13.312	14.336
10^3	112.64	122.88	133.12	143.36
10^4	1126.4	1228.8	1331.2	1433.6
10^5	11 264	12 288	13 312	14 336

Table 5.1.: Illustration of the storage requirement to integrate the material model developed in Section 3.4 using an s-stage DIRK method. Left: length of the history array to save all material related internal variable data (m is the number of relaxation mechanisms). Right: storage requirement in Megabytes (MB) assuming $m = 20$ and 8 integration points per element. $\mathcal{N}$ is the total number of elements within the mesh implementing the material model.

on the left shows individual contributions which need to be saved in the history fields. For single-step methods such as DIRK methods, the previous solution of the internal variables $\boldsymbol{\mathcal{E}}_n$ is required in order to calculate the solution at the following time step. The solution $\boldsymbol{\mathcal{E}}_{n+1}$ itself is updated after each global iteration. Rate terms $\dot{\boldsymbol{\mathcal{E}}}_{n+c_i}$, $i = 1, \dots, s$, have to be saved for all stages simultaneously, as already indicated above. Finally, it is advisable to save the solutions of the local system of equations with multiple right-hand sides (5.13) on page 97 in order to spare computational overhead when updating the internal variables after each global iteration, see Section 5.2.2. In total, the history field requires storage for $8 \times m \times (10 + s)$ floating point numbers at each integration point, where m denotes the number of Maxwell elements and s is the number of stages of the Runge-Kutta method. The tabular data shown on the right of Table 5.1 summarizes the storage requirement in Megabytes to integrate the material model developed in Section 3.4, depending on the total number $\mathcal{N}$ of elements and the total number of Runge-Kutta stages for the special case of $m = 20$ relaxation mechanisms and 8-node solid elements. As is evident, increasing the stage number of the Runge-Kutta scheme does not significantly increase the storage requirement compared to the influence of the total number of elements within the mesh implementing the material model.

Estimation of the Local Time Integration Error

The adaptive time-stepping procedure outlined in Section 4.3 requires the error estimation of the internal variables. The error is calculated on local integration point level at the end of each time step according to equation $(4.73)_2$ on page 92 using the maximum norm. A fragment of the code illustrating the error calculation on integration point

level in the FEM program `FEAP` is depicted in Figure 5.1. To this end, a nested loop over all Maxwell elements and every stage of the Runge-Kutta method is used (line 20 and 24 in the code snippet, respectively). Within the inner loop, the known stage velocities of the ith Maxwell element are successively read. For EDIRK methods with an explicit first stage the velocity of the first stage is simply given by the corresponding value of the former time step (line 27), hence the abbreviation FSAL meaning first same as last. The values of the previous time step are collectively saved in the history field `h1`. Otherwise, the velocity is read from history field `h2` corresponding to the current time step (line 29). The evaluation of the mixed absolute error norm $(4.73)_2$ on page 92 is done in lines 37 and 38. By using an *embedded* Runge-Kutta scheme, the local error estimation is simply carried out in line 32. Since the error calculation is performed in parallel using `OpenMP`, each thread is assigned a local copy of the global variable `int_var_error`, which represents the error stemming from the numerical integration of the evolution equations of the internal variables (`int_var_error` is declared as `!$omp threadprivate` on program level).

```
1  subroutine calculate_error
2  !
3  !   PURPOSE:
4  !       Calculate error of internal variables (IV) for automatic
5  !       time-stepping algorithm using the maximum norm.
6  !
7      use Runge_Kutta, only: mat_e_r, mat_e_a, &   ! User specified error tolerances.
8                             int_var_err           ! Global variable "int_var_err" is
9                                                   ! declared as !$OMP THREADPRIVATE.
10     use Butcher_tableaux, only: e                ! Error parameters of DIRK method.
11
12     real(8) :: local_error(8)                    ! Local error.
13     real(8) :: xi_velo(8)                        ! Rates of IV.
14     real(8) :: ratio(8)                          ! Auxiliary variable.
15     integer :: stage                             ! Loop variable.
16
17     local_error = 0.d0
18
19     ! Loop over all Maxwell elements.
20     do i = 1, nv
21         index = 1+8*(stages+1)*(i-1)+(stages-1)*8
22
23         ! Estimate local error.
24         do stage = 1, stages
25             ! Get velocities of all stages.
26             if (edirk .and. stage == 1) then
27                 xi_velo = h1(index:index+7)   ! (FSAL)
28             else
29                 xi_velo = h2(index+:index+7)
30             end if
31
32             local_error = local_error + dt*(e(stage)-b(stage))*xi_velo  ! See equ. (4.68).
33         end do
34
35         ! Calulate error of internal variables using maximum norm.
36         index = 1+8*(stages+1)*(i-1)+8*stages
37         ratio = abs(local_error)/(mat_e_r*abs(h1(index:index+7)+mat_e_a)
38         int_var_err = max(int_var_err, maxval(ratio))
39     end do
40
41 end subroutine calculate_error
```

Figure 5.1.: Fortran code fragment showing the calculation of the integration error of the internal variables at integration point level in `FEAP`. The error is calculated according to equation $(4.73)_2$ on page 92 using the maximum norm (lines 37 and 38). Special care has to be taken when these calculations happen in parallel. The `OpenMP` directive `!$omp threadprivate` (on program level, not shown here) ensures that each thread contains a local copy of global variable `int_var_error`. See text for further explanations.

Part III.

Modeling and Simulations

6. Validation of the Material Framework

The constitutive framework developed in Section 3.3 to model amorphous polymers through the glass transition region is validated in various experimental settings on four different polymeric systems. The experiments include dilatometry, calorimetry, uniaxial tension and compression tests as well as three-point and four-point bending tests. The polymers comprise one thermoplastic and three thermosets. Specifically, the thermosets include Diglycidyl Ether of Bisphenol A (DGEBA for short), Epoxy 459 and TCR composite 3325, while plasticized polyvinyl butyral (PVB) represents the thermoplastic. Special emphasis is on PVB, which is of major importance in civil engineering applications (see Section 3.2). Consistent experimental data for the thermosetting polymers along with comprehensive material parameters are well documented in the literature [41]. In contrast, the literature on "standard" PVB is quite restricted to DMTA. The lack of consistent experimental data on the thermomechanical behavior of PVB posed a major difficulty during the validation process. The set of material parameters used during the simulations of the different polymers are summarized in Appendix B.

6.1. Dilatometric Experiments

The validation starts with dilatometric simulations to determine the thermal expansion properties of the polymers [87]. This boils down to the determination of the temperature-dependent coefficient of thermal expansion (CTE) and related material parameters. These include the equilibrium values ψ_4 and ψ_7 (see Table 3.3 on page 52) as well as the Prony parameters α_l and the glassy parameter $\tilde{C}_2$ (see Table 3.4 on page 54). As outlined in Section 3.1.1, an amorphous polymer will change its thermal properties through the glass transition region, as indicated by the change in slope of the specific volume vs temperature curve shown in Figure 3.2 on page 34. It is of utmost importance to accurately capture the dilatation behavior of an amorphous polymer subjected to *nonisothermal* conditions during transient analyses. As is evident from the literature [16–19, 21–23, 27–31], most engineering approaches to model PVB not even consider the volumetric behavior under *isothermal* conditions. Hence, these material models are restricted to homogeneous temperature states above the glass transition, where the polymer is incompressible and in a state of thermodynamic equilibrium. In order to determine the temperature dependency of the *volumetric* coefficient of thermal expansion, a simple difference equation is derived, which is evaluated in a post-processing step. The formula is given for an isotropic body under homogeneous deformation due to a variation in temperature as

$$\frac{1}{v}\frac{dv}{d\theta} \approx 3\hat{\alpha}(\theta) \quad \Rightarrow \quad 3\alpha_{n+1} \approx \frac{1}{\mathrm{tr}\boldsymbol{H}_{n+1}} \frac{\mathrm{tr}\boldsymbol{H}_{n+1} - \mathrm{tr}\boldsymbol{H}_n}{\theta_{n+1} - \theta_n} \tag{6.1}$$

in terms of the Hencky strain $\boldsymbol{H}(\boldsymbol{X}, t)$. The simulations run with a single 8-node solid finite element with prescribed temperature values at the nodal points (*temperature driven experiment*). The temporal integration follows the Radau-IIA scheme from Table 4.4 on page 91 (*implicit Euler method*).

6.1.1. Thermoplastic—Plasticized PVB

The validation of plasticized PVB bases on dilatometric measurements found in [70], which are the only one available to the best of our knowledge. The author mixed 72 wt.% of PVB resin (Mowital® B 70 SFP)[1] with 28 wt.% of triethylene glycol-di-(2-ethylbutyrate) as plasticizer. In order to erase the thermal history, the sample was first heated well above the glass transition temperature. Afterwards, it was cooled from 140 °C down to −35 °C at constant rate 15 °C h^{-1}. For the actual measurement of the specific volume the sample was reheated at 14 °C h^{-1}. For the numerical simulation a constant step size $\Delta t_n = 200$ s was chosen to allow for a sufficiently accurate approximation of the volumetric coefficient of thermal expansion (CTE) by means of formula $(6.1)_2$. The material parameters used for the simulation of PVB are summarized in Appendix B. A comparison between the predicted values with those of the measurements is shown in Figure 6.1.

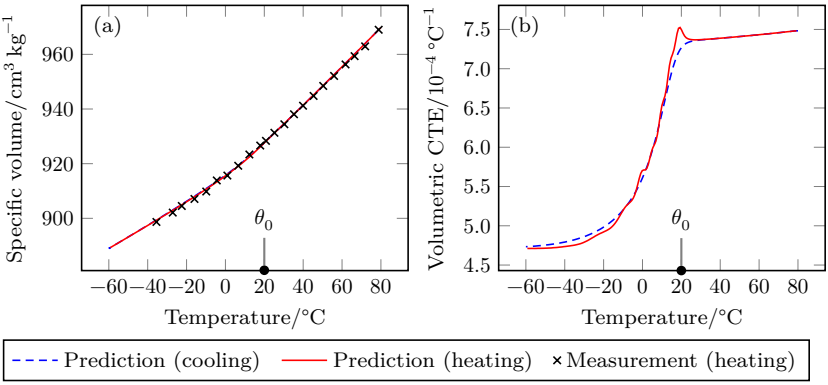

Figure 6.1.: Results of the dilatometric analysis of PVB: (a) comparison of the measured specific volume [70] and numerical predictions and (b) *volumetric* coefficient of thermal expansion (CTE) inferred from the first diagram by means of equation $(6.1)_2$. The cooling rate was 15 °C/h, while the heating rate was 14 °C/h. The reference temperature is $\theta_0 = 20$ °C.

On the left-hand side the specific volume is plotted against the temperature. Notice that the simulation goes down to −60 °C to span a wider range of temperature values. The agreement is excellent. The change in slope is less pronounced for the plasticized product compared to the PVB resin, see Figure 3.2 on page 34. The diagram on the right illustrates the change of the volumetric CTE derived from the left diagram using formula $(6.1)_2$. The small bumps on the heating curve (near 0 °C) stem from

[1] The experiment was conducted in 1968. The product name does not appear in current product sheets [122].

the quality and number of the Prony parameters K_l and α_l. We had to choose these parameters manually and, therefore, only considered eight relaxation mechanisms for the sake of simplicity[2]. The author of [70] also provided values for the volumetric CTE at approximately $\pm 50\,°\mathrm{C}$. These are $3\alpha_{-50\,°\mathrm{C}} = 4.71 \times 10^{-4}\,°\mathrm{C}^{-1}$ and $3\alpha_{50\,°\mathrm{C}} = 7.49 \times 10^{-4}\,°\mathrm{C}^{-1}$, which are in good agreement with our prediction.

6.1.2. Thermosetting Polymers

Next, we consider the thermosetting polymers DGEBA, epoxy 459 and epoxy 3325, whose material data and experimental curves are described in [41]. The authors used *thermomechanical analysis* (TMA) to determine the specific volume and to derive the temperature-dependent volumetric CTE. Following the usual heating into the rubbery regime, the samples were cooled at a rate of $2\,°\mathrm{C\,min}^{-1}$ well below the glass transition and subsequently reheated at the same rate. In order to account for the faster thermal treatment compared to the PVB experiment, the step size for the simulation was reduced to take on the constant value $\Delta t_n = 10\,\mathrm{s}$. A compilation of the material parameters of the thermosetting polymers used for the simulations is given in Appendix B. Figures 6.2 to 6.4 summarize the results of the analyses. The diagrams on the left show

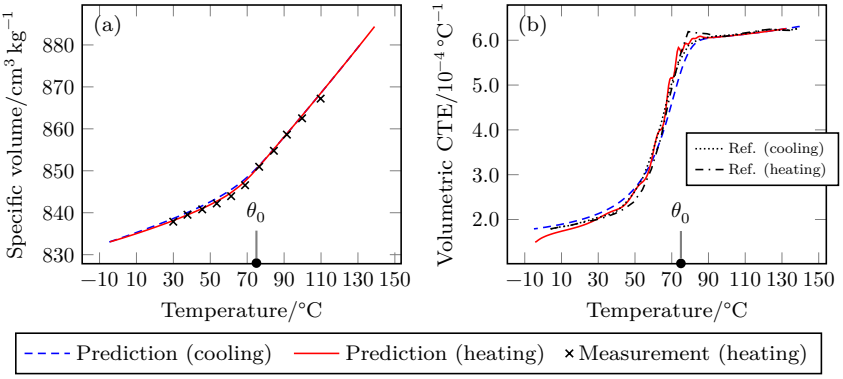

Figure 6.2.: Results of the dilatometric analysis of DGEBA: (a) comparison of the measured specific volume [41] and numerical predictions and (b) comparison of the *volumetric* coefficient of thermal expansion (CTE) with reference values taken from the same literature. The volumetric CTE has been inferred from the left diagram by means of equation $(6.1)_2$. The cooling and heating rates were $2\,°\mathrm{C/min}$. The reference temperature is $\theta_0 = 75\,°\mathrm{C}$.

the numerical prediction of the specific volume. The agreement with the measurements for the DGEBA sample is excellent (no data are available for the remaining polymers). The numerical prediction for the volumetric CTE depicted on the right is also in good agreement with the literature values. Notice that the ratio between the rubbery and the glassy CTE is roughly three, indicating its significance when thermal stresses occur inside engineering structures made up of amorphous polymers under nonisothermal

[2] The values α_l were all equated, only the bulk parameters K_l were chosen such that the curve of the specific volume is reproducible with the simulation. In practice, this is the usual modus operandi, since viscoelastic data on the bulk behavior is rare.

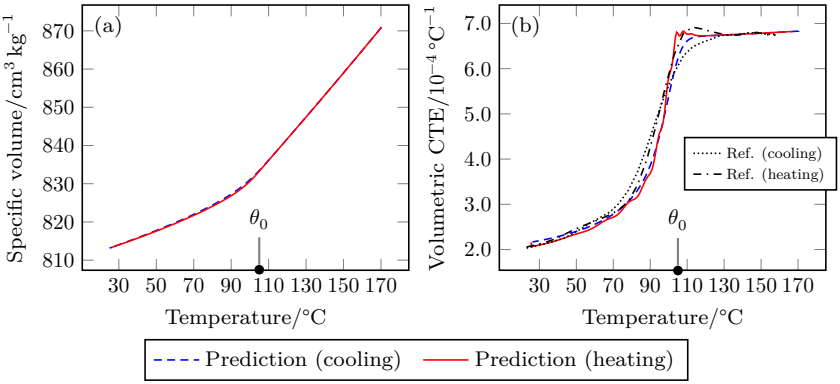

Figure 6.3.: Results of the dilatometric analysis of the 459 epoxy: (a) predictions for the cooling and heating curve of the specific volume and (b) comparison of the *volumetric* coefficient of thermal expansion (CTE) with reference values taken from the literature [41]. The volumetric CTE has been inferred from the left diagram by means of equation $(6.1)_2$. The cooling and heating rates were 2 °C/min. The reference temperature is $\theta_0 = 105\,°C$.

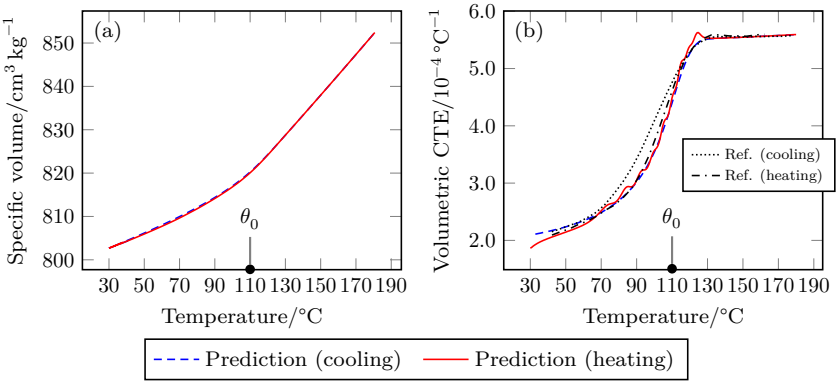

Figure 6.4.: Results of the dilatometric analysis of the 3325 epoxy: (a) predictions for the cooling and heating curve of the specific volume and (b) comparison of the *volumetric* coefficient of thermal expansion (CTE) with reference values taken from the literature [41]. The volumetric CTE has been inferred from the left diagram by means of equation $(6.1)_2$. The cooling and heating rates were 2 °C/min. The reference temperature is $\theta_0 = 110\,°C$.

conditions. Although it may appear that plasticized polymers tend to have a reduced ratio of the rubbery and the glassy CTE (compare with plasticized PVB), this is generally not the case. For further information on the influence of plasticizer content on the thermal expansion coefficient of plastic materials the reader is referred to [87, p. 281].

6.2. Calorimetric Experiments

Calorimetric experiments serve as the second test case to validate the thermal properties of the polymers [87]. This boils down to the determination of the material parameters related to the *constant deformation* specific heat capacity (3.65). These comprise the equilibrium values ψ_5 and ψ_8 (see Table 3.3 on page 52) as well as the Prony parameters β_l and the glassy parameters $\tilde{C}_4$ and $\tilde{C}_5$ (see Table 3.4 on page 54). At this point it is important to differentiate the specific heat at constant deformation from that at constant pressure. While the former is usually the appropriate choice for theoretical considerations, the latter is more pertinent to experimental investigations [123, p. 159]. The measurements found in the literature were made using either *adiabatic calorimetry* [124] or *differential scanning calorimetry* (DSC) to measure the *constant pressure* heat capacities. Strictly speaking, it is therefore inaccurate to infer, for example, the equilibrium values ψ_5 and ψ_8 directly from the experimental findings, since these relate to experiments with different boundary conditions. Nevertheless, the measurements referring to constant pressure experiments serve as a reasonable starting point[3]. Plotting of the predicted heat capacity at constant pressure is performed during post-processing and first requires an analytical expression. To this end, we apply the Legendre transformation to calculate the *Gibbs energy* $g(\boldsymbol{X}, t)$ [48, p. 323], from which the specific heat *at constant stress* follows by differentiating twice with respect to temperature,

$$g(\boldsymbol{X}, t) = \psi(\boldsymbol{X}, t) + \frac{1}{\rho_0(\boldsymbol{X})} \boldsymbol{\sigma}(\boldsymbol{X}, t) \cdot \boldsymbol{H}(\boldsymbol{X}, t) \quad \Rightarrow \quad c(\boldsymbol{X}, t) = -\theta \frac{\partial^2 g}{\partial \theta^2}(\boldsymbol{X}, t). \tag{6.2}$$

However, formula $(6.2)_2$ does not capture the effect of a change in the internal variables. Instead, we calculate the entropy $S(\boldsymbol{X}, t)$ at constant stress and apply a simple difference equation to approximate the heat capacity according to

$$S(\boldsymbol{X}, t) = -\frac{\partial g}{\partial \theta}(\boldsymbol{X}, t) \quad \overset{(6.2)}{\Rightarrow} \quad c_{n+1}(\boldsymbol{X}) \approx \theta_{n+1}(\boldsymbol{X}) \frac{S_{n+1}(\boldsymbol{X}) - S_n(\boldsymbol{X})}{\theta_{n+1}(\boldsymbol{X}) - \theta_n(\boldsymbol{X})}. \tag{6.3}$$

Equation $(6.3)_2$ will be used for the upcoming calculations of the specific heat capacity. As with the dilatometric experiments, the simulations run with a single 8-node solid finite element with prescribed nodal temperature values and use the Radau-IIA scheme from Table 4.4 on page 91 as the temporal integrator.

6.2.1. Thermoplastic—Plasticized PVB

The validation of plasticized PVB bases on adiabatic calorimetric measurements found in [70]. The properties of the PVB sample are the same as those outlined in Section 6.1.1. To erase the thermal history, the sample was first heated well above the glass transition temperature ("phyiscal aging is thermoreversible" [82, p. 14]). Afterwards, it was cooled from 140 °C down to −60 °C at constant rate 15 °C h^{-1}. For the actual measurement of the specific heat the sample was reheated at constant rate 14 °C h^{-1} up to 120 °C, followed by a heating rate of 11 °C h^{-1}. We do not know whether the measurement was performed at constant deformation or at constant pressure, but we opted for a simulation assuming constant pressure for the sake of convenience. A constant step size

[3] See [125] for a comparison between the heat capacities at constant pressure and constant deformation of several amorphous and semi-crystalline polymers.

$\Delta t_n = 200\,\mathrm{s}$ proved sufficient for a good approximation of the specific heat capacity by means of formula $(6.3)_2$. The material parameters used for the simulation of PVB are summarized in Appendix B. Figure 6.5 shows the results of the analysis.

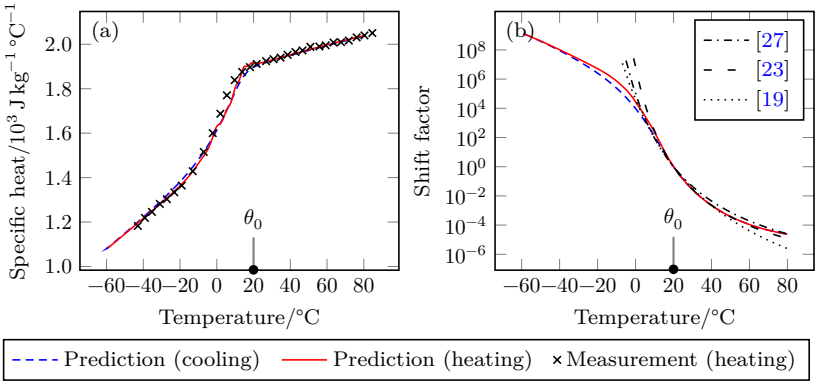

Figure 6.5.: Results of the calorimetric analysis of PVB: (a) comparison of the measured specific heat capacity [70] and numerical predictions *at constant pressure* via equation $(6.3)_2$ and (b) corresponding shift factor and some WLF fits taken from the literature. The cooling rate was 15 °C/h, while the heating rate was 14 °C/h. The reference temperature is $\theta_0 = 20\,°\mathrm{C}$.

On the left-hand side the numerical prediction of the (constant stress) specific heat capacity is compared with experimental findings. The agreement is quite good. On the right-hand side the shift factor is plotted as a function of temperature, calculated by equation (3.68) on page 62. To determine the material parameter $U_\mathrm{p}^\mathrm{ref}$ we used the WLF approximations taken from the literature as an indication for the shift function. Note, however, that the curves derived from DMTA relate to distinct PVB products from different manufactures. Clearly, the shift factor defined by equation (3.68) shows the characteristic leveling-off in the glassy state. In contrast, the empirical WLF approach (3.69) diverges at low temperatures, making it unsuitable for calculations within the glassy regime.

6.2.2. Thermosetting Polymers

Next, we consider the thermosetting polymers DGEBA, epoxy 459 and epoxy 3325, whose material data and experimental curves are described in [41]. The experimental situation is different from that of PVB. The authors used DSC to determine the constant pressure specific heat capacities. Following the usual heating into the rubbery regime, the samples were cooled with a rate of $5\,°\mathrm{C\,min^{-1}}$ well below the glass transition and subsequently reheated at the same rate. To account for the faster thermal treatment the step size for the simulation is reduced to take on the constant value $\Delta t_n = 10\,\mathrm{s}$. A compilation of the material parameters of the thermosetting polymers used during the simulations is given in Appendix B. The results of the simulations are summarized in Figures 6.6 to 6.8. The first diagram in Figure 6.6 compares the numerical predictions with the experimental findings of the DGEBA polymer.

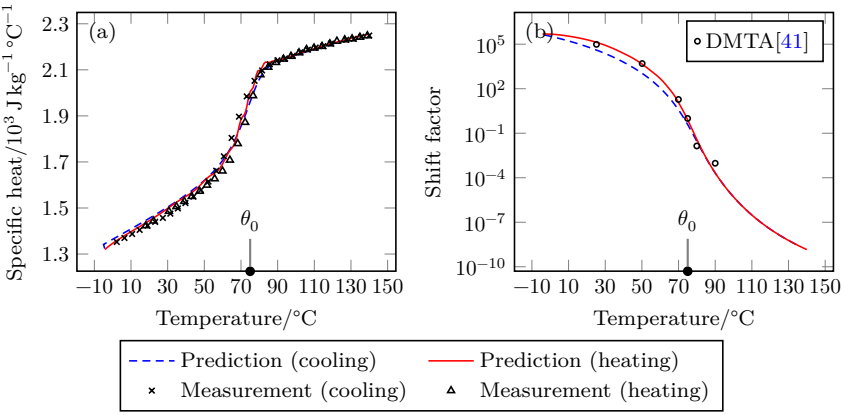

Figure 6.6.: Results of the calorimetric analysis of DGEBA: (a) comparison of the measured specific heat capacity *at constant pressure* [41] and numerical predictions via equation $(6.3)_2$ and (b) corresponding shift factor (3.68) and measurements from Dynamic Mechanical Thermal Analysis (DMTA) taken from the literature. The cooling and heating rates were 5 °C/min (the cooling rate of the DMTA was 1 °C/min). The reference temperature is $\theta_0 = 75\,°C$.

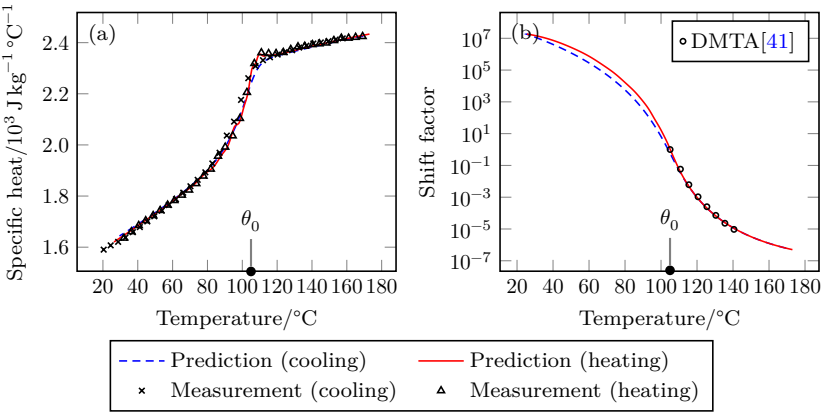

Figure 6.7.: Results of the calorimetric analysis of the 459 epoxy: (a) comparison of the measured specific heat capacity *at constant pressure* [41] and numerical predictions via equation $(6.3)_2$ and (b) corresponding shift factor (3.68) and measurements from Dynamic Mechanical Thermal Analysis (DMTA) taken from the literature. The cooling and heating rates were 5 °C/min (the cooling rate of the DMTA was 1 °C/min). The reference temperature is $\theta_0 = 105\,°C$.

The agreement of the curves is quite good. The quality of the curves directly depends on the Prony parameters β_l, which were chosen manually for all polymers. The diagram

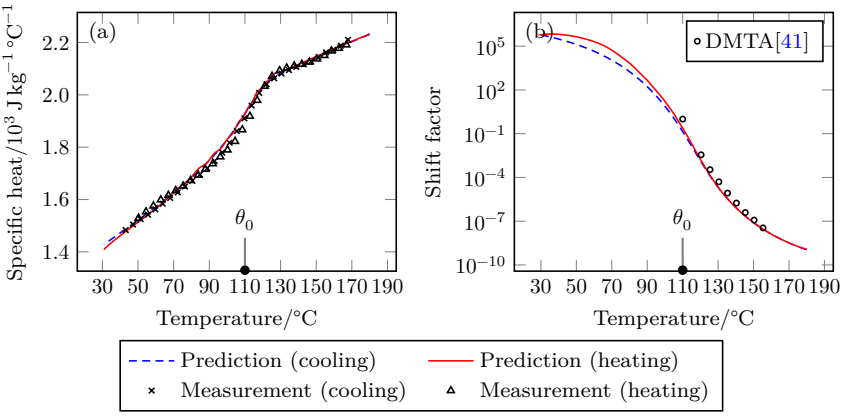

Figure 6.8.: Results of the calorimetric analysis of epoxy 3325: (a) comparison of the measured specific heat capacity *at constant pressure* [41] and numerical predictions via equation $(6.3)_2$ and (b) corresponding shift factor (3.68) and measurements from Dynamic Mechanical Thermal Analysis (DMTA) taken from the literature. The cooling and heating rates were 5 °C/min (the cooling rate of the DMTA was 1 °C/min). The reference temperature is $\theta_0 = 110\,°C$.

on the right reflects the temperature dependence of the thermoviscoelastic shift factor. The numerical prediction for cooling lies below the measurements. This is just as expected, since the cooling rates between the measurement ($1\,°C\,min^{-1}$) of the DMTA and the calorimetric simulation ($5\,°C\,min^{-1}$) differ. When the cooling rate decreases the shift factor increases, since it tends towards its equilibrium value in the glassy regime.

Since the authors also conducted experiments concerning *enthalpy relaxation* of the epoxy 459 and DGEBA polymers, we can validate our constitutive model in terms of physical aging effects described in Section 3.1.4. To this end, the experimental setting was slightly modified [41]: after cooling at $5\,°C\,min^{-1}$ from well above the glass transition, the samples were slightly aged below the glass transition temperature for two hours. Afterwards, the samples were further cooled at $5\,°C\,min^{-1}$ into the glassy regime, followed by reheating at the same rate. Figures 6.9 and 6.10 depict the results for different aging temperatures. As is evident, the reheating curves show the characteristic 'overshoot' near the glass transition [82, p. 64], [88, p. 373], a direct consequence of the aging procedure. When the aged sample is heated above the glass transition temperature, it absorbs the heat it lost during aging [82, p. 64]. The height of the peak increases with aging time, whereas the aging temperature influences its position. The (horizontal) discrepancy between the measured curves and the numerical predictions likely stem from the thermal lag inherent to DSC scans at a rate of $5\,°C\,min^{-1}$ [41, p. 4612]. The peaks of the specific heat for the DGEBA sample during reheating deviate from the experimental curves and stem from the manually fitted parameters β_l. Likewise, the aging effect is revealed by plotting the shift function against the temperature, as depicted on the right of Figures 6.9 and 6.10. During the aging phase, the shift factor grows vertically towards its equilibrium value, thereby increasing the

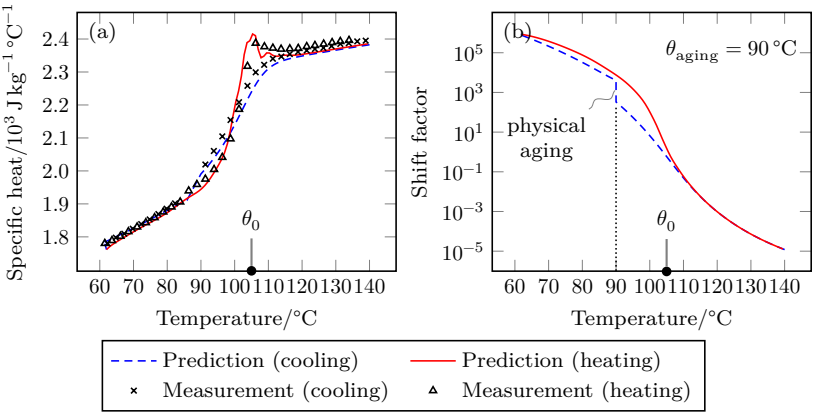

Figure 6.9.: Enthalpy relaxation using the example of epoxy 459: (a) comparison of the measured specific heat capacity *at constant pressure* [41] and numerical predictions via equation $(6.3)_2$ and (b) corresponding shift factor (3.68) for the aging temperature $\theta_{\text{aging}} = 90\,°\text{C}$. The cooling curve of the shift factor grows upwards during physical aging, resulting in the characteristic bump in the specific heat during heating. The cooling and heating rates were 5 °C/min, the aging time was 2 hours. The reference temperature is $\theta_0 = 105\,°\text{C}$.

relaxation times. Upon reheating above the glass transition temperature, the polymer rapidly reaches thermodynamic equilibrium and the shift function eventually converges into the rubbery regime.

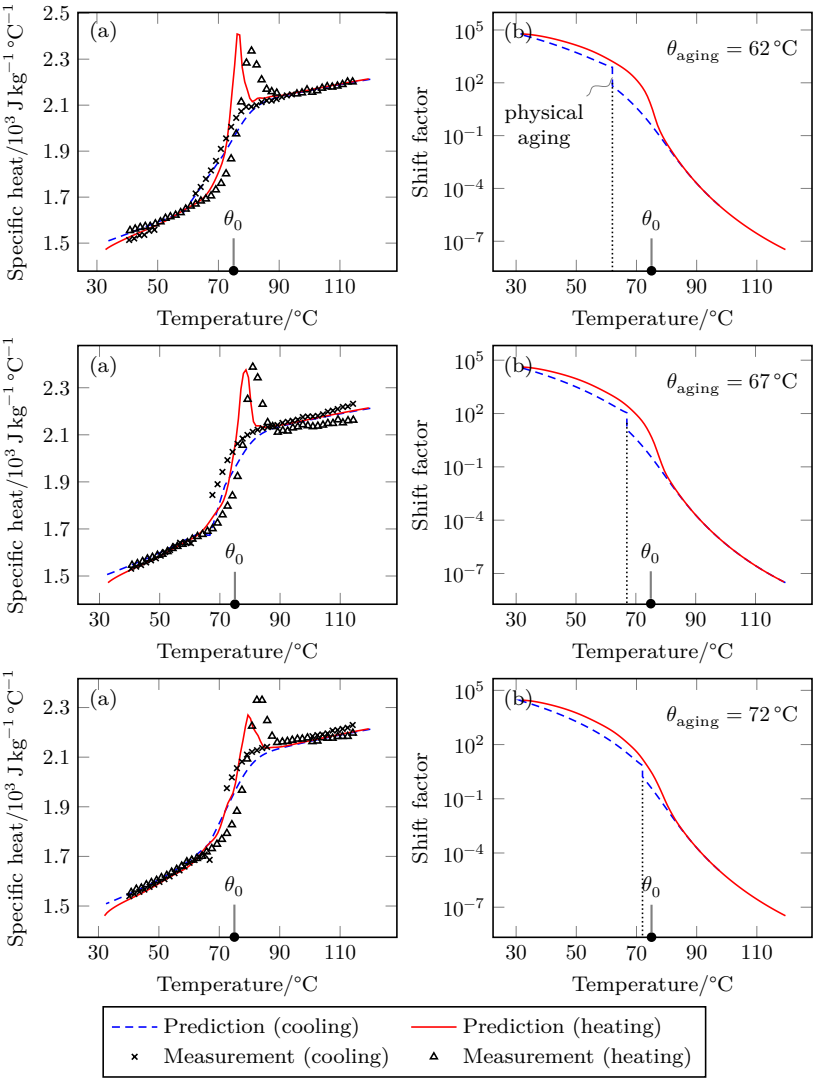

Figure 6.10.: Enthalpy relaxation using the example of DGEBA: (a) comparison of the measured specific heat capacities *at constant pressure* [41] and numerical predictions via equation $(6.3)_2$ and (b) shift factors (3.68) for three different aging temperatures θ_{aging}. The cooling curves of the shift factors grow upwards during physical aging, resulting in the characteristic bumps in the specific heat capacities during reheating. The cooling and heating rates were 5 °C/min, the aging time was 2 hours. The reference temperature is $\theta_0 = 75\,°\text{C}$.

6.3. Uniaxial Tension and Compression Tests

The next stage lies in the validation through uniaxial tension and compression tests, which are performed at different temperatures to trial the constitutive model under various thermal and mechanical load scenarios. Related material parameters are the equilibrium value ψ_2 (see Table 3.3 on page 52), glassy parameter $\tilde{C}_6$ and Prony parameters G_l (see Table 3.4 on page 54), which are usually determined via Dynamic Mechanical Thermal Analyses (DMTA). Amorphous polymers such as PVB exhibit a strong rate and temperature dependency. After cooling into the glassy state, the polymer becomes rigid and stiff and associated stress-strain relationships are nonlinear even in the small strain regime, characterized by *yield-like* behavior [68, p. 483], [36], [11]. In what follows we investigate the capability of the material formalism based on the internal variables approach to predict these phenomena for all four polymer systems. The simulations likewise run with a single 8-node solid finite element, but the procedure is different than in the preceding sections to account for the change in boundary conditions. First, a *temperature controlled* thermal simulation is performed, where the nodal temperatures change from the reference temperature at a defined rate to the test temperature at which the tension and compression tests are performed. This temperature is kept constant for a definite period of time. Afterwards, the thermodynamic state of the finite element is saved on disk. Subsequently, a mechanical simulation is performed, which uses the last state of the thermal analysis as its initial conditions. The mechanical simulation is *displacement controlled*, with the temperature degrees of freedom being fixed at the test temperature. As with the previous simulations, the temporal integration follows the Radau-IIA scheme from Table 4.4 on page 91.

6.3.1. Thermoplastic—Plasticized PVB

The difficulty inherent to the validation of "standard" polyvinyl butyral is the lack of consistent experimental data on its thermomechanical properties. While the literature is abundant with experimental findings on the dynamic shear behavior of PVB, only one reference [16] was found to quantify its bulk modulus, which the author eventually set constant[4]. The thermal behavior of PVB investigated in the preceding sections was based on experiments performed by [70], which dates back to the 1960's. However, the author did not study its mechanical behavior. Therefore, we have to base our simulations on different experiments conducted by different authors on different PVB products. Furthermore, mechanical related experiments often lack documentation on the thermal history of the PVB sample prior to testing, which is of major importance for a reliable validation of the constitutive model. Hence, we assess the thermomechanial validation of standard PVB as questionable due to the specified inconsistencies. The following simulations base on the studies of [36], who conducted uniaxial tensile tests at various strain rates and temperatures. The author did not mention the product name of the PVB sample, nor its chemical composition or plasticizer content. The paper contains stress-strain curves at various temperatures for a strain rate of $10\,\%\,\mathrm{s}^{-1}$ (engineering strain), which we adopted for the simulations, knowing that the constitutive model developed in Section 3.4 is restricted to *small* rates of strain and temperature[5]. We do

[4] The author also investigated the bulk relaxation behavior of PVB, but did not publish related material data.

[5] According to [33], experiments with strain rates up to $31.7\,\%\,\mathrm{s}^{-1}$ may be regarded as *quasistatic*. Higher strain rates suggest dynamic analyses, which are outside the scope of this communication.

not know the thermal history prior to the tensile tests. However, the simulations are based on the following thermal treatment: first, the element temperature is changed from the reference temperature at a rate of $1\,°\mathrm{C}\,\mathrm{min}^{-1}$ to the test temperature and kept there for ten minutes. Afterwards, the tensile tests are performed. Four different test temperatures are considered: 23 °C, 10 °C, 0 °C and −10 °C. The step sizes for the thermal and mechanical simulations are $\Delta t_n = 10\,\mathrm{s}$ and $\Delta t_n = 0.01\,\mathrm{s}$, respectively. The material parameters used for the tensile tests of PVB are the same as before and summarized in Appendix B. A comparison between the predicted values with those of the measurements is shown in Figure 6.11.

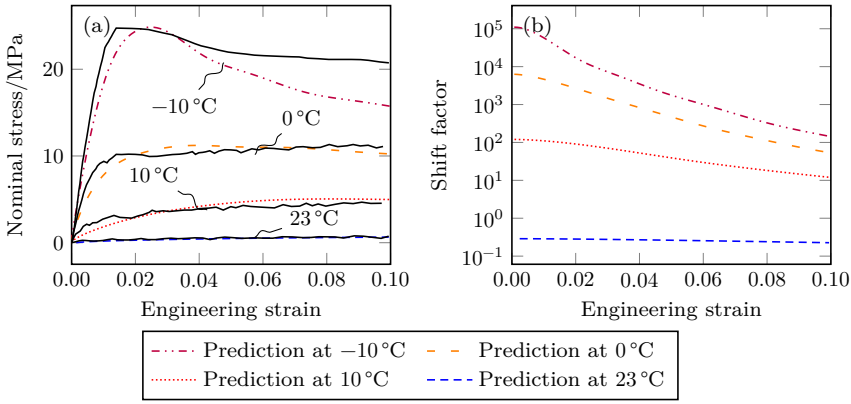

Figure 6.11.: Results of the uniaxial tensile tests of PVB at various temperatures: (a) comparison of the measured stress-strain relationships [36] for an engineering strain rate of $10\,\%\,\mathrm{s}^{-1}$ with predictions and (b) plot of the shift factors (3.68) during elongation of the material. As the sample deforms, the potential internal energy increases, leading to a reduction in the shift factor and the relaxation times. The consequence is a decrease in stiffness, resulting in a pseudo yielding-like behavior.

With the exception of the curve at −10 °C, the overall quantitative agreement is quite good. However, the results should not be overestimated in view of the inconsistencies of the literature data mentioned above and the lack in information on the thermal history prior to testing. Nevertheless, the tendency of a pronounced yield stress visible at lower temperatures proves the capability of the material model to predict (pseudo) yield-like behavior. Notice that yielding already occurs at about 1 % engineering strain (2.5 % for the simulation) at −10 °C, which is well within the usual strain and temperature range relevant for the design process of structural components. Figure 6.11 also illustrates the dependence of the shift function on current strain[6]. During elongation of the PVB sample at low temperatures, the potential internal energy increases. Consequently, the shift factor decreases, resulting in smaller relaxation times and, therefore, reduced stiffness. Hence, yielding is naturally predicted.

[6] For all the simulations, the modified version of the shift factor according to the potential internal energy (3.81) on page 67 was used.

6.3.2. Thermosetting Polymers

Experimental data on the material response of the thermosetting polymers under uniaxial tension and compression tests at various temperatures give further opportunity to investigate the nonlinear thermoviscoelastic constitutive model developed in Section 3.4. In contrast to PVB, the investigations of the thermosetting polymers are well documented in the literature [41]. The thermal history of the polymers prior to testing was as follows: first, the samples were equilibrated at the reference temperature. Next, they were cooled at a rate of $1\,°\mathrm{C}\,\mathrm{min}^{-1}$ to the test temperature, which was then held constant for 10 minutes. Finally, the samples were deformed at constant rate $1\,\%\,\mathrm{s}^{-1}$ (engineering strain). The tensile test of the DGEBA polymer was conducted on a dog-bone sample. For the compression tests, on the other hand, cylindric samples were used. All experiments were carried out below the glass transition temperature, but the test temperatures vary among the polymers due to the differences in the individual glass transition temperatures. The constant step sizes for the thermal and mechanical simulations are $\Delta t_n = 10\,\mathrm{s}$ and $\Delta t_n = 0.1\,\mathrm{s}$, respectively. The material parameters of the different polymers are the same as before, see Appendix B. Figures 6.12 to 6.14 compare the numerical predictions with the experimental findings.

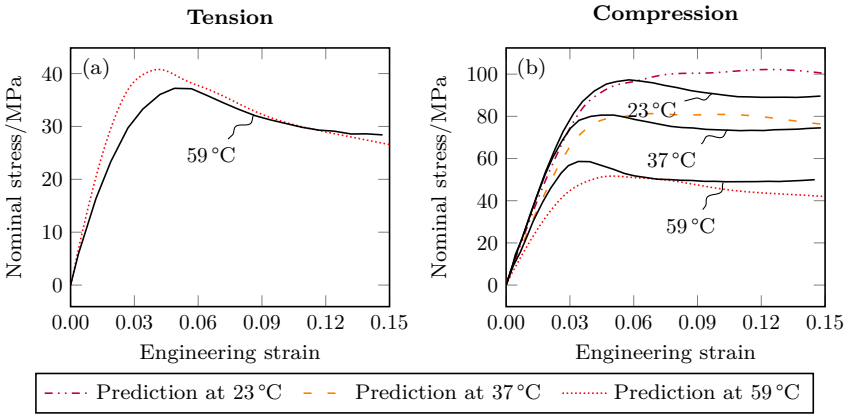

Figure 6.12.: Results of the uniaxial tension and compression tests of DGEBA at various temperatures within the glassy regime: (a) comparison of the measured stress-strain relationships [41] with predictions for tensile loading and (b) comparison for compressive loading. Clearly, pseudo yielding is predicted for both types of load application. The prescribed engineering strain rate was $1\,\%\,\mathrm{s}^{-1}$.

As is evident, the shift factor based on the potential internal energy introduced in [39] and adapted for the constitutive framework developed in Section 3.4 is capable of producing yield-like behavior in both tension and compression, see Figure 6.12. The constitutive model developed in [39], which bases on rational thermodynamics, was first applied to predict this behavior on glassy polymers alongside other phenomena such as those investigated in preceding sections. However, the internal variables approach used here is equally capable of reproducing a wide range of material behavior intrinsic to

amorphous polymers through the glass transition region. For the remaining thermosets, only compression tests were performed. Besides the stress-strain curves, Figures 6.13 and 6.14 also include the strain-dependent shift factors corresponding to the three compression tests. As is evident, the drop in the shift factor is quite pronounced at low temperatures, implying a reduction of relaxation times of several orders of magnitude during the deformation of the sample.

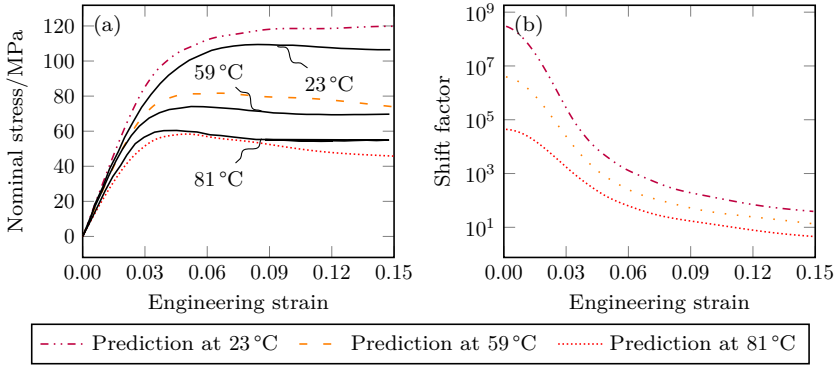

Figure 6.13.: Results of the uniaxial compression tests of the 459 epoxy at various temperatures within the glassy regime: (a) comparison of the measured stress-strain relationships [41] with predictions and (b) plot of the shift factors during compression of the material. The reduction of the shift factors leads to a reduction in stiffness, resulting in a pseudo yielding-like behavior. The prescribed engineering strain rate was $1\,\%\,\mathrm{s}^{-1}$.

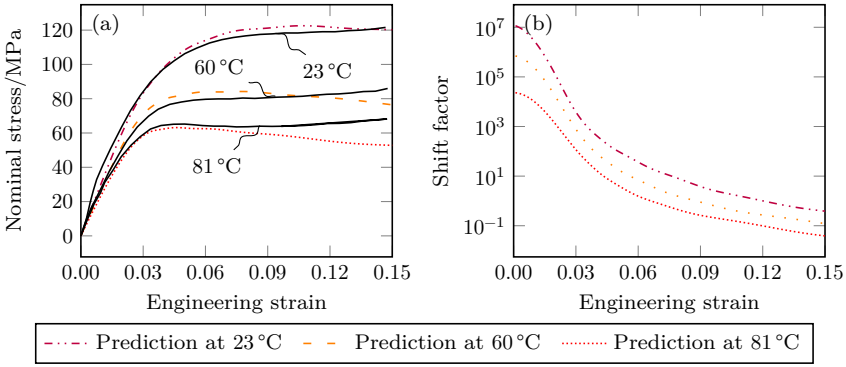

Figure 6.14.: Results of the uniaxial compression tests of the 3325 epoxy at various temperatures within the glassy regime: (a) comparison of the measured stress-strain relationships [41] with predictions and (b) plot of the shift factors during compression of the material. The reduction of the shift factors leads to a reduction in stiffness, resulting in a pseudo yielding-like behavior. The prescribed engineering strain rate was $1\,\%\,\mathrm{s}^{-1}$.

6.4. Three-Point and Four-Point Bending Tests

In this section, three-point and four-point bending tests of laminated glass with a polyvinyl butyral interlayer are simulated using the material model developed in Section 3.4. This will not only indicate whether the material implementation is correct in terms of shear deformation (the former experiments are shear stress-free configurations), but also serve as a good example to apply higher-order DIRK methods with adaptive step size selection. The material parameters for PVB are the same as in the preceding sections and can be found in Appendix B. The float glass is modeled as thermoelastic with constant material parameters, see Table 6.1. Various shear relaxation curves of standard

Parameter	Value
Young's modulus E	$68\,500\,\mathrm{N/mm^2}$
Poisson's ratio ν	0.2
Linear CTE α	$3 \times 10^{-6}/\mathrm{K}$
Reference density ρ_0	$2500\,\mathrm{kg/m^3}$
Specific heat c	$720\,\mathrm{J/(kg\,K)}$
Thermal conductivity λ	$1\,\mathrm{W/(m\,K)}$

Table 6.1.: Material parameters of float glass used for the simulations.

PVB with respect to the reference temperature $\theta_0 = 20\,^\circ\mathrm{C}$ are summarized in the left diagram of Figure 6.15. The different curves have been normalized by dividing through the glassy shear modulus G_g in order to increase the comparability. The diagram on the right of Figure 6.15 shows the corresponding WLF shift factors (except for the curve taken from [17]). Clearly, below the glass transition temperature the WLF curves diverge and are therefore not applicable for the validation of the thermomechanical behavior of PVB. Additionally, the left diagram includes a solid line representing the shear relaxation data of PVB used for the simulations (see Appendix B, Table B.5). The inconsistency introduced by this manual parameter choice is justified as follows:

- there is no information on the true shape of the shift factor in the glassy regime (such as that of the DGEBA polymer in Figure 6.6), which is critical for the determination of material parameters $U_\mathrm{p}^\mathrm{ref}$, β_r, $\tilde{C}_4$ and $\tilde{C}_5$,
- some of the Prony parameters include unreasonable small relaxation times in the order of 10^{-13} or even smaller,
- others do not include enough relaxation times to adequately predict the long-term material response of PVB,
- the tension tests of the PVB sample in the last section are simulated based on an assumption for the cooling rate prior to testing (the Prony shear parameters G_r are critical for the tension tests).

Note that the Prony parameters G_r represented by the solid line have already been used for the validation of the uniaxial tension tests of PVB described in Section 6.3.1. For the spatial discretization of the glass laminate we use solid elements with 27 nodes (tri-quadratic elements). The temporal integration is performed in terms of the DIRK2PR variant listed in Table 4.4 on page 91. This is a three-stage, second-order SDIRK method

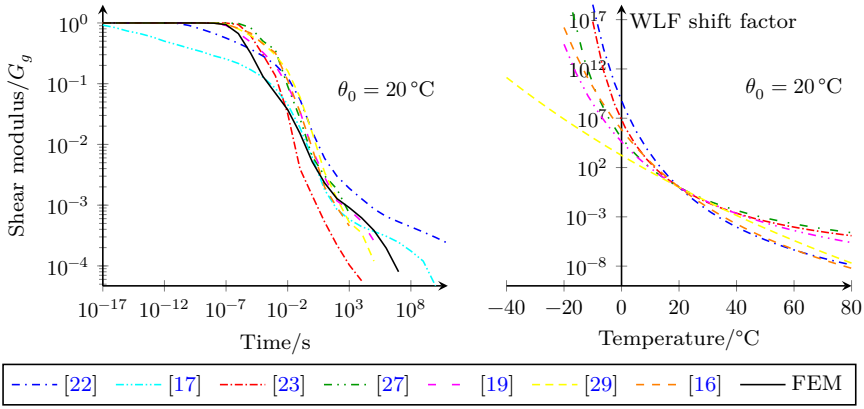

Figure 6.15.: Different (normalized) shear relaxation curves and corresponding shift factors of standard PVB with respect to reference temperature $\theta_0 = 20\,°C$, taken from the literature. The solid curve represents the simulation data used in this thesis. The relaxation spectrum corresponding to this curve is summarized in Appendix B, Table B.5.

which is both A- and L-stable (the embedded method is third-order accurate). For the automatic step size control we apply the classic approach outlined in Section 4.3.1 on page 90. The step size parameters were chosen as follows: $f_{\text{safety}} = 0.89$, $f_{\min} = 0.2$ and $f_{\max} = 2.5$ (see equation (4.74)). We first consider the three-point bending test.

6.4.1. Three-Point Bending Test

The experimental data of the three-point bending test of laminated glass plates under long-term load duration are taken from the literature [17, p. 161 ff.]. Figure 6.16 depicts the model geometry, the applied load and the finite element mesh (blue). The mesh consists of two elements for each layer in thickness direction. This suffices in order that the solution converges. For the sake of convenience, only the lower left quarter of the system is modeled with finite elements. Since the temperature during the experiment ($\theta = 22\,°C$) deviates from the reference temperature ($\theta_0 = 20\,°C$), two consecutive simulations become necessary. In the first simulation the temperature jump of $2\,°C$ is applied and hold until the laminate has reached a state of internal equilibrium (disregarding the external loads). The equilibrium state is saved on disk and afterwards reloaded for the mechanical simulation. Here, the external loads are increased linearly within the first 136 seconds to their maximum values (resultant force $F = 400\,N$ for the line load) and afterwards kept constant for 24 hours. The creep curve of the midpoint of the laminate is calculated and compared to the experimental results, see Figure 6.17. 43 time steps are required to model the 24 hour time interval (only 4 steps were rejected). However, the number of steps could be reduced if the specified load followed a smooth curve instead of a ramp function. In general, a smooth curve is the appropriate choice in case of nonlinear calculations. Furthermore, it is important that the shear relaxation spectra include relaxation times of high magnitude. Otherwise it is not possible to simulate the long-term behavior of the polymer interlayer (the equilibrium state is

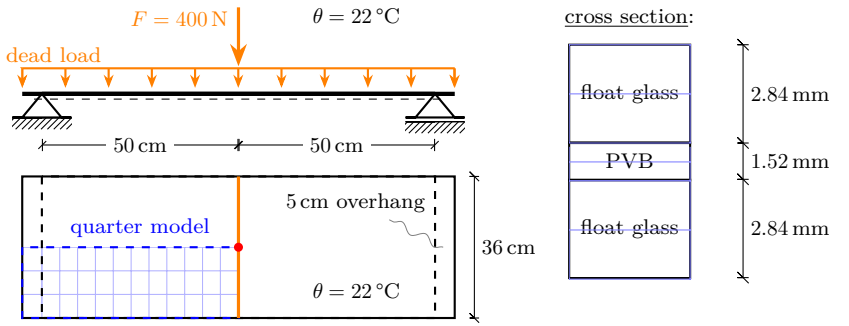

Figure 6.16.: Model geometry and external loads of the three-point bending test. The finite element mesh (blue) is also indicated. Only the lower left quarter of the system is modeled. The calculation of the time-dependent vertical displacement curve of the center point of the plate (red mark) is calculated with the finite element model. The temperature is kept constant at 22 °C during the experiment (the reference temperature is 20 °C).

reached too early in this case). Though the agreement between the experimental curve and the numerical prediction is quite good, the results of the simulation should not be overestimated regarding the inconsistency of the shear relaxation curve depicted in Figure 6.15. This becomes clear in the following section, where a four-point bending test under varying temperature field is examined.

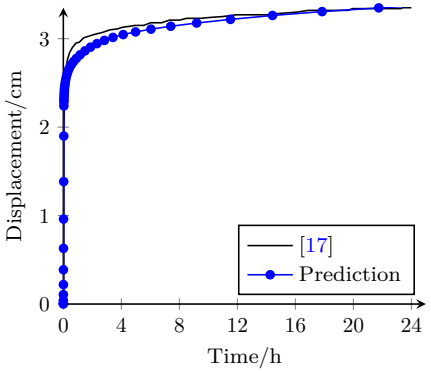

Figure 6.17.: Comparison of the measured displacement curve of the midpoint node (red mark in Figure 6.16) with the numerical prediction. The temperature is kept constant at 22 °C during the simulation. In this particular case, 43 time steps are required to span a time interval of 24 hours (5 steps were rejected).

6.4.2. Four-Point Bending Test

In contrast to the preceding section, the test setting now corresponds to a four-point bending test [23]. However, while the external load is kept constant, the temperature is now altered to study the thermal influence on the creep curve of the laminate structure. Specifically, starting from the reference temperature $\theta_0 = 20\,°\text{C}$, a temperature jump of $10\,°\text{C}$ is applied every 24 hours. Figure 6.18 illustrates the model geometry, the external load and the finite element mesh (blue) used for the simulation. The external loads follow a ramp function within the first 136 seconds until they reach their maximum values (resultant force $F = 256\,\text{N}$ for a single line load). Afterwards, they are kept constant for 72 hours. For the sake of simplicity, the temperature jumps also follow a ramp function, which take place during a time interval of 10 minutes. Here, the temperature is only prescribed at the surface of the model (excluding the symmetry axes). Remaining temperature degrees of freedom in the finite element mesh may adjust freely during the simulation. As before, only a quarter model is used to determine the creep curve of the midpoint of the plate (red mark in Figure 6.18). Figure 6.19

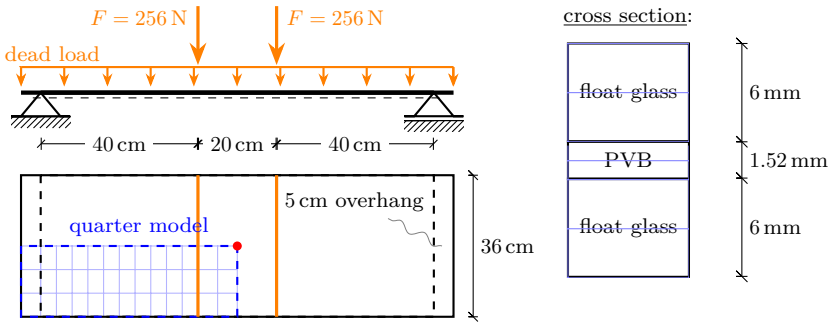

Figure 6.18.: Model geometry and external loads of the four-point bending test. The finite element mesh (blue) is also indicated. Only the lower left quarter of the system is modeled. The calculation of the time-dependent displacement curve of the center point of the plate (red mark) is calculated with the finite element model. While the external load is kept constant during the test, the temperature changes every 24 hours by $10\,°\text{C}$.

compares the numerical prediction with the experimental findings. While the curves in the first section are in good agreement ($\theta = 20\,°\text{C}$), the first temperature jump already leads to an increased deflection compared to the experiment. This is most likely due to the inconsistency of the shear relaxation data mentioned above. In addition, differences might occur as a result of the simplified temperature boundary conditions applied in the finite element model. In a laboratory setting, the heat transfer may be convective in nature. In the simulation, however, we use simple ramp functions to model the temperature jumps in the form of prescribed temperature values at the boundary. We do not know the actual time-dependent temperature distribution of the laminate. Especially in the $40\,°\text{C}$ interval the creep response of the laminate is observed not until approximately 2 hours after the 48 hours time stamp, which is not reproducible with the numerical simulation. We conclude that the numerical investigations into PVB and laminated glass containing a PVB interlayer should be repeated when reliable

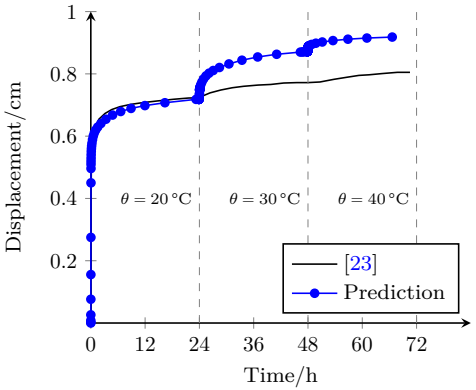

Figure 6.19.: Comparison of the measured displacement curve of the midpoint node (red mark in Figure 6.18) with the numerical prediction. The temperature increases every 24 hours by 10 °C, leading to a reduced stiffness of the system. The differences in the curves most likely stem from the inconsistency of the shear relaxation data and the shift factor (see text for further explanation). In this particular case, 124 time steps are required to span a time interval of 72 hours.

experimental data on the shift function in the glassy state is available.

7. Conclusion and Outlook

We have developed a three-dimensional, thermodynamically consistent constitutive model based on the internal variables approach, which captures essential material characteristics observed on amorphous polymers. These include yield-like behavior under both tension and compression, physical aging as well as relaxation in shear and bulk deformation under arbitrary thermal and mechanical loading histories. Similar to engineering approaches of the constitutive modeling of polymer structures, the material model uses discrete relaxation spectra in the form of Prony parameters. All the material parameters required stem from independent linear-viscoelastic input data such as DMTA and dilatometric experiments. The different relaxation mechanisms comprise bulk and shear deformation as well as thermal stress and entropy relaxation. The key ingredient of the model is the thermoviscoelastic shift function defined in terms of the potential internal energy of the polymer, which has already been successfully applied in the literature. A particularly attractive feature of the nonlinear constitutive model lies in its similarity with linear-viscoelastic models in terms of the relaxation mechanisms described by the evolution of internal variables. This allows for efficient time integration schemes such as diagonally implicit Runge-Kutta methods embedded with automatic time-stepping mechanisms. We have implemented a complete thermomechanical interface which allows to simulate amorphous polymers under a wide range of load applications. The interface includes several finite elements and Runge-Kutta time integration schemes in the form of diagonally implicit Runge-Kutta methods. Finally, the constitutive model and the implementation have thoroughly been tested by validating four different polymers (one thermoplastic and three thermosets) in different experimental settings. These include dilatometric and calorimetric experiments, tension and compression tests at various temperatures as well as three-point and four-point bending tests.

The constitutive framework based on the internal variables approach allows for several extensions. The following list compiles possible future perspectives of the work:

- introduction of higher-order terms in the Helmholtz energy to allow for arbitrary strain magnitudes,
- refinement of the simplified heat flux law used here to account for the dependence of the thermal conductivity on temperature, strain and internal variables,
- extension to include damage effects controlled by the evolution of further internal variables,
- extension to a hygrothermomechanical framework to include hygroscopic effects.

We hope that this thesis not only helps in better understanding the thermomechanics of polymeric materials, but also to provide assistance in the intricate numerical treatment of initial boundary value problems stemming from finite element analyses in the context of thermomechanically coupled theories.

Part IV.

Appendix

A. Derivation of the Material Tangent

Influence of the Second Evolution Equation

In the following we derive the partial derivatives for the scalar internal variable $\zeta_l(\boldsymbol{X},t)$. Its evolution equation $(3.38)_2$ is given on page 54 and the corresponding residual is defined as

$$\mathcal{H}_l(t) = \dot{\zeta}_l(t) - \mathcal{B}_l\left(\boldsymbol{H}(t),\theta(t),\boldsymbol{\mathcal{Z}}_k(t),\zeta_k(t),\chi_k(t)\right), \qquad l,k = l,\dots,m. \tag{A.1}$$

The corresponding discretized version reads

$$\mathcal{H}^h_{l(1\times1)} = \dot{\zeta}^h_l - \mathcal{B}_l\left(\boldsymbol{H}^h,\theta^h,\boldsymbol{\mathcal{Z}}^h_k,\zeta^h_k,\chi^h_k\right), \qquad l,k = 1,\dots,m. \tag{A.2}$$

Substitution of the rate term according to the definition of the DIRK velocities (4.37) on page 84 yields

$$\begin{aligned}\mathcal{H}^h_{l,n+c_i} &= \dot{\zeta}^h_{l,n+c_i} - \mathcal{B}_{l,n+c_i},\\ &= \frac{\zeta^h_{l,n+c_i} - \zeta^h_{l,n}}{a_{ii}\Delta t_n} - \frac{1}{a_{ii}}\sum_{j=1}^{i-1} a_{ij}\dot{\zeta}^h_{l,n+c_j}\\ &\quad + \frac{1}{a\left(\boldsymbol{H}^h,\theta^h,\boldsymbol{\mathcal{Z}}^h_k,\zeta^h_k,\chi^h_k\right)\tau^K_l}\left(3\alpha_l(\theta^h_{n+c_i}-\theta_0)+\zeta^h_{l,n+c_i}\right).\end{aligned} \tag{A.3}$$

Application of the chain rule to calculate the change with respect to internal variables $\boldsymbol{\mathcal{Z}}_l(\boldsymbol{X},t)$ results in

$$\begin{aligned}\frac{\partial\mathcal{H}^h_l}{\partial\boldsymbol{\mathcal{Z}}^h_r} = &-\frac{1}{a^2\tau^K_l}\left(3\alpha_l\left(\theta^h-\theta_0\right)+\zeta^h_l\right)\frac{\partial a}{\partial \mathrm{tr}\boldsymbol{\mathcal{Z}}^h_r}\boldsymbol{I}\\ &-\frac{1}{a^2\tau^K_l}\left(3\alpha_l\left(\theta^h-\theta_0\right)+\zeta^h_l\right)\left(\mathrm{dev}\frac{\partial a}{\partial \mathrm{dev}\boldsymbol{\mathcal{Z}}^h_r}\right).\end{aligned} \tag{A.4}$$

In an analogue fashion the partial derivatives with respect to the remaining internal variables $\zeta_l(\boldsymbol{X},t)$ and $\chi_l(\boldsymbol{X},t)$ give

$$\begin{aligned}\frac{\partial\mathcal{H}^h_l}{\partial\zeta^h_r} &= \left(\frac{1}{a_{ii}\Delta t_n}+\frac{1}{a\tau^K_l}\right)\delta_{lr} - \frac{1}{a^2\tau^K_l}\left(3\alpha_l\left(\theta^h-\theta_0\right)+\zeta^h_l\right)\frac{\partial a}{\partial\zeta^h_r},\\ \frac{\partial\mathcal{H}^h_l}{\partial\chi^h_r} &= -\frac{1}{a^2\tau^K_l}\left(3\alpha_l\left(\theta^h-\theta_0\right)+\zeta^h_l\right)\frac{\partial a}{\partial\chi^h_r}.\end{aligned} \tag{A.5}$$

Finally, we calculate the partial derivatives with respect to strain $\boldsymbol{H}(\boldsymbol{X},t)$ and temperature $\theta(\boldsymbol{X},t)$. Application of the chain rule results in

$$\begin{aligned}\frac{\partial \mathcal{H}_l^h}{\partial \boldsymbol{H}^h} = &-\frac{1}{a^2\tau_l^K}\left(3\alpha_l\left(\theta^h-\theta_0\right)+\zeta_l^h\right)\frac{\partial a}{\partial \mathrm{tr}\boldsymbol{H}^h}\boldsymbol{I}\\ &-\frac{1}{a^2\tau_l^K}\left(3\alpha_l\left(\theta^h-\theta_0\right)+\zeta_l^h\right)\left(\mathrm{dev}\frac{\partial a}{\partial \mathrm{dev}\boldsymbol{H}^h}\right)\end{aligned} \tag{A.6}$$

as well as

$$\frac{\partial \mathcal{H}_l^h}{\partial \theta^h} = -\frac{1}{a^2\tau_l^K}\left(3\alpha_l\left(\theta^h-\theta_0\right)+\zeta_l^h\right)\frac{\partial a}{\partial \theta^h}+\frac{3\alpha_l}{a\tau_l^K}. \tag{A.7}$$

Influence of the Third Evolution Equation

In the following we derive the partial derivatives for the scalar internal variable $\chi_l(\boldsymbol{X},t)$. Its evolution equation $(3.38)_3$ is given on page 54 and the corresponding residual is defined as

$$\mathcal{R}_l(t) = \dot{\chi}_l(t) - \mathcal{C}_l\left(\boldsymbol{H}(t),\theta(t),\boldsymbol{\mathcal{Z}}_k(t),\zeta_k(t),\chi_k(t)\right), \qquad l,k = l,\dots,m. \tag{A.8}$$

The corresponding discretized version reads

$$\mathcal{R}_{l(1\times1)}^h = \dot{\chi}_l^h - \mathcal{C}_l\left(t,\boldsymbol{H}^h,\theta^h,\boldsymbol{\mathcal{Z}}_k^h,\zeta_k^h,\chi_k^h\right), \qquad l,k = 1,\dots,m. \tag{A.9}$$

Substitution of the rate term according to the definition of the DIRK velocities (4.37) on page 84 yields

$$\begin{aligned}\mathcal{R}_{l,n+c_i}^h &= \dot{\chi}_{l,n+c_i}^h - \mathcal{C}_{l,n+c_i},\\ &= \frac{\chi_{l,n+c_i}^h-\chi_{l,n}^h}{a_{ii}\Delta t_n} - \frac{1}{a_{ii}}\sum_{j=1}^{i-1}a_{ij}\dot{\chi}_{l,n+c_j}^h\\ &\quad+\frac{1}{a\left(\boldsymbol{H}^h,\theta^h,\boldsymbol{\mathcal{Z}}_k^h,\zeta_k^h,\chi_k^h\right)\tau_l^K}\left(3\beta_l\left(\theta_{n+c_i}^h-\theta_0\right)+\chi_{l,n+c_i}^h\right).\end{aligned} \tag{A.10}$$

Application of the chain rule to calculate the change with respect to internal variables $\boldsymbol{\mathcal{Z}}_l(\boldsymbol{X},t)$ results in

$$\begin{aligned}\frac{\partial \mathcal{R}_l^h}{\partial \boldsymbol{\mathcal{Z}}_r^h} = &-\frac{1}{a^2\tau_l^K}\left(3\beta_l\left(\theta^h-\theta_0\right)+\chi_l^h\right)\frac{\partial a}{\partial \mathrm{tr}\boldsymbol{\mathcal{Z}}_r^h}\boldsymbol{I}\\ &-\frac{1}{a^2\tau_l^K}\left(3\beta_l\left(\theta^h-\theta_0\right)+\chi_l^h\right)\left(\mathrm{dev}\frac{\partial a}{\partial \mathrm{dev}\boldsymbol{\mathcal{Z}}_r^h}\right).\end{aligned} \tag{A.11}$$

In an analogue fashion the partial derivatives with respect to the remaining internal variables $\zeta_l(\boldsymbol{X},t)$ and $\chi_l(\boldsymbol{X},t)$ give

$$\begin{aligned}\frac{\partial \mathcal{R}_l^h}{\partial \zeta_r^h} &= -\frac{1}{a^2\tau_l^K}\left(3\beta_l\left(\theta^h-\theta_0\right)+\chi_l^h\right)\frac{\partial a}{\partial \zeta_r^h},\\ \frac{\partial \mathcal{R}_l^h}{\partial \chi_r^h} &= \left(\frac{1}{a_{ii}\Delta t_n}+\frac{1}{a\tau_l^K}\right)\delta_{lr}-\frac{1}{a^2\tau_l^K}\left(3\beta_l\left(\theta^h-\theta_0\right)+\chi_l^h\right)\frac{\partial a}{\partial \chi_r^h}.\end{aligned} \tag{A.12}$$

Finally, we calculate the partial derivatives with respect to strain $\boldsymbol{H}(\boldsymbol{X},t)$ and temperature $\theta(\boldsymbol{X},t)$. Application of the chain rule results in

$$\begin{aligned}\frac{\partial \mathcal{R}_l^h}{\partial \boldsymbol{H}^h} = & -\frac{1}{a^2\tau_l^K}\left(3\beta_l\left(\theta^h-\theta_0\right)+\chi_l^h\right)\frac{\partial a}{\partial \mathrm{tr}\boldsymbol{H}^h}\boldsymbol{I} \\ & -\frac{1}{a^2\tau_l^K}\left(3\beta_l\left(\theta^h-\theta_0\right)+\chi_l^h\right)\left(\mathrm{dev}\frac{\partial a}{\partial \mathrm{dev}\boldsymbol{H}^h}\right),\end{aligned} \tag{A.13}$$

as well as

$$\frac{\partial \mathcal{R}_l^h}{\partial \theta^h} = -\frac{1}{a^2\tau_l^K}\left(3\beta_l\left(\theta^h-\theta_0\right)+\chi_l^h\right)\frac{\partial a}{\partial \theta^h}+\frac{3\beta_l}{a\tau_l^K}. \tag{A.14}$$

Influence of the Internal Dissipation

The internal dissipation (3.51) is defined on page 58. Its partial derivative with respect to internal variables $\boldsymbol{\mathcal{Z}}_l(\boldsymbol{X},t)$ is given by means of the chain rule as

$$\begin{aligned}\frac{\partial \mathcal{D}^h_{\mathrm{int},n+c_i}}{\partial \boldsymbol{\mathcal{Z}}^h_{l,n+c_i}} &= \frac{\partial \mathcal{D}^h_{\mathrm{int},n+c_i}}{\partial \mathrm{tr}\boldsymbol{\mathcal{Z}}^h_{l,n+c_i}}\frac{\partial \mathrm{tr}\boldsymbol{\mathcal{Z}}^h_{l,n+c_i}}{\partial \boldsymbol{\mathcal{Z}}^h_{l,n+c_i}}+\frac{\partial \mathcal{D}^h_{\mathrm{int},n+c_i}}{\partial \mathrm{dev}\boldsymbol{\mathcal{Z}}^h_{l,n+c_i}}\frac{\partial \mathrm{dev}\boldsymbol{\mathcal{Z}}^h_{l,n+c_i}}{\partial \boldsymbol{\mathcal{Z}}^h_{r,n+c_i}} \\ &= \frac{\partial \mathcal{D}^h_{\mathrm{int},n+c_i}}{\partial \mathrm{tr}\boldsymbol{\mathcal{Z}}^h_{l,n+c_i}}\boldsymbol{I}+\mathrm{dev}\frac{\partial \mathcal{D}^h_{\mathrm{int},n+c_i}}{\partial \mathrm{dev}\boldsymbol{\mathcal{Z}}^h_{l,n+c_i}},\end{aligned} \tag{A.15}$$

where the two derivative terms are given without the time subscript by

$$\begin{aligned}\frac{\partial \mathcal{D}^h_{\mathrm{int}}}{\partial \mathrm{tr}\boldsymbol{\mathcal{Z}}^h_l}\boldsymbol{I} = & -\frac{2\Psi_K\left(\theta^h\right)}{a\tau_l^K}K_l\left(\mathrm{tr}\boldsymbol{H}^h-\mathrm{tr}\boldsymbol{\mathcal{Z}}^h_l\right)\boldsymbol{I}+\Phi_D\left(\boldsymbol{H}^h,\theta^h,\boldsymbol{\mathcal{Z}}^h_i,\zeta^h_i,\chi^h_i\right)\frac{\partial a}{\partial \mathrm{tr}\boldsymbol{\mathcal{Z}}^h_l}\boldsymbol{I} \\ & +\frac{2\Psi_\alpha\left(\mathrm{tr}\boldsymbol{H}^h,\theta^h\right)}{a\tau_l^K}K_l\left(3\alpha_l\left(\theta^h-\theta_0\right)+\zeta^h_l\right)\boldsymbol{I}\end{aligned} \tag{A.16}$$

for the volumetric part and

$$\begin{aligned}\mathrm{dev}\frac{\partial \mathcal{D}^h_{\mathrm{int}}}{\partial \mathrm{dev}\boldsymbol{\mathcal{Z}}^h_l} = & -\frac{2\Psi_G\left(\theta^h\right)}{a\tau_l^G}2G_l\left(\mathrm{dev}\boldsymbol{H}^h-\mathrm{dev}\boldsymbol{\mathcal{Z}}^h_l\right) \\ & +\Phi_D\left(\boldsymbol{H}^h,\theta^h,\boldsymbol{\mathcal{Z}}^h_i,\zeta^h_i,\chi^h_i\right)\left(\mathrm{dev}\frac{\partial a}{\partial \mathrm{dev}\boldsymbol{\mathcal{Z}}^h_l}\right)\end{aligned} \tag{A.17}$$

for the deviatoric part. Here and in the sequel we use the definition

$$\begin{aligned}\Phi_D\left(\boldsymbol{H}^h,\theta^h,\boldsymbol{\mathcal{Z}}_i^h,\zeta_i^h,\chi_i^h\right) \coloneqq \sum_r \Bigg[&- \frac{\Psi_K\left(\theta^h\right)}{a^2\tau_r^K} K_r \left(\mathrm{tr}\boldsymbol{H}^h - \mathrm{tr}\boldsymbol{\mathcal{Z}}_r^h\right)^2 \\ &- \frac{\Psi_G\left(\theta^h\right)}{a^2\tau_r^{\mathrm{G}}} 2G_r \left(\mathrm{dev}\boldsymbol{H}^h - \mathrm{dev}\boldsymbol{\mathcal{Z}}_r^h\right) \cdot \left(\mathrm{dev}\boldsymbol{H}^h - \mathrm{dev}\boldsymbol{\mathcal{Z}}_r^h\right) \\ &+ \frac{2\Psi_\alpha\left(\mathrm{tr}\boldsymbol{H}^h,\theta^h\right)}{a^2\tau_r^K} K_r \left(\mathrm{tr}\boldsymbol{H}^h - \mathrm{tr}\boldsymbol{\mathcal{Z}}_r^h\right)\left(3\alpha_r\left(\theta^h-\theta_0\right)+\zeta_r^h\right) \\ &- \frac{\Psi_\beta\left(\theta^h\right)}{a^2\tau_r^K} K_r \left(3\beta_r\left(\theta^h-\theta_0\right)+\chi_r^h\right)^2 \Bigg].\end{aligned} \tag{A.18}$$

The partial derivatives with respect to the remaining internal variables $\zeta_l(\boldsymbol{X},t)$ and $\chi_l(\boldsymbol{X},t)$ read

$$\begin{aligned}\frac{\partial\mathcal{D}_{\mathrm{int}}^h}{\partial\zeta_l^h} &= -\frac{2\Psi_\alpha\left(\mathrm{tr}\boldsymbol{H}^h,\theta^h\right)}{a\tau_l^K} K_l\left(\mathrm{tr}\boldsymbol{H}^h - \mathrm{tr}\boldsymbol{\mathcal{Z}}_l^h\right) + \Phi_D\left(\boldsymbol{H}^h,\theta^h,\boldsymbol{\mathcal{Z}}_i^h,\zeta_i^h,\chi_i^h\right)\frac{\partial a}{\partial\zeta_l^h}, \\ \frac{\partial\mathcal{D}_{\mathrm{int}}^h}{\partial\chi_l^h} &= \frac{2\Psi_\beta\left(\theta^h\right)}{a\tau_l^K} K_l\left(3\beta_l\left(\theta^h-\theta_0\right)+\chi_l^h\right) + \Phi_D\left(\boldsymbol{H}^h,\theta^h,\boldsymbol{\mathcal{Z}}_i^h,\zeta_i^h,\chi_i^h\right)\frac{\partial a}{\partial\chi_l^h}.\end{aligned} \tag{A.19}$$

Finally, we calculate the partial derivatives with respect to strain $\boldsymbol{H}(\boldsymbol{X},t)$ and temperature $\theta(\boldsymbol{X},t)$. Application of the chain rule results in

$$\begin{aligned}\frac{\partial\mathcal{D}_{\mathrm{int},n+c_i}^h}{\partial\boldsymbol{H}_{n+c_i}^h} &= \frac{\partial\mathcal{D}_{\mathrm{int},n+c_i}^h}{\partial\mathrm{tr}\boldsymbol{H}_{n+c_i}^h}\frac{\partial\mathrm{tr}\boldsymbol{H}_{n+c_i}^h}{\partial\boldsymbol{H}_{n+c_i}^h} + \frac{\partial\mathcal{D}_{\mathrm{int},n+c_i}^h}{\partial\mathrm{dev}\boldsymbol{H}_{n+c_i}^h}\frac{\partial\mathrm{dev}\boldsymbol{H}_{n+c_i}^h}{\partial\boldsymbol{H}_{n+c_i}^h} \\ &= \frac{\partial\mathcal{D}_{\mathrm{int},n+c_i}^h}{\partial\mathrm{tr}\boldsymbol{H}_{n+c_i}^h}\boldsymbol{I} + \mathrm{dev}\frac{\partial\mathcal{D}_{\mathrm{int},n+c_i}^h}{\partial\mathrm{dev}\boldsymbol{H}_{n+c_i}^h}.\end{aligned} \tag{A.20}$$

Here, the first derivative term is given by the expression

$$\begin{aligned}\frac{\partial\mathcal{D}_{\mathrm{int}}^h}{\partial\mathrm{tr}\boldsymbol{H}^h}\boldsymbol{I} = &\sum_r \frac{2\Psi_K\left(\theta^h\right)}{a\tau_r^K} K_r\left(\mathrm{tr}\boldsymbol{H}^h - \mathrm{tr}\boldsymbol{\mathcal{Z}}_r^h\right)\boldsymbol{I} \\ &- \sum_r \frac{2}{a\tau_r^K}\frac{\partial\Psi_\alpha\left(\mathrm{tr}\boldsymbol{H}^h,\theta^h\right)}{\partial\mathrm{tr}\boldsymbol{H}^h} K_r\left(\mathrm{tr}\boldsymbol{H}^h - \mathrm{tr}\boldsymbol{\mathcal{Z}}_r^h\right)\left(3\alpha_r\left(\theta^h-\theta_0\right)+\zeta_r^h\right)\boldsymbol{I} \\ &- \sum_r \frac{2\Psi_\alpha\left(\mathrm{tr}\boldsymbol{H}^h,\theta^h\right)}{a\tau_r^K} K_r\left(3\alpha_r\left(\theta^h-\theta_0\right)+\zeta_r^h\right)\boldsymbol{I} \\ &+ \Phi_D\left(\boldsymbol{H}^h,\theta^h,\boldsymbol{\mathcal{Z}}_i^h,\zeta_i^h,\chi_i^h\right)\frac{\partial a}{\partial\mathrm{tr}\boldsymbol{H}^h}\boldsymbol{I},\end{aligned} \tag{A.21}$$

while the second term reads

$$\begin{aligned}\operatorname{dev}\frac{\partial \mathcal{D}^h_{\text{int}}}{\partial \operatorname{dev}\boldsymbol{H}^h} = &\sum_r \frac{2\Psi_G\left(\theta^h\right)}{a\tau_r^{\text{G}}} 2G_r\left(\operatorname{dev}\boldsymbol{H}^h - \operatorname{dev}\boldsymbol{\mathcal{Z}}_r^h\right)\\ &+ \Phi_D\left(\boldsymbol{H}^h, \theta^h, \boldsymbol{\mathcal{Z}}_i^h, \zeta_i^h, \chi_i^h\right)\left(\operatorname{dev}\frac{\partial a}{\partial \operatorname{dev}\boldsymbol{H}^h}\right).\end{aligned} \tag{A.22}$$

The temperature derivative is given by the longer expression

$$\begin{aligned}\frac{\partial \mathcal{D}^h_{\text{int}}}{\partial \theta^h} = &\sum_r \frac{1}{a\tau_r^K}\frac{\partial \Psi_K\left(\theta^h\right)}{\partial \theta^h} K_r\left(\operatorname{tr}\boldsymbol{H}^h - \operatorname{tr}\boldsymbol{\mathcal{Z}}_r^h\right)^2\\ &+ \sum_r \frac{1}{a\tau_r^{\text{G}}}\frac{\partial \Psi_G\left(\theta^h\right)}{\partial \theta^h} 2G_r\left(\operatorname{dev}\boldsymbol{H}^h - \operatorname{dev}\boldsymbol{\mathcal{Z}}_r^h\right)\cdot\left(\operatorname{dev}\boldsymbol{H}^h - \operatorname{dev}\boldsymbol{\mathcal{Z}}_r^h\right)\\ &- \sum_r \frac{2}{a\tau_r^K}\frac{\partial \Psi_\alpha\left(\operatorname{tr}\boldsymbol{H}^h, \theta^h\right)}{\partial \theta^h} K_r\left(\operatorname{tr}\boldsymbol{H}^h - \operatorname{tr}\boldsymbol{\mathcal{Z}}_r^h\right)\left(3\alpha_r\left(\theta^h - \theta_0\right) + \zeta_r^h\right)\\ &+ \sum_r \frac{1}{a\tau_r^K}\frac{\partial \Psi_\beta\left(\theta^h\right)}{\partial \theta^h} K_r\left(3\beta_r\left(\theta^h - \theta_0\right) + \chi_r^h\right)^2\\ &+ \sum_r \frac{\Psi_\beta\left(\theta^h\right)}{a\tau_r^K} 6\beta_r K_r\left(3\beta_r\left(\theta^h - \theta_0\right) + \chi_r^h\right)\\ &- \sum_r \frac{\Psi_\alpha\left(\operatorname{tr}\boldsymbol{H}^h, \theta^h\right)}{a\tau_r^K} 6\alpha_r K_r\left(\operatorname{tr}\boldsymbol{H}^h - \operatorname{tr}\boldsymbol{\mathcal{Z}}_r^h\right)\\ &+ \Phi_D\left(\boldsymbol{H}^h, \theta^h, \boldsymbol{\mathcal{Z}}_i^h, \zeta_i^h, \chi_i^h\right)\frac{\partial a}{\partial \theta^h}.\end{aligned} \tag{A.23}$$

Influence of Structural Viscous Heating

Structural viscous heating (3.51) is defined on page 58. Its partial derivative with respect to internal variables $\boldsymbol{\mathcal{Z}}_l(\boldsymbol{X}, t)$ is given by means of the chain rule as

$$\begin{aligned}\frac{\partial \mathcal{H}^h_{\text{in},n+c_i}}{\partial \boldsymbol{\mathcal{Z}}^h_{l,n+c_i}} &= \frac{\partial \mathcal{H}^h_{\text{in},n+c_i}}{\partial \operatorname{tr}\boldsymbol{\mathcal{Z}}^h_{l,n+c_i}}\frac{\partial \operatorname{tr}\boldsymbol{\mathcal{Z}}^h_{l,n+c_i}}{\partial \operatorname{tr}\boldsymbol{\mathcal{Z}}^h_{l,n+c_i}} + \frac{\partial \mathcal{H}^h_{\text{in},n+c_i}}{\partial \operatorname{dev}\boldsymbol{\mathcal{Z}}^h_{l,n+c_i}}\frac{\partial \operatorname{dev}\boldsymbol{\mathcal{Z}}^h_{l,n+c_i}}{\partial \boldsymbol{\mathcal{Z}}^h_{r,n+c_i}}\\ &= \frac{\partial \mathcal{H}^h_{\text{in},n+c_i}}{\partial \operatorname{tr}\boldsymbol{\mathcal{Z}}^h_{l,n+c_i}}\boldsymbol{I} + \operatorname{dev}\frac{\partial \mathcal{H}^h_{\text{in},n+c_i}}{\partial \operatorname{dev}\boldsymbol{\mathcal{Z}}^h_{l,n+c_i}}.\end{aligned} \tag{A.24}$$

where the two derivative terms are given without the time subscript by

$$\begin{aligned}\frac{\partial \mathcal{H}^h_{\text{in}}}{\partial \operatorname{tr}\boldsymbol{\mathcal{Z}}^h_l}\boldsymbol{I} = &-\frac{2\theta^h}{a\tau_l^K}\frac{\partial \Psi_K\left(\theta^h\right)}{\partial \theta^h} K_l\left(\operatorname{tr}\boldsymbol{H}^h - \operatorname{tr}\boldsymbol{\mathcal{Z}}_l^h\right)\boldsymbol{I} + \Phi_H\left(\boldsymbol{H}^h, \theta^h, \boldsymbol{\mathcal{Z}}_i^h, \zeta_i^h, \chi_i^h\right)\frac{\partial a}{\partial \operatorname{tr}\boldsymbol{\mathcal{Z}}_l^h}\boldsymbol{I}\\ &+ \frac{2\theta^h}{a\tau_l^K}\frac{\partial \Psi_\alpha\left(\operatorname{tr}\boldsymbol{H}^h, \theta^h\right)}{\partial \theta^h} K_l\left(3\alpha_l\left(\theta^h - \theta_0\right) + \zeta_l^h\right)\boldsymbol{I} + \frac{\theta^h \Psi_\alpha\left(\operatorname{tr}\boldsymbol{H}^h, \theta^h\right)}{a\tau_l^K} 3\alpha_l K_l \boldsymbol{I}\end{aligned} \tag{A.25}$$

for the volumetric part and

$$\mathrm{dev}\frac{\partial \mathcal{H}_{\mathrm{in}}^{h}}{\partial \mathrm{dev}\boldsymbol{\mathcal{Z}}_{l}^{h}} = -\frac{2\theta^{h}}{a\tau_{l}^{G}}\frac{\partial \Psi_{G}\left(\theta^{h}\right)}{\partial \theta^{h}} 2G_{l}(\mathrm{dev}\boldsymbol{H}^{h} - \mathrm{dev}\boldsymbol{\mathcal{Z}}_{l}^{h}) + \Phi_{H}\left(\boldsymbol{H}^{h}, \theta^{h}, \boldsymbol{\mathcal{Z}}_{i}^{h}, \zeta_{i}^{h}, \chi_{i}^{h}\right)\frac{\partial a}{\partial \mathrm{dev}\boldsymbol{\mathcal{Z}}_{l}^{h}} \tag{A.26}$$

for the deviatoric part. Here and in the sequel we use the definition

$$\begin{aligned}
&\Phi_{H}(\boldsymbol{H}^{h},\theta^{h},\boldsymbol{\mathcal{Z}}_{i}^{h},\zeta_{i}^{h},\chi_{i}^{h}) := \\
&\quad\sum_{r}\Bigg[-\frac{\theta^{h}}{a^{2}\tau_{r}^{K}}\frac{\partial \Psi_{K}\left(\theta^{h}\right)}{\partial \theta^{h}} K_{r}\left(\mathrm{tr}\boldsymbol{H}^{h} - \mathrm{tr}\boldsymbol{\mathcal{Z}}_{r}^{h}\right)^{2} \\
&\qquad + \frac{2\theta^{h}}{a^{2}\tau_{r}^{K}}\frac{\partial \Psi_{\alpha}\left(\mathrm{tr}\boldsymbol{H}^{h},\theta^{h}\right)}{\partial \theta^{h}} K_{r}\left(3\alpha_{r}\left(\theta^{h}-\theta_{0}\right)+\zeta_{r}^{h}\right)\left(\mathrm{tr}\boldsymbol{H}^{h} - \mathrm{tr}\boldsymbol{\mathcal{Z}}_{r}^{h}\right) \\
&\qquad + \frac{\theta^{h}\Psi_{\alpha}\left(\mathrm{tr}\boldsymbol{H}^{h},\theta^{h}\right)}{a^{2}\tau_{r}^{K}} 3\alpha_{r}K_{r}\left(\mathrm{tr}\boldsymbol{H}^{h} - \mathrm{tr}\boldsymbol{\mathcal{Z}}_{r}^{h}\right) \\
&\qquad - \frac{\theta^{h}}{a^{2}\tau_{r}^{K}}\frac{\partial \Psi_{\beta}\left(\theta^{h}\right)}{\partial \theta^{h}} K_{r}\left(3\beta_{r}\left(\theta^{h}-\theta_{0}\right)+\chi_{r}^{h}\right)^{2} \\
&\qquad - \frac{\theta^{h}\Psi_{\beta}\left(\theta^{h}\right)}{a^{2}\tau_{r}^{K}} 3\beta_{r}K_{r}\left(3\beta_{r}\left(\theta^{h}-\theta_{0}\right)+\chi_{r}^{h}\right) \\
&\qquad - \frac{\theta^{h}}{a^{2}\tau_{r}^{\mathrm{G}}}\frac{\partial \Psi_{G}\left(\theta^{h}\right)}{\partial \theta^{h}} 2G_{r}(\mathrm{dev}\boldsymbol{H}^{h} - \mathrm{dev}\boldsymbol{\mathcal{Z}}_{r}^{h})\cdot\left(\mathrm{dev}\boldsymbol{H}^{h} - \mathrm{dev}\boldsymbol{\mathcal{Z}}_{r}^{h}\right)\Bigg].
\end{aligned} \tag{A.27}$$

The partial derivatives with respect to the remaining internal variables $\zeta_{l}(\boldsymbol{X},t)$ and $\chi_{l}(\boldsymbol{X},t)$ read

$$\begin{aligned}
\frac{\partial \mathcal{H}_{\mathrm{in}}^{h}}{\partial \zeta_{l}^{h}} &= -\frac{2\theta^{h}}{a\tau_{l}^{K}}\frac{\partial \Psi_{\alpha}\left(\mathrm{tr}\boldsymbol{H}^{h},\theta^{h}\right)}{\partial \theta^{h}} K_{l}\left(\mathrm{tr}\boldsymbol{H}^{h} - \mathrm{tr}\boldsymbol{\mathcal{Z}}_{l}^{h}\right) + \Phi_{H}\left(\boldsymbol{H}^{h},\theta^{h},\boldsymbol{\mathcal{Z}}_{i}^{h},\zeta_{i}^{h},\chi_{i}^{h}\right)\frac{\partial a}{\partial \zeta_{l}^{h}}, \\
\frac{\partial \mathcal{H}_{\mathrm{in}}^{h}}{\partial \chi_{l}^{h}} &= \frac{2\theta^{h}}{a\tau_{l}^{K}}\frac{\partial \Psi_{\beta}\left(\theta^{h}\right)}{\partial \theta^{h}} K_{l}\left(3\beta_{l}\left(\theta^{h}-\theta_{0}\right)+\chi_{l}^{h}\right) + \frac{\theta^{h}\Psi_{\beta}\left(\theta^{h}\right)}{a\tau_{l}^{K}} 3\beta_{l}K_{l} \\
&\quad + \Phi_{H}\left(\boldsymbol{H}^{h},\theta^{h},\boldsymbol{\mathcal{Z}}_{i}^{h},\zeta_{i}^{h},\chi_{i}^{h}\right)\frac{\partial a}{\partial \chi_{l}^{h}}.
\end{aligned} \tag{A.28}$$

Finally, we calculate the partial derivatives with respect to strain $\boldsymbol{H}(\boldsymbol{X},t)$ and temperature $\theta(\boldsymbol{X},t)$. Application of the chain rule results in

$$\begin{aligned}\frac{\partial \mathcal{H}^h_{\text{in},n+c_i}}{\partial \boldsymbol{H}^h_{n+c_i}} &= \frac{\partial \mathcal{H}^h_{\text{in},n+c_i}}{\partial \text{tr}\boldsymbol{H}^h_{n+c_i}} \frac{\partial \text{tr}\boldsymbol{H}^h_{n+c_i}}{\partial \boldsymbol{H}^h_{n+c_i}} + \frac{\partial \mathcal{H}^h_{\text{in},n+c_i}}{\partial \text{dev}\boldsymbol{H}^h_{n+c_i}} \frac{\partial \text{dev}\boldsymbol{H}^h_{n+c_i}}{\partial \boldsymbol{H}^h_{n+c_i}} \\ &= \frac{\partial \mathcal{H}^h_{\text{in},n+c_i}}{\partial \text{tr}\boldsymbol{H}^h_{n+c_i}} \boldsymbol{I} + \text{dev} \frac{\partial \mathcal{H}^h_{\text{in},n+c_i}}{\partial \text{dev}\boldsymbol{H}^h_{n+c_i}}.\end{aligned} \tag{A.29}$$

Here, the first term is given by the expression

$$\begin{aligned}\frac{\partial \mathcal{H}^h_{\text{in}}}{\partial \text{tr}\boldsymbol{H}^h} \boldsymbol{I} = &\sum_r \frac{2\theta^h}{a\tau_r^K} \frac{\partial \Psi_K\left(\theta^h\right)}{\partial \theta^h} K_r \left(\text{tr}\boldsymbol{H}^h - \text{tr}\boldsymbol{\mathcal{Z}}^h_r\right) \boldsymbol{I} \\ &- \sum_r \frac{2\theta^h}{a\tau_r^K} \frac{\partial \Psi_\alpha\left(\text{tr}\boldsymbol{H}^h, \theta^h\right)}{\partial \theta^h} K_r \left(3\alpha_r \left(\theta^h - \theta_0\right) + \zeta^h_r\right) \boldsymbol{I} \\ &- \sum_r \frac{\theta^h}{a\tau_r^K} \frac{\partial \Psi_\alpha\left(\text{tr}\boldsymbol{H}^h, \theta^h\right)}{\partial \text{tr}\boldsymbol{H}^h} 3\alpha_r K_r \left(\text{tr}\boldsymbol{H}^h - \text{tr}\boldsymbol{\mathcal{Z}}^h_r\right) \boldsymbol{I} \\ &- \sum_r \frac{\theta^h \Psi_\alpha\left(\text{tr}\boldsymbol{H}^h, \theta^h\right)}{a\tau_r^K} 3\alpha_r K_r \boldsymbol{I} + \Phi_H\left(\boldsymbol{H}^h, \theta^h, \boldsymbol{\mathcal{Z}}^h_i, \zeta^h_i, \chi^h_i\right) \frac{\partial a}{\partial \text{tr}\boldsymbol{H}^h} \boldsymbol{I},\end{aligned} \tag{A.30}$$

while the second term reads

$$\begin{aligned}\text{dev} \frac{\partial \mathcal{H}^h_{\text{in},n+c_i}}{\partial \text{dev}\boldsymbol{H}^h_{n+c_i}} = &\sum_r \frac{2\theta^h}{a\tau_r^G} \frac{\partial \Psi_G\left(\theta^h\right)}{\partial \theta^h} 2G_r (\text{dev}\boldsymbol{H}^h - \text{dev}\boldsymbol{\mathcal{Z}}^h_r) \\ &+ \Phi_H\left(\boldsymbol{H}^h, \theta^h, \boldsymbol{\mathcal{Z}}^h_i, \zeta^h_i, \chi^h_i\right) \text{dev} \frac{\partial a}{\partial \text{dev}\boldsymbol{H}^h}.\end{aligned} \tag{A.31}$$

The temperature derivative is given by the longer expression

$$
\begin{aligned}
\frac{\partial \mathcal{H}_{\text{in}}^{h}}{\partial \theta^{h}} \boldsymbol{I} = & \sum_{r} \frac{1}{a \tau_{r}^{K}} \frac{\partial \Psi_{K}\left(\theta^{h}\right)}{\partial \theta^{h}} K_{r}\left(\operatorname{tr} \boldsymbol{H}^{h}-\operatorname{tr} \boldsymbol{\mathcal{Z}}_{r}^{h}\right)^{2} \\
& -\sum_{r} \frac{2}{a \tau_{r}^{K}} \frac{\partial \Psi_{\alpha}\left(\operatorname{tr} \boldsymbol{H}^{h}, \theta^{h}\right)}{\partial \theta^{h}} K_{r}\left(3 \alpha_{r}\left(\theta^{h}-\theta_{0}\right)+\zeta_{r}^{h}\right)\left(\operatorname{tr} \boldsymbol{H}^{h}-\operatorname{tr} \boldsymbol{\mathcal{Z}}_{r}^{h}\right) \\
& -\sum_{r} \frac{2 \theta^{h}}{a \tau_{r}^{K}} \frac{\partial \Psi_{\alpha}\left(\operatorname{tr} \boldsymbol{H}^{h}, \theta^{h}\right)}{\partial \theta^{h}} 3 \alpha_{r} K_{r}\left(\operatorname{tr} \boldsymbol{H}^{h}-\operatorname{tr} \boldsymbol{\mathcal{Z}}_{r}^{h}\right) \\
& -\sum_{r} \frac{\Psi_{\alpha}\left(\operatorname{tr} \boldsymbol{H}^{h}, \theta^{h}\right)}{a \tau_{r}^{K}} 3 \alpha_{r} K_{r}\left(\operatorname{tr} \boldsymbol{H}^{h}-\operatorname{tr} \boldsymbol{\mathcal{Z}}_{r}^{h}\right) \\
& -\sum_{r} \frac{\theta^{h}}{a \tau_{r}^{K}} \frac{\partial \Psi_{\alpha}\left(\operatorname{tr} \boldsymbol{H}^{h}, \theta^{h}\right)}{\partial \theta^{h}} 3 \alpha_{r} K_{r}\left(\operatorname{tr} \boldsymbol{H}^{h}-\operatorname{tr} \boldsymbol{\mathcal{Z}}_{r}^{h}\right) \\
& +\sum_{r} \frac{1}{a \tau_{r}^{K}} \frac{\partial \Psi_{\beta}\left(\theta^{h}\right)}{\partial \theta^{h}} K_{r}\left(3 \beta_{r}\left(\theta^{h}-\theta_{0}\right)+\chi_{r}^{h}\right)^{2} \\
& +\sum_{r} \frac{\theta^{h}}{a \tau_{r}^{K}} \frac{\partial^{2} \Psi_{\beta}\left(\theta^{h}\right)}{\partial \theta^{h^{2}}} K_{r}\left(3 \beta_{r}\left(\theta^{h}-\theta_{0}\right)+\chi_{r}^{h}\right)^{2} \\
& +\sum_{r} \frac{\theta^{h}}{a \tau_{r}^{K}} \frac{\partial \Psi_{\beta}\left(\theta^{h}\right)}{\partial \theta^{h}} 9 \beta_{r} K_{r}\left(3 \beta_{r}\left(\theta^{h}-\theta_{0}\right)+\chi_{r}^{h}\right) \\
& +\sum_{r} \frac{\Psi_{\beta}\left(\theta^{h}\right)}{a \tau_{r}^{K}} 3 \beta_{r} K_{r}\left(3 \beta_{r}\left(\theta^{h}-\theta_{0}\right)+\chi_{r}^{h}\right)+\sum_{r} \frac{\theta^{h} \Psi_{\beta}\left(\theta^{h}\right)}{a \tau_{r}^{K}} 9 \beta_{r}^{2} K_{r} \\
& +\sum_{r} \frac{1}{a \tau_{r}^{G}} \frac{\partial \Psi_{G}\left(\theta^{h}\right)}{\partial \theta^{h}} 2 G_{r}\left(\operatorname{dev} \boldsymbol{H}^{h}-\operatorname{dev} \boldsymbol{\mathcal{Z}}_{r}^{h}\right) \cdot\left(\operatorname{dev} \boldsymbol{H}^{h}-\operatorname{dev} \boldsymbol{\mathcal{Z}}_{r}^{h}\right) \\
& +\Phi_{H}\left(\boldsymbol{H}^{h}, \theta^{h}, \boldsymbol{\mathcal{Z}}_{i}^{h}, \zeta_{i}^{h}, \chi_{i}^{h}\right) \frac{\partial a}{\partial \theta^{h}}.
\end{aligned}
\tag{A.32}
$$

Influence of the Specific Heat

The specific heat capacity *at constant deformation* (3.65) is defined on page 61. Its partial derivatives with respect to the internal variables $\boldsymbol{\mathcal{Z}}_{l}(\boldsymbol{X}, t)$ and $\zeta_{l}(\boldsymbol{X}, t)$ read

$$
\begin{aligned}
\frac{\partial c^{h}}{\partial \operatorname{tr} \boldsymbol{\mathcal{Z}}_{l}^{h}} &= -\frac{1}{\rho_{0}} 6 \alpha_{l} K_{l} \frac{\partial \Psi_{\alpha}\left(\operatorname{tr} \boldsymbol{H}^{h}, \theta^{h}\right)}{\partial \theta^{h}} \theta^{h}, \\
\frac{\partial c^{h}}{\partial \chi_{l}^{h}} &= -\frac{1}{\rho_{0}} K_{l} \frac{\partial^{2} \Psi_{\beta}\left(\theta^{h}\right)}{\partial \theta^{h^{2}}} \theta^{h}\left(3 \beta_{l}\left(\theta^{h}-\theta_{0}\right)+\chi_{l}^{h}\right)-\frac{1}{\rho_{0}} 6 \beta_{l} K_{l} \frac{\partial \Psi_{\beta}\left(\theta^{h}\right)}{\partial \theta^{h}} \theta^{h},
\end{aligned}
\tag{A.33}
$$

where we have dropped the time superscript $(\bullet)_{n+c_i}$ for the sake of notational simplicity. The change with respect to strain $\boldsymbol{H}(\boldsymbol{X}, t)$ is given by

$$
\frac{\partial c_{n+c_{i}}^{h}}{\partial \boldsymbol{H}_{n+c_{i}}^{h}}=\frac{\partial c_{\text{eq}}^{h}}{\partial \boldsymbol{H}^{h}}=-\frac{1}{\rho_{0}} \psi_{7} \theta^{h} \boldsymbol{I}+\frac{1}{\rho_{0}} \sum_{r} 6 \alpha_{r} K_{r} \frac{\partial \Psi_{\alpha}\left(\operatorname{tr} \boldsymbol{H}^{h}, \theta^{h}\right)}{\partial \theta^{h}} \theta^{h} \boldsymbol{I}.
\tag{A.34}
$$

The partial derivative with respect to temperature $\theta(\boldsymbol{X},t)$ is expediently split into equilibrium and transient parts,

$$\frac{\partial c^h_{n+c_i}}{\partial \theta^h_{n+c_i}} = \frac{\partial c^h_{\mathrm{eq,n+c_i}}}{\partial \theta^h_{n+c_i}} + \frac{\partial c^h_{\mathrm{tr,n+c_i}}}{\partial \theta^h_{n+c_i}}. \tag{A.35}$$

The equilibrium contribution simply reads

$$\frac{c^h_{\mathrm{eq}}}{\partial \theta^h} = -\frac{1}{\rho_0}\psi_7\left(\mathrm{tr}\boldsymbol{H}^h\right) + \frac{1}{\rho_0}\psi_8, \tag{A.36}$$

while the transient contribution assumes the more complicated form

$$\begin{aligned}\frac{\partial c^h_{\mathrm{tr}}}{\partial \theta^h} = \frac{1}{\rho_0}\sum_r \Bigg[& 6\alpha_r K_r \frac{\partial \Psi_\alpha\left(\mathrm{tr}\boldsymbol{H}^h,\theta^h\right)}{\partial \theta^h}\left(\mathrm{tr}\boldsymbol{H}^h - \mathrm{tr}\boldsymbol{\mathcal{Z}}^h_r\right) - 27\beta_r^2 K_r \frac{\partial \Psi_\beta\left(\theta^h\right)}{\partial \theta^h}\theta^h \\ & - \frac{1}{2}\frac{\partial^2 \Psi_\beta\left(\theta^h\right)}{\partial {\theta^h}^2} K_r\left(3\beta_r\left(\theta^h-\theta_0\right)+\chi^h_r\right)^2 - 9\beta_r^2 K_r \Psi_\beta\left(\theta^h\right) \\ & - 9\beta_r K_r \frac{\partial^2 \Psi_\beta\left(\theta^h\right)}{\partial {\theta^h}^2}\theta^h\left(3\beta_r\left(\theta^h-\theta_0\right)+\chi^h_r\right) \\ & - 6\beta_r K_r \frac{\partial \Psi_\beta\left(\theta^h\right)}{\partial \theta^h}\left(3\beta_r\left(\theta^h-\theta_0\right)+\chi^h_r\right)\Bigg].\end{aligned} \tag{A.37}$$

Influence of the Thermoviscoelastic Shift Factor

The thermoviscoelastic shift factor (3.68) is defined on page 62 in terms of the potential internal energy $U_{\mathrm{p}}(\boldsymbol{X},t)$. Its partial derivative with respect to the volumetric part of the internal variable $\boldsymbol{\mathcal{Z}}_l(\boldsymbol{X},t)$ reads

$$\frac{\partial a}{\partial \mathrm{tr}\boldsymbol{\mathcal{Z}}^h_l} = -C_1 \ln(10) \underbrace{10^{C_1\left(\frac{U^{\mathrm{ref}}_{\mathrm{p}}}{U_{\mathrm{p}}}-1\right)}}_{a} \frac{U^{\mathrm{ref}}_{\mathrm{p}}}{U^2_{\mathrm{c}}}\frac{\partial U_{\mathrm{p}}}{\partial \mathrm{tr}\boldsymbol{\mathcal{Z}}^h_l}, \tag{A.38}$$

where we have left out the time subscript $(\bullet)_{n+c_i}$ to allow for a shorthand notation. Here, the last term is given by the expression

$$\begin{aligned}\frac{\partial U_{\mathrm{p}}}{\partial \mathrm{tr}\boldsymbol{\mathcal{Z}}^h_l} = & -\frac{1}{\rho_0}\left(\Psi_K\left(\theta^h\right) - \frac{\partial \Psi_K\left(\theta^h\right)}{\partial \theta^h}\theta^h\right) K_l\left(\mathrm{tr}\boldsymbol{H}^h - \mathrm{tr}\boldsymbol{\mathcal{Z}}_l\right) \\ & - \frac{1}{\rho_0}\Psi_\alpha\left(\mathrm{tr}\boldsymbol{H}^h,\theta^h\right)3\alpha_l K_l\theta_0 - \frac{1}{\rho_0}\frac{\partial \Psi_\alpha\left(\mathrm{tr}\boldsymbol{H}^h,\theta^h\right)}{\partial \theta^h}\theta^h 3\alpha_l K_l\left(\theta^h-\theta_0\right) \\ & + \frac{1}{\rho_0}\left(\Psi_\alpha\left(\mathrm{tr}\boldsymbol{H}^h,\theta^h\right) - \frac{\partial \Psi_\alpha\left(\mathrm{tr}\boldsymbol{H}^h,\theta^h\right)}{\partial \theta^h}\theta^h\right) K_l\zeta^h_l.\end{aligned} \tag{A.39}$$

The corresponding change in terms of the deviatoric part of $\boldsymbol{\mathcal{Z}}_l(\boldsymbol{X},t)$ results in

$$\frac{\partial a}{\partial \mathrm{dev}\boldsymbol{\mathcal{Z}}^h_l} = -C_1 \ln(10) \underbrace{10^{C_1\left(\frac{U^{\mathrm{ref}}_{\mathrm{p}}}{U_{\mathrm{p}}}-1\right)}}_{a} \frac{U^{\mathrm{ref}}_{\mathrm{p}}}{U^2_{\mathrm{c}}}\frac{\partial U_{\mathrm{p}}}{\partial \mathrm{dev}\boldsymbol{\mathcal{Z}}^h_l}, \tag{A.40}$$

which requires the derivative shown below,

$$\frac{\partial U_{\mathrm{p}}}{\partial \mathrm{dev}\boldsymbol{\mathcal{Z}}_l^h} = -\frac{1}{\rho_0}\left(\Psi_G\left(\theta^h\right) - \frac{\partial \Psi_G\left(\theta^h\right)}{\partial \theta^h}\theta^h\right) 2G_l\left(\mathrm{dev}\boldsymbol{H}^h - \mathrm{dev}\boldsymbol{\mathcal{Z}}_l^h\right). \tag{A.41}$$

Similarly, we calculate the partial derivative with respect to internal variable $\zeta_l(\boldsymbol{X},t)$,

$$\frac{\partial a}{\partial \zeta_l^h} = -C_1 \ln(10) \underbrace{10^{C_1\left(\frac{U_{\mathrm{p}}^{\mathrm{ref}}}{U_{\mathrm{p}}}-1\right)}}_{a} \frac{U_{\mathrm{p}}^{\mathrm{ref}}}{U_{\mathrm{c}}^2}\frac{\partial U_{\mathrm{p}}}{\partial \zeta_l^h}, \tag{A.42}$$

which relies on the following expression

$$\frac{\partial U_{\mathrm{p}}}{\partial \zeta_l^h} = -\frac{1}{\rho_0}\left(\Psi_\alpha\left(\mathrm{tr}\boldsymbol{H}^h,\theta^h\right) - \frac{\partial \Psi_\alpha\left(\mathrm{tr}\boldsymbol{H}^h,\theta^h\right)}{\partial \theta^h}\theta^h\right) K_l\left(\mathrm{tr}\boldsymbol{H}^h - \mathrm{dev}\boldsymbol{\mathcal{Z}}_l^h\right). \tag{A.43}$$

The change with respect to the third internal variable $\chi_l(\boldsymbol{X},t)$ results in

$$\frac{\partial a}{\partial \chi_l^h} = -C_1 \ln(10) \underbrace{10^{C_1\left(\frac{U_{\mathrm{p}}^{\mathrm{ref}}}{U_{\mathrm{p}}}-1\right)}}_{a} \frac{U_{\mathrm{p}}^{\mathrm{ref}}}{U_{\mathrm{c}}^2}\frac{\partial U_{\mathrm{p}}}{\partial \chi_l^h}. \tag{A.44}$$

Here, the corresponding change of the potential internal energy reads

$$\begin{aligned}\frac{\partial U_{\mathrm{p}}}{\partial \chi_l^h} =& -\frac{1}{\rho_0}\Psi_\beta\left(\theta^h\right)3\beta_l K_l\theta_0 - \frac{1}{\rho_0}\frac{\partial \Psi_\beta\left(\theta^h\right)}{\partial \theta^h}\theta^h 3\beta_l K_l\left(\theta^h-\theta_0\right)\\ &+\frac{1}{\rho_0}\left(\Psi_\beta\left(\theta^h\right) - \frac{\partial \Psi_\beta\left(\theta^h\right)}{\partial \theta^h}\theta^h\right)K_l\chi_l^h.\end{aligned} \tag{A.45}$$

Next, we determine the partial derivative with respect to strain $\boldsymbol{H}(\boldsymbol{X},t)$. The volumetric change gives

$$\frac{\partial a}{\partial \mathrm{tr}\boldsymbol{H}^h} = -C_1 \ln(10) \underbrace{10^{C_1\left(\frac{U_{\mathrm{p}}^{\mathrm{ref}}}{U_{\mathrm{p}}}-1\right)}}_{a} \frac{U_{\mathrm{p}}^{\mathrm{ref}}}{U_{\mathrm{c}}^2}\frac{\partial U_{\mathrm{p}}}{\partial \mathrm{tr}\boldsymbol{H}^h}, \tag{A.46}$$

where the volumetric change of the potential internal energy becomes

$$\begin{aligned}\frac{\partial U_{\mathrm{p}}}{\partial \mathrm{tr}\boldsymbol{H}^h} =& \frac{1}{\rho_0}\psi_1\left(\mathrm{tr}\boldsymbol{H}^h\right) + \frac{1}{3\rho_0}(\mathrm{tr}\boldsymbol{\psi_3})\\ &+\frac{1}{\rho_0}\sum_r\Bigg[K_r\left(\mathrm{tr}\boldsymbol{H}^h\right) - \frac{\partial \Psi_\alpha\left(\mathrm{tr}\boldsymbol{H}^h,\theta^h\right)}{\partial \mathrm{tr}\boldsymbol{H}^h}3\alpha_r K_r\left(\mathrm{tr}\boldsymbol{\mathcal{Z}}_r^h\right)\theta_0\\ &\quad - \frac{\partial \Psi_\alpha\left(\mathrm{tr}\boldsymbol{H}^h,\theta^h\right)}{\partial \mathrm{tr}\boldsymbol{H}^h}K_r\left(\mathrm{tr}\boldsymbol{H}^h - \mathrm{tr}\boldsymbol{\mathcal{Z}}_r^h\right)\zeta_r^h\\ &\quad - \left(\Psi_K\left(\theta^h\right) - \frac{\partial \Psi_K\left(\theta^h\right)}{\partial \theta^h}\theta^h\right)K_r\left(\mathrm{tr}\boldsymbol{\mathcal{Z}}_r^h\right)\\ &\quad - \left(\Psi_\alpha\left(\mathrm{tr}\boldsymbol{H}^h,\theta^h\right) - \frac{\partial \Psi_\alpha\left(\mathrm{tr}\boldsymbol{H}^h,\theta^h\right)}{\partial \theta^h}\theta^h\right)K_r\zeta_r^h\Bigg].\end{aligned} \tag{A.47}$$

A. Derivation of the Material Tangent

The isochoric contribution follows to

$$\frac{\partial a}{\partial \mathrm{dev}\boldsymbol{H}^h} = -C_1 \ln(10) \underbrace{10^{C_1\left(\frac{U_\mathrm{p}^\mathrm{ref}}{U_\mathrm{p}}-1\right)}}_{a} \frac{U_\mathrm{p}^\mathrm{ref}}{U_\mathrm{c}^2} \frac{\partial U_\mathrm{p}}{\partial \mathrm{dev}\boldsymbol{H}^h}, \tag{A.48}$$

in terms of the corresponding change of the potential internal energy,

$$\begin{aligned}\frac{\partial U_\mathrm{p}}{\partial \mathrm{dev}\boldsymbol{H}^h} = &\frac{1}{\rho_0} 2\psi_2 \left(\mathrm{dev}\boldsymbol{H}^h\right) + \frac{1}{\rho_0} \mathrm{dev}\boldsymbol{\psi_3} \\ &+ \frac{1}{\rho_0} \sum_r \left(\Psi_G\left(\theta^h\right) - \frac{\partial \Psi_G\left(\theta^h\right)}{\partial \theta^h} \theta^h \right) 2G_r \left(\mathrm{dev}\boldsymbol{H}^h - \mathrm{dev}\boldsymbol{\mathfrak{Z}}_r^h\right).\end{aligned} \tag{A.49}$$

Finally, the partial derivative of the shift factor with respect to temperature $\theta(\boldsymbol{X}, t)$ yields

$$\frac{\partial a}{\partial \theta^h} = -C_1 \ln(10) \underbrace{10^{C_1\left(\frac{U_\mathrm{p}^\mathrm{ref}}{U_\mathrm{p}}-1\right)}}_{a} \frac{U_\mathrm{p}^\mathrm{ref}}{U_\mathrm{c}^2} \frac{\partial U_\mathrm{p}}{\partial \theta^h}, \tag{A.50}$$

where the last term is given by the expression

$$\begin{aligned}\frac{\partial U_\mathrm{p}}{\partial \theta^h} = \frac{1}{\rho_0} \sum_r \Bigg[&- 6\alpha_r K_r \frac{\partial \Psi_\alpha\left(\mathrm{tr}\boldsymbol{H}^h, \theta^h\right)}{\partial \theta^h} \left(\mathrm{tr}\boldsymbol{\mathfrak{Z}}_r^h\right) \theta^h - 6\beta_r K_r \frac{\partial \Psi_\beta\left(\theta^h\right)}{\partial \theta^h} \chi_r^h \theta^h \\ &- 3\beta_r K_r \frac{\partial^2 \Psi_\beta\left(\theta^h\right)}{\partial {\theta^h}^2} \theta^h \left(\theta^h - \theta_0\right) \chi_r^h - \frac{1}{2} \frac{\partial^2 \Psi_\beta\left(\theta^h\right)}{\partial {\theta^h}^2} \theta^h K_r \left(\chi_r^h\right)^2 \Bigg].\end{aligned} \tag{A.51}$$

B. Summary of the Material Parameters

Polyvinyl Butyral

$\alpha_\infty = 2.45 \times 10^{-4}\ \frac{1}{\mathrm{K}}$	[70, Tab. 1]
$c_\infty = 2.05 \times 10^{6}\ \frac{\mathrm{J}}{\mathrm{K\,m^3}} = 190.372\ \frac{\mathrm{kN\,cm}}{\mathrm{kg\,K}}$	[70, Tab. 1]
$\lambda_\infty = 2.36 \times 10^{-4}\ \frac{\mathrm{kN}}{\mathrm{K\,s}}$	[83]
$\frac{\partial c_\infty}{\partial \theta} = 2600\ \frac{\mathrm{J}}{\mathrm{K^2\,m^3}} = 2.6 \times 10^{-4}\ \frac{\mathrm{kN\,cm}}{\mathrm{K^2\,cm^3}}$	[70, Fig. 1]
$\frac{\partial \alpha_\infty}{\partial \theta} = 2 \times 10^{-7}\ \frac{1}{\mathrm{K^2}}$	assumption
$\frac{\partial K_\infty}{\partial \theta} = -0.507\ \frac{\mathrm{kN}}{\mathrm{K\,cm^2}}$	assumption
$\frac{\partial G_\infty}{\partial \theta} = 0\ \frac{\mathrm{kN}}{\mathrm{K\,cm^2}}$	assumption

Table B.1.: *Equilibrium* material parameters of PVB with respect to reference temperature θ_0 required for the input data shown in Table B.2. Note that the specific heat capacity above relates to constant pressure, which is different from the constant deformation specific heat capacity required as model input.

$\theta_0 = 293.15\,\mathrm{K}$	reference temperature
$\rho_0 = 1.078 \times 10^{-3}\ \frac{\mathrm{kg}}{\mathrm{cm^3}}$	[70, Tab. 1]
$\psi_1 = 200\ \frac{\mathrm{kN}}{\mathrm{cm^2}}$	[16]
$\psi_2 = 0.022005\ \frac{\mathrm{kN}}{\mathrm{cm^2}}$	[17]
$\psi_3 = 0\ \frac{\mathrm{kN}}{\mathrm{cm^2}}$	zero initial stresses
$\psi_4 = -0.147\ \frac{\mathrm{kN}}{\mathrm{K\,cm^2}}$	derived quantity
$\psi_5 = -6.856 \times 10^{-4}\ \frac{\mathrm{kN}}{\mathrm{K^2\,cm^2}}$	see Table 3.3
$\psi_6 = -0.507\ \frac{\mathrm{kN}}{\mathrm{K\,cm^2}}$	assumption
$\psi_7 = 7.1 \times 10^{-4}\ \frac{\mathrm{kN}}{\mathrm{K^2\,cm^2}}$	see formula (3.89) in Section 3.4.10
$\psi_8 = 3.6 \times 10^{-4}\ \frac{\mathrm{kN}}{\mathrm{K^2\,cm^2}}$	experimental fit
$\lambda_\infty = 2.36 \times 10^{-4}\ \frac{\mathrm{kN}}{\mathrm{K\,s}}$	[83]

Table B.2.: First set of model input data (11 *equilibrium* values for $\theta > \theta_g$) with respect to reference temperature θ_0 used for the simulations of PVB. Note that material inputs ψ_5 and ψ_8 relate to constant deformation. For the physical significance of the material parameters see Table 3.3 on page 52 and Figure 3.11 on page 70.

$K_{\mathrm{g}} = 265\ \frac{\mathrm{kN}}{\mathrm{cm}^2}$	assumption
$G_{\mathrm{g}} = 50.022005\ \frac{\mathrm{kN}}{\mathrm{cm}^2}$	assumption
$\alpha_{\mathrm{g}} = 1.57 \times 10^{-4}\ \frac{1}{\mathrm{K}}$	[70, Tab. 1]
$\lambda_g = 2.36 \times 10^{-4}\ \frac{\mathrm{kN}}{\mathrm{K\,s}}$	assumption
$\frac{\partial K_{\mathrm{g}}}{\partial \theta} = -0.637\ \frac{\mathrm{kN}}{\mathrm{K\,cm}^2}$	assumption
$\frac{\partial G_g}{\partial \theta} = -1.1666\ \frac{\mathrm{kN}}{\mathrm{K\,cm}^2}$	assumption
$\frac{\partial \alpha_{\mathrm{g}}}{\partial \theta} = 1.357 \times 10^{-7}\ \frac{1}{\mathrm{K}^2}$	assumption

Table B.3.: *Glassy* material parameters of PVB required for the input data shown in Table B.4.

$C_1 = 13$	experimental fit (usually DMTA)
$U_{\mathrm{p}}^{\mathrm{ref}} = 2.3\ \frac{\mathrm{kN}}{\mathrm{cm}^2}$	experimental fit
$\tilde{C_1} = -0.002\ \frac{1}{\mathrm{K}}$	derived from Table 3.5
$\tilde{C_2} = -0.0035\ \frac{1}{\mathrm{K}}$	derived from Table 3.5
$\tilde{C_3} = 0$	
$\tilde{C_4} = -0.0065\ \frac{1}{\mathrm{K}}$	experimental fit
$\tilde{C_5} = 0.000026\ \frac{1}{\mathrm{K}^2}$	experimental fit
$\tilde{C_6} = -0.023\ \frac{1}{\mathrm{K}}$	derived from Table 3.5

Table B.4.: Second set of model input data (8 *glassy* values for $\theta < \theta_{\mathrm{g}}$) used for the simulations of PVB. Note that the formulas from Table 3.5 on page 69 for the calculation of the parameters $\tilde{C_i}$ $(i = 1, \ldots, 6)$ represent first approximations stemming from the infinitely fast quench assumption. Thus, actual values chosen may differ. For the physical significance of the material parameters see Table 3.3 on page 54 and Figure 3.11 on page 70.

τ_l (in s)	G_l (in $\frac{\text{kN}}{\text{cm}^2}$)	K_l (in $\frac{\text{kN}}{\text{cm}^2}$)	α_l (in $\frac{1}{\text{K}}$)	β_l (in $\frac{1}{\text{K}}$)
10^{-7}	1.5500	0.00	0	0
10^{-6}	21.0000	0.00	0	0
10^{-5}	17.5000	0.65	-1×10^{-4}	0
10^{-4}	5.0000	3.25	-1×10^{-4}	0
10^{-3}	2.0000	6.50	-1×10^{-4}	-3.10×10^{-4}
10^{-2}	1.5000	9.10	-1×10^{-4}	-4.65×10^{-4}
10^{-1}	1.0000	9.75	-1×10^{-4}	-4.65×10^{-4}
10^{0}	0.2350	13.00	-1×10^{-4}	-4.65×10^{-4}
10^{1}	0.1000	13.00	-1×10^{-4}	-4.65×10^{-4}
10^{2}	0.0250	9.75	-1×10^{-4}	-3.10×10^{-4}
10^{3}	0.0150	0.00	0	0
10^{4}	0.0150	0.00	0	0
10^{5}	0.0100	0.00	0	0
10^{6}	0.0100	0.00	0	0
10^{7}	0.0035	0.00	0	0
10^{8}	0.0030	0.00	0	0

Table B.5.: Third set of model input data used for the simulation of PVB. The Prony parameters were chosen manually to fit experimental curves (in general, the shear-related parameters G_l follow from Dynamic Mechanical Thermal Analyses). The chosen shear relaxation spectrum is much wider than those of the thermosetting polymers to describe the long-term behavior of PVB more realistically.

Diglycidyl Ether of Bisphenol A

$\alpha_\infty = 2.0 \times 10^{-4}\ \frac{1}{\mathrm{K}}$	[41, Tab. 4]
$c_\infty = 2.48 \times 10^{6}\ \frac{\mathrm{J}}{\mathrm{K\,m^3}} = 211\ \frac{\mathrm{kN\,cm}}{\mathrm{kg\,K}}$	[41, Tab. 4]
$\lambda_\infty = 2 \times 10^{-4}\ \frac{\mathrm{kN}}{\mathrm{K\,s}}$	assumption
$\frac{\partial c_\infty}{\partial \theta} = 2822.4\ \frac{\mathrm{J}}{\mathrm{K^2\,m^3}} = 2.8224 \times 10^{-4}\ \frac{\mathrm{kN\,cm}}{\mathrm{K^2\,cm^3}}$	[41, Tab. 4]
$\frac{\partial \alpha_\infty}{\partial \theta} = 1.33 \times 10^{-7}\ \frac{1}{\mathrm{K^2}}$	[41, Tab. 4]
$\frac{\partial K_\infty}{\partial \theta} = -1.2\ \frac{\mathrm{kN}}{\mathrm{K\,cm^2}}$	[41, Tab. 4]
$\frac{\partial G_\infty}{\partial \theta} = 0\ \frac{\mathrm{kN}}{\mathrm{K\,cm^2}}$	assumption

Table B.6.: *Equilibrium* material parameters of DGEBA with respect to reference temperature θ_0 required for the input data shown in Table B.7. Note that the specific heat capacity above relates to constant pressure, which is different from the constant deformation specific heat capacity required as model input. Further note that the constitutive model developed here bases on the *linear* CTE, while the reference uses the *cubic* CTE.

$\theta_0 = 348.15\,\mathrm{K}$	[41, Tab. 4]
$\rho_0 = 1.176 \times 10^{-3}\ \frac{\mathrm{kg}}{\mathrm{cm^3}}$	[41, Tab. 4]
$\psi_1 = 320\ \frac{\mathrm{kN}}{\mathrm{cm^2}}$	[41, Tab. 4]
$\psi_2 = 0.445\ \frac{\mathrm{kN}}{\mathrm{cm^2}}$	[41, Tab. 4]
$\psi_3 = 0\ \frac{\mathrm{kN}}{\mathrm{cm^2}}$	zero initial stresses
$\psi_4 = -0.192\ \frac{\mathrm{kN}}{\mathrm{K\,cm^2}}$	derived quantity
$\psi_5 = -6.456 \times 10^{-4}\ \frac{\mathrm{kN}}{\mathrm{K^2\,cm^2}}$	see Table 3.3
$\psi_6 = -1.176\ \frac{\mathrm{kN}}{\mathrm{K\,cm^2}}$	[41, Tab. 4]
$\psi_7 = 1.31 \times 10^{-3}\ \frac{\mathrm{kN}}{\mathrm{K^2\,cm^2}}$	see formula (3.89) in Section 3.4.10
$\psi_8 = 6.4 \times 10^{-4}\ \frac{\mathrm{kN}}{\mathrm{K^2\,cm^2}}$	experimental fit, see also [41, Tab. 4]
$\lambda_\infty = 2 \times 10^{-4}\ \frac{\mathrm{kN}}{\mathrm{K\,s}}$	assumption

Table B.7.: First set of model input data (11 *equilibrium* values for $\theta > \theta_g$) with respect to reference temperature θ_0 used for the simulations of DGEBA. Note that material inputs ψ_5 and ψ_8 relate to constant deformation. For the physical significance of the material parameters see Table 3.3 on page 52 and Figure 3.11 on page 70.

$K_{\mathrm{g}} = 490\ \frac{\mathrm{kN}}{\mathrm{cm}^2}$	[41, Tab. 5]
$G_{\mathrm{g}} = 75\ \frac{\mathrm{kN}}{\mathrm{cm}^2}$	[41, Tab. 5]
$\alpha_{\mathrm{g}} = 8 \times 10^{-5}\ \frac{1}{\mathrm{K}}$	[41, Tab. 5]
$\lambda_g = 2 \times 10^{-4}\ \frac{\mathrm{kN}}{\mathrm{K\,s}}$	assumption
$\frac{\partial K_{\mathrm{g}}}{\partial \theta} = -1.4\ \frac{\mathrm{kN}}{\mathrm{K\,cm}^2}$	[41, Tab. 5]
$\frac{\partial G_g}{\partial \theta} = -0.42\ \frac{\mathrm{kN}}{\mathrm{K\,cm}^2}$	[41, Tab. 5]
$\frac{\partial \alpha_{\mathrm{g}}}{\partial \theta} = 2.33 \times 10^{-7}\ \frac{1}{\mathrm{K}^2}$	[41, Tab. 5]

Table B.8.: *Glassy* material parameters of DGEBA required for the input data shown in Table B.9. Note that the constitutive model developed here bases on the *linear* CTE, while the reference uses the *cubic* CTE.

$C_1 = 16.5$	[41, Tab. 5]
$U_{\mathrm{p}}^{\mathrm{ref}} = 2.5\ \frac{\mathrm{kN\,cm}}{\mathrm{cm}^3}$	experimental fit, see also [41, Tab. 6]
$\tilde{C}_1 = -0.002682461\ \frac{1}{\mathrm{K}}$	derived from Table 3.5
$\tilde{C}_2 = -0.004595999\ \frac{1}{\mathrm{K}}$	derived from Table 3.5
$\tilde{C}_3 = 0$	
$\tilde{C}_4 = 0.001\ \frac{1}{\mathrm{K}}$	experimental fit
$\tilde{C}_5 = 0\ \frac{1}{\mathrm{K}^2}$	experimental fit
$\tilde{C}_6 = -0.005633168\ \frac{1}{\mathrm{K}}$	derived from Table 3.5

Table B.9.: Second set of model input data (8 *glassy* values for $\theta < \theta_{\mathrm{g}}$) used for the simulations of DGEBA. Note that the formulas from Table 3.5 on page 69 for the calculation of the parameters $\tilde{C}_i$ $(i = 1, \ldots, 6)$ represent first approximations stemming from the infinitely fast quench assumption. Thus, actual values chosen may differ. For the physical significance of the material parameters see Table 3.3 on page 54 and Figure 3.11 on page 70.

τ_l (in s)	G_l (in $\frac{\mathrm{kN}}{\mathrm{cm}^2}$)	K_l (in $\frac{\mathrm{kN}}{\mathrm{cm}^2}$)	α_l (in $\frac{1}{\mathrm{K}}$)	β_l (in $\frac{1}{\mathrm{K}}$)
10^{-8}	0.746	0.00	0	0
10^{-7}	1.491	0.00	0	0
10^{-6}	2.237	0.00	0	0
10^{-5}	5.219	1.19	-2×10^{-4}	-2.295×10^{-4}
10^{-4}	4.473	5.95	-2×10^{-4}	-2.295×10^{-4}
10^{-3}	8.947	10.20	-2×10^{-4}	-1.295×10^{-4}
10^{-2}	12.674	16.66	-2×10^{-4}	-2.040×10^{-4}
10^{-1}	14.165	34.00	-2×10^{-4}	-1.530×10^{-4}
10^{0}	13.420	39.10	-2×10^{-4}	-2.040×10^{-4}
10^{1}	8.470	34.00	-2×10^{-4}	-2.550×10^{-4}
10^{2}	2.237	17.00	-2×10^{-4}	-4.335×10^{-4}
10^{3}	0.000	8.50	-2×10^{-4}	-4.080×10^{-4}
10^{4}	0.000	3.40	-2×10^{-4}	-2.550×10^{-4}

Table B.10.: Third set of model input data used for the simulation of DGEBA. The Prony parameters were chosen manually to fit relaxation spectra found in the literature [41, Tab. 6].

Epoxy 459

$\alpha_\infty = 2.23333 \times 10^{-4}\ \frac{1}{\mathrm{K}}$	[41, Tab. 4]
$c_\infty = 2.796 \times 10^{6}\ \frac{\mathrm{J}}{\mathrm{K\,m^3}} = 233\ \frac{\mathrm{kN\,cm}}{\mathrm{kg\,K}}$	[41, Tab. 4]
$\lambda_\infty = 2 \times 10^{-4}\ \frac{\mathrm{kN}}{\mathrm{K\,s}}$	assumption
$\frac{\partial c_\infty}{\partial \theta} = 2160\ \frac{\mathrm{J}}{\mathrm{K^2\,m^3}} = 2.16 \times 10^{-4}\ \frac{\mathrm{kN\,cm}}{\mathrm{K^2\,cm^3}}$	[41, Tab. 4]
$\frac{\partial \alpha_\infty}{\partial \theta} = 1 \times 10^{-7}\ \frac{1}{\mathrm{K^2}}$	[41, Tab. 4]
$\frac{\partial K_\infty}{\partial \theta} = -1.2\ \frac{\mathrm{kN}}{\mathrm{K\,cm^2}}$	[41, Tab. 4]
$\frac{\partial G_\infty}{\partial \theta} = 0\ \frac{\mathrm{kN}}{\mathrm{K\,cm^2}}$	assumption

Table B.11.: *Equilibrium* material parameters of epoxy 459 with respect to reference temperature θ_0 required for the input data shown in Table B.12. Note that the specific heat capacity above relates to constant pressure, which is different from the constant deformation specific heat capacity required as model input. Further note that the constitutive model developed here bases on the *linear* CTE, while the reference uses the *cubic* CTE.

$\theta_0 = 378.15\,\mathrm{K}$	[41, Tab. 4]
$\rho_0 = 1.2 \times 10^{-3}\ \frac{\mathrm{kg}}{\mathrm{cm^3}}$	[41, Tab. 4]
$\psi_1 = 320\ \frac{\mathrm{kN}}{\mathrm{cm^2}}$	[41, Tab. 4]
$\psi_2 = 0.65\ \frac{\mathrm{kN}}{\mathrm{cm^2}}$	[41, Tab. 4]
$\psi_3 = 0\ \frac{\mathrm{kN}}{\mathrm{cm^2}}$	zero initial stresses
$\psi_4 = -0.2144\ \frac{\mathrm{kN}}{\mathrm{K\,cm^2}}$	derived quantity
$\psi_5 = -6.792 \times 10^{-4}\ \frac{\mathrm{kN}}{\mathrm{K^2\,cm^2}}$	see Table 3.3
$\psi_6 = -0.54\ \frac{\mathrm{kN}}{\mathrm{K\,cm^2}}$	[41, Tab. 4]
$\psi_7 = 6.7 \times 10^{-4}\ \frac{\mathrm{kN}}{\mathrm{K^2\,cm^2}}$	see formula (3.89) in Section 3.4.10
$\psi_8 = 3.5 \times 10^{-4}\ \frac{\mathrm{kN}}{\mathrm{K^2\,cm^2}}$	experimental fit
$\lambda_\infty = 2 \times 10^{-4}\ \frac{\mathrm{kN}}{\mathrm{K\,s}}$	assumption

Table B.12.: First set of model input data (11 *equilibrium* values for $\theta > \theta_\mathrm{g}$) with respect to reference temperature θ_0 used for the simulations of epoxy 459. Note that material inputs ψ_5 and ψ_8 relate to constant deformation. For the physical significance of the material parameters see Table 3.3 on page 52 and Figure 3.11 on page 70.

$K_{\mathrm{g}} = 490\ \frac{\mathrm{kN}}{\mathrm{cm}^2}$	[41, Tab. 5]
$G_{\mathrm{g}} = 93.36\ \frac{\mathrm{kN}}{\mathrm{cm}^2}$	[41, Tab. 5], slightly modified here
$\alpha_{\mathrm{g}} = 9.666 \times 10^{-5}\ \frac{1}{\mathrm{K}}$	[41, Tab. 5]
$\lambda_g = 2 \times 10^{-4}\ \frac{\mathrm{kN}}{\mathrm{K\,s}}$	assumption
$\frac{\partial K_{\mathrm{g}}}{\partial \theta} = -1.4\ \frac{\mathrm{kN}}{\mathrm{K\,cm}^2}$	[41, Tab. 5]
$\frac{\partial G_g}{\partial \theta} = -0.42\ \frac{\mathrm{kN}}{\mathrm{K\,cm}^2}$	[41, Tab. 5]
$\frac{\partial \alpha_{\mathrm{g}}}{\partial \theta} = 3.33 \times 10^{-7}\ \frac{1}{\mathrm{K}^2}$	[41, Tab. 5]

Table B.13.: *Glassy* material parameters of epoxy 459 required for the input data shown in Table B.14. Note that the constitutive model developed here bases on the *linear* CTE, while the reference uses the *cubic* CTE.

$C_1 = 11$	[41, Tab. 5]
$U_{\mathrm{p}}^{\mathrm{ref}} = 1.836\ \frac{\mathrm{kN\,cm}}{\mathrm{cm}^3}$	[41, Tab. 7]
$\tilde{C}_1 = -0.005058824\ \frac{1}{\mathrm{K}}$	derived from Table 3.5
$\tilde{C}_2 = -0.002146815\ \frac{1}{\mathrm{K}}$	derived from Table 3.5
$\tilde{C}_3 = 0$	
$\tilde{C}_4 = -0.003\ \frac{1}{\mathrm{K}}$	experimental fit
$\tilde{C}_5 = 0.0000075\ \frac{1}{\mathrm{K}^2}$	experimental fit
$\tilde{C}_6 = -0.00166\ \frac{1}{\mathrm{K}}$	derived from Table 3.5

Table B.14.: Second set of model input data (8 *glassy* values for $\theta < \theta_{\mathrm{g}}$) used for the simulations of epoxy 459. Note that the formulas from Table 3.5 on page 69 for the calculation of the parameters $\tilde{C}_i$ $(i = 1, \ldots, 6)$ represent first approximations stemming from the infinitely fast quench assumption. Thus, actual values chosen may differ. For the physical significance of the material parameters see Table 3.3 on page 54 and Figure 3.11 on page 70.

τ_l (in s)	G_l (in $\frac{\mathrm{kN}}{\mathrm{cm}^2}$)	K_l (in $\frac{\mathrm{kN}}{\mathrm{cm}^2}$)	α_l (in $\frac{1}{\mathrm{K}}$)	β_l (in $\frac{1}{\mathrm{K}}$)
10^{-8}	5.602	0.0	0	0
10^{-7}	6.535	0.0	0	0
10^{-6}	8.402	0.0	0	0
10^{-5}	10.270	5.1	-1.7×10^{-4}	-1.82×10^{-4}
10^{-4}	13.070	8.5	-1.7×10^{-4}	-1.82×10^{-4}
10^{-3}	14.938	13.6	-1.7×10^{-4}	-1.82×10^{-4}
10^{-2}	14.938	18.7	-1.7×10^{-4}	-1.82×10^{-4}
10^{-1}	13.070	30.6	-1.7×10^{-4}	-2.08×10^{-4}
10^{0}	4.668	42.5	-1.7×10^{-4}	-1.30×10^{-4}
10^{1}	1.867	34.0	-1.7×10^{-4}	-2.47×10^{-4}
10^{2}	0.000	13.6	-1.7×10^{-4}	-3.77×10^{-4}
10^{3}	0.000	3.4	-1.7×10^{-4}	-3.12×10^{-4}

Table B.15.: Third set of model input data used for the simulation of epoxy 459. The Prony parameters were chosen manually to fit relaxation spectra found in the literature [41, Tab. 7].

TCR Composites Epoxy 3325

$\alpha_\infty = 1.833 \times 10^{-4}\ \frac{1}{\mathrm{K}}$	[41, Tab. 4]
$c_\infty = 2.4034 \times 10^{6}\ \frac{\mathrm{J}}{\mathrm{K\,m^3}} = 197\ \frac{\mathrm{kN\,cm}}{\mathrm{kg\,K}}$	[41, Tab. 4]
$\lambda_\infty = 2 \times 10^{-4}\ \frac{\mathrm{kN}}{\mathrm{K\,s}}$	assumption
$\frac{\partial c_\infty}{\partial \theta} = 4148\ \frac{\mathrm{J}}{\mathrm{K^2\,m^3}} = 4.184 \times 10^{-4}\ \frac{\mathrm{kN\,cm}}{\mathrm{K^2\,cm^3}}$	[41, Tab. 4]
$\frac{\partial \alpha_\infty}{\partial \theta} = 3.33 \times 10^{-8}\ \frac{1}{\mathrm{K^2}}$	[41, Tab. 4]
$\frac{\partial K_\infty}{\partial \theta} = -1.2\ \frac{\mathrm{kN}}{\mathrm{K\,cm^2}}$	[41, Tab. 4]
$\frac{\partial G_\infty}{\partial \theta} = 0\ \frac{\mathrm{kN}}{\mathrm{K\,cm^2}}$	assumption

Table B.16.: *Equilibrium* material parameters of epoxy 3325 with respect to reference temperature θ_0 required for the input data shown in Table B.17. Note that the specific heat capacity above relates to constant pressure, which is different from the constant deformation specific heat capacity required as model input. Further note that the constitutive model developed here bases on the *linear* CTE, while the reference uses the *cubic* CTE.

$\theta_0 = 383.15\,\mathrm{K}$	[41, Tab. 4]
$\rho_0 = 1.22 \times 10^{-3}\ \frac{\mathrm{kg}}{\mathrm{cm^3}}$	[41, Tab. 4]
$\psi_1 = 320\ \frac{\mathrm{kN}}{\mathrm{cm^2}}$	[41, Tab. 4]
$\psi_2 = 1.2\ \frac{\mathrm{kN}}{\mathrm{cm^2}}$	[41, Tab. 4]
$\psi_3 = 0\ \frac{\mathrm{kN}}{\mathrm{cm^2}}$	zero initial stresses
$\psi_4 = -0.176\ \frac{\mathrm{kN}}{\mathrm{K\,cm^2}}$	derived quantity
$\psi_5 = -5.9292 \times 10^{-4}\ \frac{\mathrm{kN}}{\mathrm{K^2\,cm^2}}$	see Table 3.3
$\psi_6 = -0.8\ \frac{\mathrm{kN}}{\mathrm{K\,cm^2}}$	assumption
$\psi_7 = 8.48 \times 10^{-4}\ \frac{\mathrm{kN}}{\mathrm{K^2\,cm^2}}$	see formula (3.89) in Section 3.4.10
$\psi_8 = 5.8 \times 10^{-4}\ \frac{\mathrm{kN}}{\mathrm{K^2\,cm^2}}$	experimental fit
$\lambda_\infty = 2 \times 10^{-4}\ \frac{\mathrm{kN}}{\mathrm{K\,s}}$	assumption

Table B.17.: First set of model input data (11 *equilibrium* values for $\theta > \theta_\mathrm{g}$) with respect to reference temperature θ_0 used for the simulations of epoxy 3325. Note that material inputs ψ_5 and ψ_8 relate to constant deformation. For the physical significance of the material parameters see Table 3.3 on page 52 and Figure 3.11 on page 70.

$K_{\mathrm{g}} = 490\ \frac{\mathrm{kN}}{\mathrm{cm}^2}$	[41, Tab. 5]
$G_{\mathrm{g}} = 88.8\ \frac{\mathrm{kN}}{\mathrm{cm}^2}$	[41, Tab. 5]
$\alpha_{\mathrm{g}} = 9.16 \times 10^{-5}\ \frac{1}{\mathrm{K}}$	[41, Tab. 5]
$\lambda_g = 2 \times 10^{-4}\ \frac{\mathrm{kN}}{\mathrm{K\,s}}$	assumption
$\frac{\partial K_{\mathrm{g}}}{\partial \theta} = -1.4\ \frac{\mathrm{kN}}{\mathrm{K\,cm}^2}$	[41, Tab. 5]
$\frac{\partial G_g}{\partial \theta} = -0.42\ \frac{\mathrm{kN}}{\mathrm{K\,cm}^2}$	[41, Tab. 5]
$\frac{\partial \alpha_{\mathrm{g}}}{\partial \theta} = 3.33 \times 10^{-7}\ \frac{1}{\mathrm{K}^2}$	[41, Tab. 5]

Table B.18.: *Glassy* material parameters of epoxy 3325 required for the input data shown in Table B.19. Note that the constitutive model developed here bases on the *linear* CTE, while the reference uses the *cubic* CTE.

$C_1 = 18.4$	[41, Tab. 5]
$U_{\mathrm{p}}^{\mathrm{ref}} = 1.6714\ \frac{\mathrm{kN\,cm}}{\mathrm{cm}^3}$	[41, Tab. 7]
$\tilde{C}_1 = -0.003529412\ \frac{1}{\mathrm{K}}$	derived from Table 3.5
$\tilde{C}_2 = -0.004283558\ \frac{1}{\mathrm{K}}$	derived from Table 3.5
$\tilde{C}_3 = 0$	
$\tilde{C}_4 = -0.001\ \frac{1}{\mathrm{K}}$	experimental fit
$\tilde{C}_5 = 0$	experimental fit
$\tilde{C}_6 = -0.0022\ \frac{1}{\mathrm{K}}$	derived from Table 3.5

Table B.19.: Second set of model input data (8 *glassy* values for $\theta < \theta_{\mathrm{g}}$) used for the simulations of epoxy 3325. Note that the formulas from Table 3.5 on page 69 for the calculation of the parameters $\tilde{C}_i$ $(i = 1, \ldots, 6)$ represent first approximations stemming from the infinitely fast quench assumption. Thus, actual values chosen may differ. For the physical significance of the material parameters see Table 3.3 on page 54 and Figure 3.11 on page 70.

τ_l (in s)	G_l (in $\frac{\text{kN}}{\text{cm}^2}$)	K_l (in $\frac{\text{kN}}{\text{cm}^2}$)	α_l (in $\frac{1}{\text{K}}$)	β_l (in $\frac{1}{\text{K}}$)
10^{-8}	0.888	0.0	0	0
10^{-7}	1.776	0.0	0	0
10^{-6}	3.552	0.0	0	0
10^{-5}	4.440	0.0	0	0
10^{-4}	7.104	6.8	-1.2×10^{-4}	-1.7333×10^{-4}
10^{-3}	8.880	11.9	-1.2×10^{-4}	-1.7333×10^{-4}
10^{-2}	14.208	15.3	-1.2×10^{-4}	-1.7333×10^{-4}
10^{-1}	14.208	18.7	-1.2×10^{-4}	-1.7333×10^{-4}
10^{0}	12.432	20.4	-1.2×10^{-4}	-1.7333×10^{-4}
10^{1}	11.544	25.5	-1.2×10^{-4}	-1.7333×10^{-4}
10^{2}	5.328	23.8	-1.2×10^{-4}	-1.7333×10^{-4}
10^{3}	4.440	23.8	-1.2×10^{-4}	-1.7333×10^{-4}
10^{4}	0.000	13.6	-1.2×10^{-4}	-1.7333×10^{-4}
10^{5}	0.000	10.2	-1.2×10^{-4}	-1.7333×10^{-4}

Table B.20.: Third set of model input data used for the simulation of epoxy 3325. The Prony parameters were chosen manually to fit relaxation spectra found in the literature [41, Tab. 7].

Bibliography

[1] P. Davies and J. Vitkala. "Delamination Issues with Laminated Glass - Causes and Prevention". In: *GLASS PROCESSING DAYS, 8th, International conference on architectural and automotive glass*. Tamglass, 2003, pp. 427–431. ISBN: 9529159102.

[2] seele. "Strasbourg Railway Station". 2006. URL: https://seele.com/references/strasbourg-railway-station (visited on 06/08/2022).

[3] kuraray. "Mowital® Thin Film". URL: https://www.kuraray.eu/products-solutions/polyvinyl-butyral (visited on 06/08/2022).

[4] J. Wang et al. "Thermomechanical Modeling of Amorphous Glassy Polymer Undergoing Large Viscoplastic Deformation: 3-Points Bending and Gas-Blow Forming". In: *Polymers* 11.4 (2019), p. 654.

[5] R. Fleischhauer et al. "A constitutive model for finite deformation of amorphous polymers". In: *International Journal of Mechanical Sciences* 65.1 (2012), pp. 48–63.

[6] J. Bouvard et al. "An internal state variable material model for predicting the time, thermomechanical, and stress state dependence of amorphous glassy polymers under large deformation". In: *International Journal of Plasticity* 42 (2013), pp. 168–193.

[7] C. Miehe et al. "Coupled thermoviscoplasticity of glassy polymers in the logarithmic strain space based on the free volume theory". In: *International Journal of Solids and Structures* 48.13 (2011), pp. 1799–1817.

[8] C. Miehe, S. Göktepe, and J. M. Diez. "Finite viscoplasticity of amorphous glassy polymers in the logarithmic strain space". In: *International Journal of Solids and Structures* 46.1 (2009), pp. 181–202.

[9] L. Anand et al. "A thermo-mechanically coupled theory for large deformations of amorphous polymers. Part I: Formulation". In: *International Journal of Plasticity* 25.8 (2009), pp. 1474–1494.

[10] N. M. Ames et al. "A thermo-mechanically coupled theory for large deformations of amorphous polymers. Part II: Applications". In: *International Journal of Plasticity* 25.8 (2009), pp. 1495–1539.

[11] C. Buckley. "Glass-rubber constitutive model for amorphous polymers near the glass transition". In: *Polymer* 36.17 (1995), pp. 3301–3312.

[12] V. Srivastava et al. "A thermo-mechanically-coupled large-deformation theory for amorphous polymers in a temperature range which spans their glass transition". In: *International Journal of Plasticity* 26.8 (2010), pp. 1138–1182.

[13] J. Richeton et al. "Modeling and validation of the large deformation inelastic response of amorphous polymers over a wide range of temperatures and strain rates". In: *International Journal of Solids and Structures* 44.24 (2007), pp. 7938–7954.

[14] R. Xiao and T. D. Nguyen. "An effective temperature theory for the nonequilibrium behavior of amorphous polymers". In: *Journal of the Mechanics and Physics of Solids* 82 (2015), pp. 62–81.

[15] R. B. Dupaix and M. C. Boyce. "Constitutive modeling of the finite strain behavior of amorphous polymers in and above the glass transition". In: *Mechanics of Materials* 39.1 (2007), pp. 39–52.

[16] A. V. Duser, A. Jagota, and S. J. Bennison. "Analysis of Glass/Polyvinyl Butyral Laminates Subjected to Uniform Pressure". In: *Journal of Engineering Mechanics* 125.4 (1999), pp. 435–442.

[17] J. K. Kuntsche. "Mechanisches Verhalten von Verbundglas unter zeitabhängiger Belastung und Explosionsbeanspruchung". PhD thesis. Darmstadt, Universität, FB 13, Bau- und Umweltingenieurwissenschaften, 2015.

[18] W. Stevels et al. "A Comparison of Different Methodologies for PVB Interlayer Modulus Characterization". In: *Challenging Glass Conference Proceedings* (2016), Vol. 5 (2016): Challenging Glass 5.

[19] F. Pelayo et al. "Study of the time-temperature-dependent behaviour of PVB: Application to laminated glass elements". In: *Thin-Walled Structures* 119 (2017), pp. 324–331.

[20] T. Bermbach. "Zum Resttragverhalten von Verbundsicherheitsglas unter kombinierter Luftstoß-Temperatur-Belastung". PhD thesis. Universität der Bundeswehr München, Fakultät für Bauingenieurwesen und Umweltwissenschaften, 2017.

[21] T. Hána et al. "Determination of PVB interlayer's shear modulus and its effect on normal stress distribution in laminated glass panels". In: *IOP Conference Series: Materials Science and Engineering* 251 (2017), p. 012076.

[22] M. Vokáč et al. "Viscoelastic Properties of PVB Interlayer for Laminated Glass Structures Used in Building Reconstructions". In: *Key Engineering Materials* 808 (2019), pp. 115–122.

[23] T. Hána et al. "Experimental and Numerical Study of Viscoelastic Properties of Polymeric Interlayers Used for Laminated Glass: Determination of Material Parameters". In: *Materials* 12.14 (2019), p. 2241.

[24] C. Schuler. "Einfluss des Materialverhaltens von Polyvinylbutyral auf das Tragverhalten von Verbundsicherheitsglas in Abhängigkeit von Temperatur und Belastung". PhD thesis. Technische Universität München, Lehrstuhl für Massivbau, Institut für Baustoffe und Konstruktion, 2003.

[25] F. Ensslen. "Zum Tragverhalten von Verbund-Sicherheitsglas unter Berücksichtigung der Alterung der Polyvinylbutyral-Folie". PhD thesis. Ruhr-Universität Bochum, Fakultät für Bauingenieurwesen, 2005.

[26] A. Kott. "Zum Trag- und Resttragverhalten von Verbundsicherheitsglas". PhD thesis. Technische Hochschule Zürich, 2006.

[27] P. A. Hooper, B. R. K. Blackman, and J. P. Dear. "The mechanical behaviour of poly(vinyl butyral) at different strain magnitudes and strain rates". In: *Journal of Materials Science* 47.8 (2011), pp. 3564–3576.

[28] J. Barredo et al. "Viscoelastic vibration damping identification methods. Application to laminated glass". In: *Procedia Engineering* 10 (2011), pp. 3208–3213.

[29] L. Hermanns et al. "Transient dynamics analysis of laminated glass panels". In: 11th International Conference on Vibration Problems, 2013.

[30] L. Andreozzi et al. "Dynamic torsion tests to characterize the thermo-viscoelastic properties of polymeric interlayers for laminated glass". In: *Construction and Building Materials* 65 (2014), pp. 1–13.

[31] B. Liu, J. Xu, and Y. Li. "Constitutive Investigation on Viscoelasticity of PolyVinyl Butyral: Experiments Based on Dynamic Mechanical Analysis Method". In: *Advances in Materials Science and Engineering* 2014 (2014), pp. 1–10.

[32] M. A. Kraus et al. "Parameter identification methods for visco- and hyperelastic material models". In: *Glass Structures & Engineering* 2.2 (2017), pp. 147–167.

[33] X. Zhang et al. "The mechanical properties of Polyvinyl Butyral (PVB) at high strain rates". In: *Construction and Building Materials* 93 (2015), pp. 404–415.

[34] B. Ellis and B. C. Lim. "Stress-softening and strain-hardening of plasticized poly(vinyl butyral)". In: *Journal of Materials Science Letters* 3.7 (1984), pp. 620–622.

[35] J. Pelfrene et al. "Experimental Characterization and Finite Element Modelling of Strain-rate Dependent Hyperelastic Properties of PVB Interlayers". en. In: *Challenging Glass Conference Proceedings* (2018), Vol. 6 (2018): Challenging Glass 6.

[36] X. Xu et al. "Research on Temperature and Strain Rate Dependent Viscoelastic Response of Polyvinyl Butaral Film". In: *SAE International Journal of Materials and Manufacturing* 9.3 (2016), pp. 788–793.

[37] S. Chen, X. Chen, and X. Wu. "The mechanical behaviour of polyvinyl butyral at intermediate strain rates and different temperatures". In: *Construction and Building Materials* 182 (2018), pp. 66–79.

[38] V. Sackmann. "Untersuchungen zur Dauerhaftigkeit des Schubverbunds in Verbundsicherheitsglas mit unterschiedlichen Folien aus Polyvinylbutyral". PhD thesis. Technische Universität Münschen, Institut für Baustoffe und Konstruktion, Lehrstuhl für Metallbau, 2008.

[39] J. M. Caruthers et al. "A thermodynamically consistent, nonlinear viscoelastic approach for modeling glassy polymers". In: *Polymer* 45.13 (2004), pp. 4577–4597.

[40] D. B. Adolf et al. "Potential energy clock model: Justification and challenging predictions". In: *Journal of Rheology* 51.3 (2007), pp. 517–540.

[41] D. B. Adolf, R. S. Chambers, and J. M. Caruthers. "Extensive validation of a thermodynamically consistent, nonlinear viscoelastic model for glassy polymers". In: *Polymer* 45.13 (2004), pp. 4599–4621.

[42] B. R. Seth. "GENERALIZED STRAIN MEASURE WITH APPLICATIONS TO PHYSICAL PROBLEMS". Tech. rep. 1961, pp. 162–172.

[43] R. Hill. "Aspects of Invariance in Solid Mechanics". In: *Advances in Applied Mechanics*. Vol. 18. Elsevier, 1979, pp. 1–75.

[44] H. Hencky. "Über die Form des Elastizitätsgesetzes bei ideal elastischen Stoffen". In: *Zeitschrift für technische Physik* 9 (1928), pp. 215–220.

[45] P. Neff, B. Eidel, and R. J. Martin. "Geometry of Logarithmic Strain Measures in Solid Mechanics". In: *Archive for Rational Mechanics and Analysis* 222.2 (2016), pp. 507–572.

[46] L. Anand. "On H. Hencky's Approximate Strain-Energy Function for Moderate Deformations". In: *Journal of Applied Mechanics* 46.1 (1979), pp. 78–82.

[47] C. Miehe and M. Lambrecht. "Algorithms for computation of stresses and elasticity moduli in terms of Seth-Hill's family of generalized strain tensors". In: *Communications in Numerical Methods in Engineering* 17.5 (2001), pp. 337–353.

[48] G. A. Holzapfel. "Nonlinear solid mechanics : a continuum approach for engineering. A Continuum Approach for Engineering". Chichester New York: Wiley, 2000. ISBN: 047182304X.

[49] P. Haupt. "Continuum Mechanics and Theory of Materials". Berlin New York: Springer, 2000. ISBN: 354066114x.

[50] K. Hutter. "The foundations of thermodynamics, its basic postulates and implications. A review of modern thermodynamics". In: *Acta Mechanica* 27.1-4 (1977), pp. 1–54.

[51] R. A. Schapery. "Application of Thermodynamics to Thermomechanical, Fracture, and Birefringent Phenomena in Viscoelastic Media". In: *Journal of Applied Physics* 35.5 (1964), pp. 1451–1465.

[52] R. M. Christensen and P. M. Naghdi. "Linear non-isothermal viscoelastic solids". In: *Acta Mechanica* 3.1 (1967), pp. 1–12.

[53] R. M. Christensen. "THEORY OF VISCOELASTICITY : An Introduction". 2nd ed. New York: Academic Press, 1982. ISBN: 0121742520.

[54] J. T. Oden. "Finite Elements of Nonlinear Continua". New York: McGraw-Hill, 1972. ISBN: 0070476047.

[55] P. Haupt. "Viskoelastizität und Plastizität : Thermomechanisch Konsistente Materialgleichungen". Berlin New York: Springer-Verlag, 1977. ISBN: 0387077308.

[56] K. C. Valanis. "UNIFIED THEORY OF THERMOMECHANICAL BEHAVIOR OF VISCOELASTIC MATERIALS". In: *Mechanical Behavior of Materials under Dyncamic Loads*. Ed. by U. S. Lindholm. Springer Berlin Heidelberg, 1968, pp. 343–364.

[57] G. A. Maugin and W. Muschik. "Thermodynamics with Internal Variables. Part I. General Concepts". In: *Journal of Non-Equilibrium Thermodynamics* 19.3 (1994), pp. 217–249.

[58] M. F. Horstemeyer and D. J. Bammann. "Historical review of internal state variable theory for inelasticity". In: *International Journal of Plasticity* 26.9 (2010), pp. 1310–1334.

[59] G. A. Maugin. "The saga of internal variables of state in continuum thermomechanics (1893–2013)". In: *Mechanics Research Communications* 69 (2015), pp. 79–86.

[60] K. C. Valanis. "Irreversible Thermodynamics of Continuous Media". Springer Vienna, 1971. ISBN: 3211811273.

[61] H. Ziegler. "An Introduction to Thermomechanics". North-Holland Publishing Company Amsterdam, Oxford, New York, 1983. ISBN: 0-444-86503-9.

[62] B. D. Coleman and M. E. Gurtin. "Thermodynamics with Internal State Variables". In: *The Journal of Chemical Physics* 47.2 (1967), pp. 597–613.

[63] I. Müller. "A History of Thermodynamics". Springer-Verlag Berlin Heidelberg, 2007. ISBN: 3-540-46226-0.

[64] G. A. Maugin. "Internal Variables and Dissipative Structures". In: *Journal of Non-Equilibrium Thermodynamics* 15.2 (1990), pp. 173–192.

[65] J. Lubliner. "On the thermodynamic foundations of non-linear solid mechanics". In: *International Journal of Non-Linear Mechanics* 7.3 (1972), pp. 237–254.

[66] C. Truesdell. "Mechanics of Solids II". Ed. by S. Flügge. Vol. VIa/2. Encyclopedia of Physics. Berlin Heidelberg New York: Springer-Verlag, 1972. ISBN: 3540055355.

[67] H. F. Brinson and B. L. C. "Polymer Engineering Science and Viscoelasticity. An introduction". Springer, 2008. ISBN: 9780387738604.

[68] J. D. Ferry. "Viscoelastic properties of polymers". 2nd ed. New York: Wiley, 1970. ISBN: 0471257745.

[69] I. M. Ward and J. Sweeney. "Mechanical Properties of Solid Polymers". 3rd ed. John Wiley & Sons, Ltd, 2012. ISBN: 9781444319507.

[70] H. Wilski. "Die spezifische Wärme des Polyvinylbutyrals". In: *Angewandte Makromolekulare Chemie* 6.1 (1969), pp. 101–108.

[71] N. Tschoegl, W. G. Knauss, and I. Emri. "Poissons ratio in linear viscoelasticity - a critical review". In: *Mechanics of Time-Dependent Materials* 6.1 (2002), pp. 3–51.

[72] L. Grassia, A. D'Amore, and S. L. Simon. "On the viscoelastic Poisson's ratio in amorphous polymers". In: *Journal of Rheology* 54.5 (2010), pp. 1009–1022.

[73] L. C. E. Struik. "Volume Relaxation in Polymers". In: *Rheologica Acta* 5.4 (1966), pp. 303–311.

[74] H. Lu, X. Zhang, and W. G. Knauss. "Uniaxial, shear, and poisson relaxation and their conversion to bulk relaxation: Studies on poly(methyl methacrylate)". In: *Polymer Composites* 18.2 (1997), pp. 211–222.

[75] S. R. Lustig, R. M. Shay, and J. M. Caruthers. "Thermodynamic constitutive equations for materials with memory on a material time scale". In: *Journal of Rheology* 40.1 (1996), pp. 69–106.

[76] M. J. Crochet and P. M. Naghdi. "On Thermomechanics of Polymers in the Transition and Rubber Regions". In: *Journal of Rheology* 22.1 (1978), pp. 73–89.

[77] E. T. J. Klompen and L. E. Govaert. "Nonlinear Viscoelastic Behaviour of Thermorheologically Complex Materials". In: *Mechanics of Time-Dependent Materials* 3.1 (1999), pp. 49–69.

[78] D. J. Plazek. "1995 Bingham Medal Address: Oh, thermorheological simplicity, wherefore art thou?" In: *Journal of Rheology* 40.6 (Nov. 1996), pp. 987–1014.

[79] N. Tschoegl, W. G. Knauss, and I. Emri. "The Effect of Temperature and Pressure on the Mechanical Properties of Thermo- and/or Piezorheologically Simple Polymeric Materials in Thermodynamic Equilibrium – A Critical Review". In: *Mechanics of Time-Dependent Materials* 6.1 (2002), pp. 53–99.

[80] W. G. Knauss, I. Emri, and H. Lu. "The Springer Handbook of Experimental Solid Mechanics". Ed. by W. N. Sharpe. Third. Springer-Verlag New York Inc., 2008. ISBN: 9780387308777.

[81] R. A. Schapery. "On the characterization of nonlinear viscoelastic materials". In: *Polymer Engineering and Science* 9.4 (1969), pp. 295–310.

[82] L. C. E. Struik. "Physical Aging in Amorphous Polymers and Other Materials". PhD thesis. Technische Hochschule Delft, 1978.

[83] C. Carrot, A. Bendaoud, and C. Pillon. "Polyvinyl Butyral". In: *Handbook of Thermoplastics*. Second. CRC Press, 2015, pp. 89–137.

[84] E. Corroyer et al. "Characterization of Commercial Polyvinylbutyrals". In: *International Journal of Polymer Analysis and Characterization* 18.5 (2013), pp. 346–357.

[85] "Polyvinyl Butyral Market Size". URL: `https://www.grandviewresearch.com/industry-analysis/polyvinyl-butyral-pvb-market` (visited on 04/26/2022).

[86] A. K. Dhaliwal and J. N. Hay. "The characterization of polyvinyl butyral by thermal analysis". In: *Thermochimica Acta* 391.1-2 (2002), pp. 245–255.

[87] R. F. Clash and L. M. Rynkiewicz. "Thermal Expansion Properties of Plastic Materials". In: *Industrial & Engineering Chemistry* 36.3 (1944), pp. 279–282.

[88] R. Davies and G. Jones. "Thermodynamic and kinetic properties of glasses". In: *Advances in Physics* 2.7 (1953), pp. 370–410.

[89] A. V. Tobolsky. "Mechanische Eigenschaften und Struktur von Polymeren". Berliner Union, 1967.

[90] P. Dashora and G. Gupta. "On the temperature dependence of the thermal conductivity of linear amorphous polymers". In: *Polymer* 37.2 (1996), pp. 231–234.

[91] C. Popelar and K. Liechti. "A Distortion-Modified Free Volume Theory for Nonlinear Viscoelastic Behavior". In: *Mechanics of Time-Dependent Materials* 7.2 (2003), pp. 89–141.

[92] G. U. Losi and W. G. Knauss. "Free volume theory and nonlinear thermoviscoelasticity". In: *Polymer Engineering and Science* 32.8 (1992), pp. 542–557.

[93] W. G. Knauss and I. Emri. "Volume change and the nonlinearly thermo-viscoelastic constitution of polymers". In: *Polymer Engineering and Science* 27.1 (1987), pp. 86–100.

[94] R. M. Shay and J. M. Caruthers. "A predictive model for the effects of thermal history on the mechanical behavior of amorphous polymers". In: *Polymer Engineering and Science* 30.20 (1990), pp. 1266–1280.

[95] M. L. Williams, R. F. Landel, and J. D. Ferry. "The Temperature Dependence of Relaxation Mechanisms in Amorphous Polymers and Other Glass-forming Liquids". In: *Journal of the American Chemical Society* 77.14 (1955), pp. 3701–3707.

[96] S. Reese. "Thermomechanische Modellierung gummiartiger Polymerstrukturen". Habilitation. Hannover, Universität, FB Bauingenieur- und Vermessungswesen, 2001. ISBN: 3980725987.

[97] C. A. Felippa and T. L. Geers. "Partitioned analysis for coupled mechanical systems". In: *Engineering Computations* 5.2 (1988), pp. 123–133.

[98] C. A. Felippa, K. Park, and C. Farhat. "Partitioned analysis of coupled mechanical systems". In: *Computer Methods in Applied Mechanics and Engineering* 190.24-25 (2001), pp. 3247–3270.

[99] B. Markert. "Weak or Strong. On Coupled Problems In Continuum Mechanics". PhD thesis. Stuttgart, Universität, Lehrstuhl II, Institut für Mechanik (Bauwesen), 2010.

[100] S. Zinatbakhsh. "Coupled Problems in the Mechanics of Multi-Physics and Multi-Phase Materials". PhD thesis. Stuttgart, Universität, Lehrstuhl für Kontinuumsmechanik, 2015.

[101] J. Schröder, F. Gruttmann, and J. Löblein. "A simple orthotropic finite elastoplasticity model based on generalized stress-strain measures". In: *Computational Mechanics* 30.1 (2002), pp. 48–64.

[102] T. J. R. Hughes. "THE FINITE ELEMENT METHOD. Linear Static and Dynamic Finite Element Analysis". Prentice-Hall, 1987. ISBN: 013317025X.

[103] P. Wriggers. "Nonlinear finite element methods". Springer, 2008. ISBN: 9783540710004.

[104] E. Hairer and G. Wanner. "Solving Ordinary Differential Equations II. Stiff and Differential-Algebraic Problems". 2nd ed. Springer-Verlag Berlin Heidelberg, 1996. ISBN: 3540604529.

[105] S. Hartmann. "Finite-Elemente Berechnung inelastischer Kontinua. Interpretation als Algebro-Differentialgleichungssystem". Habilitation. Kassel, Universität, FB 15, Maschinenbau, 2003.

[106] L. M. Skvortsov. "How to avoid accuracy and order reduction in Runge–Kutta methods as applied to stiff problems". In: *Computational Mathematics and Mathematical Physics* 57.7 (2017), pp. 1124–1139.

[107] K. Burrage and L. Petzold. "On Order Reduction for Runge–Kutta Methods Applied to Differential/Algebraic Systems and to Stiff Systems of ODEs". In: *SIAM Journal on Numerical Analysis* 27.2 (1990), pp. 447–456.

[108] A. Prothero and A. Robinson. "On the stability and accuracy of one-step methods for solving stiff systems of ordinary differential equations". In: *Mathematics of Computation* 28.125 (1974), pp. 145–162.

[109] C. A. Kennedy and M. H. Carpenter. "Diagonally implicit Runge–Kutta methods for stiff ODEs". In: *Applied Numerical Mathematics* 146 (2019), pp. 221–244.

[110] C. Bendtsen and P. G. Thomsen. "Numerical Solution of Differential Algebraic Equations". Tech. rep. Denmark, University, DEPARTMENT OF MATHEMATICAL MODELLING, 1999.

[111] S. Hartmann. "A remark on the application of the Newton-Raphson method in non-linear finite element analysis". In: 36.2 (2005), pp. 100–116.

[112] Z.-Q. Qu. "MODEL ORDER REDUCTION TECHNIQUES. WITH APPLICATIONS IN FINITE-ELEMENT ANALYSIS". Springer-Verlag London Ltd., 2004. ISBN: 1852338075.

[113] J. Jørgensen, M. Kristensen, and P. Thomsen. "A Family of ESDIRK Integration Methods". In: *arXiv: Numerical Analysis* (2018).

[114] J. Rang. "An analysis of the Prothero–Robinson example for constructing new DIRK and ROW methods". In: *Journal of Computational and Applied Mathematics* 262 (2014), pp. 105–114.

[115] K. Strehmel, R. Weiner, and H. Podhaisky. "Numerik gewöhnlicher Differentialgleichungen. Nichtsteife, steife und differential-algebraische Gleichungen". Vieweg+Teubner Verlag, 2012.

[116] G. Söderlind. "Automatic Control and Adaptive Time-Stepping". In: *Numerical Algorithms* 31.1/4 (2002), pp. 281–310.

[117] J. C. Butcher. "Numerical methods for ordinary differential equations". Second. Wiley, 2008. ISBN: 9780470723357.

[118] E. Hairer, S. P. Nørsett, and G. Wanner. "Solving Ordinary Differential Equations I. Nonstiff Problems". 2nd ed. Berlin New York: Springer-Verlag Berlin Heidelberg, 1993. ISBN: 3540566708.

[119] P. Ellsiepen and S. Hartmann. "Remarks on the interpretation of current non-linear finite element analyses as differential–algebraic equations". In: (2001).

[120] K. Gustafsson. "Stepsize Selection in Implicit Runge-Kutta Methods Viewed as a Control Problem". In: *IFAC Proceedings Volumes* 26.2 (1993), pp. 495–498.

[121] K. Gustafsson. "Control-theoretic techniques for stepsize selection in implicit Runge-Kutta methods". In: *ACM Transactions on Mathematical Software* 20.4 (1994), pp. 496–517.

[122] kuraray. "Mowital B. Technical Data Sheet". June 2, 2022. URL: https://www.mowital.com/fileadmin/user_upload/MOWITAL/downloads/technical_data_sheets/TDS_Mowital_B_EN.pdf (visited on 06/02/2022).

[123] B. Wunderlich and H. Baur. "Heat Capacities of Linear High Polymers". In: *Advances in Polymer Science*. Springer-Verlag Berlin, Heidelberg, 1970, pp. 151–368.

[124] T. Grewer and H. Wilski. "Adiabatisches Kalorimeter zur Messung der spezifischen Wärme von Hochpolymeren". In: *Kolloid-Zeitschrift & Zeitschrift für Polymere* 229.2 (Feb. 1969), pp. 137–140.

[125] P. Dashora et al. "A Study of Temperature Dependence of Heat Capacity of Amorphous and Semi-Crystalline Polymers". In: *AIP Conference Proceedings*. AIP, 2010.